Strategies to Understand Li-ion Cell Failure and Improve Lifetime

by

Ahmed Eldesoky

Submitted in partial fulfilment of the requirements
for the degree of Doctor of Philosophy

at

Dalhousie University
Halifax, Nova Scotia
May 2023

Dalhousie University is located in Mi'kma'ki, the
ancestral and unceded territory of the Mi'kmaq.
We are all Treaty people.

To my parents whose support, sacrifices, and commitment to our family made this possible

Table of Contents

List of Tables

List of Figures

xiii

xiv

xix

Abstract

The skyrocketing production of electric vehicles means fewer batteries for energy storage and a strain on Li, Ni, and Co metal supplies. Therefore, improving the lifetime of Li-ion cell chemistries is crucial to enable vehicle-to-grid applications that can support the grid, and maximizing the energy output of Li-ion cells. This thesis considers ways to understand Li-ion cell failure and improve the lifetime.

First, the impact of cycling conditions on the lifetime of $Li(Ni_{0.8}Mn_{0.1}Co_{0.1})O_2$ (NMC811) cells was studied, and various post-mortem characterizations tools were used to probe cell degradation. Second, we examined the role that the graphite negative electrode material plays in the lifetime of NMC811 cells, and proposed a cell design that combines competitive graphite materials with ideal cycling conditions for NMC811 to yield long-lived cells.

Next, we studied the impact of electrolyte, Li excess, particle size, and NMC blending of the performance and degradation of $Li_{1+x}Mn_{2-x}O_4$ (LMO) cells at different temperatures. This led to the identification of an optimal LMO composition (i.e., x in $Li_{1+x}Mn_{2-x}O_4$), and development of mixed salt electrolyte systems that can hinder Mn dissolution and improve cell lifetime. Using this knowledge, we designed cells with large "single-crystalline" LMO particles and mixed salt electrolytes with competitive lifetime. Finally, we pivoted from the LMO system and used the mixed salt electrolytes to improve the high-temperature cycling performance of $LiFePO_4$ cells.

List of Abbreviations and Symbols Used

B_0	External magnetic field
m_n	Negative electrode mass
m_p	Positive electrode mass
Q_n	Negative electrode capacity
Q_p	Positive electrode capacity
δ_n	Negative electrode slippage
δ_p	Positive electrode slippage
°C	Degrees Celsius
2H	Hexagonal graphite
3R	Rhombohedral graphite
AG	Artificial Graphite
BET	Brunauer-Emmett-Teller
C/x	"C-rate" (dis)charging time
CB	Carbon black
CC	Constant current
CCCV	Constant current constant voltage
CE	Coulombic efficiency
CEI	Cathode electrolyte interphase
CIE	Columbic inefficiency
CMC	Carboxymethyl cellulose
D_0	Initial discharge capacity
D_1	First discharge capacity after storage
D_2	Second discharge capacity after storage
DCA	Differential capacity analysis
DEC	Diethyl carbonate
DMC	Dimethyl carbonate
DOD	Depth-of-discharge

DTD	Ethylene sulfate
e^-	Electron, elementary charge
E_a	Activation energy
EC	Ethylene carbonate
EIS	Electrochemical impedance spectroscopy
EMC	Ethyl methyl carbonate
EV	Electric Vehicles
FCE	First cycle efficiency
FID	Free-induction decay
FT-IR	Fourier-transform infrared spectroscopy
g	Gravitational acceleration
GC-MS	Gas chromatography coupled with mass spectrometry
I	Current
i	Imaginary number
I	Quantum number
k	Boltzmann's constant
LEDC	Lithium ethylene dicarbonate
LFO	Lithium difluorophosphate
LFP	Lithium iron phosphate, $LiFePO_4$
$LiBF_4$	Lithium tetrafluoroborate
LiBOB	Lithium bis(oxalate)borate
LiDFOB	Lithium difluoro(oxalate)borate
LiFSI	Lithium bis(fluorosulfonyl)imide
$LiPF_6$	Lithium hexafluorophosphate
LMO	Lithium manganese oxide, $Li_{1+x}Mn_{2-x}O_4$
M	Molar concentration (mol L^{-1})
m	Molal concentration (mol kg^{-1})
mAh	Milliamp-hour
MMDS	Methylene methane disulfonate

NG	Natural Graphite
NMC	$Li(Ni_xMn_yCo_z)O_2$ where $x + y + z = 1$
NMR	Nuclear magnetic resonance
OCV	Open-circuit voltage
PC	Poly-crystal
PES	Prop-1-ene-1,3 sultone
PES211	2 % PES, 1 % MMDS, 1 % TTSPi
PES221	2 % PES, 2 % DTD, 1 % TTSPi
P_r	Turbostratic disorder probability
PS	Propane sultone
PVDF	Polyvinylidene fluoride
Q	Capacity
R_{CT}	Charge-transfer resistance
R_{el}	Electrolyte resistance
RF	Radio frequency
RT	Room temperature
SA	Succinic anhydride
SBR	Styrene butadiene rubber
SC	Single-crystal
SEI	Solid electrolyte interphase
SEM	Scanning electron microscopy
SOC	State-of-Charge
T	Temperature
T1	Pulse relaxation delay time, or spin-lattice relaxation time
TM	Transition metal
TTSPi	Tris(trimethylsilyl) phosphite
UCV	Upper cut-off voltage
UHPC	Ultra-high precision coulometry
V	Voltage

VC	Vinylene carbonate
XPS	X-ray photoelectron spectroscopy
XRD	X-ray diffraction
XRF	X-ray fluorescence
Y	Frequency factor
Z	Complex impedance
Z_C	Imaginary impedance
Z_R	Real impedance
γ	Gyromagnetic ratio
Δ	Change in volume
Δ	Change in weight
Δ_C	Charge endpoint capacity
Δ_D	Discharge endpoint capacity
ΔV	Voltage polarization
ν	Larmour frequency
ρ	Density of water
Ω	Ohm

Acknowledgements

I want to thank Ning Zhang, Animesh Dutta, Alex Louli, Eric Logan, Michael Bauer, Jessie Harlow, Michel Johnson (among many others) for their invaluable help, guidance, and support. Special thanks to undergraduate students Nicholas Kowalski, Haoqi (Skye) Ni, and Annika Benson for doing the heavy lifting and for giving me the chance to work alongside them. Marc Cormier and Christian Fitzner cannot be thanked enough for developing priceless data analysis programs that saved me countless hours of work.

I would need an extra thesis chapter to properly thank Jeff Dahn for all his support and mentorship over the years. From hiring me to work in his lab in the summer of 2017, to helping me get my foot in the door of the battery industry, and for taking me on as Ph.D. student, Jeff has supported me at every stage of my career. Your enthusiasm for our work, commitment to the professional and personal growth of your students, and tremendous support is hard to find anywhere else except Dalhousie, specifically the Dunn building.

Chapter 1.   Introduction

1.1.   Motivation

Li-ion cells are a key component in electric vehicles (EVs) and grid energy storage batteries due to their long lifetime, high energy-density and steadily decreasing cost owing to the astonishing global production scale[1]. The cost of Li-ion cells results in a high cost for EVs which is presently out of reach for a significant portion of the public[2,3]. Further cost reduction can be achieved by increasing the cell energy density—a measure of how much active Li can be "packed" into a cell—to reduce the number of cells in the battery, improving the cell lifetime to maximize the cell's energy output, and by switching to lower cost electrode materials and manufacturing processes. Increasing cell lifetime from years to decades will allow the integration of batteries in grid energy storage, where durable, decades-long, lifetimes are necessary (more so than energy density)[4,5]. Therefore, the focus of this thesis will be on understanding Li-ion cell failure, developing methods to quantify battery electrode degradation, and proposing cell designs that demonstrate improved lifetime.

1.2.   Li-ion Cells

Figure 1.1 shows a schematic of a typical Li-ion battery cell. A cell consists of an electrically insulated separator that allows ion transport (typically made out of microporous polypropylene), contained between a positive and negative electrode, and a liquid organic electrolyte containing a Li salt. A common choice of positive electrode material is the family of lithium transition metal oxides, $LiMO_2$,

where M = Ni, Mn and/or Co in various molar ratios, known as NMC. The ratio of Ni, Mn, and Co in the NMC material denotes the type of NMC used; for example, $Li(Ni_{0.8}Mn_{0.1}Co_{0.1})O_2$ is referred to as NMC811 and similar composition of NMC follow this naming convention. The composition of the NMC material dictates the energy density, stability, and lifetime of the materials and is generally tailored to the requirements of certain applications. The $LiMO_2$ electrode contains all the available Li^+ in the cell, or the Li inventory, which is intercalated between $LiMO_2$ sheets owing to its layered structure. During charge, the Li^+ de-intercalates from the positive electrode and, facilitated by the ionically conductive liquid electrolyte, migrates to the negative electrode, with electrons (e^-) travelling though the external circuit for charge balance. The negative electrode, commonly made of graphite, can intercalate Li^+ between the graphene layers of graphite, and this process is reversed during discharge.
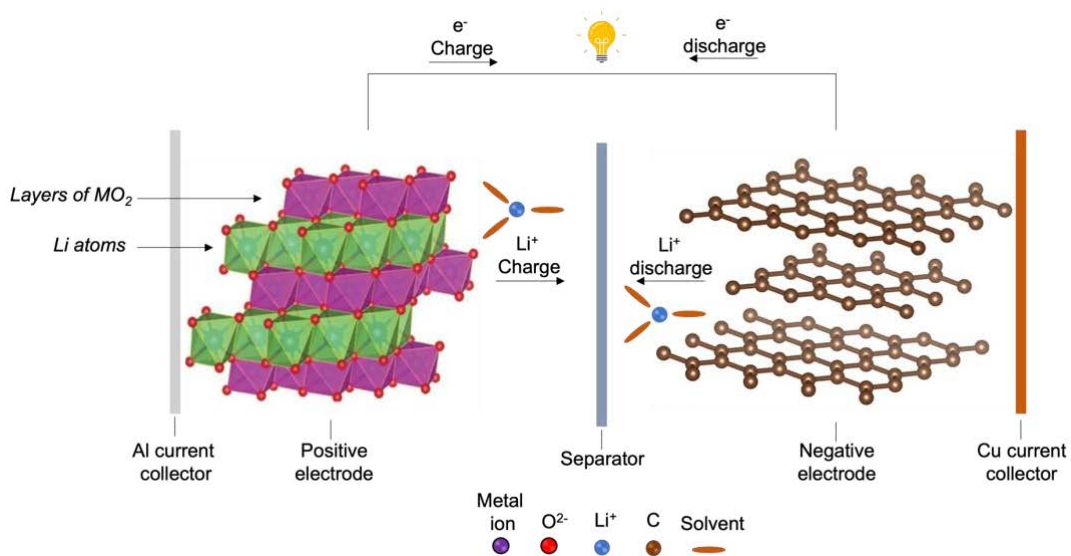
Figure 1.1. Schematic representation of a Li-ion cell with an NMC positive electrode and graphite negative electrode.

Equations 1.1-1.2 show the half-cell redox reactions occurring during charge and discharge as described above, and Equation 1.3 shows the overall redox reaction:

$$LiMO_2 \rightleftharpoons xLi^+ + xe^- + Li_{1-x}MO_2 \tag{1.1}$$

$$yC_6 + xLi^+ + xe^- \rightleftharpoons yLi_{x/y}C_6 \tag{1.2}$$

$$LiMO_2 + yC_6 \rightleftharpoons Li_{1-x}MO_2 + yLi_{x/y}C_6 \tag{1.3}$$
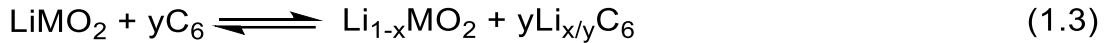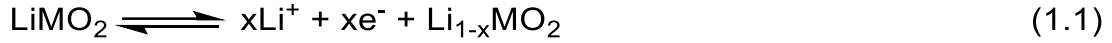
Typically, the positive and negative electrodes in a Li-ion cell consist of micron-sized active material particles, blended with a conductive additive such as carbon black and a polymeric binder. This mixture is made into a slurry which is then coated on aluminum or copper foil for the positive or negative electrode, respectively. Once the slurry-coated foil is fully dried, the electrodes can be assembled into full Li-ion cells which are then filled with the electrolyte[6]. The active material mass loading for each electrode is adjusted so that there is sufficient negative electrode capacity to intercalate all the Li^+ inventory held in the positive electrode, otherwise Li^+ would plate on the surface of the negative electrode as Li^0 once all graphite intercalation sites are occupied which presents a safety hazard.

Figure 1.2 shows the galvanostatic charge-discharge curves for a typical NMC811 and graphite electrodes cycled versus Li/Li^+. During charge, the positive electrode voltage increases while the negative electrode voltage decreases; and the full cell voltage is the difference between the positive and negative electrode voltage at any state-of-charge (SOC) along the x-axis. Figure 1.2 shows the importance of "balancing" the positive and negative electrodes in the cell so that

the total Li inventory in the positive electrode does not exceed the available capacity in the negative electrode, which would result in unwanted Li plating. Since Li plating is a significant safety issue, the negative electrode capacity in commercial Li-ion cells is typically 5-10 % more than the positive electrode capacity. This thesis uses units that are consistent with the battery industry and academic literature, so capacity is expressed in units of mAh instead of coulombs (1 mAh = 3.6 C) and the currents chosen for galvanostatic cycling are expressed in "C/x rate" where x is the number of hours it takes to fully charge or discharge the cell.
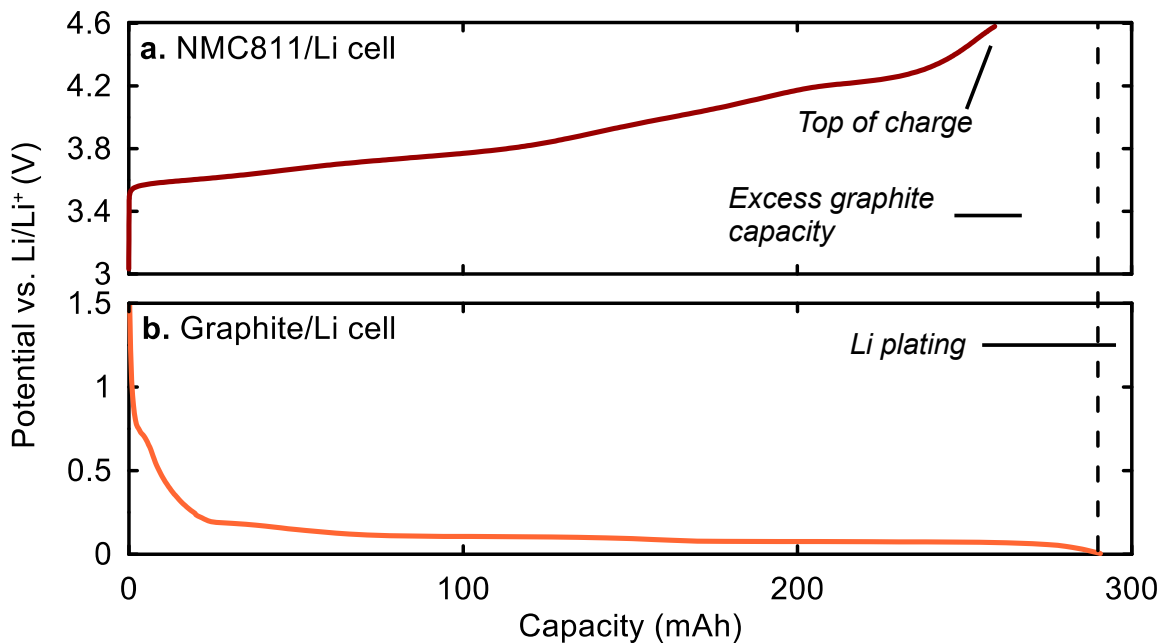
Figure 1.2. Galvanostatic charge curves for (a) NMC811 and (b) graphite cycled vs Li/Li$^+$ at 40 °C and a "C/20 rate". The C/x nomenclature is commonly used in industry and academia where "x" is the number of hours it takes to fully charge or discharge a cell.

In addition to the NMC family of layered positive electrode materials, olivine lithium iron phosphate (LiFePO$_4$, or LFP) and spinel lithium manganese oxide (Li$_{1+x}$Mn$_{2-x}$O$_4$, or LMO) attract a significant portion of the positive electrode materials market owing to their low cost compared to NMC, which uses expensive Ni and Co[7]. Figure 1.3 shows the crystal structure of all three positive electrode materials and their specific energy densities. LFP and LMO materials possess some advantages over NMC besides their lower cost.

LFP has superior safety compared to NMC, particularly the energy-dense Ni-rich NMCs (see Figure 1.3)[7–9]. Therefore, LFP materials are more suitable for energy storage applications where compromising energy density for safety is acceptable. Similarly, LMO materials have worse energy density compared to NMC and LFP, but they are significantly cheaper owing to their Ni- and Co-free precursor and their facile synthesis procedure[7,10]. Moreover, the atoms in spinel LMO materials are arranged in a fashion that created "three-dimensional" Li diffusion tunnels that allow for rapid charge and discharge compared to the two-dimensional and one-dimensional pathways in LFP and NMC, respectively (Figure 1.3a-c)[10,11]. With each class of materials having its own pros and cons, various cell chemistries can be constructed to suit certain applications where the advantage(s) of each material can be leveraged.
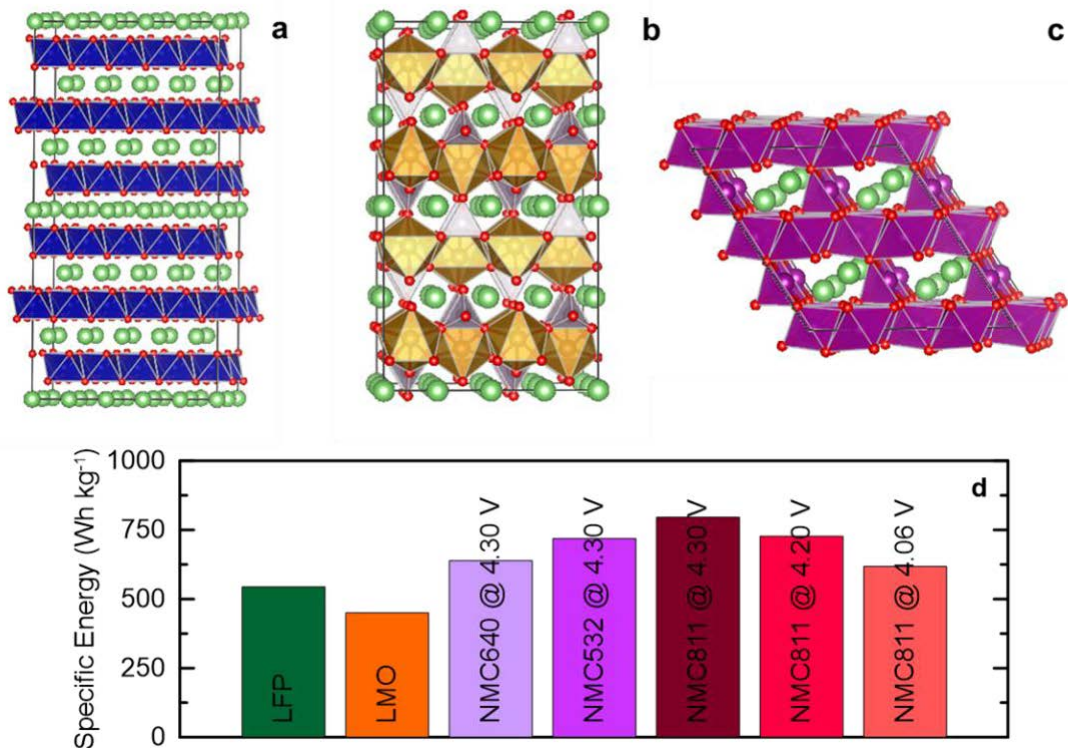
Figure 1.3. Crystal structure for (a) layered transition metal oxides, (b) olivine LFP, (c) spinel LMO positive electrode materials, and (d) specific energy densities (Wh kg^{-1}) for each.

For negative electrode design, various materials such as Si (or SiOx), lithium titanate, or graphite have been utilized, although none have come close to the utility and dominance of graphite electrodes in the battery market[12–15]. Graphite materials for Li-ion cells can be mined and processed to produce natural graphite (NG) or can be synthesized from various carbon precursors to give synthetic graphite, known in the battery field as artificial graphite (AG). The differences between NG and AG will be discussed in more detail in Chapter 4.

A fully lithiated graphite (LiC$_6$) readily reacts with the organic electrolyte used in Li-ion cells, which is unavoidable and results in an irreversible consumption

6

of Li atoms. This reaction leads to the formation of the solid-electrolyte interphase (SEI) upon the first charge of the cell[16]. The SEI layer acts as an insulating barrier between LiC_6 and the electrolyte which hinders further reactions between the electrolyte and lithiated graphite, thus prolonging the cell's lifetime at the expense of an initial loss of Li inventory. SEI composition and its formation process, which is one of the least understood phenomena in battery cells, is critical to cell operation and longevity[17]. Therefore, significant research effort is dedicated to designing electrolyte systems that yield a SEI composition that can effectively passivate the reactive surface of lithiated graphite[18–22].
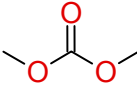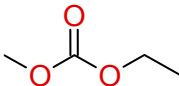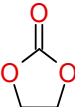
1.3. Organic Electrolyte Systems
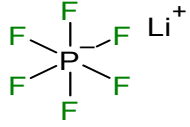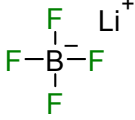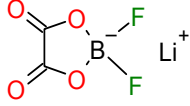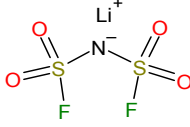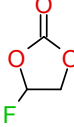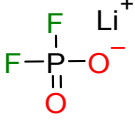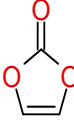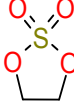
Electrolyte systems for Li-ion cells typically consistent of a lithium salt (or mixture of salts) dissolved in a mixture of organic carbonates and a small concentration (< 5 wt% typically) of sacrificial components known as electrolyte additives. Table 1.1 lists all electrolyte components used in this thesis, but one can find endless electrolyte recipes in the battery literature. The electrolyte components shown in Table 1.1 were used in this thesis because of their demonstrated excellent lifetime[17], or the ability of various salt/additive combinations to mitigate certain cell failure mechanisms which will be discussed in later chapters.
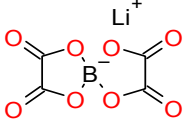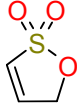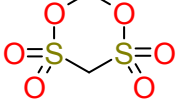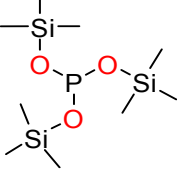
Each electrolyte component has drawbacks; therefore, a mixture of organic carbonates (as solvents or additives) and different salt(s) are used to create a balanced composition for different applications. For example, ethylene carbonate

(EC) has a large dielectric constant, but high viscosity and melting point, so linear carbonates such as dimethyl carbonate (DMC) and ethyl methyl carbonate (EMC) are often used along with EC to improve conductivity. Similarly, lithium hexafluorophosphate (LiPF$_6$) is the most commonly used salt due to its low cost, high ionic conductivity in solution, relative stability against electrochemical reactions, and its ability to passivate the aluminum foil in the positive electrode. However, LiPF$_6$ is prone to thermal decomposition that generates unwanted acidic species that can rapidly degrade the electrolyte and electrodes[23]. For that reason, other salts such as lithium tetrafluoroborate (LiBF$_4$), lithium difluoro(oxalate)borate (LiDFOB), or lithium bis(fluorosulfonyl)imide (LiFSI) are sometimes used either solely or in combination with LiPF$_6$ to improve the thermal stability of the electrolyte, high voltage performance, or to alter the SEI composition to improve the film properties[24–26].

Table 1.1. List of all electrolyte components used in this thesis and some physical properties for the solvents.

Type	Chemical	Structure	Dielectric constant (25 °C)	Melting point
Solvent	Dimethyl carbonate (DMC)		3.1075	4.6
	Ethyl methyl carbonate (EMC)		2.958	-53
	Ethylene carbonate (EC)		89.78 (40 °C)	36.4

	Lithium hexafluorophosphate (LiPF$_6$)		
Salt	Lithium tetrafluoroborate (LiBF$_4$)		
	Lithium difluoro(oxalate)borate (LiDFOB)		
	Lithium bis(fluorosulfonyl)imide (LiFSI)		
Additive	Fluoroethylene carbonate (FEC)		
	Lithium difluorophosphate (LFO)		
	Vinylene carbonate (VC)		
	Ethylene sulfate (DTD)		

	Lithium bis(oxalate)borate (LiBoB)		
	Prop-1-ene-1,3 sultone (PES)		
	Methylene methane disulfonate (MMDS)		
	Tris(trimethylsilyl) phosphite (TTSPi)		

1.4. Cell Failure Mechanisms

1.4.1. Columbic Efficiency and "Slippage"

The useable capacity and lifetime of a Li-ion cell is governed by the rate of consumption of the Li inventory. In an ideal case, the amount of Li that intercalates the negative electrode during charge will be identical to the amount of Li that intercalates back into the positive electrode during discharge. Here, the columbic efficiency (CE), which is the ratio of discharge to charge capacity, will be equal to unity. However, this does not occur in practice since Li inventory is always depleted with every cycle due to the so-called "parasitic reactions" which will be discussed in the following sections. Therefore, significant research effort is dedicated to slowing down the rate of Li inventory loss to prolong the cell's lifetime[27−30].

Smith et al showed that CE can be approximated as the sum of capacity loss due to Li inventory loss and Li inventory gain due to some electrolyte oxidation reactions involving salt anion consumption[31]. Briefly, oxidation reactions at the positive electrode side that occur during charge generally result in the addition of cyclable Li^+ to the cell's inventory since they usually involve the consumption of the Li salt anion. The additional Li^+ inventory resulting from salt anion consumption is counted as a charge, and therefore results in an apparent *increase* in the charge capacity; unlike Li inventory loss due to SEI formation which is counted as a *decrease* in the discharge capacity. Such changes to charge and discharge capacities, known as "relative shift" between the two electrodes, can be tracked well with high-precision charging equipment.

Figure 1.4 shows the voltage versus capacity curve for a NMC811/Graphite cell, where one can see the shifts in charge and discharge endpoint capacities as denoted by Δ_D and Δ_C, respectively. Combined with CE, Δ_D and Δ_C are important metrics to consider when evaluating the performance of new cell designs since the contribution of Δ_D and Δ_C to the CE elucidates which failure mechanism is dominant in the cell. While CE and slippage are useful in accounting for the cell's Li inventory, not all Li loss will necessarily be a product of parasitic reactions. Therefore, it is important to understand the various capacity loss mechanisms that occur in a Li-ion cell which are broadly categorized as: parasitic reaction, active material loss, and impedance/resistance growth.
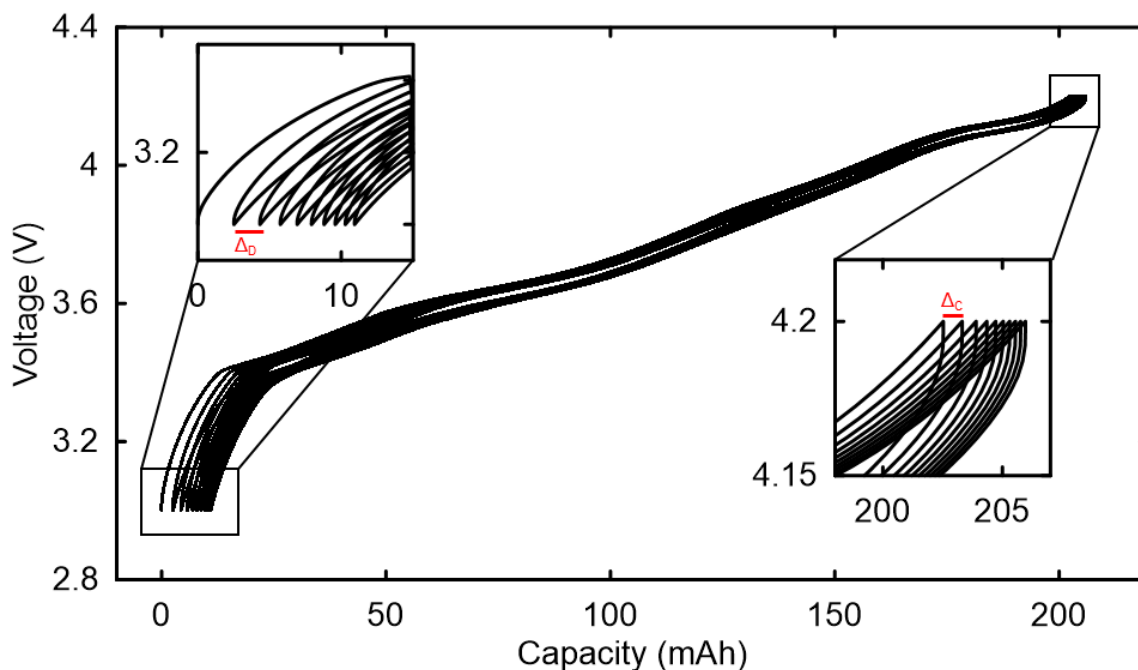
Figure 1.4. Voltage (V) versus capacity (mAh) curves for a NMC811/Graphite pouch cell cycled at 40 °C and C/20:C/20 rate in the 3.0-4.20 V range. Insets show the discharge and charge endpoint slippages, respectively.

1.4.2. Parasitic Reactions

The SEI layer forms on the surface of both the negative and positive electrodes during cell operation through a series of reactions known as parasitic reactions (since they can result in irreversible degradation of the electrolyte and/or electrodes), which in turn passivate the reactive surfaces of each electrode against further reactions with the electrolyte. The SEI on the negative electrode is the primary determinant of the cell's lifetime; however, the positive electrode SEI (called cathode electrolyte interphase, or CEI, in the literature) also contributes to the cell's lifetime especially at voltages >4.30 V[32–34].

An important step in cell manufacturing is the so-called "formation" step, where controlled cell aging takes place to allow the formation of the initial SEI. Manufacturers take different approaches to this formation step. The main goal is to sufficiently age the cell before it can be deployed to the customers. Figure 1.5 shows a voltage versus capacity curve for a NMC811/Graphite cell during the formation cycle, which was done at 40 °C and a slow C/20:C/20 charge:discharge rate to allow sufficient time for SEI formation. The lower voltage limit during the discharge was set to 3.0 V. The shaded box shows the capacity lost during charge which cannot be retrieved during discharge due to the irreversible consumption of Li inventory during SEI formation. The choice of electrolyte and negative electrode impacts the extent of Li loss during formation, which is referred to as first cycle efficiency (FCE). The goal during cell formation is to maximize FCE while ensuring that the negative electrode is well passivated.
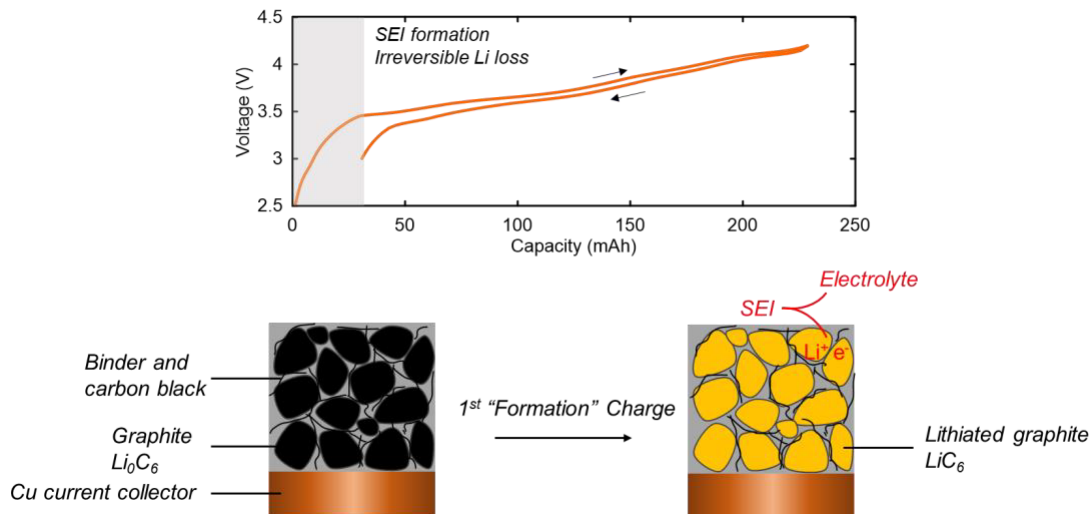
Figure 1.5. Voltage (V) versus capacity (mAh) curve for an NMC811/Graphite cell during the first formation cycle at 40 °C with C/20:C/20 rate; and schematic showing the composition of a typical graphite electrode and SEI formation reactions between the lithiated graphite and the electrolyte.

Due to the complex interplay between the different electrolyte components and electrode materials, the exact nature of parasitic reactions is hard to determine. However, studies of SEI composition and by-products of electrolyte decomposition have shed light on some of the mechanisms involved in SEI formation. EC and film-forming additives such as vinylene carbonate (VC) are known to form lithium ethylene dicarbonate (LEDC) and organic polymers, respectively, according to the pathways shown in Figure 1.6 which have been confirmed by various groups[35,36]. The poor solubility of the reduction products of EC and VC means that these by-products can precipitate on the negative electrode surface and effectively passivate it. Other film-forming additives such as ethylene sulfate (DTD) and fluoroethylene carbonate (FEC) can be used to engineer an effective SEI layer as well[37,38]. Moreover, SEI components can also be derived from reduction of linear carbonate such as EMC and DMC[36,39].
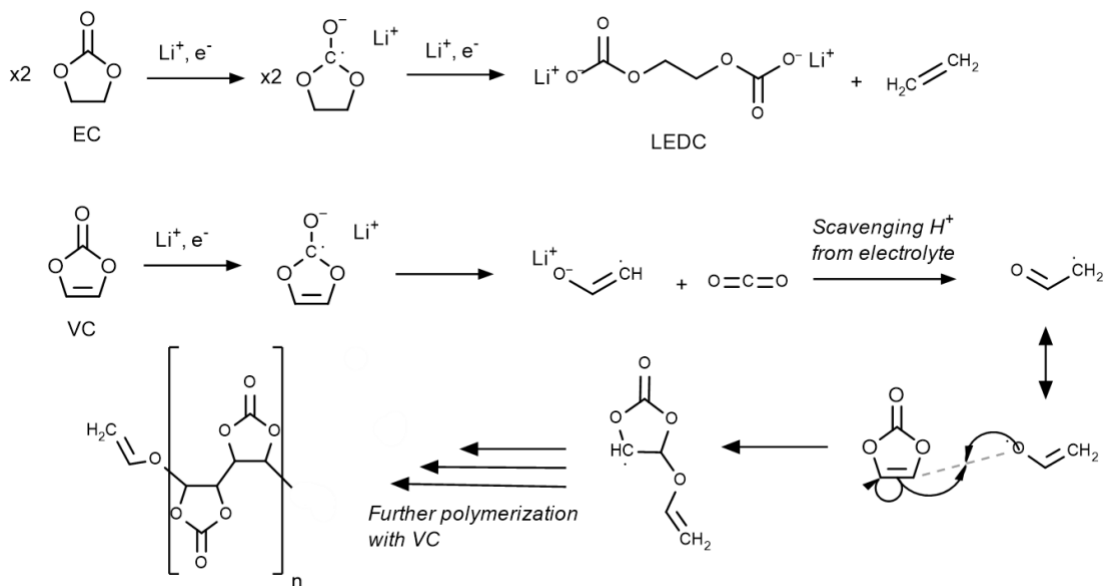
Figure 1.6. Reduction mechanisms of EC and VC.

In addition to the organic SEI components, inorganic components derived from salt decomposition also play a role in creating a robust SEI layer[16,40]. In LiPF$_6$-based electrolytes, lithium fluoride (LiF), Li$_x$POF$_{3-x}$ species, and organophosphates compromise a portion of the SEI, as well as lithium carbonates, and alkoxides[36]. Various techniques such as X-ray photoelectron spectroscopy (XPS), nuclear magnetic resonance (NMR), Fourier-transform infrared spectroscopy (FT-IR), gas chromatography coupled with mass spectrometry (GC-MS) have been extensively used to study electrolyte decomposition pathways and the resulting SEI composition, which is largely dependent on the cell's operating voltage and electrolyte composition.

1.4.3. Impedance Growth

During charge/discharge cycling, the cell's impedance (and/or resistance) can cause the measured voltage to deviate from the expected one at a given SOC, which is influenced by the thickness of SEI, particle surface area/adhesion to the current collector, charge/discharge rates and temperature, electrolyte ionic conductivity, and kinetic limitations on Li diffusion in active material particles resulting in lithium concentration gradients. One of the most significant contributors to resistance growth at high voltage is the surface reconstruction of layered oxide materials to rock-salt phase resulting from oxygen release[41], which will be discussed in later chapters.

Figure 1.7 shows voltage versus capacity curves for two identical NMC811/Graphite cells, one cycled at 40 °C and C/20:C/20 and the other at RT

and C/3:C/3. The large voltage polarization in the RT cell resulted in lower accessible capacity at the same upper cut-off voltage (UCV) than the 40 °C cell, thus lower energy and power densities. Unlike irreversible Li loss shown in Figure 1.5, the phenomena in Figure 1.7 does not always result in irreversible Li loss and the inaccessible capacity can be reached if the cell is cycled at slower rates and/or higher temperatures. In galvanostatic cycling experiments, cell resistance is monitored by taking the difference between the average charge and discharge voltages, which is referred to as ΔV in this work. At high potentials, ΔV growth is a significant contributor to capacity fade and is often a consequence of SEI growth, surface layer reconstruction to rock-salt phase, and/or electrolyte degradation resulting in poor ionic conductivity[41–43]. Another consequence of large cell resistance is the unwanted Li plating which can occur at fast charge rates, low temperatures, and/or if the SEI layer is too thick which is a serious safety concern.
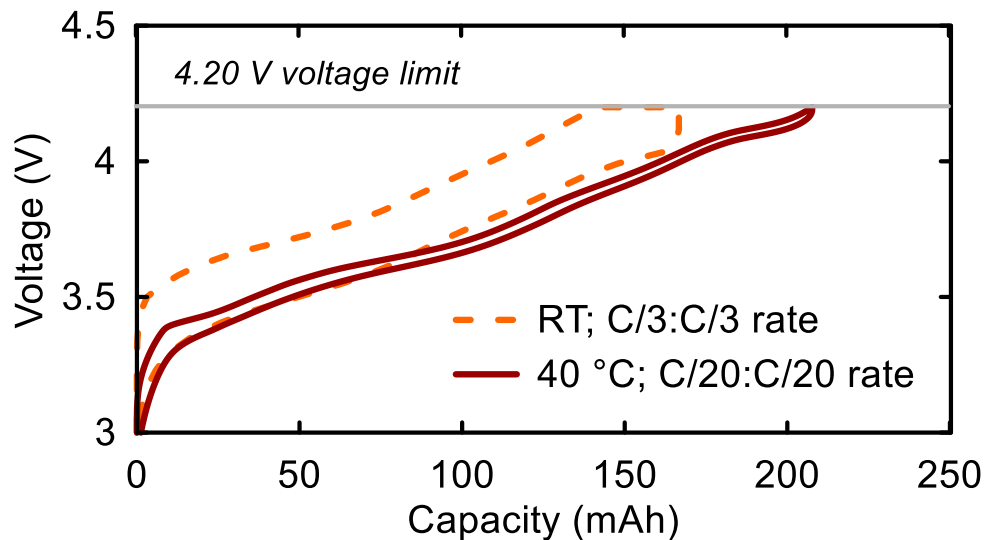
Figure 1.7. Voltage (V) versus capacity (mAh) curve for an NMC811/Graphite cell cycled at 40 °C and C/20:C/20 rate compared to the same cell cycled at RT and C/3:C/3 rate.

1.4.4. Active Material Loss

Chemical and electrochemical degradation generally dominates cell failure, but mechanical degradation of the electrode material, particularly the positive electrode, contributes to cell failure as well through "active material loss"[44–46]. During charge/discharge cycling, electrode active material expands and contracts as lithium is (de)intercalated. This volume change can result in the generation of microcracks within a particle, especially when particles have local differences in SOC, which is one of the challenges with Ni-rich positive electrode materials[47].

Once microcracks are formed, electrolyte can permeate them and react with the freshly exposed surfaces which increases the rate of parasitic reactions in the cell. Additionally, when active material particles crack, they can become electrically disconnected from the current collector which results in active material "loss", despite the presence of binders and conductive agents in the electrode to promote adhesion and conductivity. Figure 1.8 illustrates the structural evolution of a Ni-rich NMC positive electrode during cycling and the generation of microcracks due to intra-particle strain/volume change. The "isolated" active materials can trap Li inventory and decrease the cell's capacity. Strategies to mitigate microcrack formation such as dopants, coatings, or synthesis of robust monolithic particles known as "single-crystal" materials, have been deployed with varying degrees of success[47–51]. However, it has been demonstrated that microcrack generation is an unavoidable challenge with all Ni-rich (>90 % Ni) NMC positive electrode materials[52].
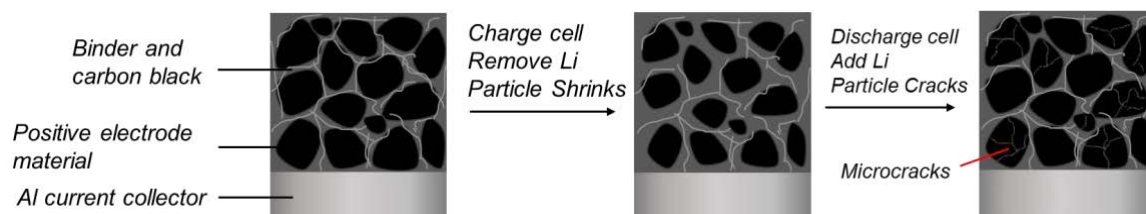
Figure 1.8. Schematic illustration of the positive electrode material volume change during charge/discharge cycling and the microcracks resulting from the volume change.

Further, active material loss can be in the form of transition metal (TM) dissolution, where metal ions from the positive electrode material can dissolve in the electrolyte and migrate to the negative electrode where they can be deposited on the surface[53]. The deposited metal species, especially manganese, are thought to be responsible for accelerated SEI growth and electrolyte degradation, resulting in a thick SEI layer and gas generation[54]. Previous work from our group showed that TM dissolution accounts for only a small (<1 %) of the total TM content in NMC cells[55,56], but it is a significant issue in LMO cell chemistries which will be discussed in Chapter 5.

1.5. Scope of This Thesis

The focus of this thesis is on studying cell failure mechanisms in different cell chemistries and proposing new designs (i.e., electrolytes, electrode material choice, operating conditions) that present an improvement to current cell lifetimes. To do so, a method to visualize and quantify TM dissolution and deposition on the negative electrode with X-ray fluorescence (XRF) was developed and applied to NMC, LFP and LMO cell chemistries. Additionally, long-term studies of the impact

of cycling conditions (C-rate, UCV, DOD, temperature) on the lifetime of NMC811, NMC532 and NMC640 cells were conducted, along with an extensive suite of post-cycling characterization to understand cell changes during operation. This was followed by a study on the gassing and electrochemical behaviour of various graphite materials and their impact on capacity retention in NMC811 cells. Finally, the impact of electrolyte choice and LMO positive electrode design on the lifetime of LMO/Graphite cells was studied using XRF, NMR, and various electrochemical tests. This study resulted in the development of mixed-salt electrolyte recipes and their impact on the lifetime and degradation of LMO/Graphite and LFP/Graphite cells will be discussed. The goal of this thesis is to provide a comprehensive study of the degradation of NMC, LMO and LFP cell chemistries and provide strategies to improve their performance and lifetime.

Chapter 2 will present all the experimental details for the work done in this thesis and introduce the XRF method developed herein.

Chapter 3 will present the impact of cycling conditions of the lifetime of NMC/Graphite pouch cells after ~1.5 years of galvanostatic cycling under different conditions.

Chapter 4 will look at the electrochemical differences between natural and artificial (i.e., synthetic) graphite materials and their impact on the lifetime of NMC811 cells and discuss models of SEI growth and lifetime predictions.

Chapter 5 will discuss the challenges associated with the high temperature performance of LMO/Graphite cells, and progress made towards improving cell lifetime and understanding its degradation modes.

Chapter 6 will present the performance and degradation SC-LMO cells with larger particles size with and without NMC blending, and the impact of mixed salt electrolytes on the cell performance.

Chapter 7 will examine the impact of mixed-salt electrolytes introduced in Chapter 5 and 6 on the performance of LFP/Graphite pouch cells.

Chapter 8 will present the final concluding remarks and directions for future work.

Chapter 2. Experimental Methods

2.1. Pouch Cells and Electrolytes

All Li-ion cells used in this work were machine-made pouch cells with a nominal capacity in the 180-240 mAh range manufactured by LiFUN Technologies (Hunan Province, China) then sent to our lab with no electrolyte. Figure 2.1 shows an image of the pouch cells used in this work. Once received, cells were cut open in an Ar-filled glovebox and dried for 14 hours under dynamic vacuum at 120 °C to remove any residual moisture. After drying, cells were filled with 0.85 mL (~1 g) of electrolyte. The use of machine-made pouch cells ensured excellent reproducibility and that commercially-relevant cell designs were considered. The drying and filling process was the same for all cell chemistries used in this work. Due to the wide range of cell types used in this thesis, the cell specifications used in a specific project will be disclosed at the beginning of each relevant chapter below.

All electrolyte components used in this thesis are listed in Table 1.1. Battery-grade electrolyte components were obtained from Capchem (China), except for $LiBF_4$ and LiDFOB which were obtained from BASF. Electrolyte components were mixed in an Ar-filled glovebox to yield the desired recipes used in each chapter. All electrolytes used in this work had a total salt concentration of 1.5 M regardless of the salt(s) used. The exact electrolyte recipes used for each project will be listed at the beginning of their relevant chapter.
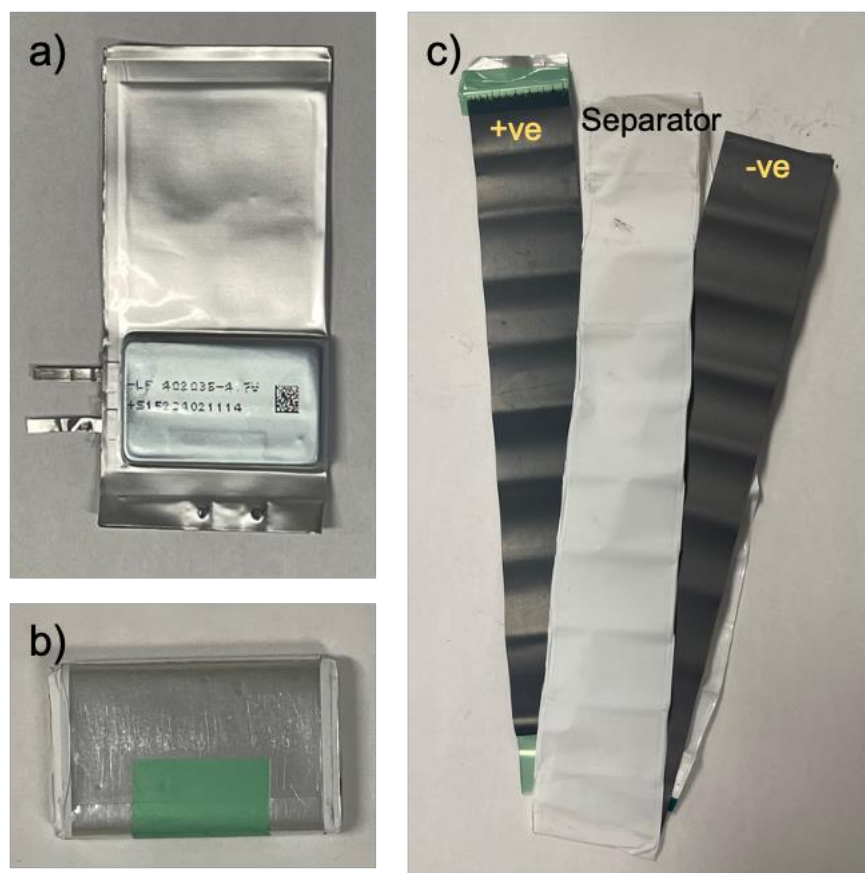
Figure 2.1. (a) Picture of a typical pouch cell used in this work, (b) the wound "jelly roll" inside the cell, and (c) the positive electrode, separator, negative electrode in the jelly roll.

2.2. Galvanostatic Cycling

Pouch cells were used in galvanostatic cycling experiments after drying and filling. The first step is cell formation which took place at 40 °C and C/20:C/20 charge:discharge rate using a Maccor Series 4000 cycler for all cells in this thesis. After filling, cells were held at 1.5 V for 16 hours at 40 °C to allow the electrolyte to sufficiently wet the jelly roll. Then, cells were charged at C/20 to their designated UCV then discharged to their lower cut-off voltage (both of which varied for each cell type and will be specified at the beginning of each chapter). After the first

formation cycle was completed, the cells were charged to ~50 % SOC for EIS measurements and degassing (see Section 2.3 and Section 2.4).

Following formation, degassing, and EIS, cells went on to either long-term cycling experiments, short-term ultra-high precision coulometry (UHPC) tests, or open-circuit voltage (OCV) storage (see Section 2.5). Cycling experiments were carried out on Neware cyclers (Shenzhen, China) at RT (20.0 ± 2.0 °C), 40 ± 0.1, 55.0 ± 0.1, or 70.0 ± 0.1 °C. Unless otherwise specified, cells were cycling at C/3:C/3 charge:discharge rates in the voltage range desired for each cell type (listed in each chapter below). Charging was done in constant current-constant voltage (CCCV) mode (i.e., C/3 charge followed by a constant voltage hold until the measured current dropped below C/20), while the discharge was in constant current (CC) mode. The CCCV charging mode allows enough time for Li^+ intercalation into the graphite at high SOCs in cases where Li diffusion is kinetically limited near the top of charge. During cycling, a full C/20:C/20 cycle was done at a regular interval (every x50 C/3 cycles in most cases) to measure the low-rate cell capacity free from any impedance effects that can impact the measured capacity (see Section 1.4.3).

In addition to long-term cycling experiments, UHPC tests were used to quantify small differences in CE, Δ_D, and Δ_C between different cell chemistries as discussed in Section 1.4.1 using the charging equipment developed at Dalhousie University and Novonix (Nova Scotia, Canada)[57,58]. As opposed to conventional charging equipment, the UHPC system possesses the accuracy and precision needed to reliably measure and compare CE, Δ_D, and Δ_C. After formation,

23

degassing, and EIS, cells were cycled at C/20:C/20 and 40.0 ± 0.1 °C in a voltage range specific for each cell chemistry (discussed in later chapters). For UHPC testing, 20 cycles are generally sufficient to age the SEI, however, sometime only 18 cycles were completed due to unplanned power outages. For both long-term and UHPC cycling, pair cells were made except for cycling experiments at 55 °C due to limited cycling channels at this temperature.

2.3. Gas Volume Measurements

Monitoring gas generation in the cell is critical to cell safety and operation and is often a consequence of parasitic reactions. In this thesis, *ex-situ* and *in-operando* gas volume measurements were utilized.

The *ex-situ* gas volume was recorded after formation and/or cell testing simply using Archimedes principle. Cells were suspended in a beaker of deionized water (~18 M) at room temperature using a hook attached to the bottom of a balance (Shimadzu AUW200D). Here, the change in cell volume due to gas evolution, ΔV, is related to the change in measured weight, Δw, by:

$$\Delta v = -\frac{\Delta w}{\rho g} \tag{2.1}$$

where ρ is the density of deionized water and g is the acceleration due to gravity.

Similarly, *in-operando* gas measurements were carried out using the same principle and an apparatus made in-house as described by Aiken et al in previous work[59]. This test setup allows for changes in cell volume (due to gas generation

and electrode volume change) to be monitored during galvanostatic cycling, thus giving insight into the onset voltage for gas evolution and consumption during cell operation. Cells were suspended in silicone vacuum pump oil and the change in weight was measured using sensitive strain gauges during electrochemical cycling in a 40.0 ± 0.1 °C temperature-controlled box. The galvanostatic cycling was done using a Neware charger and the exact cycling conditions will be discussed in the relevant chapters below.

2.4. Electrochemical Impedance Spectroscopy (EIS)

Electrochemical impedance spectroscopy (EIS) is widely used to understand how various cell components influence the cell's impedance throughout its lifetime in a non-destructive way. The cell's impedance is governed by the contact resistances between the active material and current collectors, charge-transfer resistances at the electrode/electrolyte interface, resistance of Li^+ travelling through the SEI, and capacitive and inductive effects. Therefore, many researchers have developed complex models that are used to fit EIS spectra to extract the contribution of individual cell components[60–64]. In this thesis we adopt a primitive model of Li-ion impedance that crudely interprets "charge-transfer" resistance (R_{CT}) as the total resistance a Li^+ faces as it (de)solvates at the electrode surface, migrates through the SEI, and intercalates into the active material. More complicated impedance models are outside the scope of this work.

EIS involves applying a small sinusoidal voltage (10 mV amplitude in our case) and measuring the resulting current response at different frequencies

(100 kHz to 10 mHz in this thesis) which allows us to determine the frequency-dependent impedance by:

$$Z(\omega) = \frac{V(\omega)}{I(\omega)} \tag{2.2}$$

where Z is a complex number containing information about the cell's impedance. To simplify the EIS spectra, we adopt a simple parallel RC circuit model shown in Figure 2.2.
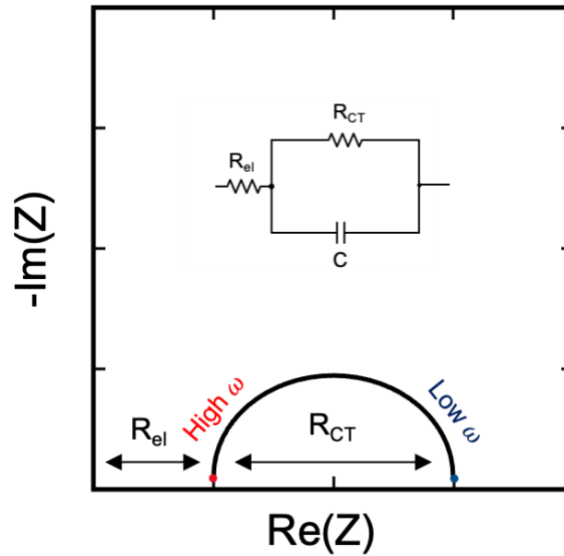
Figure 2.2. Primitive model of the impedance in a Li-ion cell which consists of a resistor and a resistor/capacitor element, as well as the Nyquist plot for this simple circuit model.

Here, R_{el} is the electrolyte solution resistance which is independent of the applied voltage frequency and follows Ohm's law:

$$Z_R = \frac{V}{I} = R_{el} \tag{2.3}$$

26

The resistor element, R_{CT}, in Figure 2.2 represents charge transfer resistance through the electrode/electrolyte interphase (such as SEI, for example). The capacitor element Z_c, which represents the capacitive charging at the electrode/electrolyte interface, will have imaginary impedance that depends on the frequency by:

$$Z_C = -i\frac{1}{\omega C} \tag{2.4}$$

When the impedance of the circuit element shown in Figure 2.2 is plotted as a Nyquist plot (i.e., imaginary component versus real one), it yields a semi-circle shifted along the x-axis by the value of the electrolyte solution resistance. The width of this semi-circle is taken as the charge-transfer resistance. In this thesis, all EIS spectra are recorded at 50 % SOC and 10 °C to magnify the contribution of R_{CT} to cell impedance.

2.5. Open-Circuit Voltage (OCV) Storage

Li-ion cells are not constantly charged/discharged throughout their lifetime since cells spend a considerable amount of time storing energy for prolonged periods of time. Open-circuit voltage (OCV) storage tests allow us to measure the rate of self-discharge that a cell undergoes when stored at a certain SOC and temperature. Ideally, a cell should not lose any of its stored capacity during storage. However, cells suffer from self-discharge due to, among other reasons, parasitic reactions that consume Li inventory at the charged state[65–68].

Previous work from our group introduced an OCV storage testing protocol that quantifies the voltage drop, reversible capacity loss, and irreversible capacity loss during storage[69]. Reversible capacity losses are ones that do not consume Li inventory during storage, but instead lead to a reversible self-discharge reaction where Li^+ is forced to move from the negative to the positive electrode to maintain charge neutrality. On the other hand, irreversible capacity loss is one resulting from the consumption of Li^+, such as SEI growth, which also results in self-discharge. Figure 2.3 shows the OCV storage protocol used in this thesis. First, the cell undergoes two C/10:C/10 cycles in the desired voltage range (3.0-4.20 V in this case), followed by a 10 hour hold at top of charge and a 500-hour OCV storage period. The discharge capacity preceding the OCV period, D_0, is taken as the initial capacity of the cell before storage. Following the OCV period, the cell is discharged to bottom of charge (3.0 V in this case) and the capacity remaining in the cell after storage, D_1, is measured. Then a third C/10:C/10 cycle takes place where the discharge capacity, D_2, is measured.

Here, the difference between the initial capacity and capacity remaining after storage, D_0-D_1, is a measure of the total capacity loss during storage (reversible and irreversible). To extract the irreversible capacity loss only, the difference between the initial discharge capacity and the second discharge after OCV, D_0-D_2, is taken. Finally, the reversible capacity loss is extracted by taking the difference between D_2 and D_1. In this thesis, all OCV storage experiments were done at 60.0 ± 0.1 °C using a high-precision storage system made in-house to accelerate cell failure and test the cells under strenuous storage conditions.
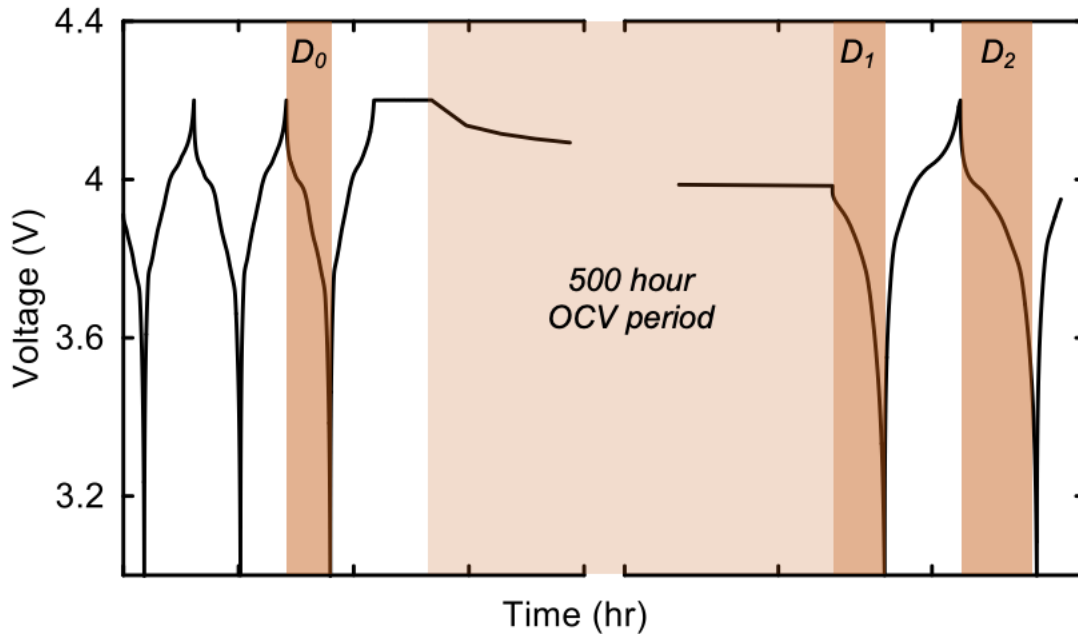
Figure 2.3. Voltage (V) versus time (hours) profile of a typical OCV storage experiment. The example shown here is for an LMO/Graphite pouch cell stored at 60 °C and 4.20 V.

2.6. *In-Operando* Jellyroll Stack Pressure Change Measurements

Pouch cells were volumetrically constrained in an aluminum enclosure such that any volume expansion of the cell would exert a force on the enclosure. The force was measured with subminiature load cells (LCKD, OMEGA Engineering), with capacities of 100 or 250 lbs. (445 and 1112 N), connected to DP25B-S-A (OMEGA Engineering) strain gauge panel meters. The load cells were fastened in the enclosure with the pouch cell, separated by a force distributing plate. The measured force was converted to PSI using the pouch cell area of ~6.0 cm^2 (0.93 square inch). For *in-operando* measurements, the pouch cells were connected to a Neware cycler. The analog 0-10 V output of the strain gauge panel meter was connected to a separate Neware channel, allowing for simultaneous voltage and

pressure measurements. These measurements were performed in a 40.0 ± 0.1 °C temperature box. This measurement was carried out by Alex Louli (Dalhousie University) according to the procedure described previously [70].

2.7. Scanning Electron Microscopy (SEM)

Scanning electron microscopy (SEM) images of pristine electrodes were taken by Michel Johnson at Dalhousie University. The SEM images were taken using a NanoScience Phenom Pro G2 Desktop Scanning Electron Microscope. Cross-section SEM images of aged electrodes were taken by Divya Rathore at Dalhousie University. Cells were charged to 4.20 V and opened in an Ar-filled glove box. Positive electrodes were rinsed with DMC twice before ion-milling with a JEOL IB19530CP cross-section polisher to remove residual electrolyte salts. Electrodes were milled with an Ar-ion beam for a 75 min and 6 kV coarse step followed by a 5 min and 4 kV fine step. SEM images were taken using a Hitachi S-4700 field emission electrode microscope with a secondary electron detector. The images were obtained using an accelerating voltage of 7 kV and current of 20 μA.

2.8. Powder X-ray Diffraction (XRD)

X-ray diffraction (XRD) is commonly used to understand the structural properties of crystalline solids. When X-ray photons are elastically scattered by electrons in a material, diffraction patterns can be observed in the event of a constructive interference of the scattered photons' wave fronts according to Bragg's law:

$$2d \sin \theta = n\lambda \qquad\qquad (2.5)$$

where n is an integer, λ is the wavelength, θ is the scattering angle, and d is the interplane spacing in the crystalline material.

XRD patterns of graphite materials were collected with a Bruker D8 diffractometer equipped with a Cu target X-ray tube and a diffracted beam monochromator. Samples were measured in the scattering angle (2θ) range of 10-110° in 0.05° increments with 20 seconds per step, and 1° divergence and 1º anti-scatter slits were used. The CARBONXS program developed by Shi et al was used to fit the XRD patterns to quantify turbostratic misalignment, P_r, and preferred orientation, P_o[71].

2.9.   X-ray Fluorescence (XRF)

X-ray fluorescence (XRF) is an effective and easy method for elemental analysis[72]. Fluorescence is the process in which an atom in an excited state emits a photon of certain energy as it relaxes back to its ground state. Figure 2.4 shows an illustration of the X-ray fluorescence mechanism. When an atom or nucleus is excited by high energy X-ray photons, an electron is emitted from the "K" or "L" energy levels which leaves behind a "hole" or electron sink. Higher energy electrons can then transition to the lower energy "K" or "L" levels, emitting a characteristic photon in the process.

The energy of the emitted photons depends on the energy transition that took place when the atom was in an excited state. Electrons that transition from

"L"-shell (2*p*) to a "K"-shell result in K radiation. While electrons that transition from "M"- or "N"-shells to a "K"-shell result in K and K radiation, respectively. Similarly, L and L radiations occur if an electron transition from the "M"- or "N"-shells to a vacancy in the "L"-shell. The K and K radiations are higher energy compared to K or L/L. Since each element results in a characteristic fluorescence radiation, XRF analysis is useful in chemical analysis.
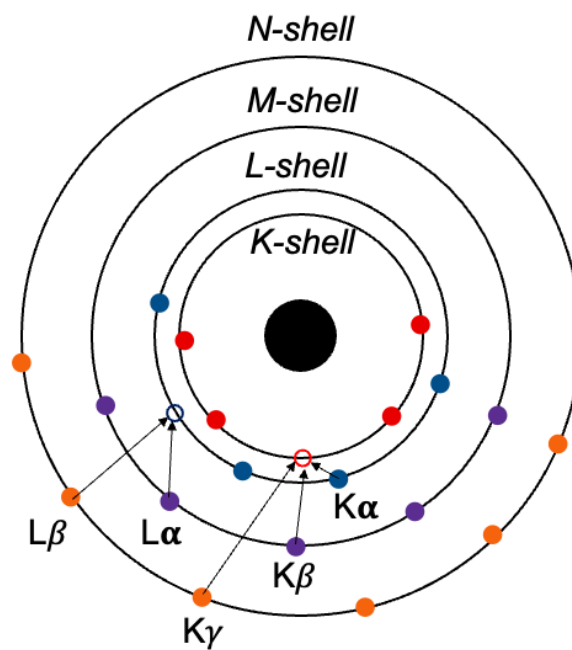
Figure 2.4. Schematic illustration of the X-ray fluorescence mechanism.

In this thesis, XRF will be used to visualize and quantify the mass loading of TMs and Al deposited on the negative electrode as the cell ages during cycling and/or storage as described by Eldesoky et al[73]. To quantify the TM and Al loading on the negative electrode from the obtained XRF spectra, matrix-matched XRF calibrants were constructed. Pristine graphite electrode taken from a fresh cell was

used a sputtering substrate, and a known gradient of Ni, Mn, Co, Fe, or Al was sputtered on five identical graphite electrodes using the sputtering masks developed by Dahn et al which can guarantee a linear gradient of deposited metals on the substrate[74].

Figure 2.5 shows a schematic of the sputtering table used in preparing the XRF calibrants and the "linear in" sputtering mask placed in front of the sputtering target. The sputtering table contains two identical graphite electrode and a series of pre-weighed Al disks placed opposite to each graphite electrode. Weighing the Al disks after sputtering allows us to know the exact mass loading gradient deposited on the graphite electrode as a function of the distance from the center of the sputtering table. Using a "linear in" sputtering mask placed in front of the target ensures that the layer of deposited metal varies in thickness moving away from the center of the table. As the sputtering table rotates, the same amount of metal is deposited on each graphite electrode and the pre-weighed Al disks. The mass loading of sputtered Ni, Mn, Co, Fe, or Al was kept in 0-50 μg cm^{-2} range to be on the same order of magnitude as the metal loading on the negative electrodes of aged cells. Calibration samples were prepared by Michel Johnson (Dalhousie University).
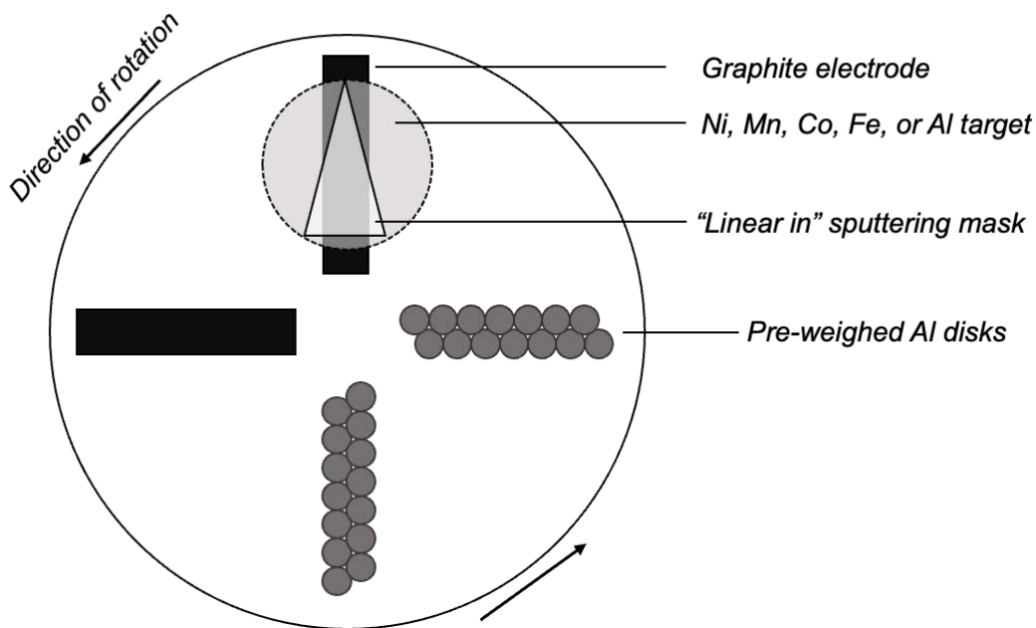
Figure 2.5. Schematic diagram of the rotating sputtering table used in preparing the XRF calibration samples using a "linear in" sputtering mask.

The XRF system used in this work was a Bruker M4 Tornado instrument at either Dalhousie University, Saint Mary's University, or the University of New Brunswick. This instrument had a 25 μm spot size which allowed for local features on the negative electrode surface to be realized. The X-ray source was a Rh X-ray tube, using a 200 µA current up to 50 keV. Scanning was done with either a 100 or 120 µm step size at a rate of 4.00 mm s^{-1}. For the calibration, graphite electrodes coated with a known gradient of Ni, Mn, Co, Fe, or Al were scanned and the known metal mass loadings at different positions along the graphite electrode (relative to the center of the table in Figure 2.5) were correlated to the signal count for each element at a given position. The ratio of metal loading to signal count was then used to convert the signal count from our samples to a loading in units of μg cm^{-2}.

2.10. Gas Chromatography Coupled with Mass Spectrometry (GCMS)

Gas chromatography coupled with mass spectrometry (GCMS) was used to identify the composition of gases generated in NMC811/Graphite cells after formation. Figure 2.6 shows a schematic of the main GCMS components (Agilent 5977B GC/MSD system). Once gaseous samples are injected into the sampling port, they pass through the column assisted by a carrier gas which is He in our case (the mobile phase). The coiled GC columns can range in length from 20 to 100 m and consist of hollow tubes coated on the inside with a stationary phase. The stationary phase can be polar or non-polar depending on the intended use. The retention time, or time it takes a separated compound to elute from the column, depends on the length of the column, ratio of stationary to mobile phase, and the linear velocity of the eluent, among other reasons. For example, compounds with greater affinity to the stationary phase will elute at longer retention times than those with less affinity to the stationary phase.
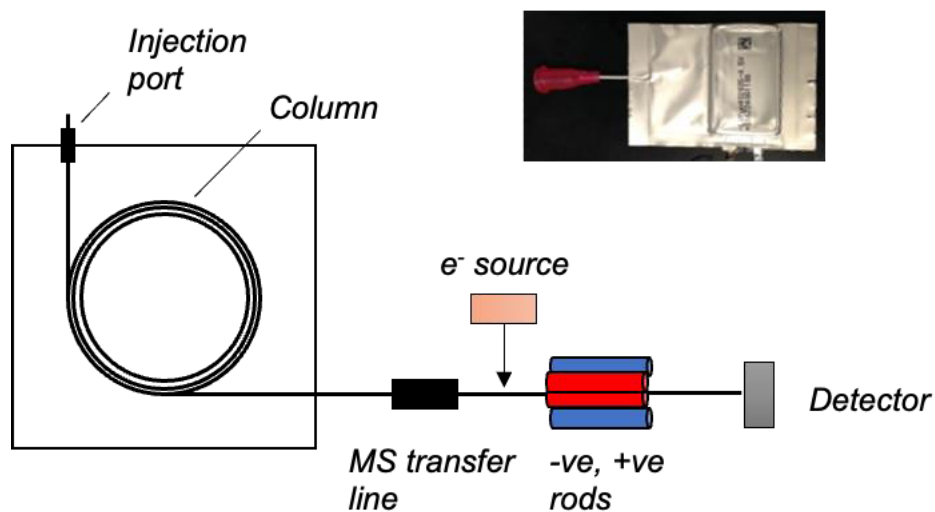
Figure 2.6. Schematic illustration of a typical GCMS setup and a pouch cell with a gas sampling port.

Once the injected gas mixture has been separated by the GC column, the separated compounds are carried to the MS detector for identification as shown in Figure 2.6. An electron source ionizes the separated compounds which generates charged fragments or molecular ions. The ions then move to the mass quadrupole which acts as a mass filter by altering the potential applied to opposing rods. Once the molecular ions/charged fragments exit the quadrupole, they reach the MS detector where the mass to charge ratio of each fragment/ion is recorded. The ions/fragments generated during ionization are unique to different compounds which allows us to identify the components of the gaseous mixture injected in the GC columns.

NMC811/Graphite pouch cells were fitted a "gas extraction port" as described by Schmiegel et al which allowed for non-destructive sampling of the gas generated in the cell[75] (see pouch cell picture in Figure 2.6). Cells were charged to a certain UCV at C/100 and 40 °C, then 100 µL of gas was injected into the GCMS column with an air-tight syringe. The MS detector used was sensitive to CO, CO_2, and light hydrocarbons.

2.11. Nuclear Magnetic Resonance (NMR)

Nuclear magnetic resonance (NMR) was used to quantify changes to salt concentration in aged LMO/Graphite pouch cells. NMR spectroscopy relies on magnetic diploes generated from nuclei, namely ^1H and ^{19}F in this thesis, to provide insight into the chemical structure of a molecule and its concentration in a sample[76]. A nucleus with an odd number of protons and/or neutrons will have a

net magnetic moment that is described by the nuclear spin quantum number I, The

quantum number I determines the number of quantum mechanical states that exist

in the presence of an external magnetic field, B_0, according to the $2I + 1$ rule. As

shown in Figure 2.7, for a ^{1}H or ^{19}F nuclei with $I = \frac{1}{2}$, the number of possible states

that can exist in an external magnetic field will be 2.

$$m = -\frac{1}{2}$$

$$B_0$$

$$\Delta E = \gamma \hbar B_0$$

$$m = +\frac{1}{2}$$
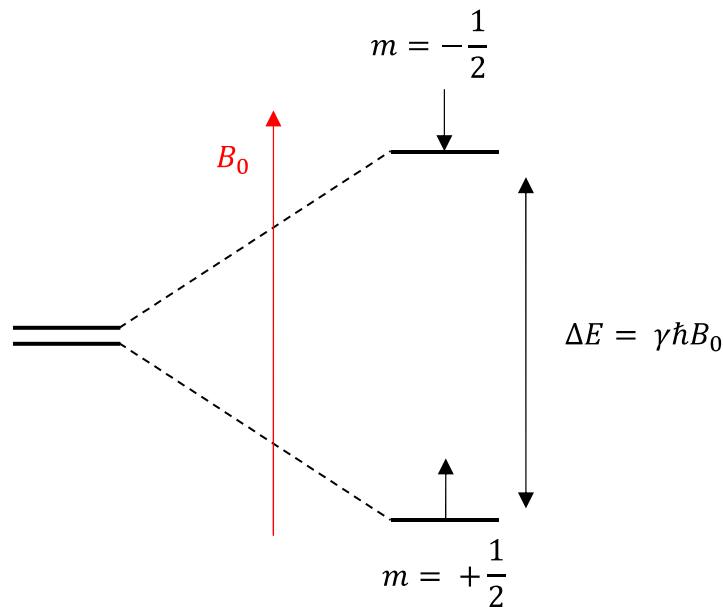
Figure 2.7. The separation of the "spin up" and "spin down" states of a spin half
nucleus in the presence of an external magnetic field.

The external field aligns the magnetic moment of the nuclei in the same

direction of the external field (preferred lower energy state) or against it (higher

energy state). The magnetic moment can be "spin up" ($m = +\frac{1}{2}$) or "spin down"

($m = -\frac{1}{2}$) depending on whether or not the nuclei was aligned with or against the

external magnetic field. At a specific B_0, the energy difference between the two spin states, ΔE, is described by:

$$\Delta E = \gamma \hbar B_0 \qquad\qquad (2.6)$$

where γ is the nuclei-specific gyromagnetic ratio and $\hbar$ is Plank's constant.

In an external magnetic field, lower energy "spin up" states will have a higher population than the higher energy "spin down" states. To transition from low to high energy states, a radio frequency (RF) pulse is applied at a specific frequency according to:

$$\nu = \frac{\gamma}{2\pi} B_0 \qquad\qquad (2.7)$$

where ν is the Larmour frequency. Therefore, $\frac{\nu}{B_0}$ must equal $\frac{\gamma}{2\pi}$ to achieve resonance for a certain nucleus which is done by adjusting the frequency of the RF pulse. A superconducting 11.74 T magnet will be referred to as a 500 MHz spectrometer since this the RF frequency that achieves resonance for ^{1}H.

Figure 2.8 shows the changes in net magnetization that occurs in the presence of an external magnetic field after applying a specific RF pulse. Once the nuclei magnetic moment has been aligned due to the external magnetic field, a short RF pulse is applied. This pulse excites the nuclei of interest in the sample tube which then relax to the ground state after the pulse stops. This relaxation occurs through "precessing" or spinning around B_0. The time it takes the magnetic moment to relax from the x-y plane back to the z-direction is recorded, which is the

free-induction decay (FID). The FID is then converted from the time domain to the

frequency domain which is conveniently presented in units of ppm (i.e., chemical

shift) so that the NMR peak position is independent of the magnetic field strength.
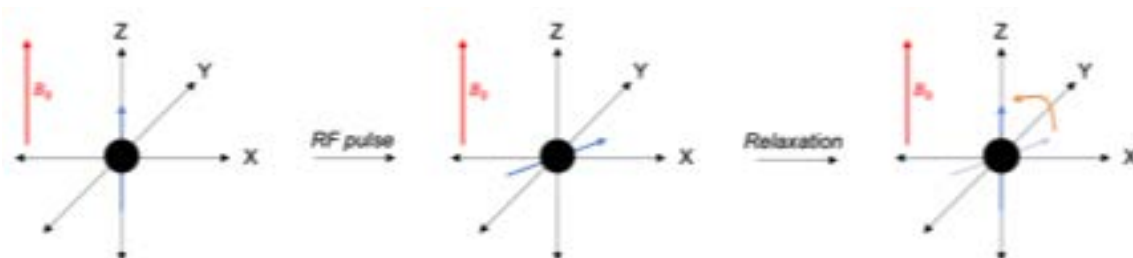
Figure 2.8. Schematic illustration of the changes in net magnetization before and after an applied RF pulse.

Figure 2.9 shows a simplified construction of a typical NMR spectrometer[77].

Once a sample is inserted in the spectrometer, the external magnetic field aligns

the magnetic moments of the nuclei as described above. The superconducting

magnet is typically kept at around 4 K using liquid He, with a surrounding liquid N_2

jacket to minimize the evaporation of liquid He. The sample is dropped in place by

an air cushion. The probe holds the RF coil which sends the RF pulse and collects

the FID. The console, which can send and receive RF pulses, sends the

programmed RF pulse to the sample, which is amplifed during transmission. The

FIDs are then Fouier-transformed to produce the familiar signal intensity versus

chemical shift plot for analysis by the user.
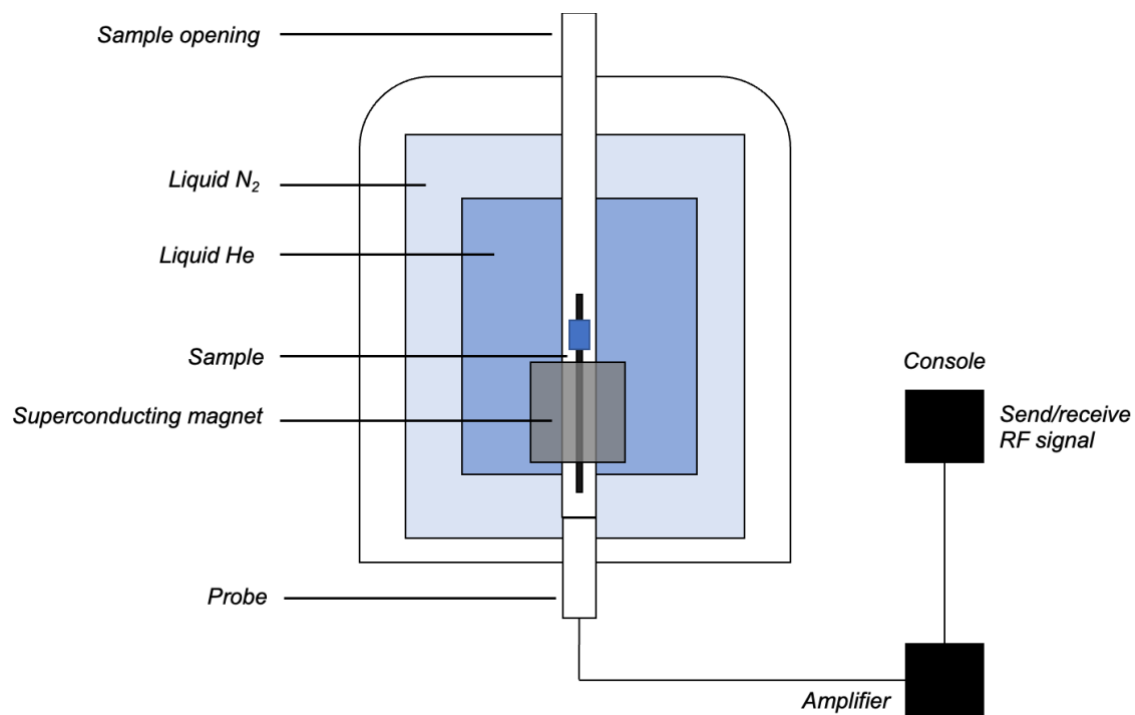
Figure 2.9. Schematic illustration of a typical NMR spectrometer.

For quantitative NMR measurements, the number of scans and time between each one must be carefully selected. The signal to noise ratio is proportional to the square root of the number of scans, so doubling the signal to noise requires quadrupling the scan number with diminishing returns after a certain scan number. The time between scans is determined based on pulse delay time, known as a T1 relaxation time, for a given nucleus in the specific sample environment (temperature, solvent, etc.). The time used between scans in quantitative NMR is at least 5-10 times T1 which ensures sufficient time for the net magnetization to return to ground state as shown in Figure 2.8. From a typical NMR spectrum, we can deduce molecular structure and nuclei chemical environment based on the location and splitting pattern of each peak. For example,

in ^{1}H NMR if the electron density around a nucleus is really high, then it will be "shielded" from the external magnetic field and will have a chemical shift close to 0 ppm, and the opposite is true for a nucleus that is less shielded by electron density. Moreover, the NMR peak for each proton can have a distinct splitting pattern depending on the number of different neighboring protons. Therefore, the NMR peak for a certain proton can be a singlet, doublet, triplet, etc., following the $n + 1$ rule where n is the number of different neighboring protons.

In this thesis, quantitative ^{19}F and ^{1}H NMR spectra were collected using a Bruker Avance 500 MHz spectrometer. ^{19}F spectra were collected using 32 scans with a 10 second relaxation delay, and ^{1}H spectra were collected using 16 scans with an 80 second relaxation delay. A known mass of 1,4-bis(trifluoromethyl)benzene (Sigma Aldrich, 98% purity) was added to each NMR tube as an internal standard for ^{19}F and ^{1}H NMR.

2.12. Isothermal Microcalorimetry (IMC) and Gassing in "Pouch Bags"

Assessing the reactivity of individual electrodes with the electrolyte is very valuable due to the complex nature of parasitic reactions. Our group previously showed that constructing "pouch bags" from positive and negative electrodes harvested from a fully charged pouch cell is an easy way to look at gas generation due to electrode/electrolyte reactions at the positive or negative electrode separately[78]. Figure 2.10 illustrates the process of constructing "pouch bags" from aged electrodes. After assembly, gas generation in pouch bags is monitored during high temperature storage. Here, gas generation (mostly CO_2) is a consequence of

reaction between the electrode/electrolyte[78–80]. While this simple test is very instructive, it only measures gas generation so reactions that create non-gaseous products will go unnoticed. Therefore, isothermal microcalorimetry (IMC) was used alongside *ex-situ* gas measurements to measure parasitic reaction heat flow.
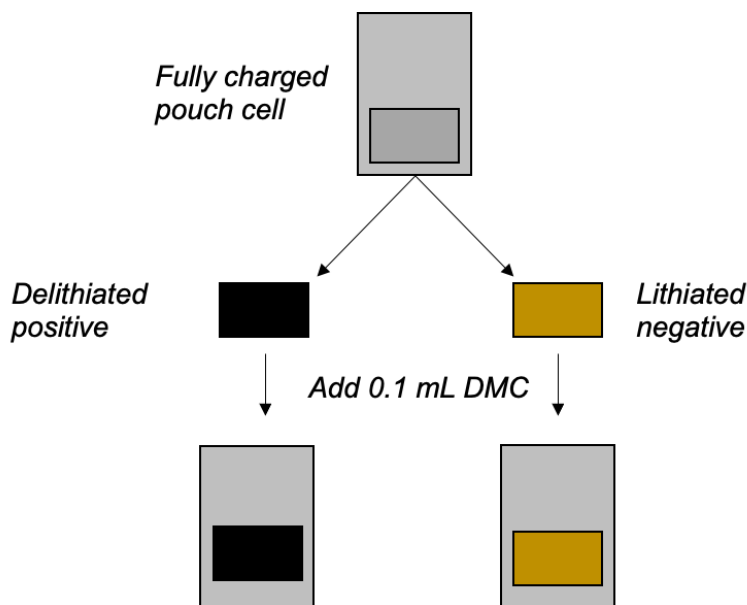
Figure 2.10. The process of assembling pouch bags from fully charged Li-ion pouch cells.

LMO/Graphite pouch cells underwent a C/20:C/20 formation cycle at 40 °C in the 3.0-4.20 V voltage range as described in Section 2.2. After the formation cycle, cells were charged to 4.20 V and held for 24 hours. After cells were equilibrated at top of charge, they were transferred to an Ar-filled glovebox, disassembled, and made into individual "pouch bags" as described in Figure 2.8 and previous work from our group[78]. The separate electrodes were wound and inserted into laminate foil bags which were then vacuum and heat sealed in the glovebox. Before sealing, 0.1 mL of DMC was added to each bag to account for

solvent loss during disassembly. Negative and positive electrode pouch bags were stored at 60 °C for 60 days and gas generation was monitored periodically using Archimedes' principle (see Section 2.3).

IMC experiments have been extensively used in our group to study parasitic reaction heat flow in Li-ion cells[81]. Therefore, we utilized IMC here to look at parasitic heat flow from individual negative electrodes and the electrolyte in pouch bags. Negative electrode pouch bags were inserted into a TAM III calorimeter (TA instruments, temperature stability ± 0.0001 °C, accuracy ± 1 µW, precision ± 1 nW) and the heat flows for the pouch bags was measured at 40.0000 °C for approx. 120 hours as described by Logan et al[82]. The IMC measurements were done by Eric Logan at Dalhousie University.

In addition to pouch bag experiments, IMC was used to measured parasitic heat flow in NMC811/Graphite pouch cells during cycling. Full details of this measurement can be found in previous work from our group[81]. Cells underwent four cycles on a Maccor 4000 series cycler at a rate of C/20 from 3.0-4.2 V after formation to ensure a well-formed SEI. The cells were then put into a TAM III Microcalorimeter, set to a temperature of 40.0000 °C. Cells were then cycled at a current of 1.5 mA under the following protocol to determine the parasitic heat flow at different cut-off voltages: 3.65-3.85 V (three times), 4.00-4.20 V (twice), and 4.00-4.30 V (twice). This measurement was done by Eric Logan at Dalhousie University.

2.13. Synchrotron Computed Tomography (CT) Scans

Computed tomography (CT) consists of illuminating a rotating object with a coherent and collimated X-ray beam and measuring the transmitted X-rays as a function of angle of rotation. This information is used to reconstruct the internal structure of the rotating object so it is useful in imaging Li-ions cells in a non-destructive way. CT scans were done at the Canadian Light Source on the Biomedical Imaging and Therapy Insertion Device beamline by Toby Bond as described in previous work[49].

2.14. N$_2$ BET Specific Surface Area

The specific surface area was measured using a single-point N$_2$ BET (Brunauer-Emmertt-Teller) with a Micromeritics FlowSorb 2300 instrument or provided by the materials' supplier. For in-house measurements, four measurements were taken for each sample and the average and standard deviation are reported.

Chapter 3.   The Impact of Cycling Conditions on The Lifetime of NMC/Graphite Pouch cells

Most of the results presented in this chapter were published in *A. Eldesoky et al* 2022 *J. Electrochem. Soc.* **169** *100531*. A. Eldesoky conceived and planned all experiments presented here, completed the data analysis and manuscript writing with supervision from J. R. Dahn. A. Eldesoky carried out all XRF measurements according to the method developed for this thesis and published in *A. Eldesoky et al* 2020 *J. Electrochem. Soc.* **167** *130539.* D. Rathore performed the cross-section SEM. T. Bond at the Canadian Light Source performed the X-ray CT scans. R. Dressler and N. Kowalski assisted A. Eldesoky with cell filling and formation.

3.1.   Introduction

Ni-rich cells (80 % Ni) have shorter lifetime compared to other NMC grades with lower Ni content, such as NMC532 for example, especially at high voltages[17,21]. However, there is a high demand for Ni-rich positive electrodes due to their higher energy densities. Strategies such as electrolyte engineering[21,83,84], and electrode coatings and/or dopants[51,85] have been utilized to improve the lifetime of NMC811 and Ni-rich cells, but Ni-rich cells operated to 4.20 V continue to show inferior lifetime regardless of advances in electrolytes or material engineering. One of the best strategies to improve the lifetime of NMC cells is the use of so-called "single crystalline" (SC) materials compared to conventional "polycrystalline" (PC) ones[47]. A typical PC material consists of small sub-micron primary particles that form larger secondary particles. On the other hand, SC

materials consist of single primary particle (typically 3-5 μm in size for NMC). This SC morphology alleviates the negative impact of anisotropic strain that occurs during cycling due to volume change and minimizes microcrack formation[86].

Battery cell degradation depends on factors such as temperature, C-rate, depth-of-discharge (DOD), and UCV, all of which will impact the cell capacity and resistance over time[87–90]. Therefore, understanding the impact of all these factors on the lifetime of Ni-rich Li-ion cells is critical to maximizing their lifetime. Numerous publications have examined the impact of cycling conditions on the degradation of various cell chemistries and form factors, but often with limited capabilities for post-mortem analysis since these studies utilize commercial cells. Despite the differences in cell design among various aging studies, some key similarities arise:

1. Cycling at higher rates and/or low temperatures can result in Li plating[91,92];

2. Generally, higher DODs and SOCs result in increased capacity fade and impedance growth[62,88,93–96];

3. Li inventory loss is the dominant source of capacity loss and positive electrode active mass loss can contribute to cell failure when particle cracking is prominent[17,43];

4. Higher temperatures exacerbate Li inventory loss and cell degradation[87,97].

In this work, we studied the impact of DOD, C-rate, UCV, and temperature on capacity retention and resistance growth of SC NMC811/Kaijin AML400 artificial

graphite (AG) pouch cells. Additionally, capacity loss and resistance growth in NMC811/AG cells were compared to NMC532/AG and NMC640/AG cells after long-term cycling under the same conditions. Figure 3.1 summarizes the design of the experiment performed here.

The UCV was fixed to either 4.06 or 4.20 V and the lower cut-off was varied according to the DODs shown in Figure 3.1. The 4.06 V UCV was chosen because NMC811 materials experience large lattice collapse past this point[42]. At high SOCs, the positive electrode becomes delithiated, and, after a certain degree of delithiation, the c-lattice parameter can significantly decrease which results in severe volume change[98,99]. Therefore, cycling just below the point of lattice collapse (4.06 V) and past it (4.20 V) allows us to study the impact of lattice volume change on cell performance. The C-rates used here were C/50, C/10, C/5, or C/3, and the DOD choices were 25, 50, 75 or 100 % DOD. Cells were cycled at RT or at 40.0 ± 0.1 °C for 12000 hours followed by a range of characterization experiments: EIS, differential thermal analysis (DTA), ultrasonic mapping, XRF, differential capacity analysis, CT imaging, and cross-section SEM, some of which will be discussed in this chapter. This extensive aging study on cells with demonstrated excellent cycle life, and subsequent characterization of aged cells, allows for optimization of charging conditions to accommodate various applications. Cell and electrolyte specifications can be found in Table 3.1.
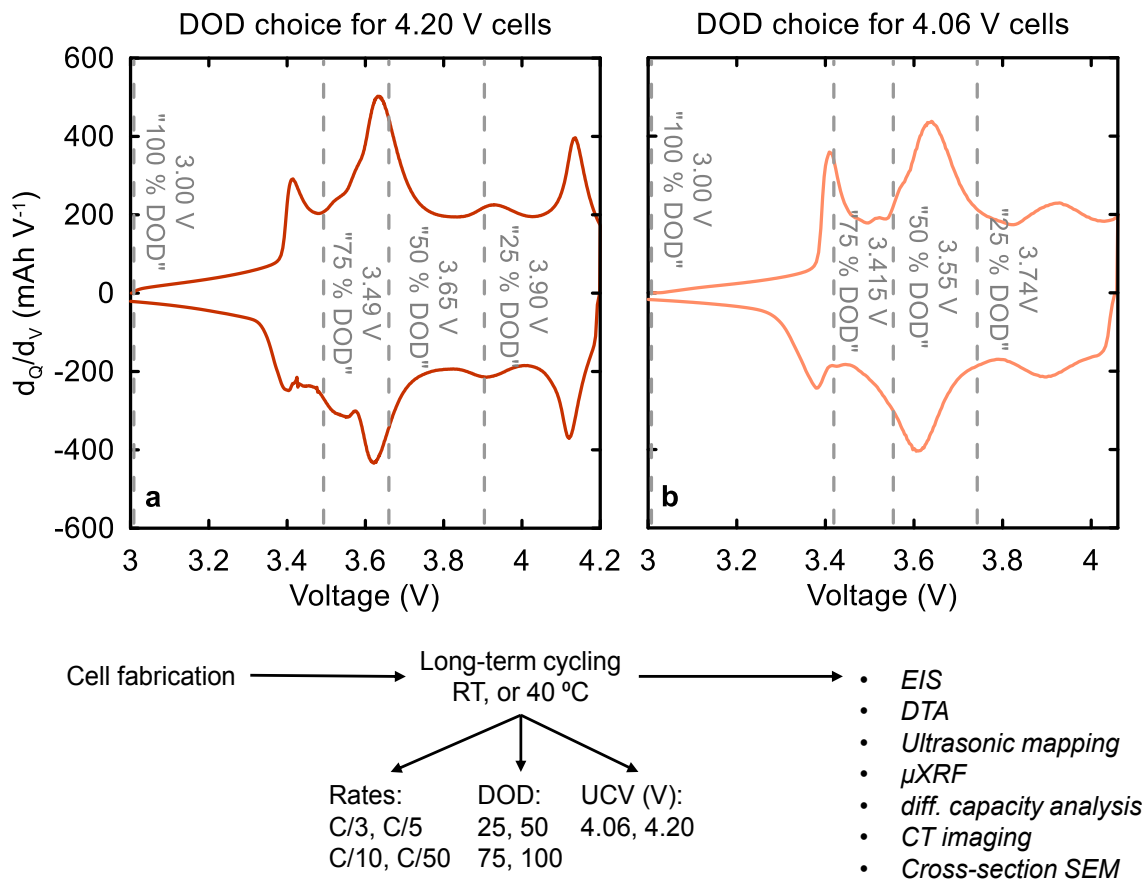
Figure 3.1. dQ/dV (mAh V^{-1}) versus voltage (V) for NMC811/AG cells cycled to (a) 4.20 or (b) 4.06 V UCV, and a summary of the experiments carried out in this work. Dashed lines indicate the lower voltage cut-off for 25, 50, 75 and 100 % DOD.

Table 3.1. Cell specifications and electrolyte formulation used in this chapter.

Neg. electrode	Loading (mg cm^{-2})	Composition	Density (g cm^{-3})	Pos. electrode	Loading (mg cm^{-2})	Composition	Density (g cm^{-3})
Kaijin AML400	~15	95.2:2.8:2 graphite:CMC/SBR:CB	1.55	SC NMC811	~21	94:2:4 NMC:PVDF:CB	3.28
Cu current collector thickness (µm)			8				
Al current collector thickness (µm)			16				
Nominal cell capacity (mAh)			~240				
Operating range (V)			3.0-4.20 (or 3.0-4.06)				
Excess graphite capacity at 4.40 V (%)			10				

Electrolyte information				
Name	**Solvent (wt. ratio)**	**[LiPF$_6$] (M)**	**Additive (wt.%)**	**Supplier**
2VC1DTD	EC:EMC:DMC (25:5:70)	1.5	VC (2 %) DTD (1 %)	Capchem

3.2. Long-term Galvanostatic Cycling of NMC811/AG cells at 40 °C

Long-term cycling experiments were carried out on NMC811/AG pouch cells cycled at 40 °C or RT with UCVs of 4.20 or 4.06 V and discharged to various DODs as described in Figure 3.1**.** All cells contained the "2VC1DTD" electrolyte described In Table 3.1 which is known to improve cell lifetime[17]. Cells were cycled at C-rates of C/3, C/5, C/10, and C/50 with periodic 100 % DOD, C/10:C/10 capacity check cycles every ~500 hours. Pair cells were cycled and one of each pair was stopped after 8600 hours (~1 year) of cycling for various characterizations, while the other cell continued cycling for another ~4000 hours. Figure 3.2 shows the discharge capacity (mAh) and normalized ΔV versus time for cells with 4.20 V UCV cycled at 40 °C, and the capacity check cycles are shown separately in Appendix A (Figure A.1). The RT counterpart to Figure 3.2 is shown in Figure A.2. The C-rate is indicated in each panel and the color intensity increases with the DOD choice. ΔV here is taken as the difference between the average charge and discharge voltages, which increases with the cell's internal resistance. The right column of Figure 3.2 shows normalized ΔV, that is ΔV value normalized by ΔV measured at the 10th cycle. The cycle number completed by each cell at t = 12000 hours is indicated in each panel.
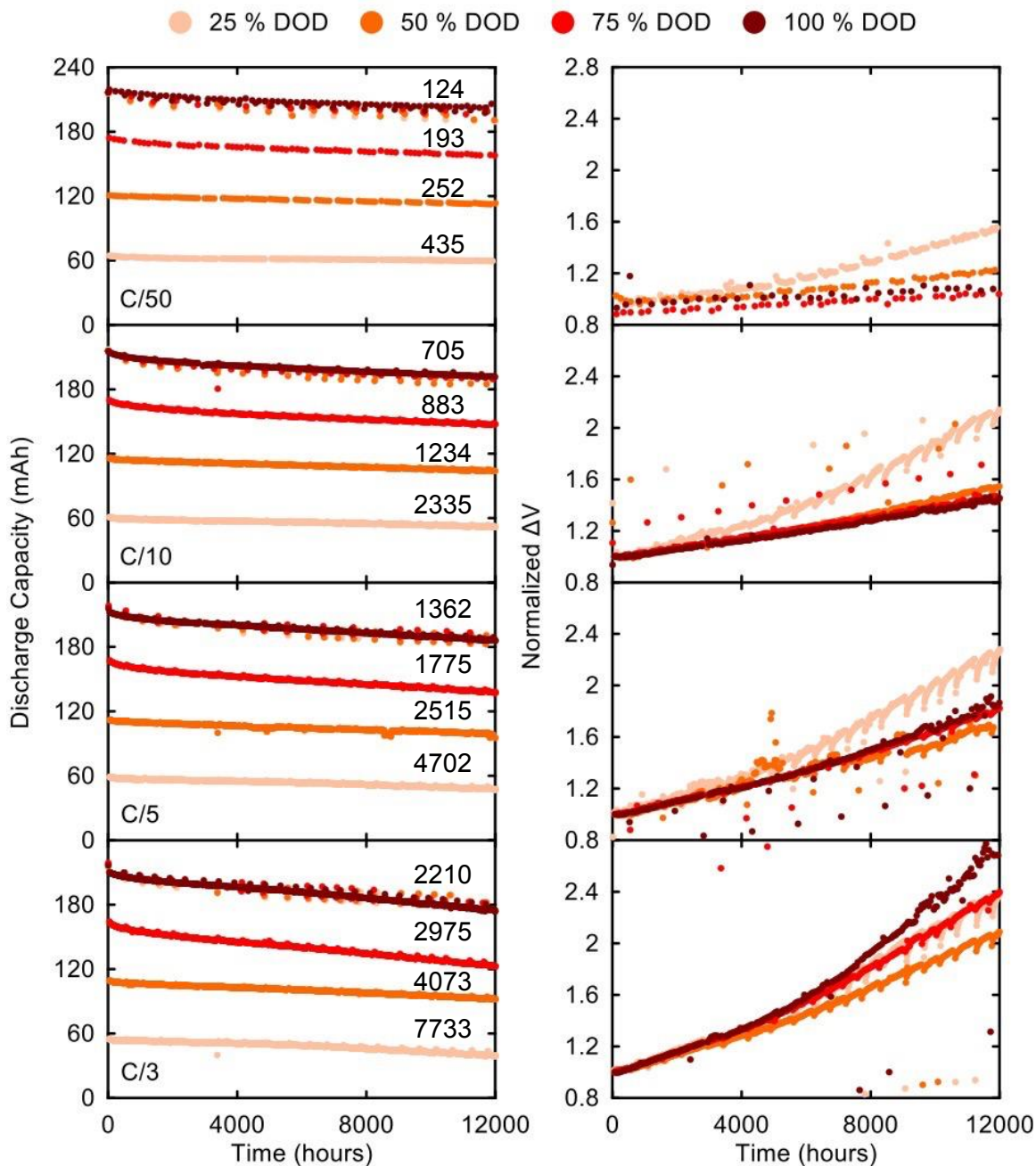
Figure 3.2. Discharge capacity (mAh) and normalized ΔV versus time (hours) for NMC811/AG cells cycling to 4.20 V UCV at 40 °C with 25, 50, 75, and 100 % DOD. The C-rate and cycle number at t = 12000 hours are indicated in each panel.

Similarly, Figure 3.3 shows the discharge capacity (mAh) and normalized ΔV versus time for cells with 4.06 V UCV cycled at 40 °C, and the RT counterpart is shown in Figure A.3. One apparent and dramatic difference between Figure 3.2 and Figure 3.3 is the minimal ΔV growth for the 4.06 V UCV cells compared to their 4.20 V counterparts. For example, ΔV for 4.20 V cells cycled at C/3 at 40 °C more than doubled after 12000 hours of cycling while the 4.06 V C/3 cells showed a ~25 % increase at the most. Additionally, the 4.06 V cells in Figure 3.3 show a significantly improved capacity retention compared to the 4.20 V cells.
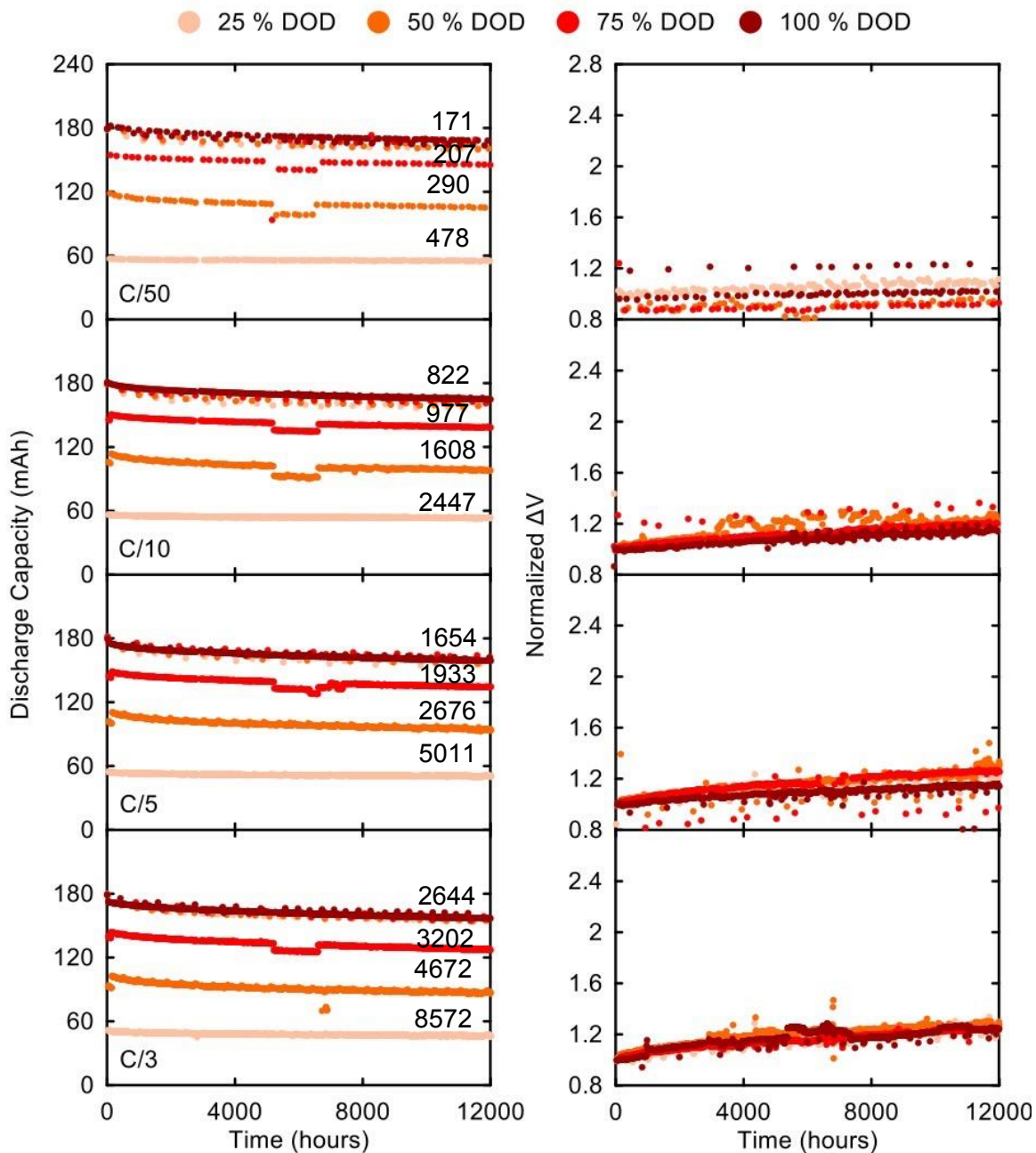
Figure 3.3. Discharge capacity (mAh) and normalized ΔV versus time (hours) for NMC811/AG cells cycling to 4.06 V UCV at 40 °C with 25, 50, 75, and 100 % DOD. The C-rate and cycle number at t = 12000 hours are indicated in each panel. The dip in capacity around ~5500 hours is due to failure of one 40 °C temperature box after a power outage.

53

Figure 3.4 shows the absolute capacity loss (mAh) at t = 12000 hours from the C/10:C/10, 100 % DOD, capacity check cycles versus C-rate. There is an overall increase in capacity fade with increasing current which can be attributed to the larger cycle number of C/3 cells versus C/50 cells. It is worth noting that larger DODs generally resulted in *smaller* capacity loss. Capacity loss for cells cycled at 40 °C with a 4.20 V UCV at C/3 and C/5, however, showed minimal DOD dependency. Overall, differences between the various DODs in Figure 3.4 were within 10-15 mAh which is very small. Some trends in Figure 3.4c-d are less clear since these cells cycle in ambient conditions with limited temperature control (20.0 ± 2.0 °C).
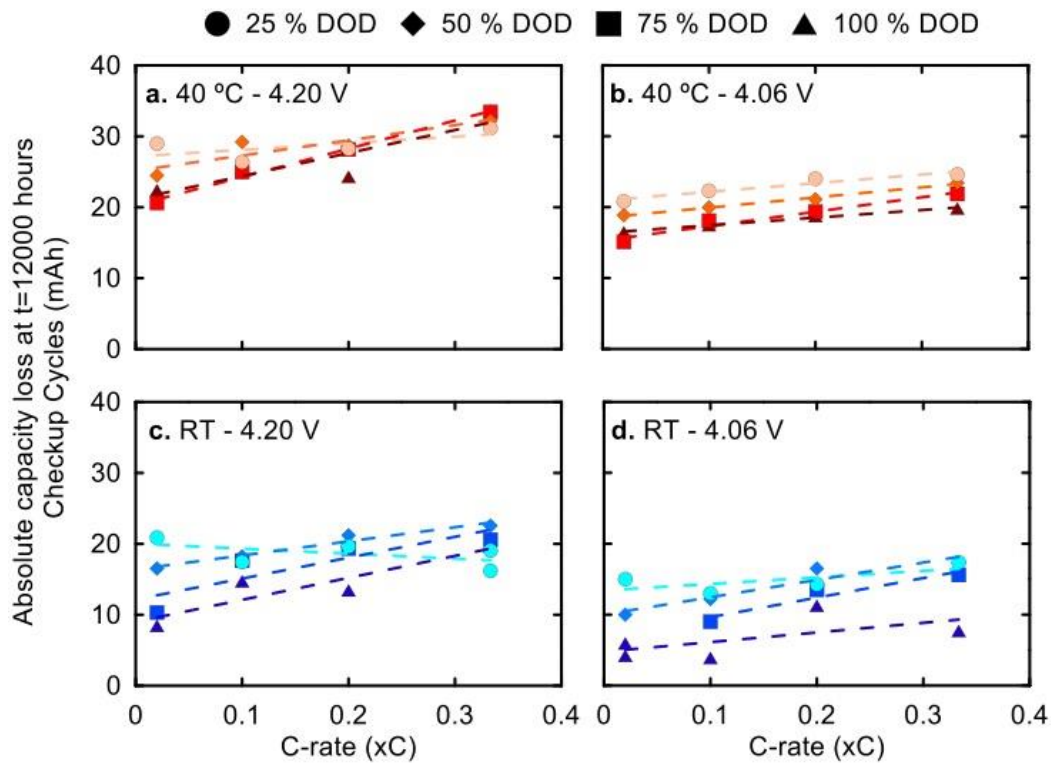
Figure 3.4. Capacity loss (mAh) from the 100 % DOD, C/10:C/10 capacity check cycles at t = 12000 hours versus C-rate for all cells in this work. (a-b) show the capacity loss for the 40 °C cells cycled to 4.20 and 4.06 V UCV, and (c-d) show the capacity loss for the equivalent RT cells. The different DODs are indicated by the different symbols.

Figure 3.5 summarizes the ΔV growth for all cells in this work at t = 12000 hours versus C-rate. Figure 3.5a-b highlights the dramatic impact of UCV on ΔV growth, where the 4.20 V cells demonstrated up to a 200 % increase in ΔV and the 4.06 V counterparts showed no more than 25 % increase. Additionally, the impact of temperature on ΔV growth is shown in Figure 3.5c-d where minimal ΔV growth (<30 %) was seen after 12000 hours of cycling at RT regardless of UCV. We believe the differences shown in Figures 3.5a-b are quite remarkable and highlight a persistent issue with Ni-rich cells.
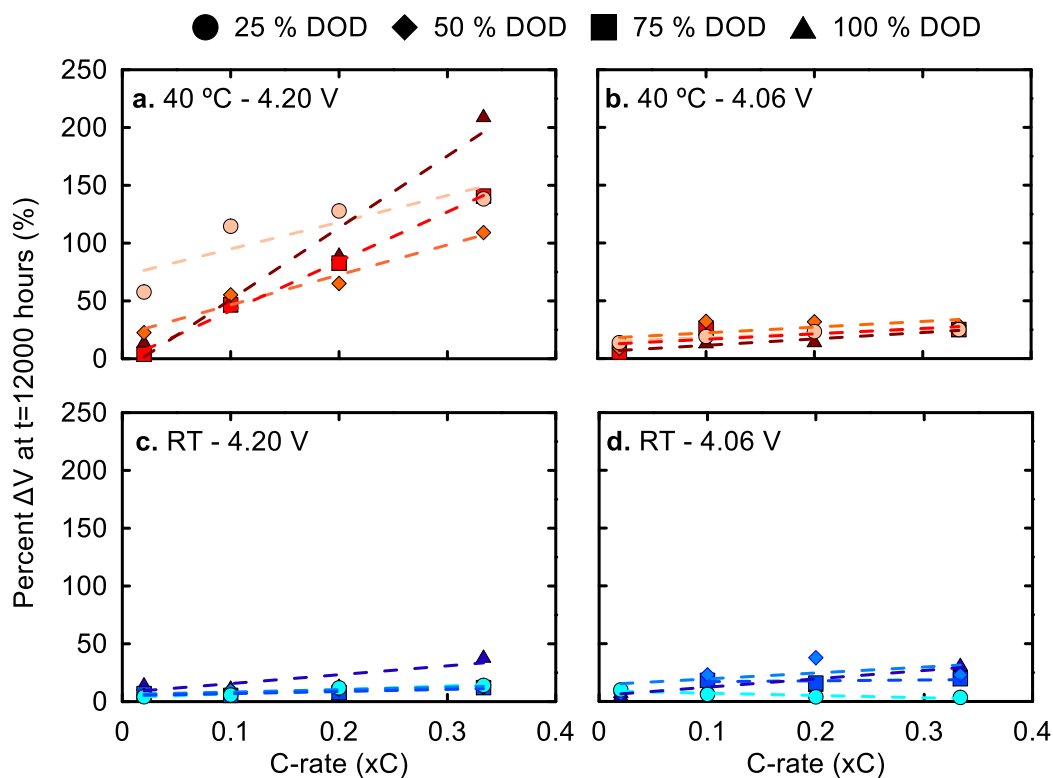
Figure 3.5. Percent ΔV growth at t = 12000 hours versus C-rate for all cells in this work. (a-b) show the ΔV increase for the 40 °C cells cycled to 4.20 and 4.06 V UCV, and (c-d) show the ΔV increase for equivalent RT cells. The different DODs are indicated by the different symbols.

NMC811 materials experience a significant lattice volume collapse past ~4.06 V, often misattributed to the so-called "H2-H3" phase transition, which in fact does not exist in NMC811 as demonstrated by Märker et al[42]. The dramatic lattice collapse occurring at high potentials could result in anisotropic lattice expansion and subsequent particle cracking coupled with the reactivity of electrolyte with freshly exposed surface. However, this effect may be minimal in single crystal materials. Additionally, lattice collapse can decrease Li mobility and thus the accessible capacity of the cell[42]. Jung et al have also shown that the NMC811 surface begins to evolve oxygen which reacts with the electrolyte during this

voltage plateau above 4.06 V in a full cell[41]. While many approaches such as positive electrode dopants and coatings have been used to address these issues with varying degrees of success[100,101], we believe Figure 3.5 provides a simple and economical approach: lowering the UCV to avoid lattice collapse and accelerated parasitic reactions. So far, the impact of UCV and temperature is well understood, so the impact of DOD and C-rate will be discussed further below.

Figures 3.4 and Figure 3.5 show that cycling at higher rates resulted in more capacity loss and larger resistance growth overall. Additionally, cycling at smaller DODs resulted in an increased capacity fade compared to larger DODs (Figure 3.4b, for example), although the difference in capacity loss as a function of DOD were fairly small (see Figure A.1). In this work, a 25 % DOD cell with a 4.06 or 4.20 V UCV discharges down to 3.74 or 3.90 V, respectively, meaning that most of the cell's lifetime is spent at voltages greater than the 100 % DOD counterpart which discharges down to 3.0 V. It is understood that operating at higher voltages increases the rate of parasitic reactions in the cell[81,102], so a cell that spends most of its lifetime at relatively higher voltages can be expected to lose more capacity. This can be seen in Figure 3.4 where the overall trend shows that smaller DODs result in more capacity fade. Moreover, Figure 3.4 shows that cycling at higher rates results in more capacity fade, which can be rationalized by the fact that C/5 cells will have 10x as many cycles as their C/50 counterpart cycling for the same total time (12000 hours in our case), which can lead to further SEI thickening with every charge[43].

3.3. Post-cycling characterization of Aged NMC811/AG cells

3.3.1. EIS After Formation and 1 Year of Cycling

Figure 3.6 shows EIS results after cell formation and after 1 year of cycling at 4.06 or 4.20 V UCV at 40 °C for the cells with different DODs and C-rates in this work. EIS spectra were collected at 50 % SOC and 10 °C, and the positive electrode area-specific impedance is reported here. All cycled cells showed an increase in charge transfer resistance (R_{CT}) compared to the post-formation results as expected. However, the changes in R_{CT} in the 4.06 V cells showed no C-rate- or DOD-dependency; in fact, all 4.06 V cells showed a nearly identical R_{CT} after 1 year of cycling at 40 °C. On the other hand, the 4.20 V cells showed that R_{CT} increases with both DOD and C-rate. However, at 25 % DOD the current dependence of R_{CT} for the 4.20 V cells after cycling is negligible.
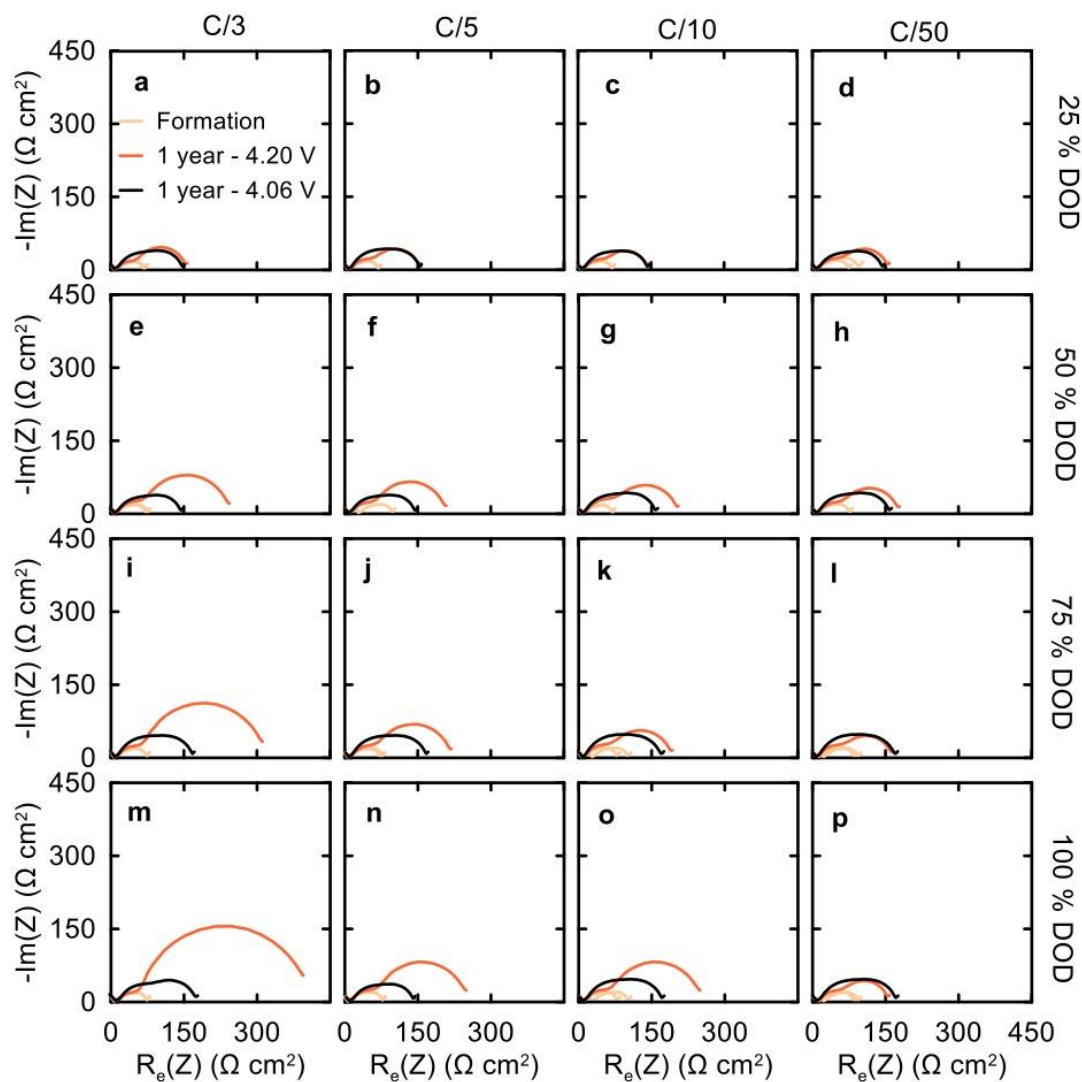
Figure 3.6. Nyquist plots collected after formation and 1 year of cycling for NMC811/AG cells cycling to 4.06 or 4.20 V UCV at 40 °C at (a-d) 25, (e-h) 50, (i-l) 75, and (m-p) 100 % DOD. C rates are indicated for each column. All EIS spectra were recorded at 10 °C and 3.80 V.

Despite some clear differences in capacity retention for 4.06 V cells cycled at different DODs and C-rates (Figure 3.4b), Figure 3.6 shows that there is no C-rate- or DOD-dependency on the R_{CT} growth after 1 year of cycling. All the 40 °C, 4.06 V, cells in Figure 3.6 showed a similar magnitude of R_{CT} increase after cycling compared to the formation data. This is consistent with the cycling data in

Figure 3.3 and Figure 3.5 where the 4.06 V cells all showed an equally small increase in ΔV.

The 4.20 V cells in Figure 3.6 are showing both a C-rate- and DOD-dependence, where R_{CT} increases with DOD and C-rate (see the C/3 column and 100 % DOD row in Figure 3.6, for example). The increase in R_{CT} with C-rate can be attributed to an increase in cycle number at faster rates, where the cells will operate at higher voltages more frequently leading to an increase in the rate of parasitic reactions, oxygen release and rock-salt surface layer formation[41], and subsequent impedance growth. However, if R_{CT} was solely dependent on cycle number, then the R_{CT} growth for the 100 % DOD cells should be smaller than 25 % DOD ones, which is not the case in Figure 3.6 for 4.20 V cells, so there must be a more complex interplay between DOD and R_{CT} in this work.

Cells cycling at 100 % DOD utilize more Li with every charge/discharge which in principle could result in SEI cracking/restructuring[103,104] and an increased rate of parasitic reactions and a higher R_{CT}, compared to the 25 % DOD cells. It is possible that cycling at higher DODs resulted in the generation of "crosstalk species" on the negative electrode that could migrate to the positive electrode and increase R_{CT} through film-forming reactions, while the lower DOD cells did not generate these species since the graphite volume change was very small at lower DODs. The generation of crosstalk species has been well documented in the literature. Sahore et al constructed a two-compartment cell with a solid-state separator that blocks the movement of electrolyte degradation species from one electrode to the other; then the electrolyte composition in the two-compartment cell

was compared to a regular Li-ion where crosstalk reactions are allowed to take place[104]. This work showed that in the presence of crosstalk reactions, species generated at one electrode could migrate to the other where they can further react and degrade the electrolyte/thicken the SEI which is corroborated by other research groups[105,106]. The generation of these crosstalk species due to increased Li utilization during cycling or SEI cracking might explain some of the trends in Figure 3.6 as described above.

3.3.2. Differential Capacity Analysis (DCA)

Differential capacity analysis (DCA) is a useful tool to deconvolute the contributions of Li inventory loss (or "shift loss") and/or active material loss to capacity fade[107]. The principle behind DCA is quite simple. A plot of the change in voltage with respect to capacity (dV/dQ) versus capacity, Q, for a full cell can be reconstructed from dV/dQ versus Q for the positive and negative electrode by:

$$\frac{dV}{dQ}(Q) = \frac{1}{m_p}\frac{dV_p}{dq_p} - \frac{1}{m_n}\frac{dV_n}{dq_n} \tag{3.1}$$

where m_p and m_n are the positive and negative electrode active masses. As the cell ages, active material loss (see Section 1.4.4) or Li inventory loss will result in a reduced cell capacity and changes in the dV/dQ versus Q plot due to changes in the cell capacity, active material mass, or both. Using reference voltage versus capacity curves collected using pristine positive and negative electrode materials, one can alter the active material mass and/or electrode slippage to reconstruct the dV/dQ versus Q plot for an aged cell with great accuracy[46,108]. This allows us to

determine the individual contributions of active material loss and Li inventory loss (i.e., "shift loss", the difference between positive and negative electrode shift) to capacity fade in a non-destructive way. In cases where the full cell capacity is limited by the negative electrode—for example, due to rapid SEI growth—one would not be able to measure the smaller contributions to capacity loss from the positive electrode, and vice versa. Therefore, DCA may show positive electrode mass loss, but the measured capacity loss could stem from the negative electrode only. DCA will be conducted using the software developed by Dahn et al throughout this thesis[107].

Figure 3.7 shows the calculated positive and negative electrode voltage curves and the measured full cell voltage curve after formation (t = 0 hours) and cycling (t = 12000 hours). The cells in Figure 3.7 were cycled at 40 °C with a 4.20 V UCV at C/3 and different DODs. The full cell charge curve has zero capacity at the point where the full cell is discharged. Figure A.4 shows excellent agreement between the measured and calculated dV/dQ vs. Q curves. Figure 3.7 shows that relative electrode slippage increased with cycling which is consistent with Li inventory loss, and the 25 and 50 % DOD cells showed more relative slippage compared to the 75 and 100 % DOD counterparts. Differential capacity analysis was performed on a representative set of cells to highlight the impact of DOD, C-rate, and UCV on inventory loss and active material loss, if any.
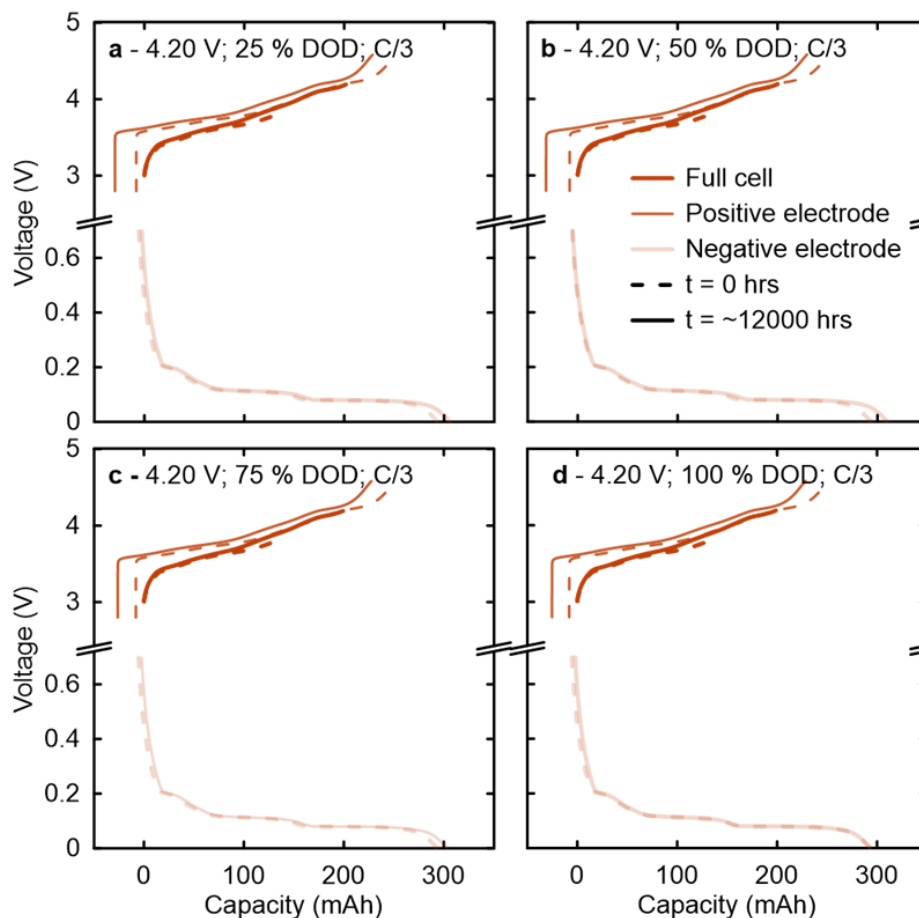
Figure 3.7. Voltage (V) versus capacity (mAh) curves of the full cell, negative, and positive electrodes obtained from differential capacity analysis at t = 0 (dashed line) and 12000 hours (solid line) for (a) 25, (b) 50, (c) 75, (d) 100 % DOD cells. All cells shown here were cycled at C/3 with 4.20 V UCV at 40 °C.

Figure 3.8 shows positive electrode active mass and shift loss versus DOD or C-rate for cells cycled at 40 °C under different conditions as shown in the panels. It is clear in Figure 3.8a-c that there is no significant change in positive electrode active mass after prolonged cycling. Figure 3.8b shows that shift loss decreases slightly with increasing DOD, from ~22 mAh at 25 % DOD to 18 mAh at 100 % DOD; and Figure 3.8d shows that shift loss increases with UCV and sharply increases for cells cycled at C/3. The observations in Figure 3.8 suggest that Li

inventory loss ("shift loss") is the primary contributor to capacity fading in these cells since no changes in electrode mass were observed. This is expected for a robust SC material where particle microcracking is not a concern at the cycling conditions used here[86].
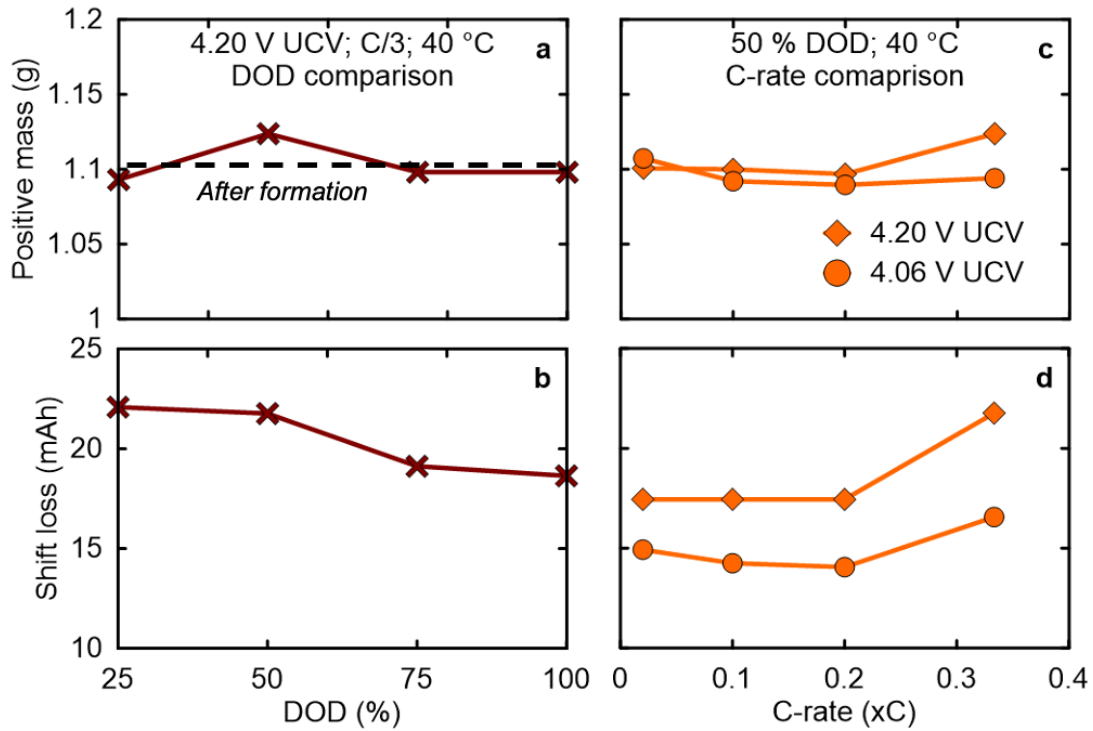
Figure 3.8. Calculated positive mass (g) and shift loss (mAh) versus (a-b) DOD or (c-d) C-rate for various NMC811/AG cells cycled for 12000 hours. UCV, DOD, C-rate, and/or temperature are indicated in the panels. Dashed line shows the calculated positive electrode active mass after formation (t = 0 hours).

3.3.3. XRF on Negative Electrodes After 1 Year of Cycling

A commonly proposed failure mechanism in NMC cells is TM dissolution and deposition on the negative electrode. Here, we used XRF to quantify the amount of Ni, Mn, and Co deposited on the negative electrode extracted from cells cycled for 1 year at 40 °C. Figure 3.9 shows the concentration of Ni, Mn, and Co (μg cm^{-2}) detected on negative electrodes taken from 4.20 and 4.06 V cells cycled at 40 °C for 1 year compared to levels of TM detected after formation. Overall, insignificant amounts of TMs were found on the negative electrodes of these cells, which is expected for a robust SC NMC material where TM dissolution and deposition is not an issue[55,56,109], which is consistent with the absence of positive electrode mass loss seen in Figure 3.8. In previous work, Thompson et al showed that [Mn] found on the negative electrodes of NMC532 cells cycled at UCVs of 4.0 to 4.40 V at 55 °C was between 1-3.5 μg cm^{-2} (<0.1 % of total Mn in the positive electrode), which did not significantly contribute to capacity loss[110]. While it possible that some small amounts of TMs did dissolve in the electrolyte and/or migrated to the anode, we do not believe that this is a significant concern in this work.
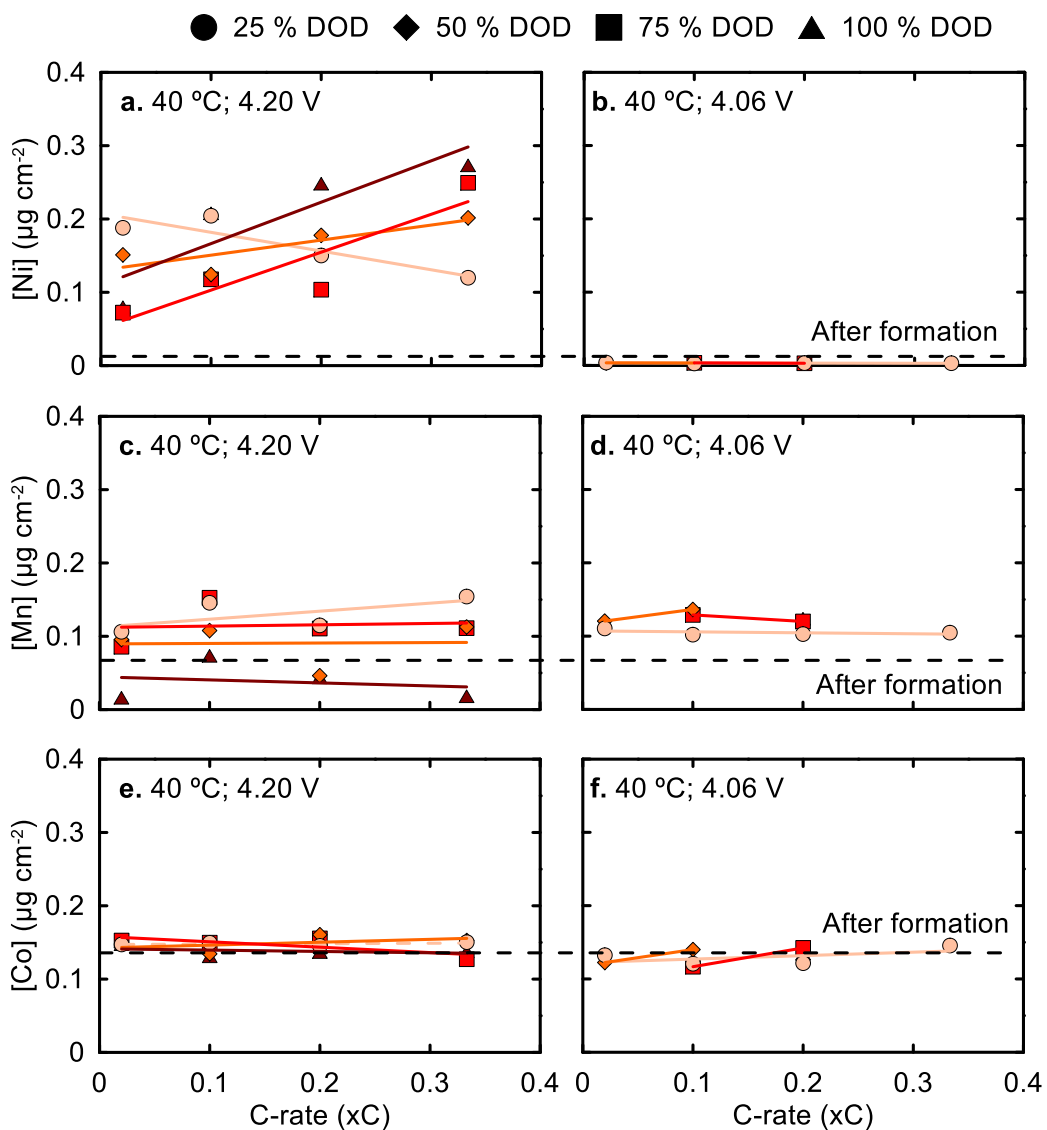
Figure 3.9. (a-b) [Ni], (c-d) [Mn], and (e-f) [Co] (µg cm^{-2}) on graphite electrodes extracted from NMC811/AG cells cycled 40 °C to 4.20 V or 4.06 V UCV for 1 year versus C-rate. Dashed lines indicate [TM] after formation only, and the DODs are indicated with different symbols.

66

3.3.4. Synchrotron CT

During cell operation, the electrodes may undergo mechanical degradation due to the continuous volume change during charge/discharge cycling. This mechanical degradation can result in electrode delamination, particle disconnection, or electrode swelling. Synchrotron CT was used to investigate the robustness of the SC NMC811 cells against mechanical degradation. Figure 3.10 shows 2D cross sections taken from NMC811 cells cycled at 40 °C with a 4.20 V UCV for 1 year. The different DODs and C-rates are indicated in the panels and a fresh comparator cell was scanned as received from our supplier.
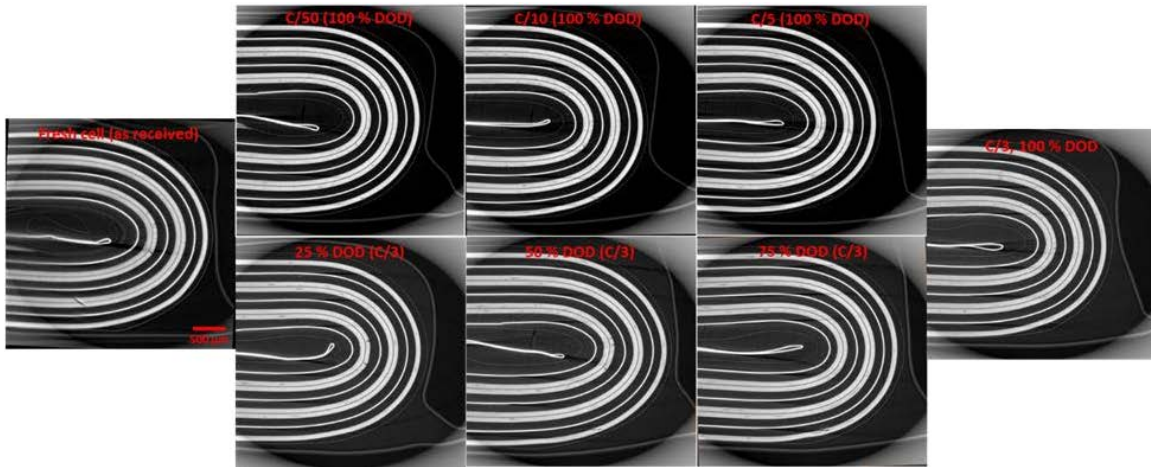
Figure 3.10. 2D cross sections taken from CT scans of NMC811/AG cells showing a region in the bottom corner of the jelly roll. All cells were cycled at 40 °C to a UCV of 4.20 V for one year. The C-rates and DODs are indicated in each panel. A dry cell with no electrolyte was scanned for comparison.

In all cells, there were no significant changes to the electrode thicknesses or degradation after 1 year of cycling, which further supports our differential capacity analysis results which showed no positive electrode mass loss. Table 3.2 lists the electrode thicknesses from CT images in Figure 3.10, where it is very clear

that thickness changes after cycling is insignificant compared to the fresh cell. By contrast, work by Gauthier et al[43] and Bond et al[49] on PC NMC622/graphite cells cycled for 2.5 years at 100 % DOD showed up to a 60 μm increase in cell electrode stack thickness.

Table 3.2. Electrode thickness measured at four different positions along the jelly roll for all NMC811/AG cells that underwent CT scanning. The cell labelled N/A was a fresh cell scanned as-received. The other cells were tested for one year under the conditions listed below.

UCV	C-rate	DOD	Temp. (°C)	Neg. electrode thickness (µm)	Pos. electrode thickness (µm)
N/A	N/A	N/A	N/A	271.4 ± 2.7	158.7 ± 1.9
4.20 V	C/3	25	40	265.4 ± 1.6	158.2 ± 1.5
	C/3	50	40	277.6 ± 3.6	159.1 ± 0.9
	C/3	75	40	273.5 ± 5.0	158.5 ± 0.7
	C/3	100	40	267.1 ± 3.5	157.1 ± 0.8
	C/5	100	40	270.2 ± 5.5	155.2 ± 0.5
	C/10	100	40	272.1 ± 2.6	155.2 ± 1.2
	C/50	100	40	270.2 ± 2.2	161.1 ± 0.8

3.3.5. Cross-section SEM

So far DCA, XRF, and CT scans have shown no signs of positive electrode mass loss, suggesting that there was no significant particle microcracking. To further investigate physical changes to the cell, disassembly at top of charge and cross-section SEM of the delithiated positive electrode were done. Cell disassembly allows visualization of any cell degradation such as separator discoloration, Li plating, or electrode delamination. Figure 3.11 shows images of

cells dissembled at top of charge and cross-section SEM images of the positive electrode. The cells in Figure 3.11 were cycled at 4.06 or 4.20 V UCV at 25 % DOD with a C/5 rate at RT. The 25 % DOD cells were imaged because the low DOD results in increased cycling over the so-called "H2-H3" phase transition region in NMC811 for the 4.20 V cell (see Figure 3.1). Figure 3.11 remarkably shows that after 12000 hours of cycling, the cells showed virtually no separator discoloration or signs of Li plating on the negative electrode. Further, cross-section SEMs of the positive electrode showed no signs of particle microcracking, consistent with the results shown above.
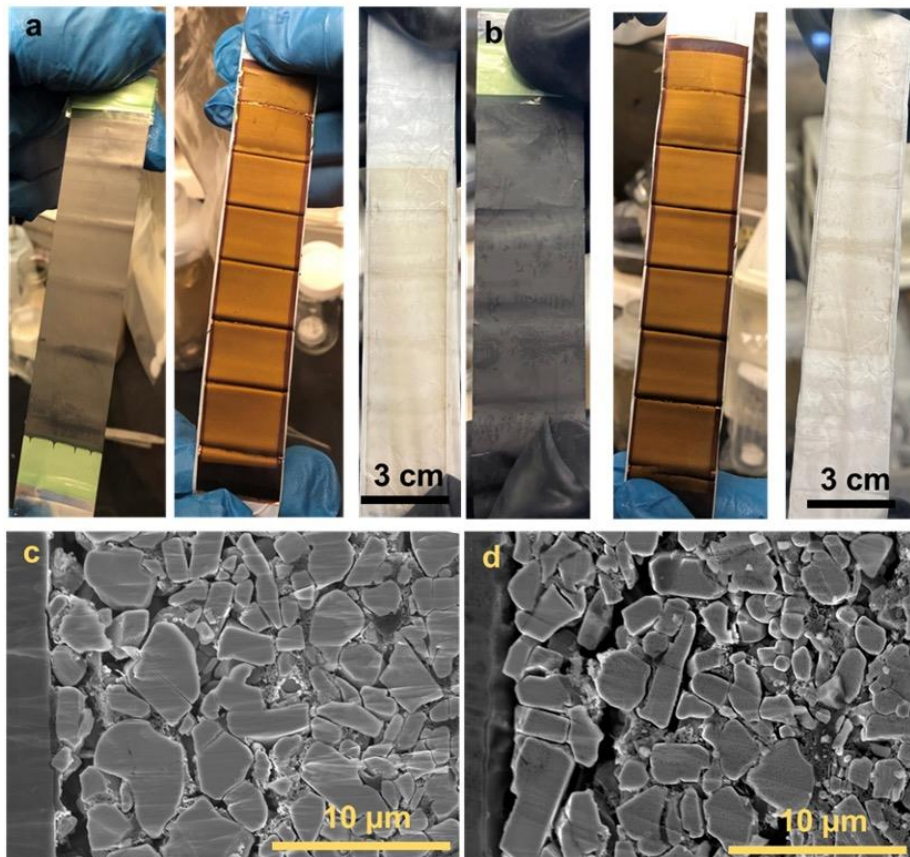
Figure 3.11. Images of dissembled cells cycled to (a) 4.06 or (b) 4.20 V UCV at C/5 and 25 % DOD at RT, as well as cross-section SEM of the positive electrodes taken from the (c) 4.06 or (d) 4.20 V cells.

3.4. Understanding the Behaviour of NMC811/Graphite Cells at Different DODs and UCVs

The capacity loss trends in this chapter are showing DOD- and C-rate-dependencies that are in contrast with a similar study from our group by Gauthier et al[43]. The differences between the two studies are summarized in Table 3.3 and will be explained in this section.

Gauthier's work used PC NMC622 positive electrode and NG negative electrode. PC NMC622 material used by Gauthier demonstrated significant microcracking and positive electrode active mass loss, especially at higher DODs. However, microcracking and positive electrode active mass loss *did not* contribute to the observed capacity fade (as shown by DCA) since Li loss at the negative electrode was the more dominant mechanism of capacity fade in the cells used by Gauthier. Similarly, the main capacity loss mechanism in the SC NMC811/AG cells in this chapter was Li inventory loss.

To reconcile the differences seen in Table 3.3 between this work and Gauthier's, specifically the opposing trends in capacity fade, one must examine the contributions of the different positive and negative electrode materials in both studies. NMC622 cycled to 4.10 V in the Gauthier study will not be prone to oxygen release, while NMC811 cells in this work will begin to evolve oxygen when the material is cycled beyond 4.06 V as shown by Jung et al[41]. The released oxygen can chemically oxidize the electrolyte[39,41] and result in the formation of rock-salt or disordered spinel-type surface layers on the NMC particle[41,47]. NMC811 cells that spend a larger fraction of time at high SOCs (such as the 25 % DOD cells) will be

more likely to evolve surface oxygen, resulting in electrolyte oxidation and subsequent Li consumption through some of the well-known pathways reported in the literature[39].

Gauthier's study used NG materials, which are known to perform worse than AG[111], and they observed an increase in capacity fade with SOC range for cells that were cycled with different lower or upper cut-off voltages (see Figure 16 in Gauthier et al). NG materials can exfoliate during charge/discharge cycling, which exposes fresh, un-passivated graphite surfaces that can react with the electrolyte[103,112,113]. Therefore, exercising the NG negative electrode over larger SOC ranges, or higher rates, resulted in more fade[43,95]. In this Chapter we saw the opposite trend: a decrease in capacity fade with increasing DOD, despite the more severe contraction/expansion of graphite particles expected at larger DODs, which we believe is due to the use of AG materials that are less prone to exfoliation during cycling[114]. However, our capacity fade at 12000 hours (Figure 3.4) was very similar to that reported at 12000 hours in Figure 16 of Gauthier et al despite our use of SC positive electrode and superior AG. We believe the similar magnitude of capacity fade stems from the fact that we are using NMC811 material which is prone to oxygen release at the UCVs used in this work. Therefore, NMC811/AG cells cycled at *lower* DODs (which spent more time at relatively high SOCs) could generate more alkoxides/unwanted electrolyte degradation, due to oxygen release, resulting in more capacity fade compared to larger DODs.

Table 3.3. Summary of this work compared to a similar study from our group by Gauthier et al

	Positive electrode	**Negative electrode**	**Capacity fade**	**Mechanism of capacity loss**	**ΔV growth**	**R_{CT}**	**Pos. electrode cracking**	**Volume expansion**
This work	SC NMC811	Artificial graphite	Worse at lower DOD and higher rates	Li inventory loss	Worse at lower DOD and higher rates	Increases with DOD and rate for 4.20 V UCV (40 °C)	No	No
Gauthier et al[43]	PC NMC622	Natural Graphite	Worse at higher DOD and higher rates	Li inventory loss	Worse at higher DOD and higher rates	Not reported	Yes	Yes, increases with DOD and rate

3.5. Impact of Charging Conditions on Different NMC Grades with the Same Negative Electrode

Section 3.4 discussed how the similar magnitude of capacity loss between this work and Gauthier, despite our use of SC positive electrodes and superior AG negative electrodes, is due to the lattice oxygen release in NMC811 and thus cycling at *lower* DODs unexpectedly resulted in *more* capacity due to longer residence time at higher SOCs. To validate the role oxygen release plays in the choice of optimal cycling conditions for NMC811, long-term cycling experiments at two different UCVs, C-rates, and DODs were carried out on SC NMC532 and NMC640 cells using the same AG materials as the SC NMC811 cells. All cycling was done at 40 °C with the same electrolyte and negative electrode, so the only difference here is the composition of the positive electrode material. NMC532 and NMC640 materials do not suffer from the large lattice volume change and oxygen release at the UCV chosen here, which were 4.10 or 4.30 V for both cell types (compared to 4.06 and 4.20 V for NMC811). The C-rates chosen for NMC532 and NMC640 were C/3:C/3 and 1C:1C to test the impact of high rate on the performance of NMC532 and NMC640.

Figure 3.12 shows the discharge capacity and ΔV growth for NMC640 and NMC532 cells cycled to 4.10 V at C/3:C/3 or 1C:1C. The lower voltage cutoff for 25 % and 100 % DOD in indicated on each panel. The 1C:1C NMC640 cells cycled at 100 % DOD showed the worst capacity retention and ΔV growth. In contrast, NMC532 cells, regardless of DOD or C-rate, showed significantly better ΔV control as is expected for this robust positive electrode material[17].
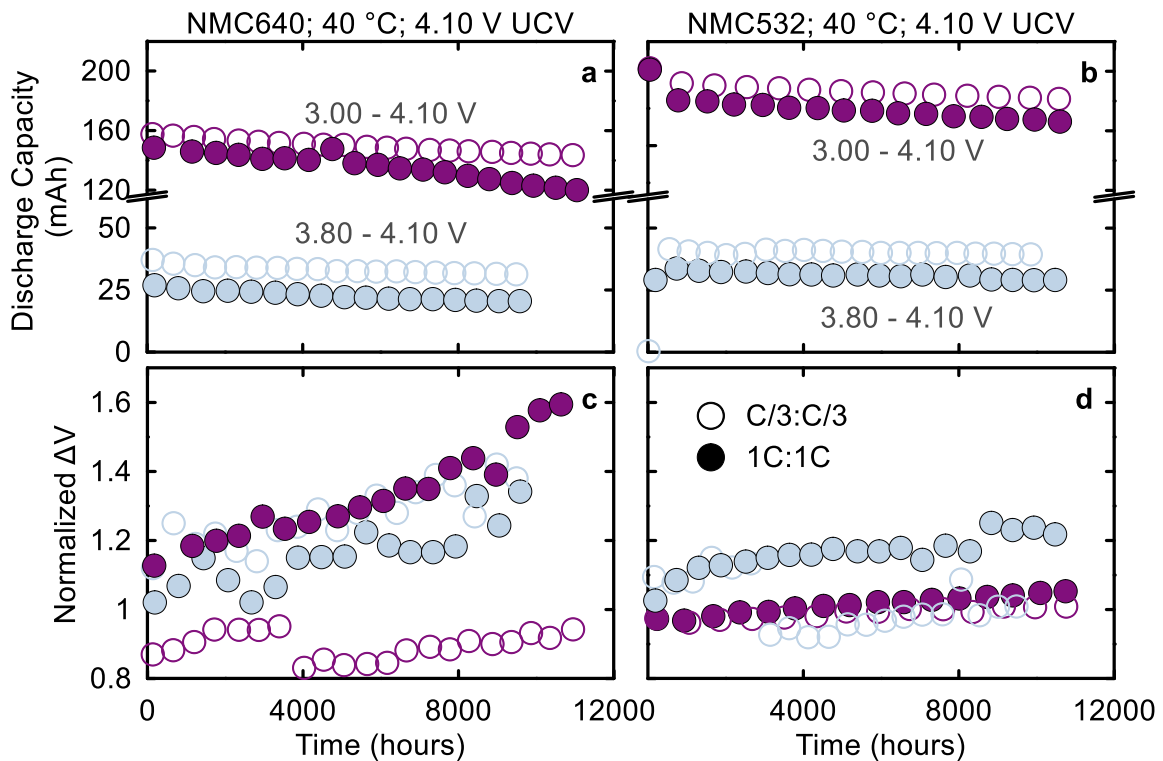
Figure 3.12. (a-b) discharge capacity (mAh) and (c-d) normalized ΔV versus cycling time for NMC532 and NMC640 pouch cells cycled at 40 °C. Cells were cycled at C/3:C/3 or 1C:1C with a 4.10 V UCV. The lower cut-off voltage was 3.0 V (100 % DOD) or 3.80 V (25 % DOD).

Figure 3.13 shows the discharge capacity and ΔV growth for NMC640 and NMC532 cells cycled to 4.30 V at C/3:C/3 or 1C:1C. The lower voltage cutoff for 25 % and 100 % DOD in indicated on each panel. NMC640 cells cycled at 1C:1C show rapid failure after only 500 hours at 100 % DOD. This is likely due to severe Li plating which is made worse by the choice of VC. The use of VC as an additive contributed to the drastic failure of NMC640 at 1C:1C due to its high R_{CT}[115], but the electrolyte blend was kept the same across all cells for comparison. Once again, NMC532 cells are showing much better ΔV control compared to NMC640 at all cycling conditions.
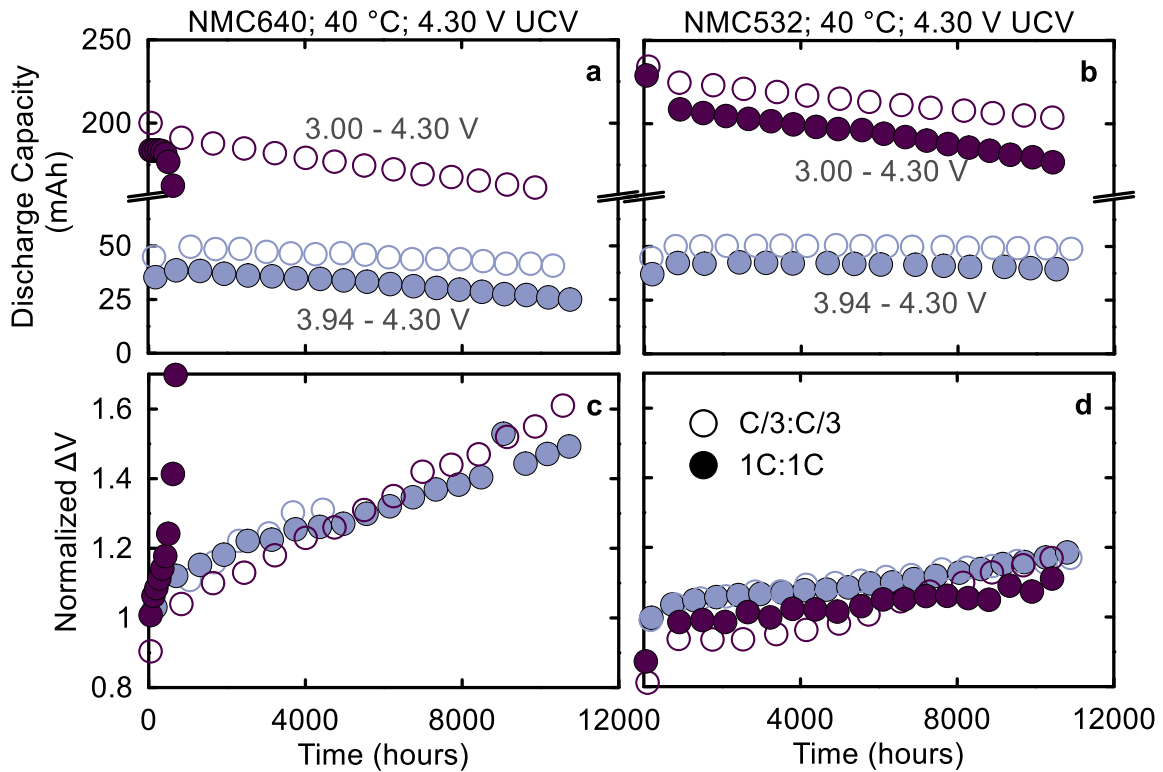
Figure 3.13. (a-b) discharge capacity (mAh) and (c-d) normalized ΔV versus cycling time for NMC532 and NMC640 pouch cells cycled at 40 °C. Cells were cycled at C/3:C/3 or 1C:1C with a 4.30 V UCV. The lower cut-off voltage was 3.0 V (100 % DOD) or 3.94 V (25 % DOD).

Figure 3.14 shows the capacity loss from the C/10:C/10 checkup cycles at

t = 12000 hours for SC NMC811, NMC532 and NMC640 cells. C-rate, DOD, and

UCV are indicated for each panel. NMC532 and NMC640 cells cycled at 1C:1C

show that high DOD results in more capacity fade. Similar trend can be seen in

NMC640 cells cycled at C/3:C/3 with a 4.30 V UCV, but differences due to DOD

were very small for NMC532 and NMC640 cycled to a 4.10 V UCV. While NMC640

cells showed poor retention at 1C:1C, this performance can be greatly improved

by tailoring the electrolyte additive to improve high-rate performance. The NMC811 cells were the only ones showing the opposite trend as discussed in Section 3.4.
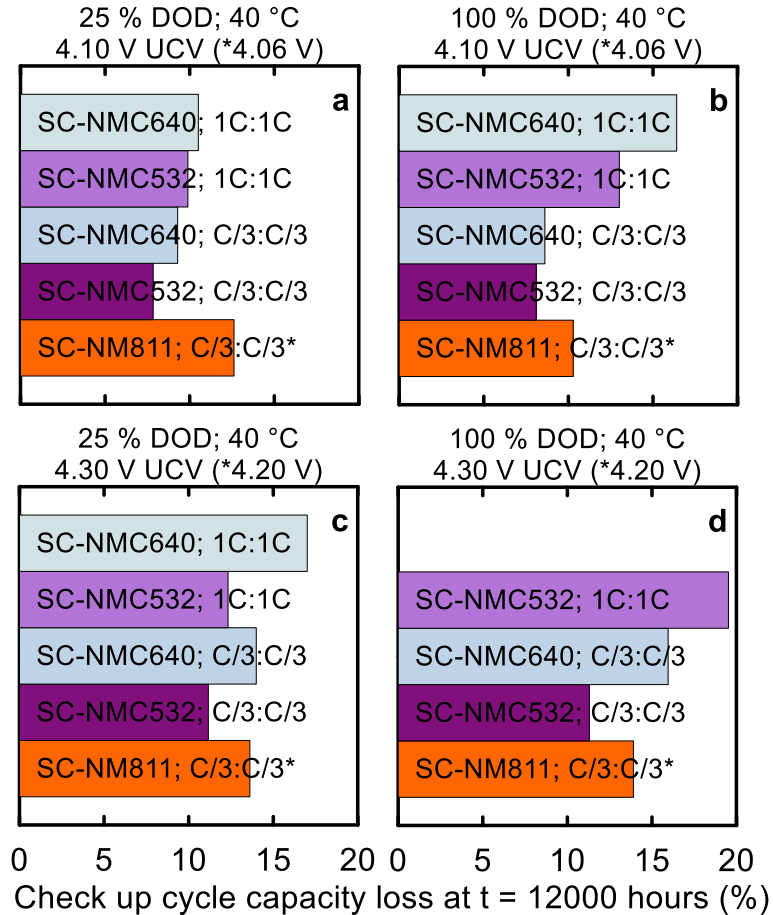
Figure 3.14. Checkup cycle capacity loss at t = 12000 hours for SC NMC811, NMC532 and NMC640 cells with the same AG negative electrode. All cycling was at 40 °C and the lower cutoff voltage was 3.0 V. The UCVs for NMC811 cells were 4.06 or 4.20, while the UCV for NMC532 and NMC640 were 4.10 or 4.30 V. C-rates and DODs are as indicated in the panels.

Figure 3.15 shows the ΔV growth at t = 12000 hours for the cells in Figure 3.14. Low voltage cells in the top row show small ΔV growth after 12000 hours. NMC640 had the most severe ΔV growth at 1C:1C and C/3:C/3 for both DODs compared to NMC532. NMC811 materials showed the largest ΔV growth at 4.20 V followed by NMC640 and NMC532. The severe ΔV growth for NMC811 shown in Figure 3.15 will drastically impact the power density of these cells, therefore keeping the UCV at or below 4.06 V is critical for NMC811.
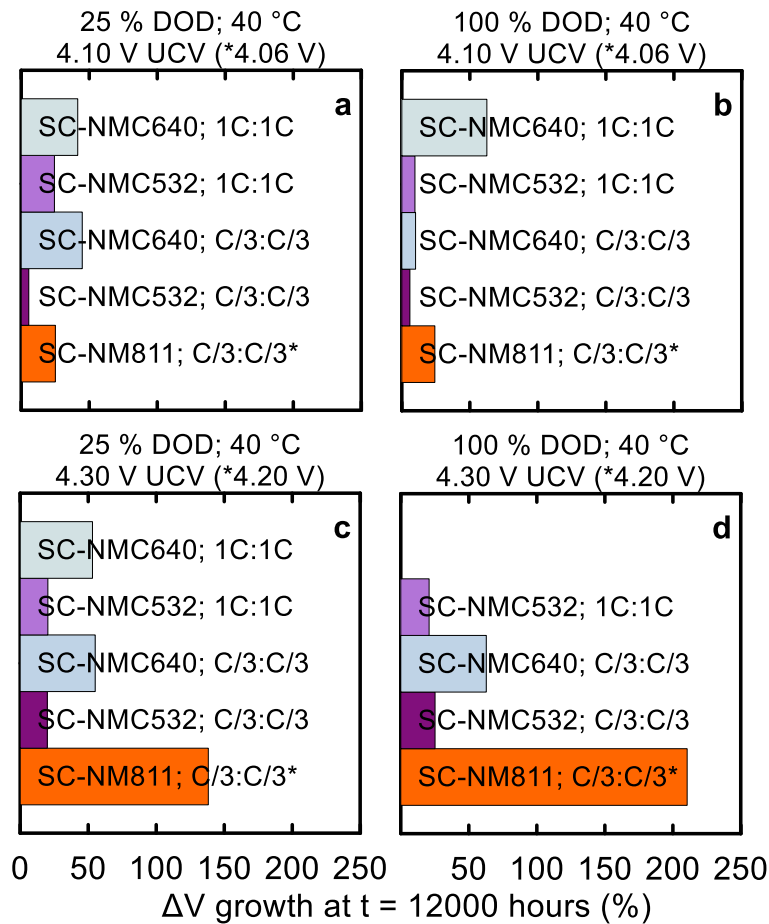
Figure 3.15. Percent ΔV growth at t = 12000 hours for SC NMC811, NMC532 and NMC640 cells with the same AG negative electrode. All cycling was at 40 °C and the lower cutoff voltage was 3.0 V. The UCVs for NMC811 cells were 4.06 or 4.20, while the UCV for NMC532 and NMC640 were 4.10 or 4.30 V. C-rates and DODs are as indicated in the panels.

3.6. Conclusion

This chapter examined the impact of DOD, C-rate, UCV, and temperature on the lifetime of NMC811/AG pouch cells. After cycling, cells underwent various characterization tests to study the impact of cycling conditions on cell aging and degradation. The main findings of this work can be summarized as follows:

1. Capacity loss and ΔV growth generally increased with C-rate;

2. Overall, the impact of DOD on capacity loss and ΔV growth was small, but we saw an increase in capacity loss with smaller DODs which we attributed to the fact that the NMC811 cells spent more time at higher voltages when the DODs were small;

3. EIS measurements at 50 % SOC and 10 °C showed that R_{CT} increased with DOD and decreased with C-rate for 4.20 V cells cycled at 40 °C, but no C-rate- or DOD-dependency for their 4.06 V counterparts;

4. XRF mapping of the negative electrode after 1 year of cycling at 40 °C showed no significant TM concentrations for 4.06 or 4.20 V cells;

5. Differential capacity analysis and cross-section SEM of the positive electrode showed no signs of positive electrode mass loss or particle microcracking, consistent with the robustness of the SC NMC811 used here;

6. Synchrotron CT showed no significant thickness increases for 4.20 V cells cycled at 40 °C, and no signs of electrode damage or delamination;

7. When cells are cycled at larger DOD, the greater Li utilization and volume change of the graphite increases capacity loss for both NG and AG materials, but will be much less severe in AG negative electrodes;

8. SC NMC532 and NMC640 cells cycled at 1C:1C (and NMC640 cells cycled at C/3:C/3 with a 4.30 V UCV) showed *more* capacity loss at larger DOD, contrary to NMC811 with the same AG material, indicating that oxygen release in NMC811 at high SOCs contributes to capacity fade trends observed above.

We hope this study will provide useful guidelines for determining the cycling conditions needed to prolong the lifetime of NMC811. While this chapter demonstrates that optimal cycling conditions greatly depends on the cell chemistry, it is clear that charging to lower SOCs is beneficial for the cell's lifetime. Low SOC cycling will result in low cell-level energy density, which is undesirable for EV applications, but can be an attractive option for energy storage applications where lifetime is much more important than energy density. At low SOCs, Li inventory loss will be the main and only contributor to capacity loss because oxygen release from the positive electrode will be hindered. Therefore, optimizing the electrochemical performance of the graphite negative electrode, coupled with low SOC cycling, can yield an even longer-lived energy storage cell.

Chapter 4. Electrochemical Behaviour of Different Graphite Materials and Their Impact on the Lifetime of NMC811/Graphite Cells

The results presented in this chapter were published in the following papers: A. Eldesoky et al 2022 J. Electrochem. Soc. **169** 100531; A. Eldesoky et al 2021 J. Electrochem. Soc. **168** 110543; A. Eldesoky et al 2022 J. Electrochem. Soc. **169** 010501. A. Eldesoky conceived and planned all experiments presented here, completed the data analysis and manuscript writing with supervision from J. R. Dahn, as well as performed the XRD measurements, GCMS experiments and in-operando gas measurements. S. Azam, E. Zsoldos, and N. Kowalski assisted with electrolyte filling. E. Logan and A. Louli performed the IMC and in-operando pressure measurements, respectively. W. Song provided some baseline cycling data for comparison. R. Weber, S. Hy, and R. Petibon provided the commercial-grade graphite materials studied here.

4.1.   Introduction

Graphite materials are categorized as natural or artificial (synthetic) depending on their origin. NG materials are mined from the Earth's crust and processed into negative electrode materials. AG materials are synthesized from a carbon precursor, such as a petroleum coke, that is heated in an inert atmosphere at temperatures near 3000 °C. NG materials are normally more crystalline than AG and possess fewer instances of misaligned graphene sheets (i.e., probability of turbostratic misalignment, P_r), thus resulting in greater specific capacity closer to theoretical 372 mAh g^{-1} for LiC$_6$. The higher the P_r is, the lower the specific capacity

will be since Li^+ do not intercalate between misaligned graphene sheets[114]. However, it is believed that the higher P_r of AG materials resulting, from a higher degree of turbostratic misalignment, helps pin some adjacent graphene layers together, thus minimizing exfoliation and improving lifetime[114].

Understanding the interplay between NMC811 and various graphite materials is critical for the lifetime of NMC811/Graphite cells. In this Chapter, we study the properties and performance of three NGs and three AGs from reputable suppliers in NMC811 cells with "bimodal" positive electrode morphology (i.e., a mixture of SC and PC particles). The bimodal composition increases energy density since smaller SC particles can fill any gaps between the larger PC particles, therefore packing more active material in the same volume. Table 4.1 shows some physical properties of the different graphite materials in this work as provided by the suppliers. AGA material is the Kaijin AML400 negative electrode used in Chapter 3 and subsequent chapters, which will be used here as a baseline in cycling experiments. The three NGs are called NGA, NGB, and NGC, and the other two AGs are called AGB and AGC. The names of the suppliers of these materials have been withheld at the request of Tesla our industrial partner.

Table 4.1. Some physical properties for the graphite materials used in this Chapter.

Material	D50 (µm)	N$_2$ BET area (m^2 g^{-1})	Tap density (g cc^{-1})
NGA	17.33	1.46	1.07
NGB	16.59	1.50	1.20
NGC	16.40	1.67	1.09
AGA	16.02	1.29	1.08
AGB	17.94	1.08	1.40
AGC	15.64	1.00	1.12

This chapter uses NMC811/Graphite cell with identical construction, except for the choice of graphite material, and Table 4.2 shows the cell and electrolyte specifications used here. The differences between the graphite materials will be studied with XRD and SEM to determine the degree of crystallinity and particle morphology. GCMS and *in-operando* gas measurements will be used to understand the onset of gas generation and its composition during the formation charge. In addition, the electrochemical properties of each material, such as active surface area and RCT, and their impact on cell lifetime will be discussed. UHPC and long-term cycling were used to study the cell performance and lifetime at 40.0 ± 0.1, and 55.0 ± 0.1 °C. Finally, *in-operando* stack pressure measurements were used to understand the impact of the negative electrode of stack thickness change, and IMC was used to rank the parasitic heat flow for each material.

Table 4.2. Cell specifications and electrolyte formulation used in this chapter.

Neg. electrode	Loading (mg cm^{-2})	Composition (graphite:CMC/SBR:CB)	Density (g cm^{-3})	Pos. electrode	Loading (mg cm^{-2})	Composition (NMC:PVDF:CB)	Density (g cm^{-3})
AG or NG	~15	95.2:2.8:2	1.55	Bimodal NMC811	~21	94:2:4	3.3

Cu current collector thickness (µm)	8
Al current collector thickness (µm)	16
Nominal cell capacity (mAh)	~240
Operating range (V)	3-4.06 or 3-4.20
Excess graphite capacity at 4.40 V (%)	10

Electrolyte information				
Name	**Solvent (wt. ratio)**	**[LiPF$_6$] (M)**	**Additive (wt.%)**	**Supplier**
2VC1DTD	EC:EMC:DMC (25:5:70)	1.5	VC (2 %) DTD (1 %)	Capchem
2FEC1LFO	EC:EMC:DMC (25:5:70)	1.5	FEC (2 %) LFO (1 %)	Capchem

4.2. Graphite Morphology and Crystallinity

4.2.1. Negative Electrode SEM

Figure 4.1 shows top-down SEM images of pristine graphite electrodes taken from the NMC811 pouch cells used in this chapter. The NG materials had a spherical particle morphology between 10 and 20 μm in size. The AG materials had flake-like particles of a similar size but were more densely packed than the NG materials. NG materials are typically obtained in the form of flakes with a large aspect ratio, which are then processed into spherical materials through a process known as spheroidization to reduce the particle size [116,117]. The same process can be applied to AG to obtain spherical morphology if such morphology is desired.
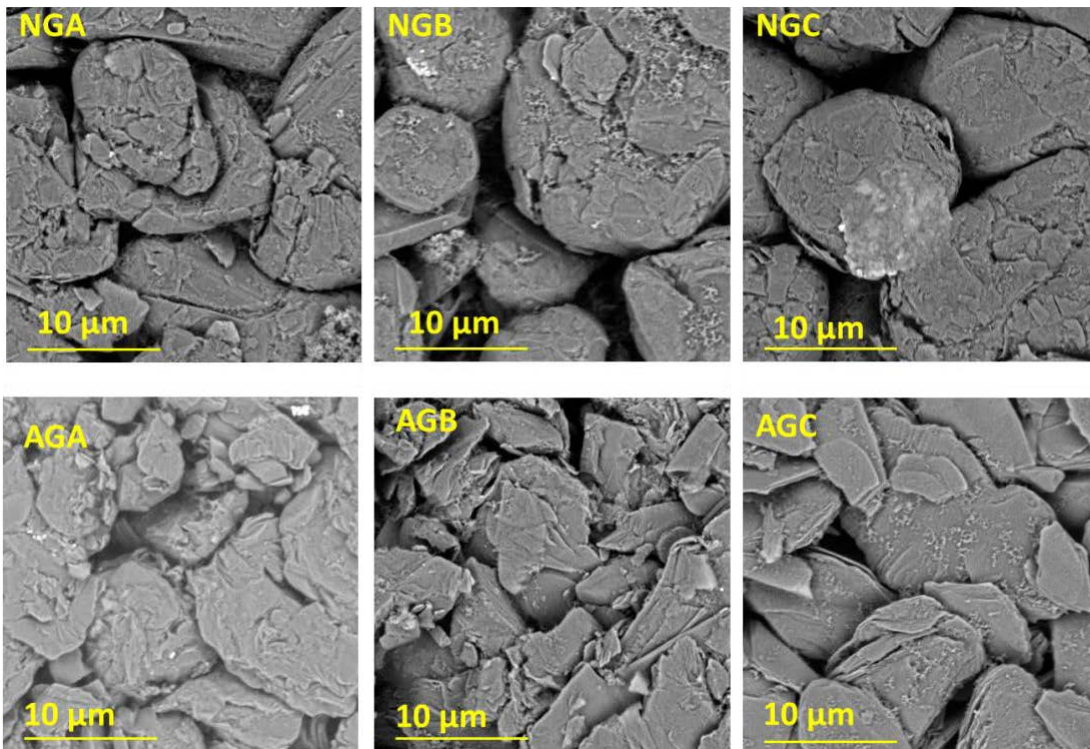
Figure 4.1. SEM images of the different graphite electrodes in this chapter.

Flakey graphite particles will have the tendency to orient themselves parallel to the Cu current collector. This preferred orientation will slow down Li^+ intercalation during charge/discharge as Li^+ cannot easily intercalate through the basal plane surface. Based on the SEM images in Figure 4.1, one would expect NG materials to have better rate capabilities compared to the AG materials, which will be discussed later.

4.2.2. Powder XRD

Graphite materials exist is two main phases depending on the stacking pattern of the graphene layers, which are known as hexagonal (2H) or rhombohedral (3R) phases. 2H graphite consists of two repeating units of graphene layers that are shifted by one C-C bond length in an ABAB… stacking pattern. 3R graphite consists of three repeating units of graphene layers that follow an ABCABC… stacking pattern. Upon intercalation, graphene layers in 2H and 3R graphite become aligned such that carbon atoms are directly above each other. A "perfect" graphite would be only 2H with $P_r = 0$, but in reality, graphite materials can be a mix of 2H and 3R with some degree of misalignment. To determine the degree of crystallinity of the various graphite materials, powder XRD was used and the XRD patterns were fitted to extract the P_r value using the CARBONXS program[71]. Figure 4.2 shows the XRD patterns for all materials in this work except AGA (no powder was available for this material) in the 40-90° range. The data is shown in black, and the fitted pattern is shown in orange, while the dashed lines show the positions of peaks associated with the rhombohedral 3R phase.
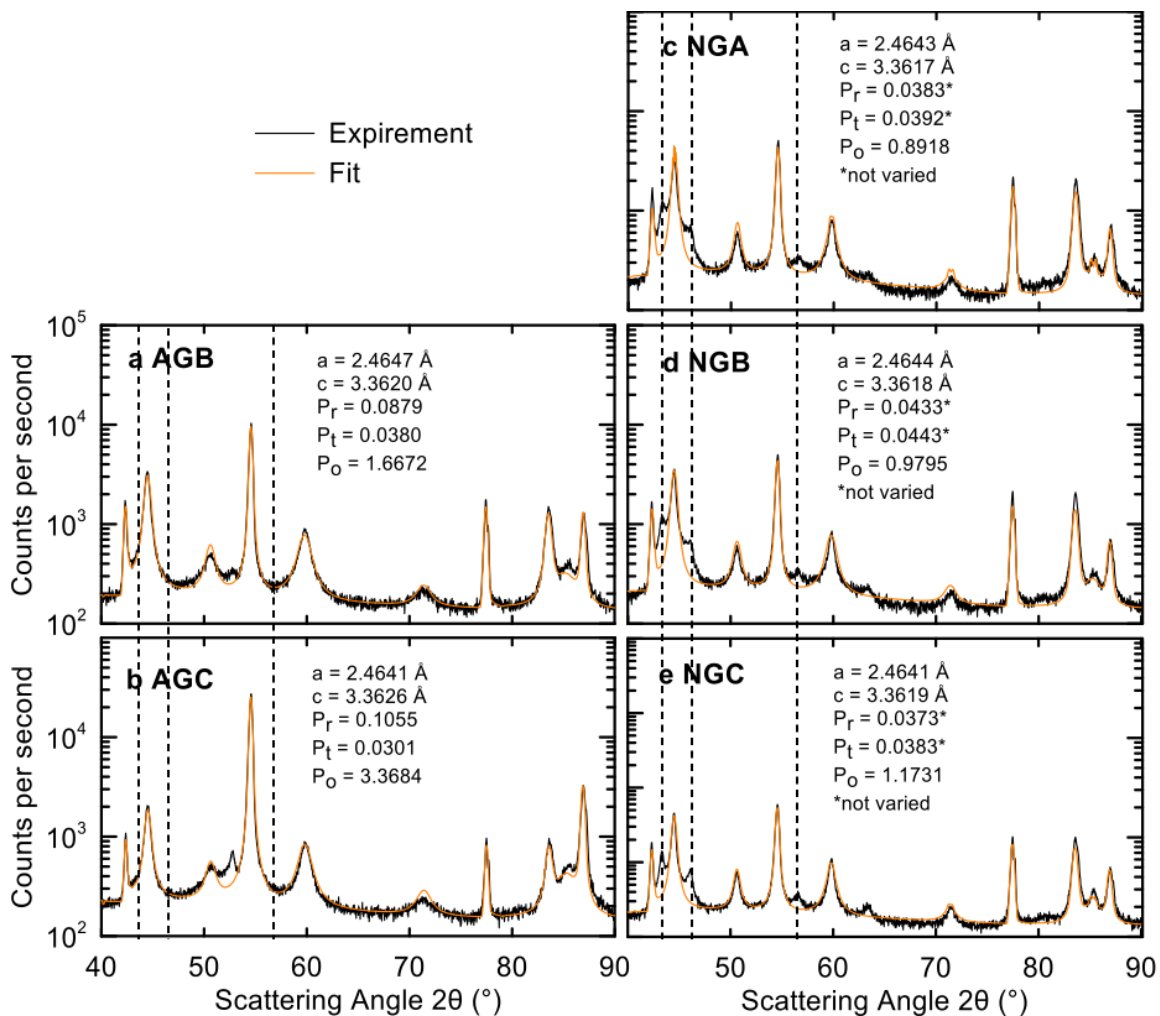
Figure 4.2. XRD patterns for different the graphite powders (black) and fits using CARBONXS (orange) in the 40-90º region. Dashed lines show the positions of peaks corresponding to 3R graphite which are absent in AGs.

Figure 4.2 show that AG materials have little to no 3R phase and that it is primarily 2H graphite but NGs have a significant 3R component (dashed lines). Fitting the XRD spectra shows that AGB and AGC have ~8.8 and 10.5 % probability of turbostratic misalignment, and a preferred orientation factor, P_o, of 1.66 and 3.36, respectively, owing to their flakey morphology compared to the NG materials. NGs showed a significantly higher degree of crystallinity with only 3-4 %

probability of turbostratic misalignment. The parameter, P_t, denotes the probability of finding a 3R stacking sequence within the 2H phase. Since NGs had a significant 3R phase, some fitting parameters were varied manually to get best agreement (denoted with *) since CARBONXS is designed to fit 2H graphite with stacking faults and cannot reliably fit a mixed phase graphite spectrum automatically. The impact of the 3R phase on the performance of NG materials, if it persists during cycling, is unknown. The presence of 3R graphite in the NG materials only could be because NG materials are buried in Earth's crust for millions of years under high pressure where highly crystalline materials (see Figure 4.2) can be produced, with a greater probability of higher energy ABCABC… stacking arrangement[118]. AG materials are synthesized with high-temperature treatments (>3000 °C), while the NG materials here are likely to have been mechanically spheroidized and may not have been exposed to temperature >3000 °C. The transformation from 2H to 3R graphite can be induced by mechanical grinding intended to reduce particle size, and the transformation from 3R to 2H can be induced by high-temperature treatments[71,118], both of which could be explain the differences in XRD patterns in Figure 4.2.

Figure 4.3 shows a closer look at the 002 peak at 25º where more differences between AG and NG are clear. The NG spectra show a hump around 22º that does not exist in the AG materials. Zheng et al showed that carbonaceous materials heated at 500-1000 °C have a hump around 22-25° in the XRD pattern, suggesting that the NGs in this work have some form of carbon coating applied at low temperature[119], which is common in the processing of NG materials[116,117].

Area, Center, FWHM, Gamma (0 = Gaussian, 1 = Lorentzian)

c NGA
002: 40375, 26.4336, 0.11255, 0.45
Coating: 2199, 25, 1.32, 1

— Data
- - Background
—— 002 Peak
—— Coating
—— Total of the fit parameters

a AGB
002: 72608, 26.445, 0.114, 0.296
Coating: -113, 25, 4.9, 1

d NGB
002: 40631, 26.4351, 0.1245, 0.47
Coating: 2184, 25, 1.32, 1

b AGC
002: 176636, 26.445, 0.1144, 0.280
Coating: -146, 25, 1.3, 1

e NGC
002: 45238, 26.4307, 0.1287, 0.427
Coating: 1788, 25, 1.76, 1
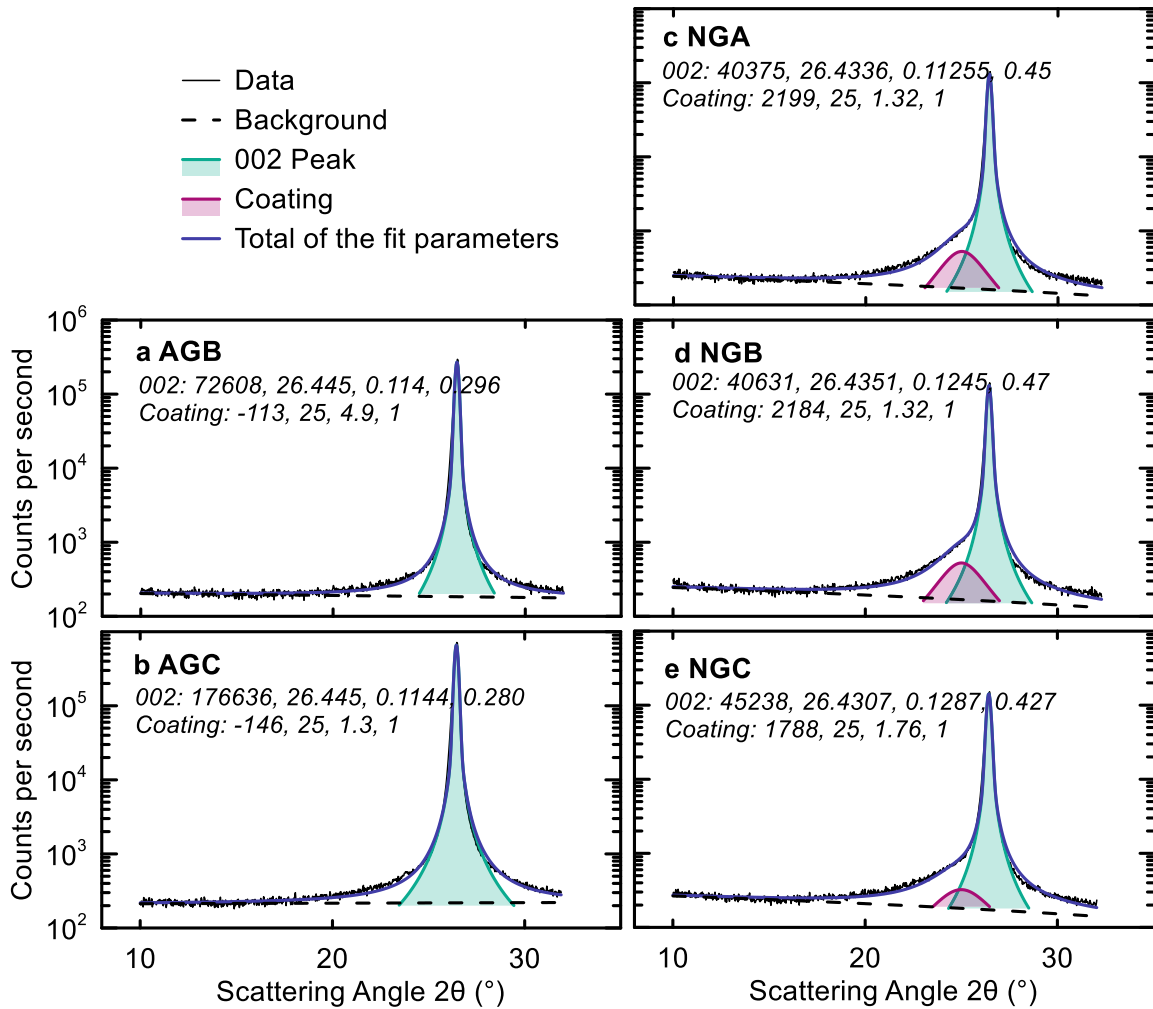
Figure 4.3. Graphite 002 peak fitting. Peak area, center, FWHM, Gamma (0 = Gaussian, 1 = Lorentzian) for 002 peak and hump around 25º are shown in each panel. Peak fitting was done using Fityk 0.9.8 with a normalized Pseudo-Voight function.

Fityk version 0.9.8 was used to fit the 002 peaks with normalized Pseudo-Voigt functions to estimate the amount of coating in the NGs. Fitting parameters are indicated in the panels in Figure 4.3. The fitting results suggest that the coating applied to NGs accounts for ~5 wt.% of the material. It has been shown before that carbon-coated NG have an improved performance compared to

uncoated materials[120–122]. For example, Ding et al showed that a CVD carbon-coating applied at 1000 °C led to improved CE, specific capacity, capacity retention in NGs, while also decreasing the BET surface area[120]. Yoshio et al showed that the CE of spherical NG particles increased with the amount of carbon coating which was attributed to decreased electrolyte reduction[121].

4.3.   Differences in FCE, Initial Gassing and R_{CT}

The initial SEI formation reaction determines the cell's FCE, gassing during formation, as well as R_{CT} at beginning of cell life, all of which will change as a function of graphite material. Figure 4.4 shows the voltage profile and dQ/dV versus voltage for NMC811/Graphite cells with 2VC1DTD or 2FEC1LFO electrolytes formed to an UCV of 4.06 V. The voltage versus capacity curves show the differences in the irreversible capacity, attributed to the Li inventory loss during SEI formation, where NGC has the largest irreversible loss and NGB, AGB, and AGC have the smallest losses. Close inspection of the voltage curve between 2.5 and 3.2 V shows some plateaus during early stages of the formation charge. These plateaus are due to SEI formation reactions, namely EC and/or film-forming additive reduction. By plotting dQ/dV versus voltage, one can see peaks corresponding to the onset and magnitude of these electrolyte reduction reactions (see Figure 4.4c-d). It is known that in an NMC/Graphite cell EC reduction occurs around 2.9 V, and VC/FEC reduction occurs between 2.5 and 2.7 V.
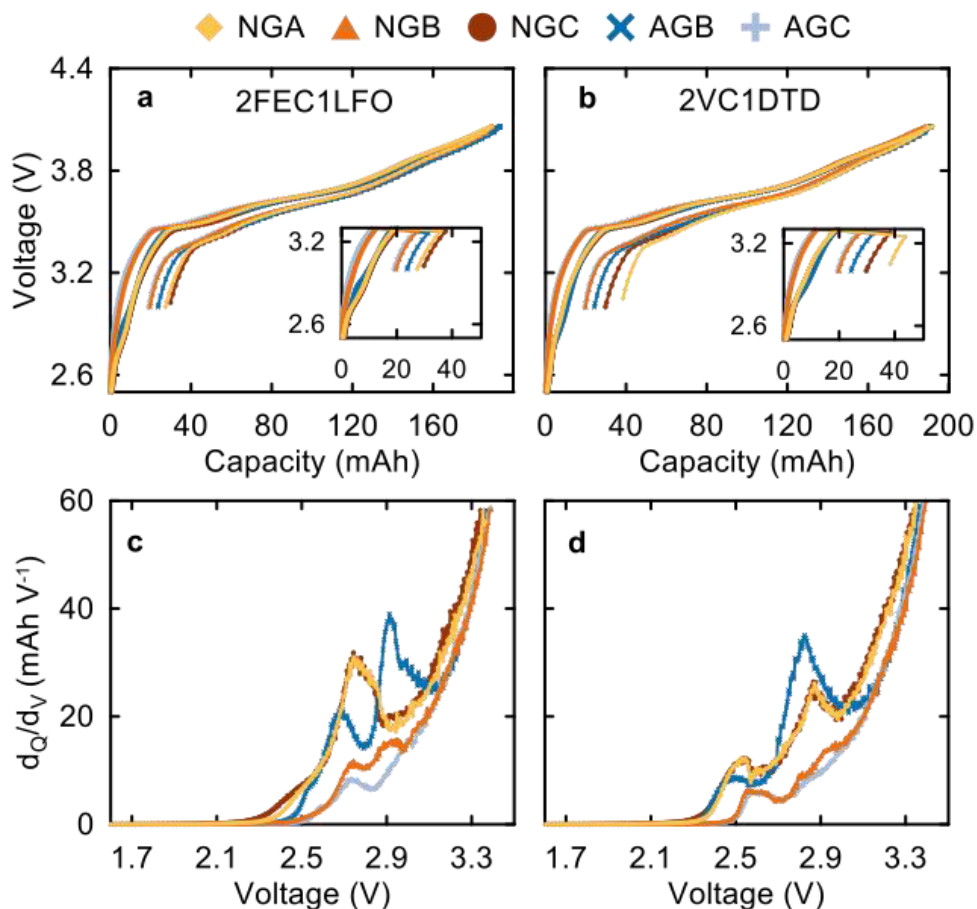
Figure 4.4. (a-b) voltage (V) versus capacity (mAh) curves and (c-d) dQ/dV versus voltage from C/20 formation cycle between 3.0-4.06 V for 2FEC1LFO and 2VC1DTD cells with the different graphite materials. Inset shows an expanded view of the V vs. Q curve between 2.6 and 3.2 V.

Based on the difference in the N_2 BET area shown in Table 4.1, one would expect graphite materials with larger surface area to show a bigger electrolyte reduction peak. Moreover, one might see both a VC/FEC reduction peak and an EC reduction peak if the additive loading used in the electrolyte was not sufficient to passivate the entire surface area of the graphite. Ideally, the additive loading should be tuned to minimize any EC reduction since solvent consumption is undesirable compared to the sacrificial additives. Looking at Figure 4, one can see

that AGC has the smallest electrolyte reduction peaks which correspond to the reduction of VC or FEC only. Interestingly, AGB (with a similar BET area to AGC) has a much large electrolyte reduction peaks corresponding to both VC/FEC and EC reduction. Moreover, NGB shows similar electrolyte reduction activity compared to AGC despite having a much large BET area. The observations in Figure 4.2 and discrepancies between BET surface area and electrolyte reduction activity suggest that N2 BET area does not reflect the electrochemically accessible surface area for the different graphite materials. While it can be complicated to directly measure the electrochemically active surface area, it can be qualitatively measured by examining electrolyte reduction peaks in dQ/dV plot, as well as FCE, gas evolution during formation, and parasitic heat flow, all of which will be discussed later. Graphite materials with smaller active surface areas will require smaller additive loading for sufficient passivation, will consume less Li during SEI formation, and will result in less gassing.

Figure 4.5 shows the volume of gas produced during formation for NMC811/Graphite cells with 2VC1DTD or 2FEC1LFO electrolytes at different UCVs. Gas volumes were relatively unchanged with UCV, which is expected since the difference in UCV is small. Cells with 2FEC1LFO had a gas volume <0.25 mL and the differences between the graphite materials were small. It is known that LFO does not produce gas during formation[123] so most gas is due to FEC reduction[35]. The main differences in gas generation are in the 2VC1DTD cells, where AGB, AGC, and NGB have the lowest gas volumes.
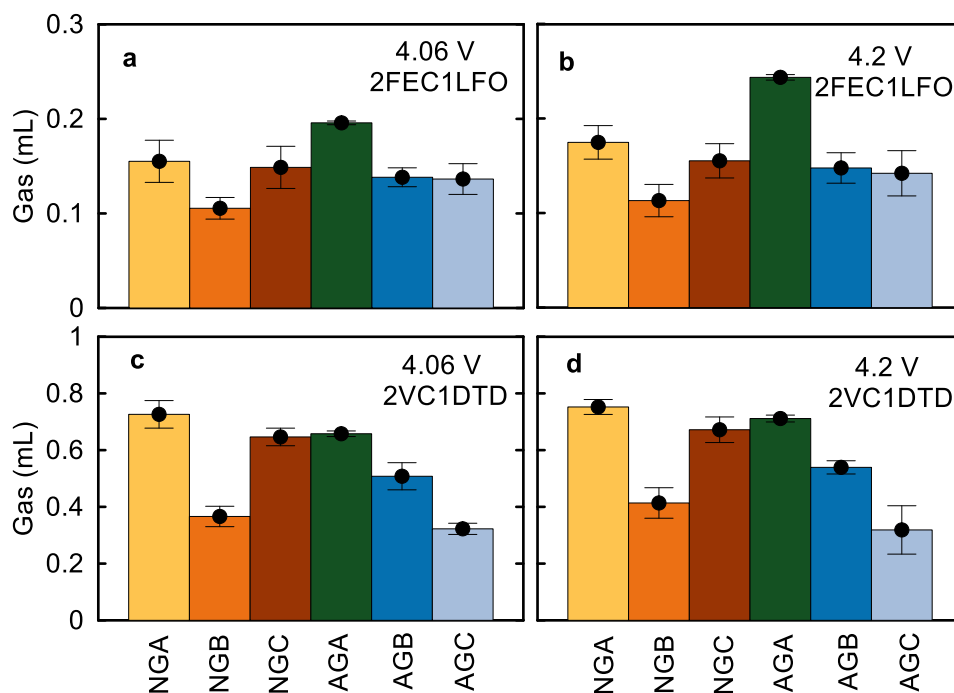
Figure 4.5. Formation gas volume for NMC811/graphite cells with 2FEC1LFO (a-b) and 2VC1DTD (c-d) electrolytes having different graphite materials formed to 4.06 or 4.20 V UCV at 40 °C.

Figure 4.6 shows the Nyquist plot for NMC811/Graphite cells with 2VC1DTD after formation and the positive electrode area-specific R_{CT} versus FCE. Since the same positive electrode is used in these cells, differences in the Nyquist plot can be attributed to contributions from the graphite. We see a clear difference in R_{CT} where AGC and NGB have the highest resistance, while NGA and NGC have the lowest. While a smaller surface area is desirable, having fewer redox active sites on the graphite means that the cell's R_{CT} will also increase with FCE as seen in Figure 4.6. This correlation highlights a challenging aspect of graphite materials design, where improving FCE by reducing redox-active sites causes an unwanted increase in R_{ct}. which can affect the cell's rate performance.
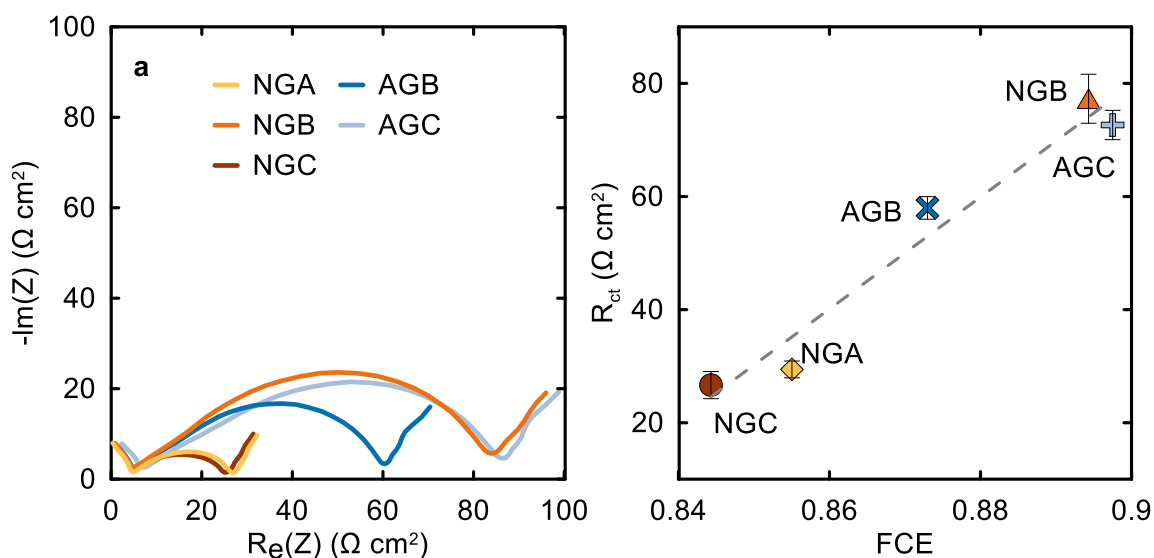
Figure 4.6. a) Nyquist plot and (b) R_{CT} versus FCE for NMC811/Graphite pouch cells with 2VC1DTD after formation to 4.06 V. EIS was done at 3.8 V and at 10 °C.

4.4. Gassing Behaviour of Different Graphite Materials

4.4.1. Onset of Gassing During Formation and its Composition

The volume and composition of gases generated in the cell during the formation charge can shed light on the composition of the SEI layer and which electrolyte component were primarily consumed during formation. For example, consumption of VC and FEC results in the production of CO_2 and the consumption of EC results in the production of C_2H_4 as shown earlier in Figure 1.6. In a cell where the graphite is sufficiently passivated by the film-forming additives, the C_2H_4 content should be very small since no EC consumption would be required to passivate the negative electrode.

To analyze the composition of gases generated during formation, we used *in-operando* gas measurements to confirm that electrolyte reductions peaks seen in Figure 4.4 correspond to gas-generating reactions. Figure 4.7 shows the change in cell volume with respect to voltage (dVol/dV) and dQ/dV versus voltage for NMC811/Graphite cells with 2VC1DTD that underwent a C/100 formation charge between up to 4.20 V at 40 °C with *in-operando* volume monitoring. Figure A.7 shows the same experiment but with 2FEC1LFO electrolyte. Peaks in the dQ/dV plot associated with gas production reactions should correlate to peaks in dVol/dV where changes in cell volume are measured. Indeed, Figure 4.7 shows a correlation between electrolyte reduction events and gas generation for all NMC811/Graphite cells. AGC and NGB materials showed a sharp volume change peak at the same voltage as VC reduction, and no indication that significant EC reduction took place. However, AGB material (with a similar BET surface area to AGC) showed more volume change due to EC reduction, but most of the volume change occurred due to VC reduction as well. By knowing precisely at what voltage can we expect gas generation during formation, we can sample the gaseous species formed at different voltages to learn about the extent of passivation brought forth by a certain additive loading for different graphite materials. This approach showed that the first onset of gas generation in 2VC1DTD and 2FEC1LFO electrolytes are ~2.6 and 2.75 V, respectively, which allows us to identify the composition of these gases using GCMS.
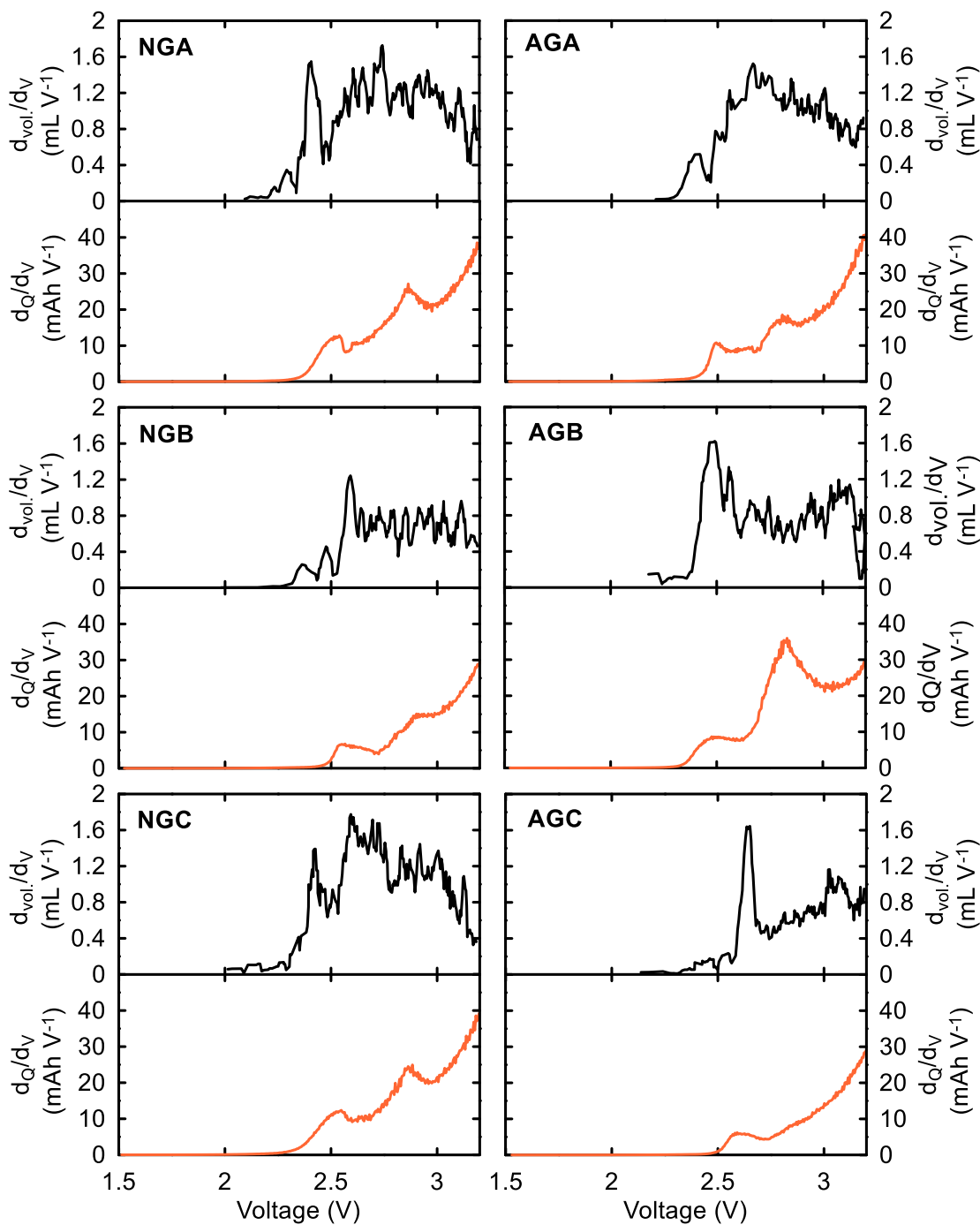
Figure 4.7. Change in volume with respect to voltage (dVol/dV, mL V^{-1}) and dQ/dV versus voltage for NMC811/Graphite pouch cells. Cells were filled with 2VC1DTD electrolyte and charged to 4.2 V at C/100 and 40 °C. A 7-point running average of dVol/dV is plotted to reduce the noise in the data.

Figure 4.8 shows the gas chromatograms for gas samples taken from NMC811/Graphite pouch cells equipped with a gas sampling port as described by Schmiegel et al[75]. Cells with 2VC1DTD or 2FEC1LFO were charged at C/100 to 2.6 or 2.75 V at 40 °C, respectively, so that the gas in the cell only corresponds to the first onset of gas generation shown in Figure 4.7 and Figure A.7. The ratio of C_2H_4/CO_2 in the cell after formation can thus be used as a marker for graphite passivation in the presence of VC or FEC (both of which produce CO_2 upon reduction), with lower C_2H_4 content corresponding to a decrease in EC reduction. To investigate the relationship between gas composition and FCE, the ratio of C_2H_4/CO_2 was extracted from the peak area in the gas chromatograms in Figure 4.8 and correlated to FCE. SEI formed in the presence of VC will result in more CO_2 production compared to a SEI that require further reduction of EC to passivate the lithiated graphite, in turn producing more C_2H_4.
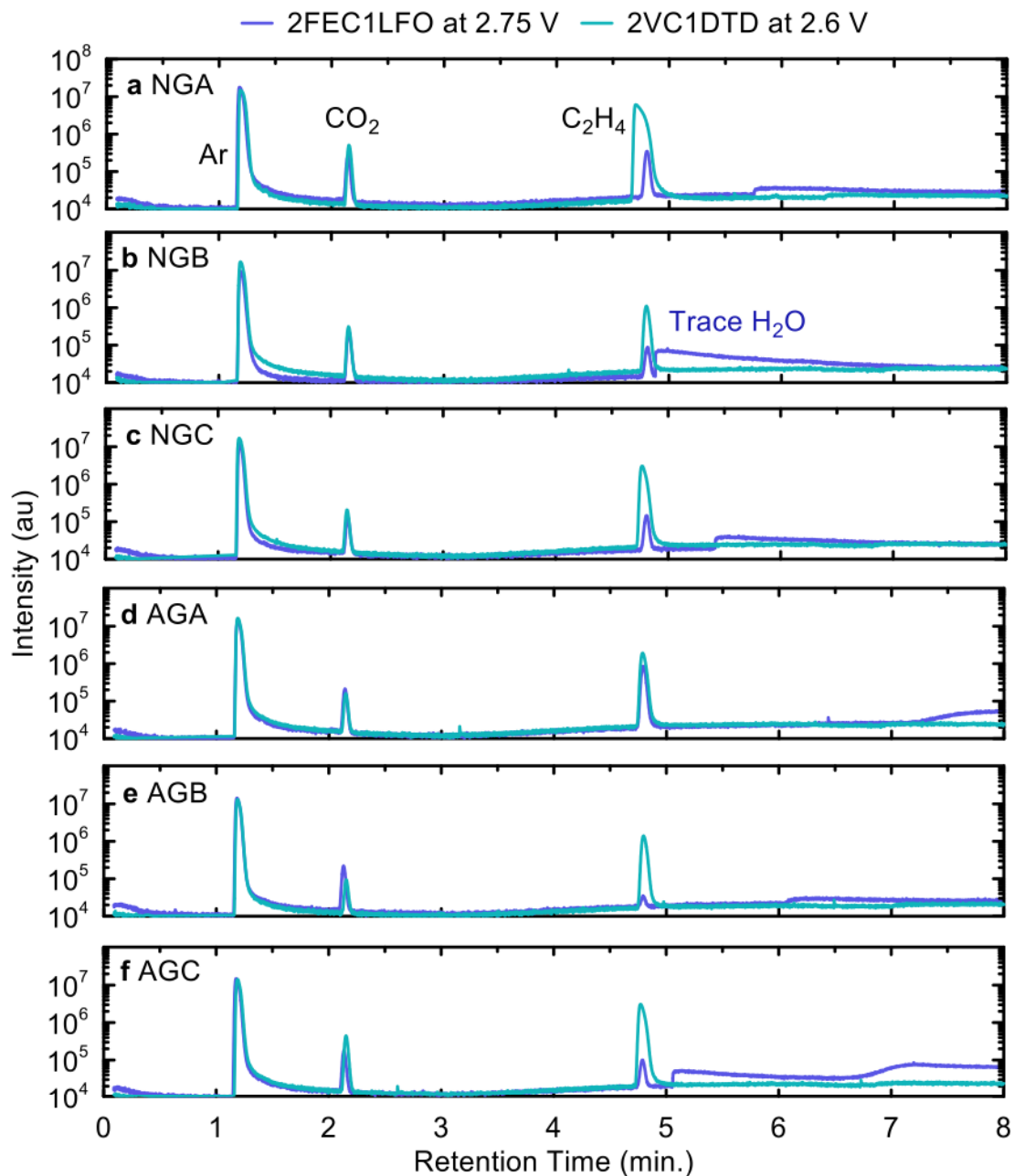
Figure 4.8. Gas chromatograms for 2FEC1LFO and 2VC1DTD cells with a gas sampling port. Cells were charged to 2.75 or 2.6 V during the formation cycle for 2VC1DTD and 2FEC1LFO, respectively, and the generated gas was extracted from the pouch cells. Cells were charged at C/100 and 40 °C.

Figure 4.9 shows the C_2H_4/CO_2 ratio plotted versus FCE for NMC811/Graphite cells with 2VC1DTD and 2FEC1LFO formed to either 4.06 or 4.20 V UCV at 40 °C. It is clear in Figure 4.9 that the higher C_2H_4 content is related to lower FCE from poor SEI passivation. Graphite electrodes that are primarily passivated by 2FEC1LFO or 2VC1DTD additive blends, such as AGC, AGB, and NGB, have the highest FCE which highlights the robustness of their SEI and is consistent with the decreased electrolyte reduction shown Figure 4.4 and Figure 4.7 The C_2H_4/CO_2 ratio for 2VC1DTD cells is higher than 2FEC1LFO case since the reduction of DTD produces C_2H_4 and CO_2, but the ethylene content in the 2VC1DTD case will increase with EC reduction since DTD produces a 1:1 ratio of C_2H_4 to CO_2[37].
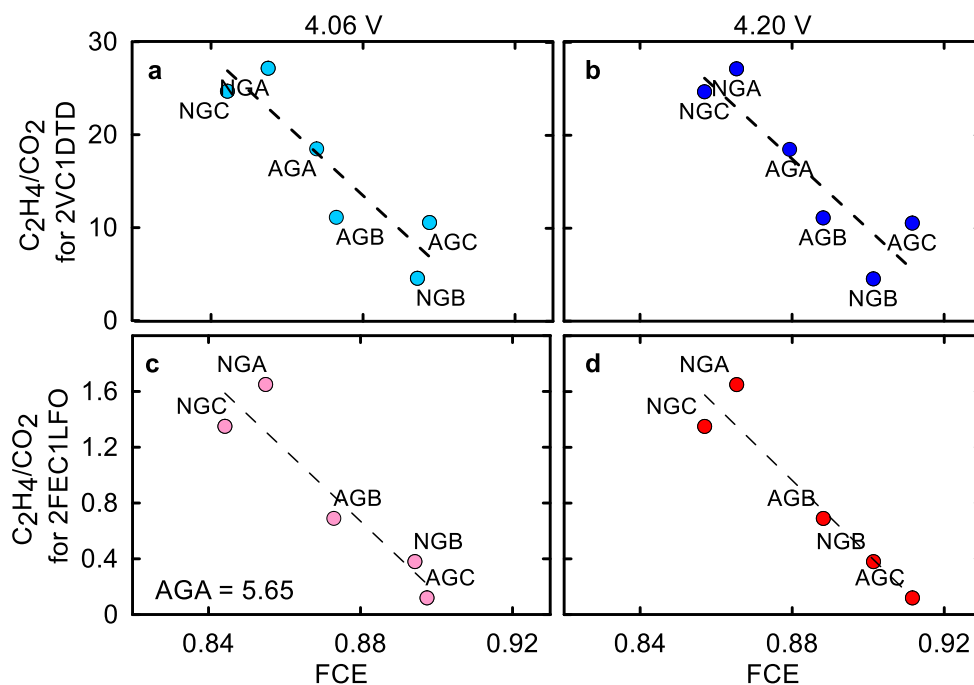
Figure 4.9. C_2H_4/CO_2 peak area ratio versus FCE for NMC811/graphite cells formed at C/20 and 40 °C for cells with (a, b) 2VC1DTD and (c, d) 2FEC1LFO formed between 3.0 and 4.06 (a, c) or 4.20 V (b, d).

4.4.2. Gassing During Galvanostatic Cycling

Graphite with large active surface area that cannot be sufficiently passivated by a typical additive loading will continue consuming electrolyte solvents during cell cycling, which results in gas generation during cell operation and poses a serious safety risk. To understand the extent of gassing for the different NMC811/Graphite cells, *in-operando* gas measurements were carried out during galvanostatic cycling at 40 °C. Figure 4.10 shows cell volume versus time in NMC811/Graphite cells with 2VC1DTD electrolyte during cycling at C/3 and 40 °C with periodic holds at top of charge (4.20 V). To evaluate the passivation of each graphite, the cell volume after formation was subtracted from the volume during cycling so that irreversible changes to cell volume can be largely attributed to gases produced after the initial SEI formation. AGB, AGC, NGB all showed very minimal increase in cell volume and gas generation after formation (<0.2 mL), while AGA, NGA, and NGC showed more gas production after the C/20 formation cycle. The NGC cell produced ~0.5 mL of gas after only 225 hours of cycle-hold testing at 40 °C, which is in stark contrast to AGB or AGC which had <0.1 mL of gas, demonstrating that the NGC electrode was not sufficiently passivated during formation with the electrolyte chosen here. It is not clear whether changes to the electrolyte or to the amounts and types of additives could passivate NGC completely and a significant number of future experiments would be required to determine this.
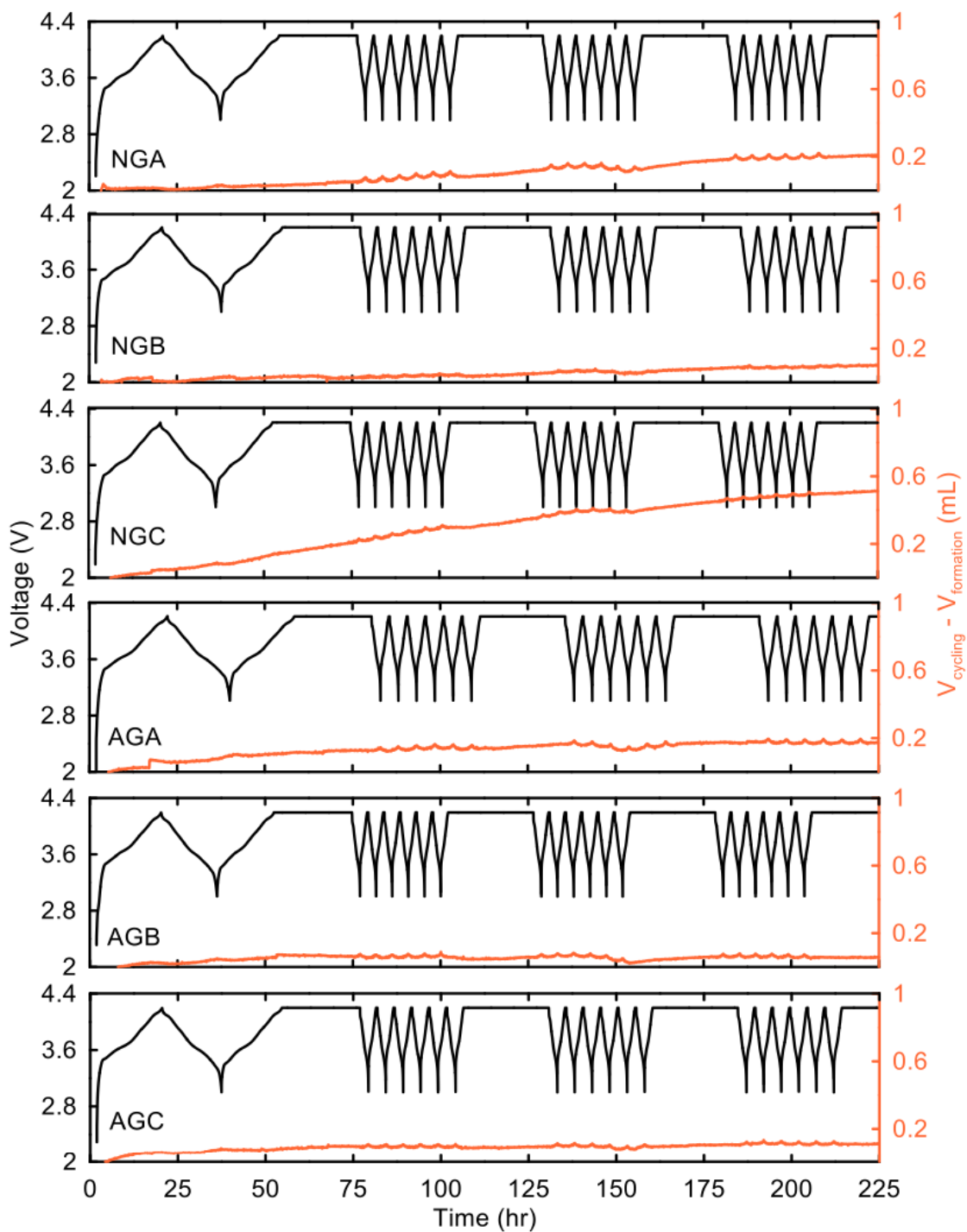
Figure 4.10. Voltage (V) and volume change during cycling (mL) versus time for NMC811/Graphite pouch cells. Cells were cycled at C/20 (first cycle) and C/3 (subsequent cycles) between 3.0-4.2 V at 40 ºC with a 12-hour CV hold at top of charge. The gas generation during the C/20 formation cycle was subtracted from subsequent C/3 cycles to probe the degree of graphite passivation against further electrolyte reduction.

4.5. Short-Term Experiments to Rank Cell Performance

4.5.1. UHPC Cycling

Figure 4.11 shows a summary of the UHPC cycling results for cells with 2VC1DTD and 2FEC1LFO electrolytes charged to 4.06 or 4.20 V. Previous data collected on NMC811/AGA cells are included for comparison, when available[21]. The quantities in Figure 4.11 are calculated from the UHPC data according to the procedure described in the literature[124]. All raw data used to generate the summary in Figure 4.11 can be found in Figures A.6-8. As a reminder, fractional charge endpoint slippage typically gives a measure of the degree of electrolyte oxidation at the positive electrode, while the fractional fade measures Li loss at the negative due to SEI growth. Since all the cells in Figure 4.11 have the same positive electrode, it is not surprising that the slippage term is similar for all cells. However, differences in columbic inefficiency (CIE) due to varying fade rates are apparent across the different graphite types. For example, AGC has the smallest fade rate in Figure 4.11 regardless of electrolyte or UCV, while NGC/NGA have the highest fade. The UHPC results in Figure 4.11 indicate that parasitic reactions that consume Li irreversibly will occur faster in NGC and NGA cells, versus NGB, AGB, and AGC cells due to their lower fade rates and CIE/hr. As discussed in Chapter 1, CIE is approximately the sum of slippage and fade terms which is consistent with Figure 4.11.
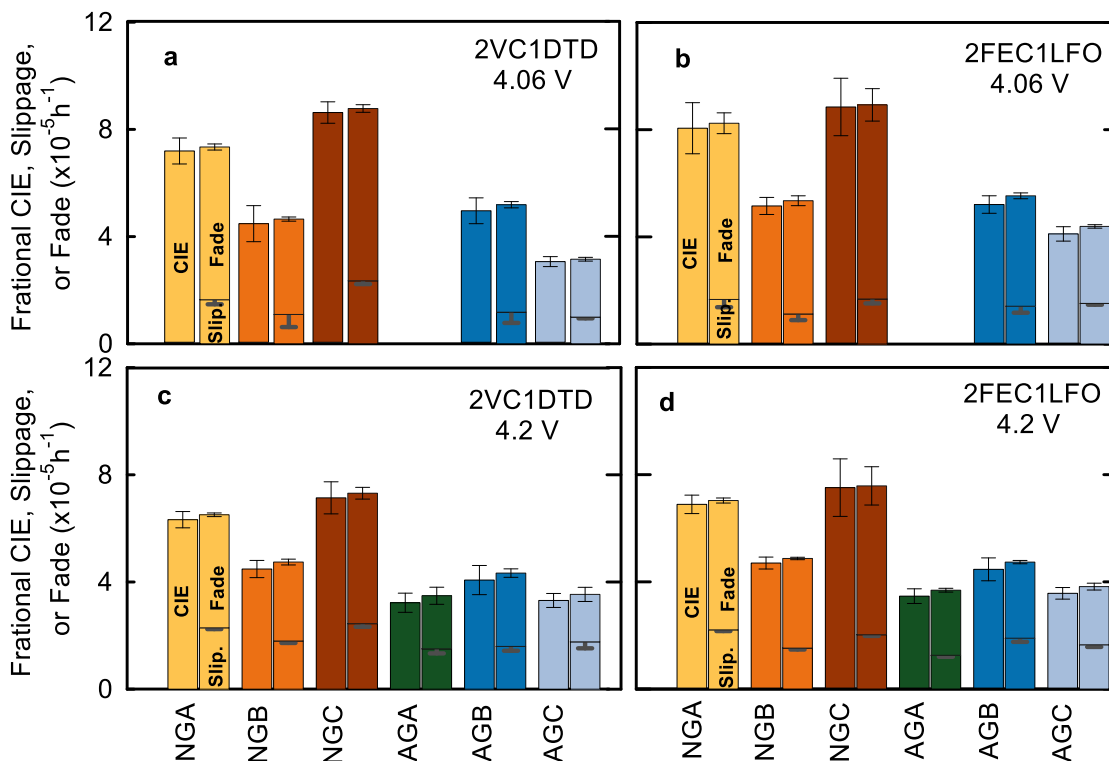
Figure 4.11. Fractional CIE/h, charge endpoint slippage per hour and capacity fade per hour for NMC811/graphite cells cycled to a UCV of 4.06 V (a-b) and 4.2 V (c-d) with 2FEC1LFO or 2VC1DTD. UHPC cycling was performed at 40 °C and C/20:C/20 for 20 cycles.

4.5.2. Measuring Parasitic Heat Flow with IMC

To corroborate the cell ranking established in Figure 4.11 from UHPC cycling, IMC was used to measure parasitic heat flow during cycling. Parasitic heat flow measured here is an indicator of parasitic reactions in the cell, so higher heat flow values reflect a greater rate of parasitic reactions in the cell[81]. Figure 4.12 shows parasitic heat flow (mW) versus voltage for NMC811/Graphite cells with 2VC1DTD cycled at 40 °C and ~C/150 rate. The cells did three low voltage cycles (3.65-3.85 V), followed by two cycles between 4.00-4.20 V, and finally two cycles between 4.00-4.30 V. The low voltage cycles measure parasitic heat primarily

associated with reactions on the negative electrode, while the higher voltage cycles account for parasitic reactions on the positive electrode side as well. Figure 4.12 shows the results from the first cycle in each voltage window, and Figure A.9 shows the results from subsequent cycles. Figure 4.12a shows that AGB, AGC, and NGB have similarly low parasitic heat flow (~0.01 mW) which was lower than AGA cells. As expected from the UHPC data, NGA and NGC showed the highest parasitic heat flow between ~0.02 and 0.04 mW. In all cases, parasitic heat flow decreases with cycle number due to the maturation of the SEI (Figure A.8). Figure 4.12b-c show parasitic heat flow for high voltage cycles. A significant rise in heat flow is seen at higher voltages as expected, and a "dip" around 4.06 V can be seen that might be associated with the large lattice volume change of NMC811[125]. Despite the increase in heat flow, AGB, AGC and NGB materials still outperformed NGA and NGC in the first and second high voltage cycles, respectively (Figure A.8). Finally, Figure 4.12c shows that heat flow increases dramatically past 4.20 V which is consistent with the demonstrated lifetime problem associated with Ni-rich materials at high voltage compared to NMC532, for example[17].
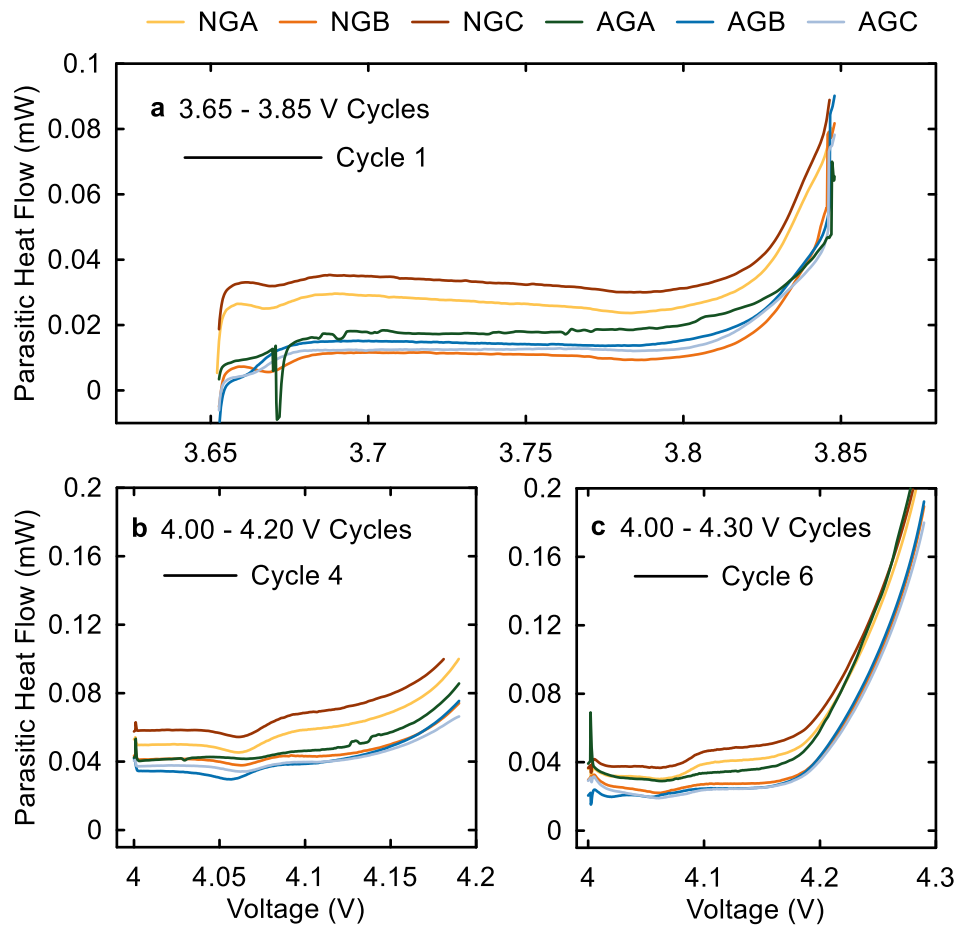
Figure 4.12. Parasitic heat flow (mW) versus voltage (V) for cells cycled between (a) 3.65-3.85 V, (b) 4.0-4.20 V, and (C) 4.0-4.30 V. The first cycle for each voltage range is shown. All cycles were at ~C/150 and 40 °C.

4.5.3. In-Operando Jellyroll Stack Swelling

Cell volume change due to gas generation or electrode swelling is a serious safety risk in commercial cells. Figure 4.10 showed how gas generation can be mitigated using AGB, AGC, or NGB graphite materials, so this section will study jellyroll swelling using *in-operando* stack pressure measurement apparatus developed by Louli et al in our group[70].

Figure 4.13 shows the normalized discharge capacity (top) and change in average pressure (bottom) for NMC811/Graphite cells with 2VC1DTD cycled at 40 °C to 4.06 or 4.20 V. Figures 4.13a-b show the superior performance of AGB, AGC, and NGB materials to NGA and NGC. Even though only 80 cycles are shown for the cells in Figure 4.13, clear differences between stack thickness change can be observed after this short period of time. Notably, AGB and AGC show no change in stack thickness, while NGA and NGC show a significant increase in stack thickness. Overall, cells cycled to 4.20 V UCV showed more stack growth compared to 4.06 V except for AGB and AGC. Surprisingly, NGB showed a comparable stack growth to NGA and NGC despite the fact that NGB otherwise showed good performance. While it is unclear why NGB showed a large increase in stack pressure, Glazier et al observed a similar trend in NMC532/Graphite cells where NGs had a much larger stack pressure increase compared to AGs[111]. A possible explanation for the observation in Figures 4.13c-d is that NG materials with a spherical morphology may experience larger strain/particle swelling than the flakey AG materials, which could lead to an irreversible expansion or exfoliation

followed by continuous SEI formation. Despite competitive performance so far, the

stack thickness growth in the NGB cell can greatly limit its utility.
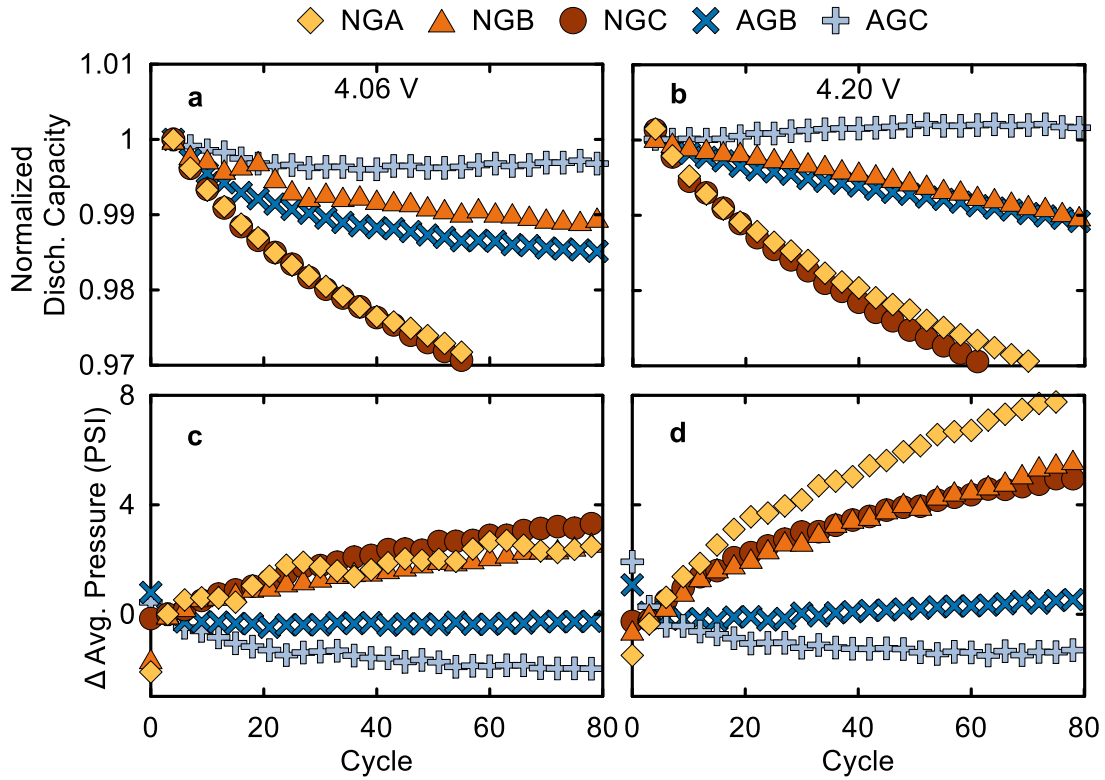
Figure 4.13. Normalized discharge capacity and change in average stack pressure (PSI) versus cycle number for the NMC811/Graphite cells with 2VC1DTD electrolyte cycled to an UCV of (a) 4.06 V or (b) 4.20 V. Cells were cycled at 40 °C at C/3:C/3 rate.

4.6. Long-Term Galvanostatic Cycling at RT, 40 °C, and 55 °C

Having established the primary physical and electrochemical differences between the five graphite materials of interest in this work relative to our baseline AGA material (whenever data was available), it is now important to examine the long-term cycling performance at RT, 40 °C, and 55 °C.

Figure 4.14 shows discharge capacity (mAh), normalized discharge capacity and normalized ΔV growth for NMC811/Graphite cells cycled at RT with 2VC1DTD or 2FEC1LFO with a 4.20 V UCV. NGA and NGC cells were removed from cycling earlier since they were uncompetitive. All cells were cycled at C/3 except for AGA cells which were cycled at 1C:1C as part of another study by Song et al and are included here as a baseline for comparison[21]. After over 3000 cycles, 2FEC1LFO cells showed better capacity retention compared to 2VC1DTD. Similarly, ΔV growth for 2FEC1LFO cells did not exceed 20 % while 2VC1DTD cells showed upwards of 50 % ΔV growth. It is well known that VC can increase the cell's charge transfer resistance, so it could have contributed to the poor retention and ΔV growth at RT[126]. Looking at the different graphite materials, AGB and AGC cells had the best capacity retention. Near the end of cycling, NGB and AGB cells with 2VC1DTD are showing a decline in capacity for some cycles which could be due to short-circuits induced by Li plating,
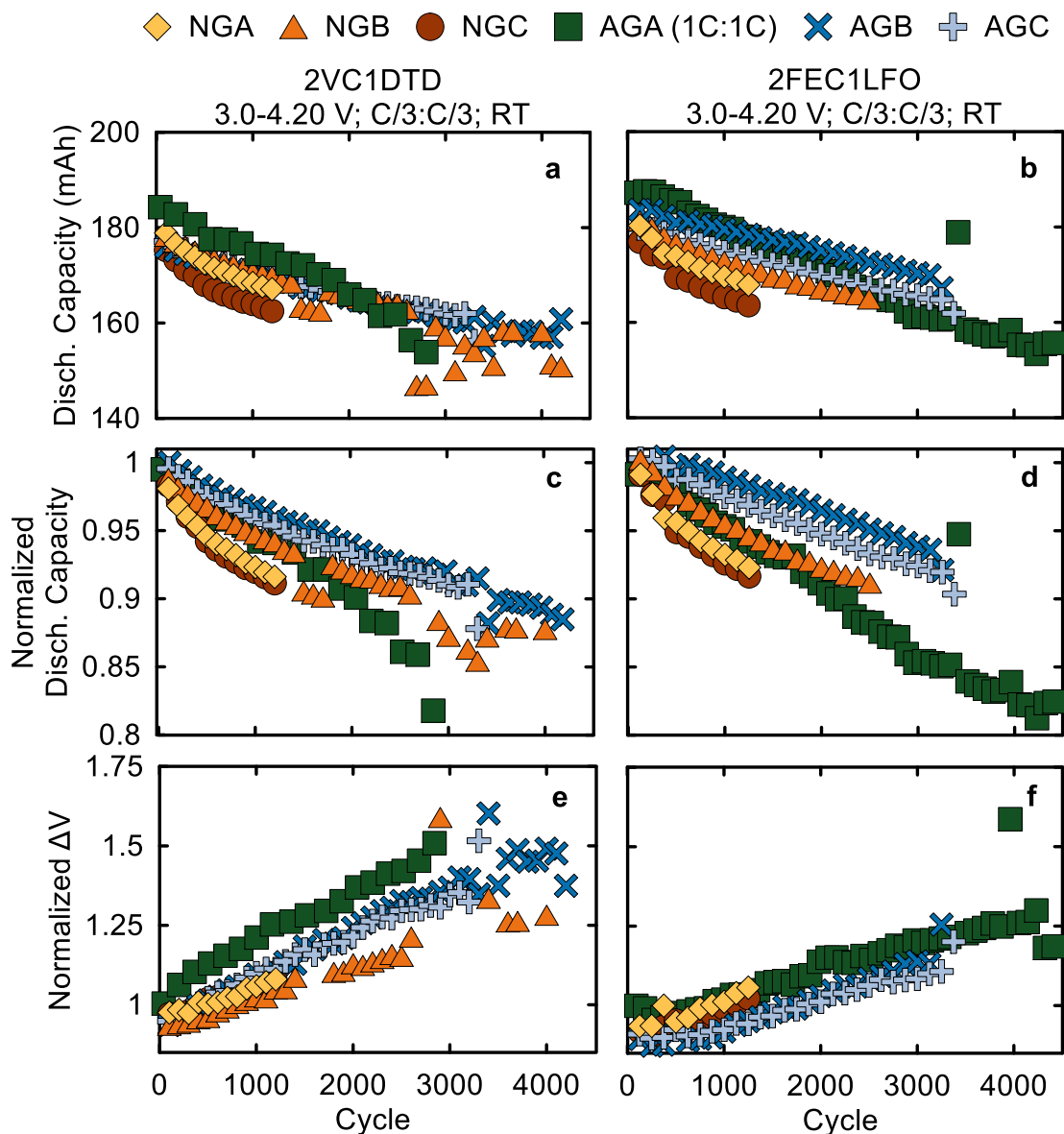
Figure 4.14. (a-b) discharge capacity (mAh), (c-d) normalized discharge capacity, and (e-f) normalized ΔV versus cycle number for NMC811/Graphite cells with 2VC1DTD (left) or 2FEC1LFO (right) electrolytes. Cycling was done at RT with C/3:C/3 (except for AGA which was 1C:1C) between 3.0-4.20 V, and a C/20:C/20 checkup cycle every 100 cycles. Every 50th data point is shown for clarity.

Figure 4.15 shows cycling results for the same cells in Figure 4.14 but cycled to 4.06 V UCV. The RT cycling systems operate under ambient conditions with poor temperature control which results in significant fluctuations in the charge/discharge capacities (particularly with the change in weather with each season). Nonetheless, it is clear that cycling at 4.06 V improves capacity retention. AGB, AGC, and NGB cells practically did not lose more than 2 % capacity after 2500-3000 cycles while the 4.20 V counterparts in Figure 4.14 lost 5-7 % at cycle 2000. The ΔV growth was minimal for the 4.06 V cells and the impact of the additives choice here was relatively small.
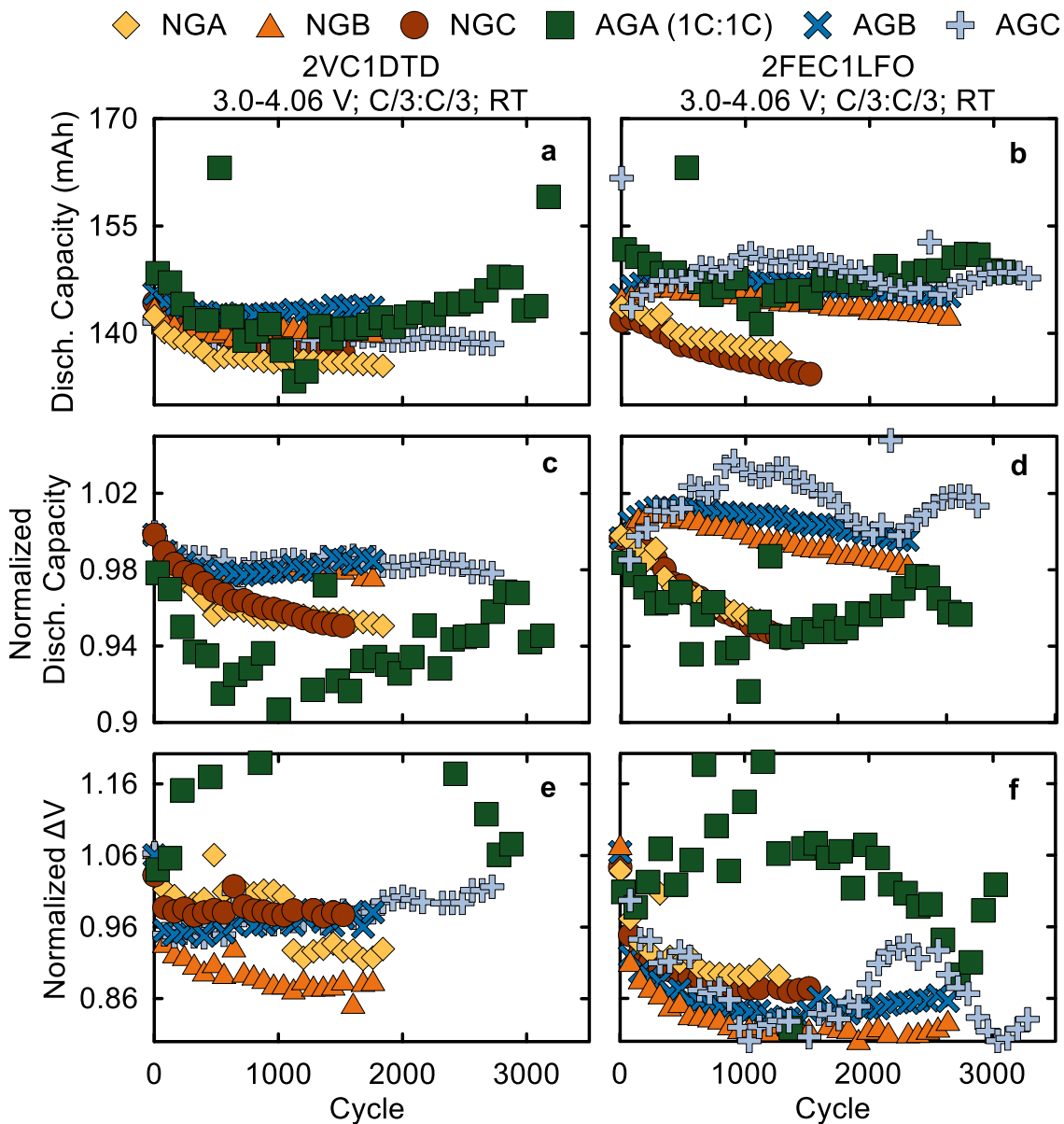
Figure 4.15. (a-b) discharge capacity (mAh), (c-d) normalized discharge capacity, and (e-f) normalized ΔV versus cycle number for NMC811/Graphite cells with 2VC1DTD (left) or 2FEC1LFO (right) electrolytes. Cycling was done at RT with C/3:C/3 (except for AGA which was 1C:1C) between 3.0-4.06 V, and a C/20:C/20 checkup cycle every 100 cycles. Every 50th data point is shown for clarity.

Figure 4.16 shows discharge capacity (mAh), normalized discharge capacity, and normalized ΔV for NMC811/Graphite cells with 2VC1DTD and 2FEC1LFO electrolytes cycled at 40 °C and C/3 with a 4.20 V UCV. The NMC811/AGA data by Song et al was from a different cell batch, thus the difference in discharge capacities[21]. NGA and NGC cells were removed from cycling early since it was clear that they had uncompetitive performance. Overall, the performance of the cells in Figure 4.16 is similar despite the additive blend used. After 1200 cycles, the capacity retention of AGB and AGC is the most competitive here (~90 %), but it can be seen that AGC might have had worse capacity retention compared to AGB if the cycling had continued for longer than ~1900 cycles. NGB and AGA had similar retention (~88 %) after 1200 cycles. Of note in Figures 4.16e-f is the large increase in ΔV for all NMC811/Graphite cells. Figure 4.16 shows that the large ΔV growth associated with NMC811 cells cycling to high SOCs is largely independent of the graphite choice. However, the impact of any "cross-talk" reactions on cell lifetime might not be clear at 40 °C after ~1 year of cycling, so we will look at long-term cycling to 4.20 V UCV but at 55 °C to accelerate these reactions.
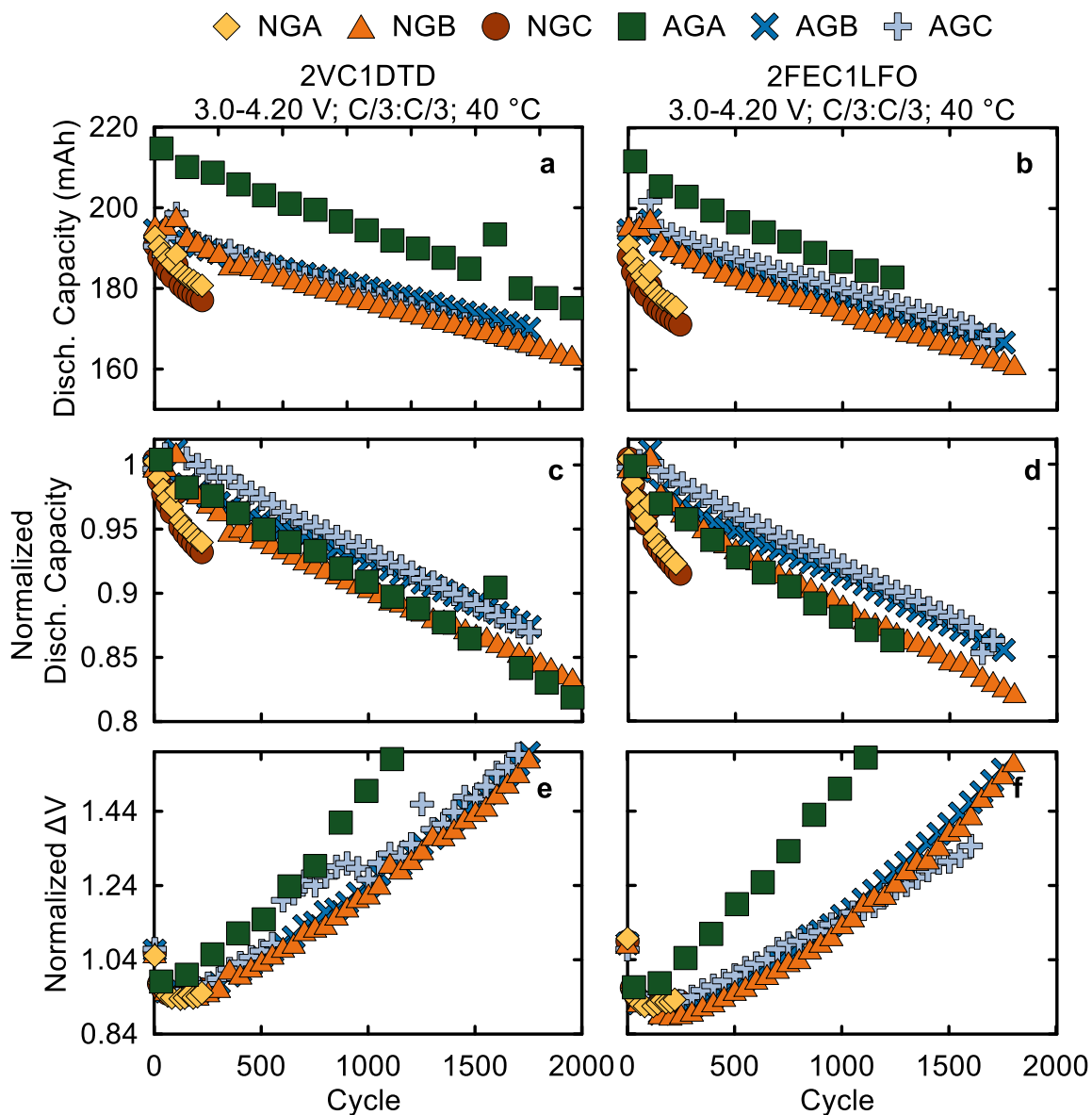
Figure 4.16. (a-b) discharge capacity (mAh), (c-d) normalized discharge capacity, and (e-f) normalized ΔV versus cycle number for NMC811/Graphite cells with 2VC1DTD (left) or 2FEC1LFO (right) electrolytes. Cycling was done at 40 °C with C/3:C/3 between 3.0-4.20 V, and a C/20:C/20 checkup cycle every 100 cycles. Every 50th data point is shown for clarity.

Figure 4.17 shows discharge capacity (mAh), normalized discharge capacity, and normalized ΔV for NMC811/Graphite cells with 2VC1DTD and 2FEC1LFO electrolytes cycled at 40 °C and C/3 with a 4.06 V UCV. AGC cells with 2VC1DTD were the most competitive here. After 2000 cycles, AGC cells lost around 5 % capacity only while the 4.20 V counterparts lost 15 %. Similar drastic improvements to capacity retention (and ΔV) can be seen for the other graphite materials compared to the same cells cycled to 4.20 V in Figure 4.16.
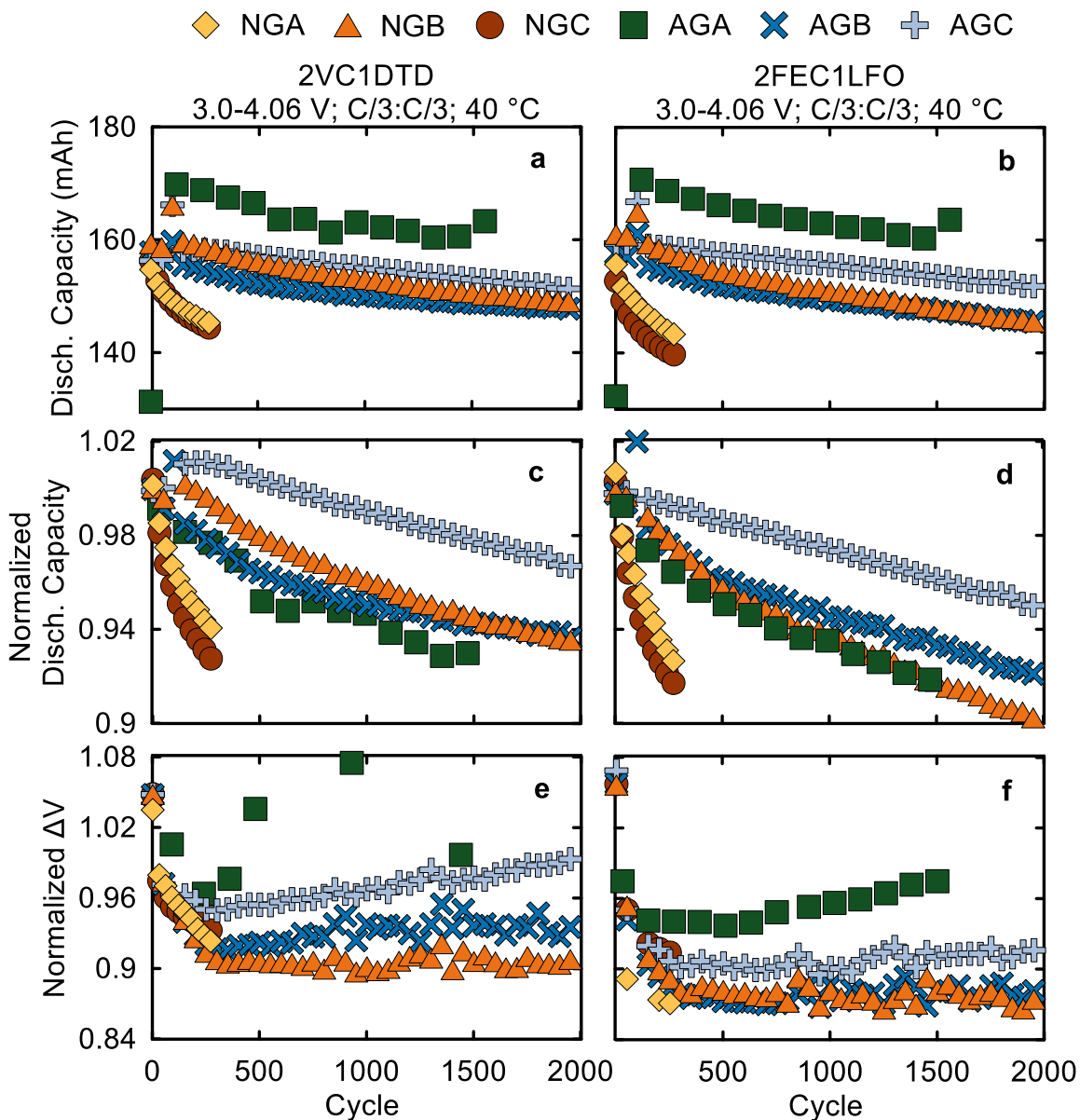
Figure 4.17. (a-b) discharge capacity (mAh), (c-d) normalized discharge capacity, and (e-f) normalized ΔV versus cycle number for 2VC1DTD (left) and 2FEC1LFO (right) cells. Cycling was done at 40 °C with C/3:C/3 between 3.0-4.06 V, and a C/20:C/20 checkup cycle every 100 cycles. Every 50th data point is shown for clarity.

The trends in capacity retention and ΔV growth were similar for RT and 40 °C cycling so operating temperatures can reveal any drawbacks associated with the different graphite materials that are not apparent at lower temperatures. Figure 4.18 shows discharge capacity (mAh), normalized discharge capacity, and normalized ΔV for NMC811/Graphite cells with 2VC1DTD and 2FEC1LFO cycled at 55 °C and C/3 with a 4.20 V UCV. Early on in the cycling, AGC cells were outperforming the other graphite material with 2VC1DTD or 2FEC1LFO. However, the AGC cells eventually experienced a large increase in ΔV around 600 cycles (Figure 4.18e) followed by rapid decrease in capacity (Figure 4.18c). A similar "rollover" in capacity retention and ΔV growth can be seen for NGB cells as well, and the choice of electrolyte seems to change the onset of this rapid failure. NGB cells with 2VC1DTD experienced this rapid failure after ~800 cycles, while NGB cells with 2FEC1LFO did not show this for over ~1000 cycles. Recall that AGC material had fewer redox active sites which was favorable in terms of FCE, gassing, stack swelling, and parasitic heat flow. However, high-temperature cycling at high SOCs results in the generation of various electrolyte degradation products at both the positive and negative electrodes which can rapidly thicken the SEI and "clog" the limited active sites on the AGC graphite[20,36,104–106]. This is consistent with the sudden failure of AGC and NGB materials despite promising capacity retention early on. A simple way to eliminate any electrode degradation products at high SOCs is limit the cell voltage to 4.06 V to also avoid any contribution to cell failure from the positive electrode.
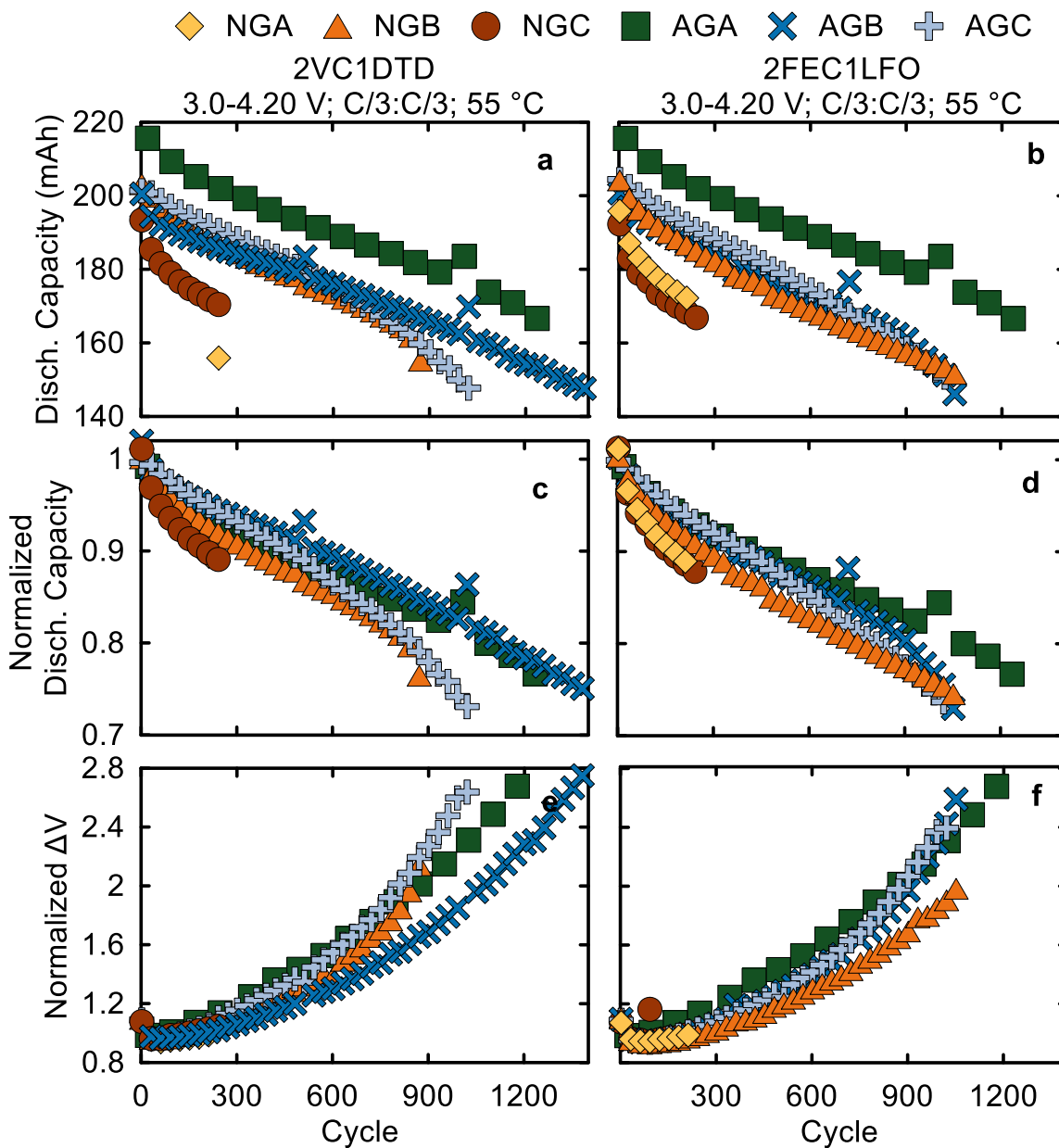
Figure 4.18. (a-b) discharge capacity (mAh), (c-d) normalized discharge capacity, and (e-f) normalized ΔV versus cycle number for NMC811/Graphite cells with 2VC1DTD (left) and 2FEC1LFO (right) electrolytes. Cycling was done at 55 °C with C/3:C/3 between 3.0-4.20 V, and a C/20:C/20 checkup cycle every 100 cycles. No duplicates were made here due to limited cycler availability. Every 50th data point is shown for clarity.

Figure 4.19 shows discharge capacity (mAh), normalized discharge capacity, and normalized ΔV for NMC811/Graphite cells with 2VC1DTD and 2FEC1LFO cycled at 55 °C and C/3 with a 4.06 V UCV. As discussed above, the NMC811/Graphite cells in Figure 4.19 had superior capacity retention and ΔV growth compared to their 4.20 V counterparts in Figure 4.18. None of the cells in Figure 4.19 reached 80 % capacity after 1200 cycles, while 4.20 V cells in Figure 4.18 reached 80 % retention after ~750-900 cycles depending on the graphite material. Furthermore, 4.06 V cells in Figures 4.16e-f showed virtually no ΔV growth after 1200 cycles compared to 4.20 V cells where we observed a ~160 % increase in ΔV. At 4.06 V and 55 °C, the trends in capacity retention are similar to those seen at RT and 40 °C but cycling at 4.20 V at 55 °C introduced issues in the AGC that were not seen at lower UCVs.

When NMC811 cells are cycled to a UCV of 4.06 V, the capacity fade is primarily Li consumption at the negative electrode since there is no ΔV growth. Therefore, an ultra-long lived NMC811/Graphite cell can be made with a choice of a superior graphite material, a competitive additive blend, and, most importantly, a limited UCV that avoids the large lattice volume change seen in Ni-rich materials. If high SOC operation is required, AGA and AGB graphite materials will be desirable, but for a low-energy long-lived NMC811 cell, AGC material is very competitive.
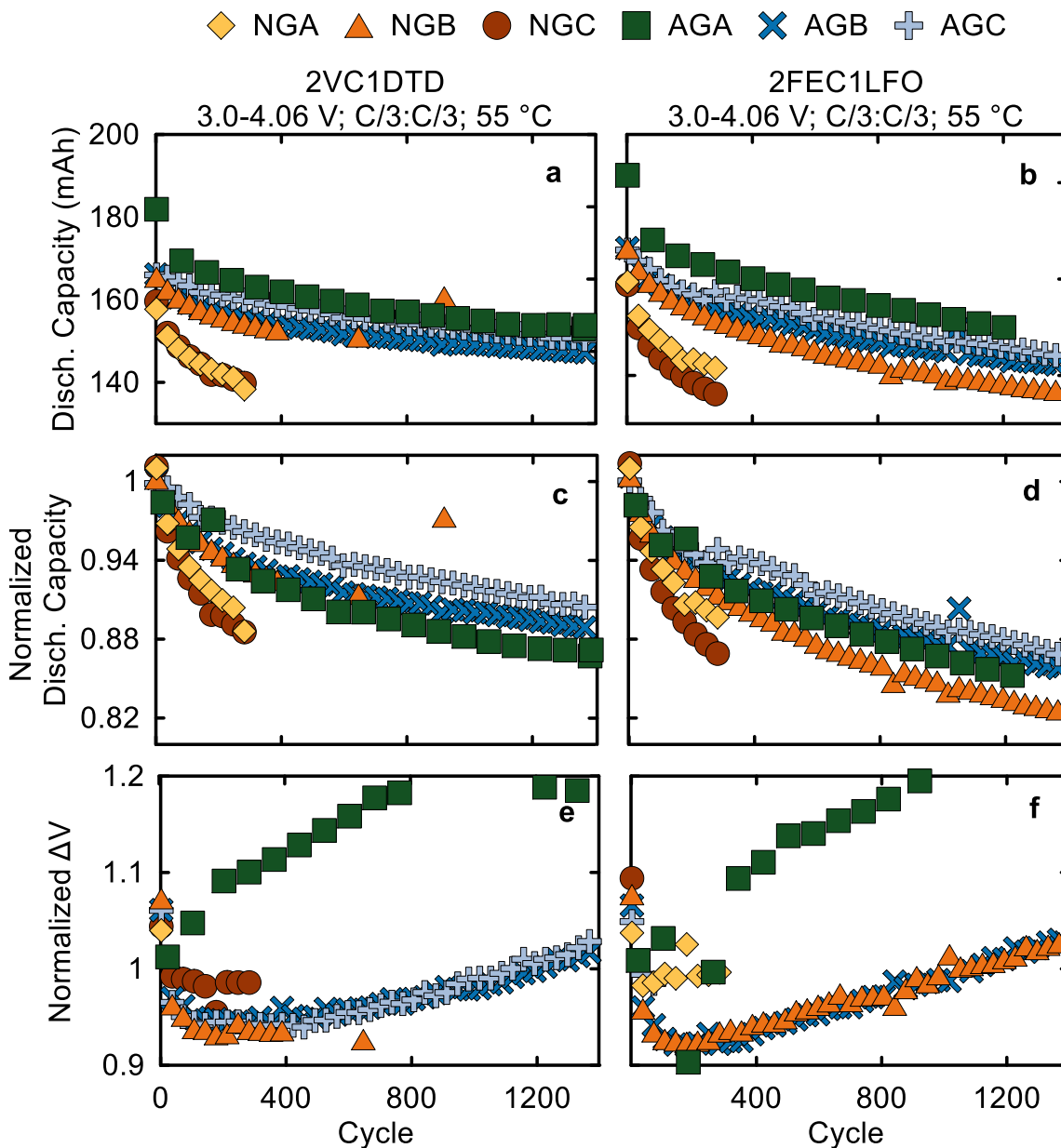
Figure 4.19. (a-b) discharge capacity (mAh), (c-d) normalized discharge capacity, and (e-f) normalized ΔV versus cycle number for NMC811/Graphite cells with 2VC1DTD (left) and 2FEC1LFO (right) electrolytes. Cycling was done at 55 °C with C/3:C/3 between 3.0-4.06 V, and a C/20:C/20 checkup cycle every 100 cycles. No duplicates were made here due to limited cycler availability. Every 50th data point is shown for clarity.

4.7. Pros and Cons of Using a Simple SEI Growth Model to Rank Cell Performance and Predict Lifetime

4.7.1. Challenges with Modeling SEI Growth to Predict Cell Lifetime

Capacity fade in Li-ion cells is complicated by the physical and electrochemical properties of the electrodes, chemical and electrochemical parasitic reactions, cross-talk reactions between the positive and negative electrode, and kinetic limitations of Li ion diffusion in the electrodes and electrolytes. Despite that, many efforts have been made to model cell failure and project cell lifetimes. In this section, we will discuss one common model and its pros and cons.

The choice of graphite material directly impacts the extent of Li inventory loss in Li-ion cells due to ongoing SEI formation as shown above. Previous works have shown that capacity loss and resistance growth increase with temperature approximately following Arrhenius law[58,127–130]. For example, Broussely et al showed that Li loss as a function of time for Ni-based and LCO cell chemistries with graphite negative electrodes follows an Arrhenius-type relationship, arising from the fact that the SEI layer is not a total electronic insulator where irreversible Li consumption occurs constantly[127]. Additionally, the rate of SEI growth can be greatly hindered with the use of additives such as VC. Further work from Broussely et al examined the impact of temperature on capacity loss in commercial cells designed for satellite applications, and indeed showed again that Li loss due to SEI growth followed an Arrhenius model[128].

The square-root time model considers that SEI thickness increases with time and that this consumes lithium inventory, leading to capacity loss according to the following equation:

$$Q(t) = Q_o(1 - A\sqrt{t}) \tag{4.1}$$

where $Q(t)$ is the capacity at time t, Q_0 is the initial capacity, and A is a proportionality constant. The term will be large in cases where SEI thickness is increasing quickly, and capacity loss is rapid. By fitting the capacity checkup cycles in our long-term cycling experiments at various temperatures, where impedance contribution to capacity fade is minimal, one can plot ln(A) vs 1/T, where T is temperature in Kelvin, and the slope is the activation energy, Ea, associated with SEI growth according to:

$$A = Ye^{-\frac{E_a}{kT}} \tag{4.2}$$

where Y is a frequency factor and k is Boltzmann's constant. Knowing Y, k, Ea, and T, one can make predictions about the lifetime on NMC811/Graphite cells in situations where capacity loss is only due to Li inventory loss using the following equation:

$$t_x = \frac{(1-x)^2}{\left(Ye^{-\frac{E_a}{kT}}\right)^2} \tag{4.3}$$

where x is desired fractional capacity at end of life. Capacity fade in cells cycled to 4.20 V UCV is complicated by oxygen release from NMC811 and subsequent

electrolyte degradation as discussed in Chapter 3. The square-root time model assumes that Li loss is the only mode of capacity fade, which is not always the case in real cells, but it is a good approximation, nonetheless.

By applying this simple model to the NMC811/Graphite cells discussed above, one can see the impact of graphite materials on the rate of SEI growth and make a crude lifetime estimation based on equation 4.3. Figures 4.20 and A.10 show the comparison between measured and calculated capacity loss for a set of NMC811/Graphite cells with 2VC1DTD or 2FEC1LFO cycled at 40 °C or 55 °C. Table A.1 shows the fitting parameters for all NMC811/Graphite cells that underwent long-term cycling as shown above. With good temperature control for the 40 °C and 55 °C cycling systems, as well as maintaining a 4.06 V UCV where other capacity fade mechanisms do not contribute to the fade, we saw good agreement between the measured capacity fade trajectory and the square root time model (see residuals in Figure 4.20).
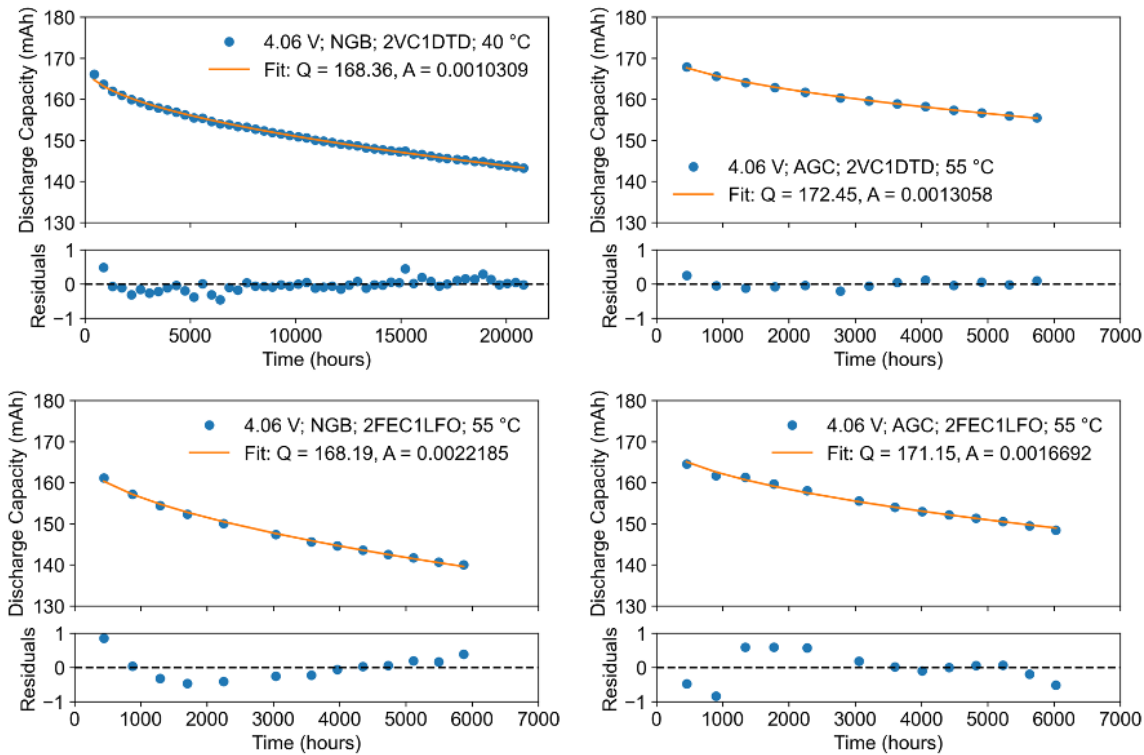
Figure 4.20. Measured and calculated capacity loss for some NMC811/Graphite cells with 2VC1DTD or 2FEC1LFO electrolyte cycled at 40 °C or 55 °C.

While Figure 4.20 suggests that one can use equations 4.1-4.3 to make projections about cell lifetime using the data in this chapter, the temperature fluctuations in the RT cycling (Figures 4.14-15) will present a challenge when fitting this data. Figure 4.21 shows the measured and calculated loss for NMC811/AGC cell cycled at RT with 2VC1DTD electrolyte. Here, we clearly see poor agreement with the square root time model, especially during the first 2500 hours of cycling. While the fit quality can be improved with proper temperature control, this highlights an issue with lifetime prediction models that rely on field-tested data from consumer devices where well-controlled cycling conditions are not always possible[131]. In the absence of temperature control, cells cycling at RT could suffer

from some degree of Li plating in the winter months which results in short-circuits and accelerated Li loss, especially with VC as an additive. Indeed, we see that 2VC1DTD cells performed worse than 2FEC1LFO at RT but not at 40 °C or 55 °C as shown in Figure 4.14-15 compared to Figure 4.16-19. One can expect the error associated with fitting RT cells to be significantly larger than 40 °C or 55 °C cells which is clear from the residuals in Figure 4.21 compared to Figures 4.20 and A.10.
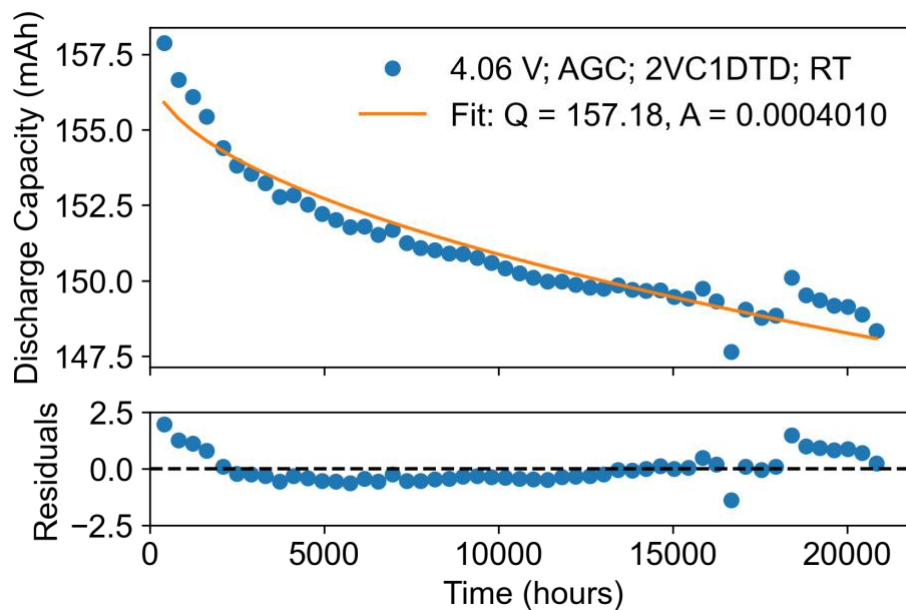
Figure 4.21. Measured and calculated capacity loss for some NMC811/AGC cell with 2VC1DTD electrolyte cycled at RT.

Nevertheless, we can use this simple model to approximate the cell's capacity fade trajectory and use the rate of SEI growth to make crude projections of the cell's lifetime according to equation 4.3. Figure 4.22 shows the extracted A term versus the inverse of temperature in Kelvin for the NMC811/Graphite cells that underwent long-term cycling. As expected from equation 4.2, an Arrhenius

relationship can be seen in Figures 4.22a-b. The RT cells showed the largest error due to the poor temperature control. Based on equation 4.3 and using NMC811/AGC (2VC1DTD) as an example, we can plot the time it takes the cell to reach 90 or 80 % capacity as a function of temperature. Based on Figure 4.22c, we can see that NMC811/AGC cell with 2VC1DTD (and a limited UCV of 4.06 V) is expected to reach 80 % after ~5 years at 40 °C or ~20 years at 30 °C. However, this prediction assumes that the cell is operating under a constant C-rate (C/3 in this case) and a constant temperature. Additionally, this simple prediction does not account for any degradation that may occur when the cell is used to store energy rather than continuously charge/discharge, and it is well-known that Li-ion cells degrade rapidly when they are stored at high SOCs[69,130,132].
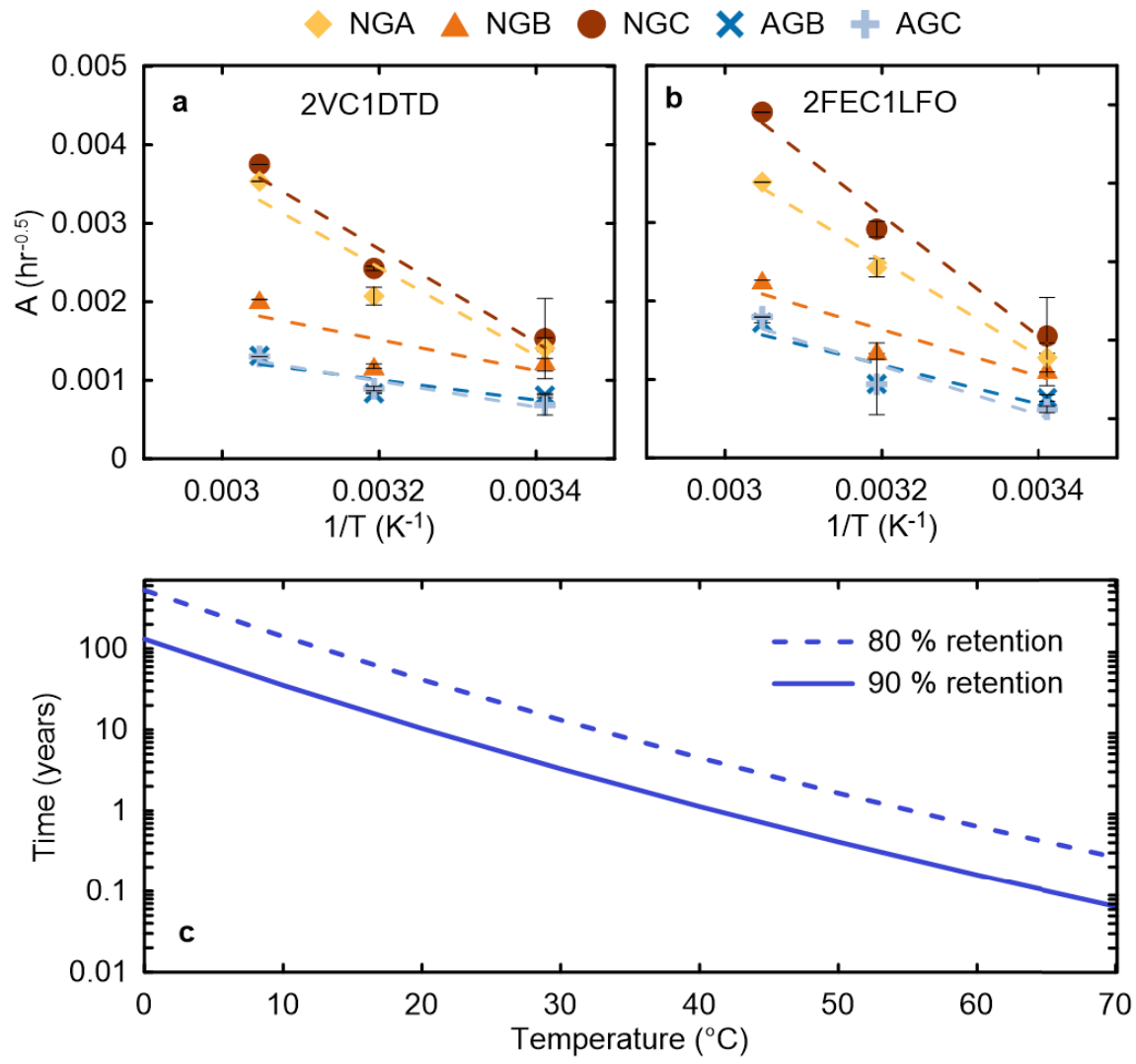
Figure 4.22. (a) A parameter (hr$^{-0.5}$) versus 1/T (K^{-1}) for (a) 2VC1DTD and (b) 2FEC1LFO cells cycled to 4.06 V at RT, 40 °C and 55 °C; (c) projected lifetime in years to 80 and 90 % capacity retention versus temperature (°C) for an AGC cell.

Looking at the Figure 4.22c outside the 30-40 °C range, one can start to see where the lifetime predictions deviate from reality. For example, if the NMC811/AGC cell was cycled at 10 °C, this model predicts a century of operation before reaching 80 % capacity. Outside the 30-40 °C range, new cell failure modes start to contribute significantly to capacity loss. At 10 °C with a VC-containing electrolyte, Li plating is likely to occur in the cell under typical charge/discharge rates (1C to C/5, for example), which can be avoided if the cell operation is limited to extremely slow rates (such as C/20 or slower). Logan et al studied the physical properties of various electrolyte mixtures and found that the conductivity of EC:DMC (3:7) with 1.0 mol kg^{-1} (m) of salt decreased from 13.25 mS cm^{-1} at 30 °C to 9.05 mS cm^{-1} at 10 °C[133]. While this is not the exact same electrolyte formulation used here, it is quite similar and a significant reduction in conductivity will occur in our electrolyte as well if the cell is operated at 10 °C. Besides Li plating, LiPF$_6$-based electrolytes suffer at elevated temperatures due to the poor thermal stability of LiPF$_6$[134]. The decomposition of the salt generates acidic species that contribute to further electrolyte reactions, which can both consume Li inventory and lower the conductivity of the electrolyte. Since our model does not account for this, our lifetime prediction might overestimate the performance at elevated temperatures.

In addition to electrochemical and chemical degradation at various temperatures, commercial Li-ion cells can fail due to very slow electrolyte leakage, hardware failures, physical/mechanical damage, etc., all of which are difficult to model. While similar lifetime predictions were carried out by other research groups,

we acknowledge that cell failure is fairly complicated by the factors mentioned above (among others) and that presents a serious challenge to lifetime prediction[89,131]. Results such as the one in Figure 4.22c, while based on sound logic, will fail to capture the multitude of degradation modes that field-tested cells will face.

4.7.2. Impact of Negative Electrode Overhang on Capacity Fade Trajectory

The negative electrode in commercial Li-ion cells typically has 5-10 % more available capacity than what is contained in the positive electrode's Li inventory. The negative electrode area is also slightly larger than the opposing positive electrode to ensure that any minor electrode misalignment during manufacturing will not result in Li plating, which will occur if a portion of the positive electrode does not face a negative electrode during charge. In the pouch cells used in this thesis, there is a 1 mm negative electrode "overhang". The excess capacity and geometric overhang of the negative electrode are both important safety precautions that cell manufacturers incorporate in their designs. Intercalated Li ions can diffuse into the negative electrode overhang during cell operation which can trap some Li inventory in the overhang. Since the overhang does not face a positive electrode, the Li ions in this region will not immediately intercalate back in the positive electrode during discharge. This results in some amount of "trapped" Li inventory in the overhang which increases with the degree of graphite lithiation.

Figure 4.23 shows the measured and calculated capacity for some NMC811/AGA cells discussed in Chapter 3. These cells were cycled with a 25 %,

50 %, 75 %, or 100 % DOD and C/3 or C/50 rates. All cells were cycled at 40 °C with 2VC1DTD electrolyte. The NMC811 cells in Chapter 3 were fitted with the square root time model to highlight the impact of negative electrode overhang on the measured capacity fade. Recall that despite differences in DOD and C-rate, all capacity checkup cycles (the ones used in all fits discussed in this section) were done at either C/10 (for cells in Chapter 3) or C/20 (for cells in Chapter 4) with a 100 % DOD. In principle, these periodic, slow cycles allow us to measure the cell's capacity with minimal losses due to impedance growth and/or kinetically-limited processes that can impact the cells' capacity at higher rates.

The 25 % DOD cells were discharged to 3.74 V during regular cycles, so a significant amount of Li remained in the negative electrode for most of the cell's life. Looking at the measured and calculated capacity fade in Figure 4.23, one can see poor agreement for cells cycled at C/3 or C/50. The sharp "drop" in capacity during the first 2500 hours is due to Li in the overhang as discussed above. Since the 25 % DOD cells remain at high SOC for most of the cell's lifetime, the negative electrode overhang will be more lithiated compared to a 100 % DOD cell[135]. The overhang SOC will be ~50 % that of the active portion of the negative electrode, so the overhang in a 0-100 % SOC cell (i.e., the 100 % DOD case) will be at ~50 % SOC, while the overhang in 75-100 % SOC cell (i.e., the 25 % DOD case) will be at ~87.5 % SOC. The impact of DOD (and Li inhomogeneity in the negative electrode) is clear in Figure 4.23 where the residuals from the fit decrease were small for cells cycled at higher DODs.

The negative electrode of the 25 % DOD cells will remain significantly lithiated after the first t = 0 cycle since the cells are only discharged to 3.74 V. Therefore, more Li can diffuse into the overhang throughout the course of the cycling experiment. As the DOD increases from 25 % to 100 %, the Li concentration in the overhang decreases as shown for the 50 % and 75 % DOD cells. Previous work from Gyenes et al shows the Li content in the overhang affects the charge/discharge capacity in the early stages of cell life (~1000 hours at 40 °C), after which nominally identical cells start to show similar CE values[135]. The sharp drop in capacity suggests that the C/10 rate chosen for the checkup cycle may not have been sufficiently slow to allow Li in the overhang to diffuse back into the active area. To mitigate this, capacity checkup cycles should also include a constant voltage hold at bottom of discharge (3.0 V, for example) for 12-24 hours to allow Li to diffuse into the active area of the negative electrode.
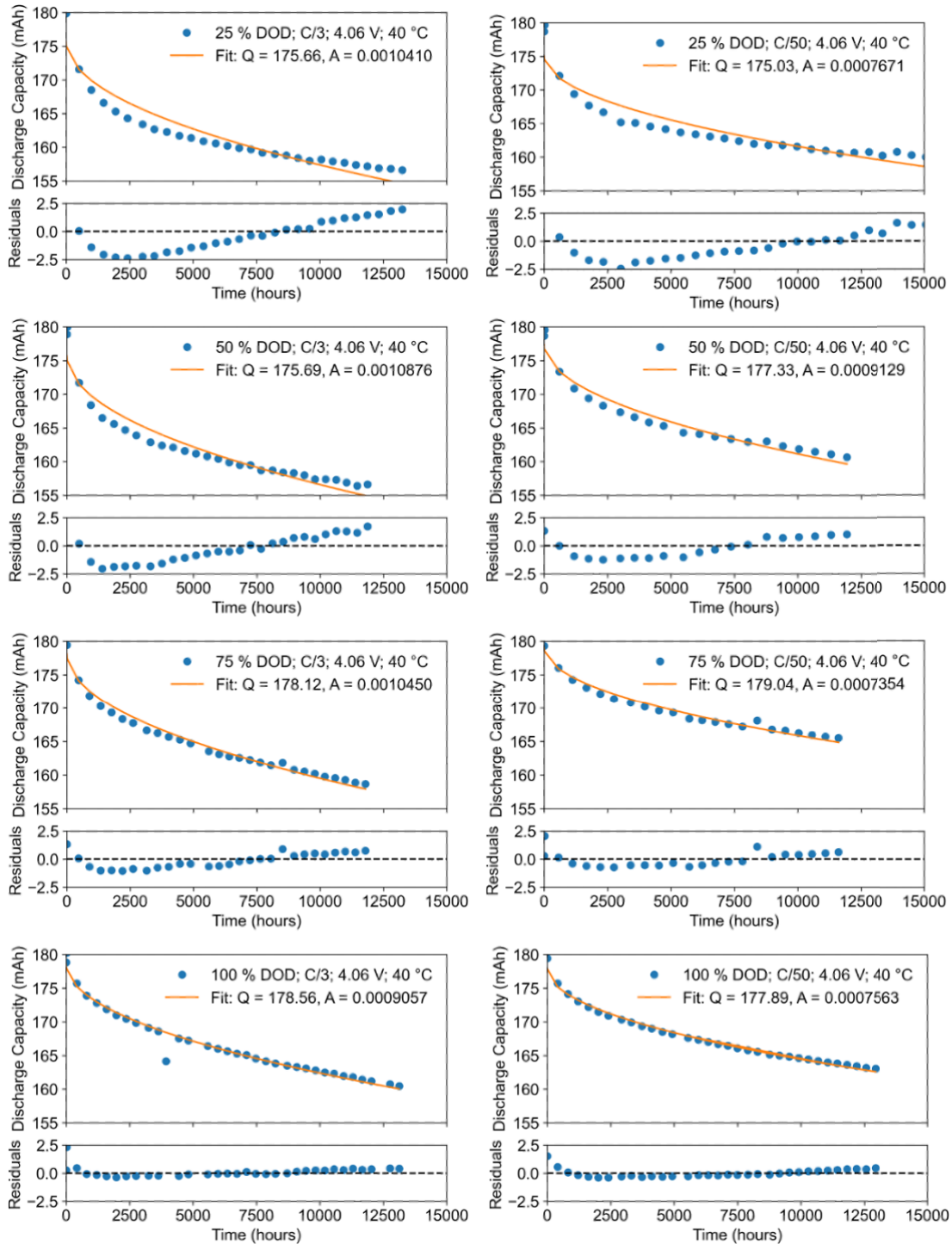
Figure 4.23. Measured and calculated capacity loss for NMC811/Graphite cycled to 25 % or 100 % DODs at different C-rates with 2VC1DTD. These cells were previously discussed in Chapter 3.

A study by Lewerenz et al looked at the contributions of irreversible (i.e., parasitic reactions) and reversible (i.e., overhang) losses on the capacity of fade of 25 Ah NMC111/Graphite cells[136]. In their study, Lewerenz et al showed that cells stored at high SOCs lost more capacity than equivalent ones stored at lower SOCs, and that high SOC storage resulted in a sharper capacity drop during the first 200 days of storage at 50 °C due to Li being "trapped" in the negative electrode overhang. To estimate the rate of capacity fade without contributions from the overhang during early stage of cell life, Lewerenz et al took the slope of the near-linear portion of the fade curve as an estimate of the fade rate during storage, since the Li distribution in the negative electrode was shown to be homogenous after 200 days of storage at 50 °C[136,137]. While the fade rates calculated by Lewerenz et al in this manner were consistent with the expected trends (i.e., faster fade at higher SOCs), the slope of the near-linear part of the fade will change (and may not even remain linear, see AGC cells in Figure 4.18) as the cell ages, which is also common to see in the so-called "rollover failure" mechanisms[138].

4.7.3. Impact of UCV and Temperature on Rate of SEI Growth

To further demonstrate the impact of UCV on SEI growth, NMC811/AGC cells were cycled to 4.04, 4.06, 4.08 and 4.10 V UCV at 40 and 70 °C. Cycling at 70 °C greatly accelerate cell failure and highlights the impact of UCV in a shorter time. Figure 4.24 shows the discharge capacity (mAh), normalized capacity, and normalized ΔV versus cycle number for NMC811/AGC cells with different UCVs. Despite the small difference of 60 mV between the 4.04 and 4.10 V cells, the

4.04 V cell lost 10 % capacity and its resistance increased by 5 % at 70 °C after 400 cycles, compared to 15 % capacity loss and 30 % resistance growth at 4.10 V UCV. Similar trends can be seen after 2500 cycles at 40 °C, where increasing the UCV resulted in more fade and ΔV growth. The importance of limiting the UCV is not just to improve capacity retention, but also to keep the resistance growth under control to avoid compromising the power capabilities of the cells.
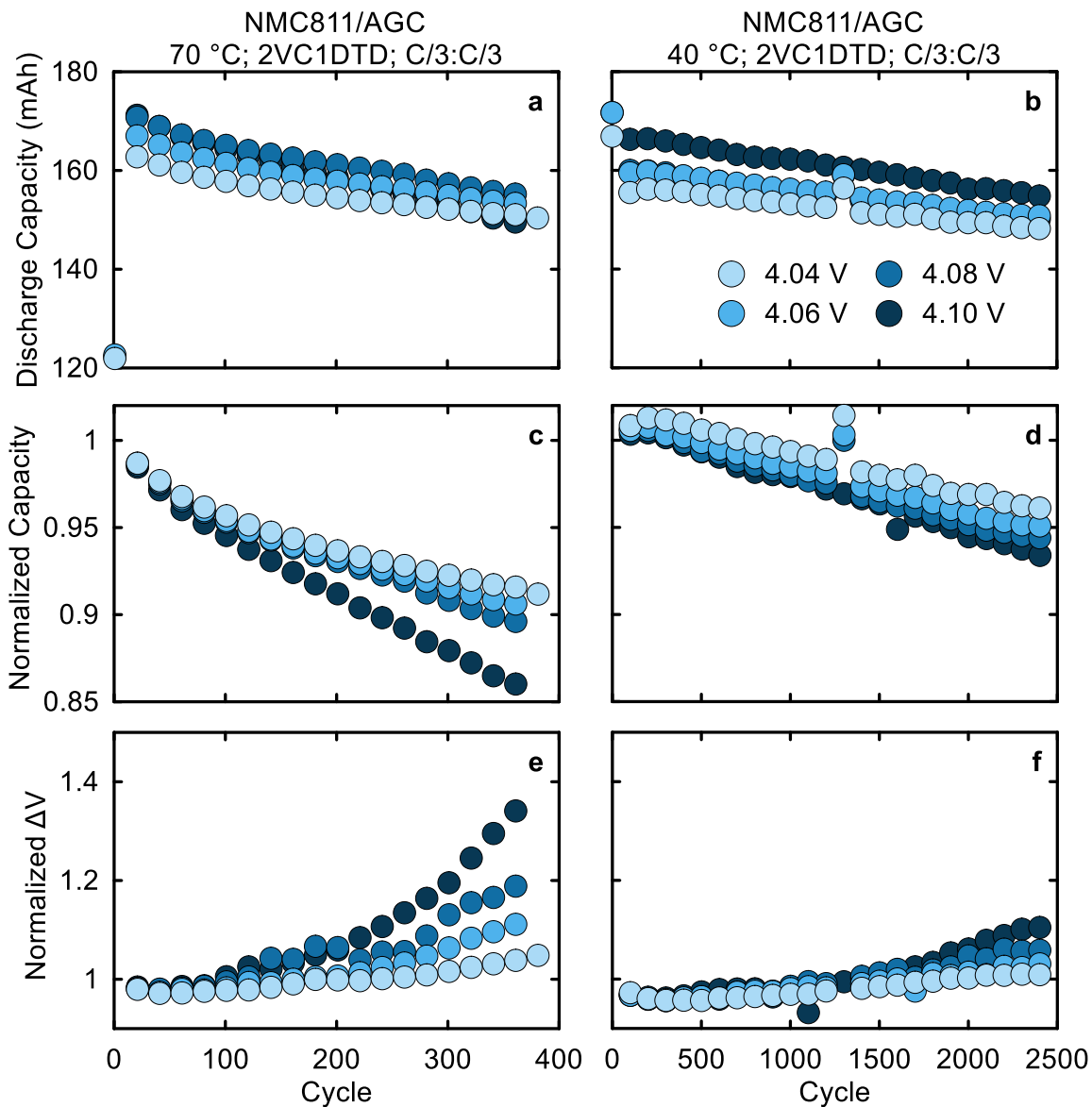
Figure 4.24. (a-b) discharge capacity (mAh), (c-d) normalized capacity, and (e-f) normalized ΔV for NMC811/AGC cells cycled to different UCVs at 70 and 40 °C with 2VC1DTD electrolyte at C/3:C/3.

Figure 4.25 shows the measured and calculated capacity loss for NMC811/AGC cells cycled at 40 °C with 2VC1DTD and different UCVs. All cycling was at C/3:C/3 with C/20:C/20 checkup cycles. Figure A.11 shows equivalent plot for the 70 °C cells. For both temperatures, the square root time model fits the

measured data quite well, and the impact of overhang is small since all cells were fully discharged to 3.0 V with every charge. Therefore, the results in Figure 4.25 show that the rate of SEI growth extracted from these fits is a good representation of SEI growth in the cells, at least during the first 12500 hours at 40 °C and ~1600 hours at 70 °C.
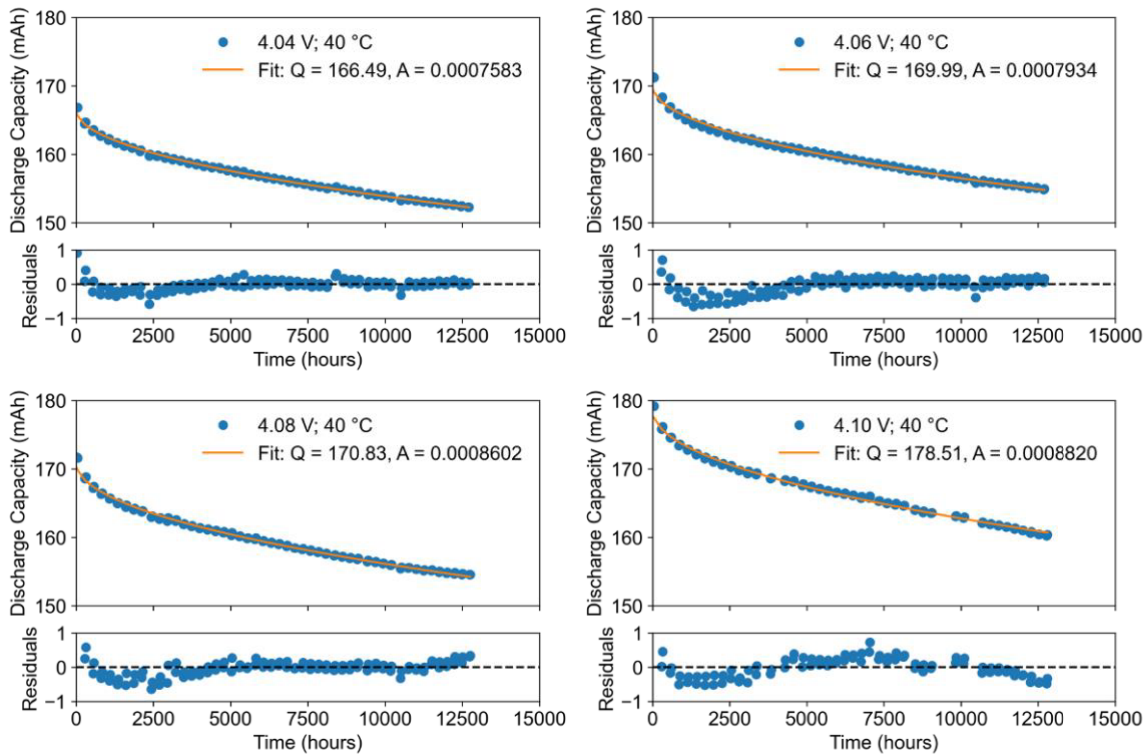
Figure 4.25. Measured and calculated capacity loss for NMC811/Graphite cells cycled to 4.04 V, 4.06 V, 4.08 V and 4.10 V UCV at 40 °C with 2VC1DTD electrolyte.

Figure 4.26 shows the extracted *A* parameter versus UCV for the cells in Figure 4.24. For 40 °C, the *A* term increases from 4.04 V to 4.06 V but the differences are fairly small and within error. However, there is a clear increase in SEI growth at 4.08 V and 4.10 V, consistent with the differences in capacity fade

and ΔV in Figure 4.24. Similarly for 70 °C, the rate of SEI growth linearly increases from 4.04 V to 4.08 V but spikes at 4.10 V. At 4.10 V, the *A* term is nearly 30 % greater than 4.08 V despite only 20 mV difference in voltage. Lowering the UCV is therefore critical for the longevity of NMC811 cells.
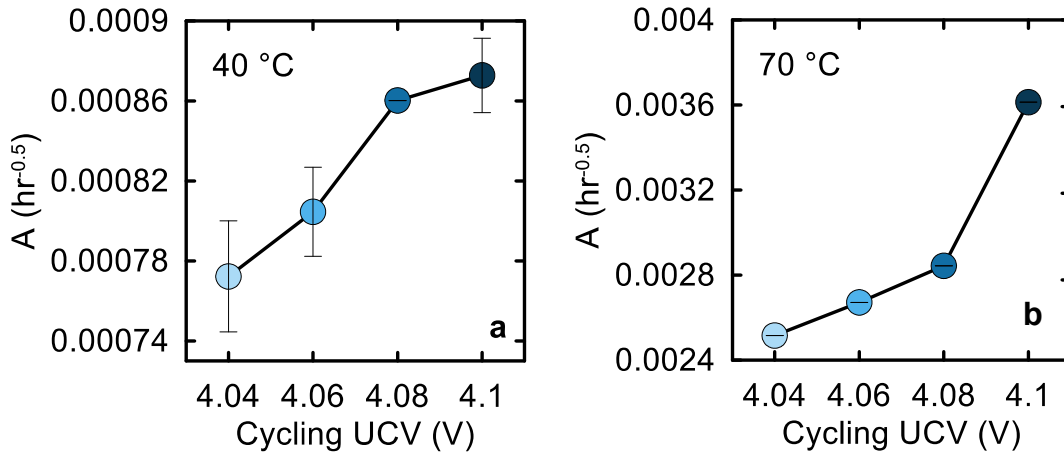
Figure 4.26. A parameter versus UCV for NMC811/Graphite cells cycled at 40 °C or 70 °C.

4.8.   Trade-off Between Energy Density and Lifetime

To highlight the importance of long-lived cells over energy-dense cells, particularly for energy storage applications, the volumetric energy density for a cylindrical 18650 cell, which is 18 mm in diameter and 65 mm long (common commercial form factor), made with NMC811/AGC electrodes was calculated. To calculate stack energy density in Wh L^{-1}, the volume of the cell stack must be calculated. Here, a cell stack is taken to a positive electrode with double-sided coating and Al current collector, a negative electrode with double-sided coating and Cu current collector, and two layers of separator so stack thickness, t_{stack} is the sum of the thickness of each component according to:

135

$$t_{stack} = 2 * (t_{pos} + t_{neg} + t_{sep}) + t_{Al} + t_{Cu} \tag{4.4}$$

The mass per unit area of each electrode, σ_i, was calculated according to:

$$\sigma_i = t_i * [(1 - \emptyset) * (\rho_i w_i + \rho_{binder} w_{binder} + \rho_{CB} w_{CB})] \tag{4.5}$$

where t_i is electrode thickness, ø is electrode porosity, ρ and w are the densities and weight fraction of the electrode material, binder, and conductive carbon in the electrode. Therefore, capacity per unit area of each electrode, q_i, is simply:

$$q_i = \sigma_i * w_i * Q_i \tag{4.6}$$

where Q_i is the specific capacity of each electrode material. In our stack energy calculation, we assumed that negative electrode capacity is 7 % greater than the positive electrode and no geometric overhang. The reversible capacity per unit area of the cell stack q_{stack}, where the electrodes are coated on both sides of the current collector, is equal to:

$$q_{stack} = 2 * q_{pos} * (1 - graphite\ irreversible\ capacity\ loss) \tag{4.7}$$

therefore, the stack energy density is:

$$Stack\ Energy\ Density = \frac{q_{stack}}{t_{stack}} * Average\ Voltage \tag{4.8}$$

Figure 4.27 shows the discharge energy (mWh) and ΔV growth versus cycling time for NMC811/AGC cells cycled at 40 or 55 °C with 4.06 or 4.20 V UCV, and the stack energy density versus positive electrode loading. All assumptions used in the energy density calculations are shown in the figure. At 55 °C, one can

see that a 4.20 V cell, with higher initial energy output, will deliver less energy per cycle compared to 4.06 V cell after ~5500 hours of operation, along with a 2-3-fold increase in ΔV compared to 4.06 V. A similar trend can be seen at 40 °C where the 4.20 V UCV will deliver less energy compared to 4.06 V after 12000+ hours of operation. This assumes that the cells will continuously undergo charge/discharge cycling, but in practice the cells will spend a significant amount of time just storing energy, occasionally at high SOCs, so this decay in energy output may occur sooner or later depending in the temperature and voltage of operation. Looking at Figure 4.27c, it is abundantly clear that designing a cell that can only cycle to 4.06 V UCV will result in lower initial energy, but the cycling data suggests that designing low energy cells is more economical since they can eventually output more energy over a longer lifetime.

While limiting the UCV is counterintuitive given the current push in academia and industry for higher energy densities, the scarcity of battery raw materials and urgent demand for more battery manufacturing can be addressed by favoring lifetime over energy density until we can develop commercially-viable strategies to push the UCV without compromising lifetime. Since it takes 50 to 60 kWh to produce 1 kWh of Li-ion cells[139], it is paramount to extend the calendar and cycle life of Li-ion cells as much as possible to avoid excess use of energy in battery manufacturing to replace the short-lived energy-dense cells.
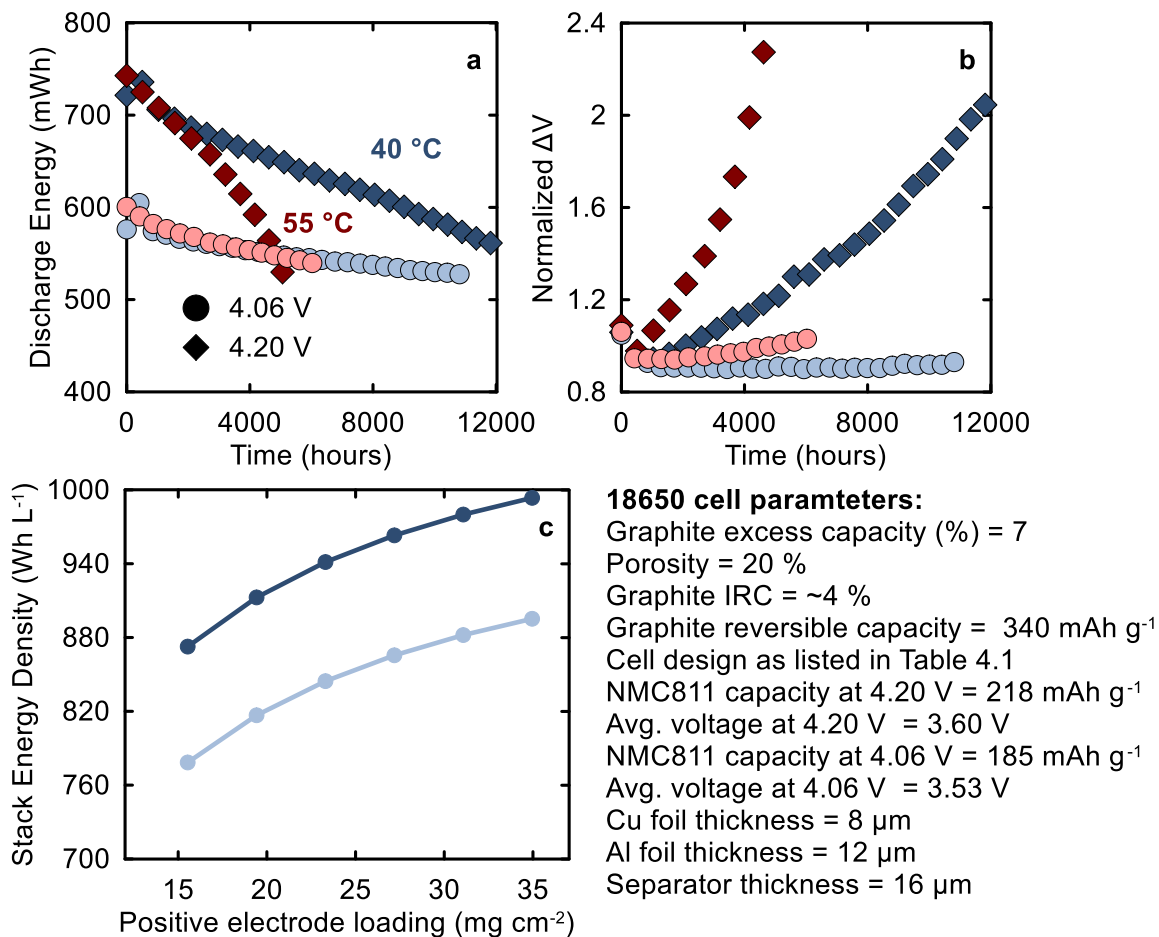
Figure 4.27. a) Discharge energy versus time for NMC811/AGC cells tested at C/3 at 40 or 55 °C. The electrolyte was 2VC1DTD and cells were tested between 3.0-4.20 V and 3.0-4.06 V as indicated in the legend. b) stack volumetric energy density for NMC811/AGC cells versus positive electrode loading (mg cm^{-2}) for cells balanced to 4.2 V or 4.06 V with 7 % excess graphite capacity. The assumptions made in the calculation are listed above.

4.9. Conclusion

Ultra-long-lived Li-ion cells are crucial for grid energy storage applications, where decades of lifetime are needed. With Li inventory loss being a significant cell failure route, optimizing and understanding the impact of graphite negative electrodes on the lifetime of NMC811 cells is important if they were to become

viable candidates for grid storage. In this chapter, we studied the differences between five graphite materials from reputable suppliers, and their impact on the performance of NMC811 pouch cells. The main findings of this work can be summarized as follows:

1. AG materials here were primarily 2H graphite, while NG had a substantial 3R component. The impact this has on cycling is unclear, and the NG materials appear to have a carbon-based coating applied at a temperature of 550-1200 °C according to powder XRD. Previous reports showed that carbon-coated NG materials offer an improved CE, lifetime, and specific capacity[121];

2. N_2 BET area does not provide a reliable measure of the electrochemically accessible area, as evident from gas generation, dQ/dV plots showing electrolyte reduction activity, formation gas composition, FCE and parasitic heat flow measurements. Therefore, an important distinction between BET area and accessible area must be made when evaluating electrode materials for Li-ion cells;

3. Low accessible surface area results in an improved fade rate, improved capacity retention and high FCE, but increases cell R_{CT}. Thus, graphite materials designed for high-rate applications will experience Li plating if the accessible surface area is small; but in applications where high-rate capabilities are not crucial, then having a small accessible area will result in excellent lifetime;

4. AGB, AGC, and NGB had low parasitic heat flow and superior capacity retention to the other graphite material, and the AG materials shown here had substantially smaller stack thickness growth according to *in-operando* pressure measurements;

5. The complicated interplay between the negative and positive electrodes, parasitic reactions, negative electrode overhang, and failure mechanisms unique to each temperature range means that modeling SEI growth to predict cell lifetime will result in crude estimations of lifetime if simple models are used;

6. NMC811/graphite cells will benefit from an enormous lifetime boost when operated at a limited UCV of 4.06 V, where they can provide greater lifetime energy output compared to high SOC cells.

The combined work in Chapters 3 and 4 highlight strategies to improve the lifetime of NMC811/Graphite through detailed studies of cycling conditions, their impact of cell degradation, and the role of graphite materials and UCV in creating ultra-long lived NMC811 cells.

Chapter 5. High-Temperature Performance and Degradation of LMO/Graphite Cells

The results shown in this chapter are part of two manuscripts that are awaiting approval for submission. A. Eldesoky conceived and planned all experiments presented here, completed the data analysis and manuscript writing with supervision from J. R. Dahn. A. Eldesoky carried out all XRF measurements according to the method developed for this thesis and published in *A. Eldesoky et al* 2020 *J. Electrochem. Soc.* **167** *130539*, as well as NMR experiments. N. Kowalski and H. Ni prepared the electrolyte recipes and filled the cells. A. Dutta measured the lattice parameters for the LMO materials used here. E. Logan carried out the IMC experiments with help from E. Zsoldos.

5.1. Introduction

To alleviate the strain on the limited supply of Ni and Co, automakers and cell manufacturers are looking at Mn-based positive electrodes as an alternative to Ni-rich ones in some applications. The spinel $Li_{1+x}Mn_{2-x}O_4$ (LMO) positive electrode has poor lifetime at elevated temperatures and lower energy density as shown in Figure 1.3. Nevertheless, LMO is gaining attention in low-cost applications where moderate energy density and lifetime are needed[140], such as short-haul, low-cost electric vehicles. LMO positive electrodes are generally safer than Ni-rich ones, and Mn is one of the more abundant transition metals that are used in battery cell manufacturing. Further, LMO possess high-power density due the three-dimensional Li diffusion channels in the spinel positive electrode structure, making them suitable for many high-power applications[141,142].

It is believed that the main degradation mode of LMO cells is the dissolution of Mn ions from the positive electrode and their deposition on the negative electrode, which can degrade the SEI and the contribute to active material loss[53,54,143,144]. Mn dissolution is temperature- and voltage-dependent, which affects the high-temperature performance of LMO cells[143].

The mechanism of Mn dissolution and deposition on the negative electrode, as well as the consequences on Mn deposition on capacity retention, remain somewhat elusive. Early reports from Yang et al showed using XPS that Mn deposits on the negative electrode surface facing the separator as Mn(II) or Mn(IV)[145]. More recent work by Gowda et al probed the oxidation state of deposited Mn on the surface of graphite particles using XANES and found that metallic Mn is the dominant species found on the negative electrode[146]. However, despite the prevalence on Mn dissolution, no consensus on the oxidation state of deposited Mn can be found in the literature[75,143,145–148]. Regardless of the oxidation state of deposited Mn, dissolution of positive electrode active material, and any subsequent physical/chemical changes in the cell, should be minimized or eliminated all together to extend cell lifetime.

Deposition of Mn on the negative electrode surface was shown to compromise the SEI layer, resulting in more Li and solvent consumption and gas generation[54]. In addition, Mn deposition can increase the impedance of the negative electrode due to the increase in SEI thickness, thus compromising power density and capacity retention[149]. Wang et al demonstrated that Mn^{2+} in solution destabilizes carbonate molecules and PF_6^- anions, resulting in severe electrolyte

discoloration after 8 days of storage at 55 °C compared to the same electrolyte stored in the absence of Mn^{2+} ions[150]. Therefore, understanding cell performance and degradation resulting from Mn dissolution is crucial to optimizing the performance of LMO/Graphite cells.

Here we investigate the performance and degradation of LMO/AG pouch cells with four different positive electrodes as outlined in Table 5.1. We study the impact of Li excess (x in $Li_{1+x}Mn_{2-x}O_4$), positive electrode particle size, and NMC blending on the cycle life of LMO/AG cells with various electrolytes blends. All electrolyte blends are listed in Table 5.2.

This chapter examines the impact of electrolyte additives and salt on capacity retention as a function of cycling temperature. Mn deposition on the negative electrode is quantified using XRF and correlated to capacity loss and cycle number. DCA was used to determine cell failure modes and quantify positive and negative electrode active mass loss. Additionally, we looked at the cell degradation at 70 °C using XRF and NMR, electrode/electrolyte reactivity via IMC, and the impact of mixed salt electrolytes on Mn dissolution and storage performance at 60 °C.

Table 5.1. List of all LMO/AG cells used in this chapter. Electrode formulation is the same as previous chapters.

Positive electrode	Li excess (x in $Li_{1+x}Mn_{2-x}O_4$)	D50 (μm)	*a* lattice parameter (Å)	LMO Capacity (mAh g^{-1})	Loading (mg cm^{-2})	Negative electrode	Loading (mg cm^{-2})
SC-LMO	0.125 ± 0.029	10.42	8.1994	105	22.7		8.5
PC-LMO	0.078 ± 0.016	~13.2	8.2150	106	22.2	Kaijin AML400	8.8
PC-LMO2	0.011 ± 0.003	10-14	8.2365	115	22.3		9.9
25 % NMC622 + 75 % PC-LMO2	-	-	-	-	22.4		10.5

Table 5.2. List of electrolytes used in this chapter.

Name	Salt	Solvent (wt. ratio)	Additive (wt.%)
2VC1DTD			VC (2 %) / DTD (1 %)
PES211			PES (2 %) / MMDS (1 %) / TTSPi (1 %)
2FEC1LFO	1.5 M LiPF$_6$		FEC (2 %) / LFO (1 %)
2FEC1LiBoB			FEC (2 %) / LiBOB (1 %)
2VC		EC:EMC:DMC (25:5:70)	VC (2 %)
2VC-LiFSI	1.5 M LiFSI		VC (2 %)
1.5LiPF$_6$	1.5 M LiPF$_6$		
0.75LiPF$_6$-0.75LiBF$_4$	0.75 M LiPF$_6$ + 0.75 M LiBF$_4$		
1.5LiBF$_4$	1.5 M LiBF$_4$		
0.75LiPF$_6$-0.75LiFSI	0.75 M LiPF$_6$ + 0.75 M LiFSI		VC (3 %) / DTD (1 %)
1.5LiFSI	1.5 M LiFSI		
1.25LiFSI-0.25LiDFOB	1.25 M LiFSI + 0.25 M LiDFOB		
1.0LiFSI-0.5LiDFOB	1.0 M LiFSI + 0.5 LiDFOB		

Figure 5.1 shows "top-down" SEM images of positive electrodes taken from the four different LMO/AG pouch cells used in this chapter. The PC-LMO and PC-LMO2 materials had the conventional morphology of a polycrystalline material: large secondary particles ~8-10 μm in size comprised of aggregates of smaller primary particles. The SC-LMO material in Figure 5.1a was composed of large primary particles about 6-10 μm in size. The NMC622/PC-LMO2 electrode in Figure 5.1d shows the physical mixture of the single-crystalline NMC622 particles (~3-4 μm) with the larger PC-LMO2 particles.
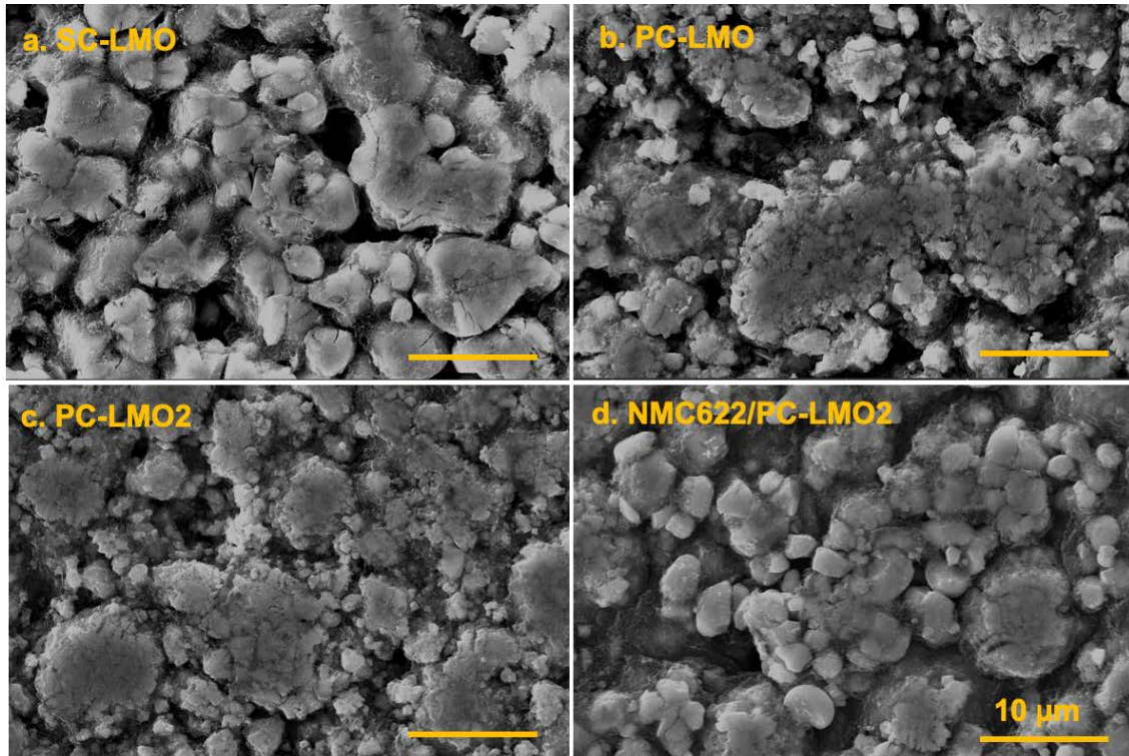
Figure 5.1. SEM images of positive electrodes taken from (a) SC-LMO; (b) PC-LMO; (c) PC-LMO2; and NMC622/PC-LMO2 pouch cells.

5.2. Galvanostatic Cycling at RT, 40 °C, 55 °C, and 70 °C

The cycling results at RT and 40 °C can be found in Figures A.12-17 and will be summarized in this section. Figure 5.2 shows normalized discharge capacity versus cycle number for LMO/AG pouch cells cycled at 55 °C with different electrolyte formulations. Absolute capacity and ΔV growth plots are shown in Figures A.18-19. The difference between the LMO materials here is striking. The best performing material is SC-LMO, but the performance of all cells remains poor at 55 °C. Cells with LiFSI as the salt had better capacity retention than their $LiPF_6$ counterparts (Figure 5.2a-b). The dissolution of Mn is a known issue in LMO cells which can be triggered by the degradation of $LiPF_6$ and oxidative decomposition of the electrolyte[106]. Replacing $LiPF_6$ with the more thermally stable LiFSI improved capacity retention for SC-LMO. However, LiFSI does not passivate Al foil at high voltages and Al corrosion is known to occur [151,152] which puts its compatibility with LMO/AG cells under scrutiny that will discussed later.

Blending 25 wt.% of NMC622 with PC-LMO2 resulted in a great capacity retention boost. Interestingly, the degree by which the capacity retention improved in blended electrodes appears to depend on the electrolyte formulation (see Figure 5.2c versus Figure 5.2e, for example). While the synergy between NMC and LMO is well-known[153,154], the impact of the electrolyte on this synergy is not often discussed. Finally, SC-LMO and PC-LMO cells showed the smallest ΔV growth compared to the other LMO types (Figure A.19). Despite the superior performance, LiFSI SC-LMO cells showed greater ΔV growth compared to their

147

LiPF$_6$ counterparts (Figure A19a-b) similar to the 40 °C cycling results in Figure A.17b.
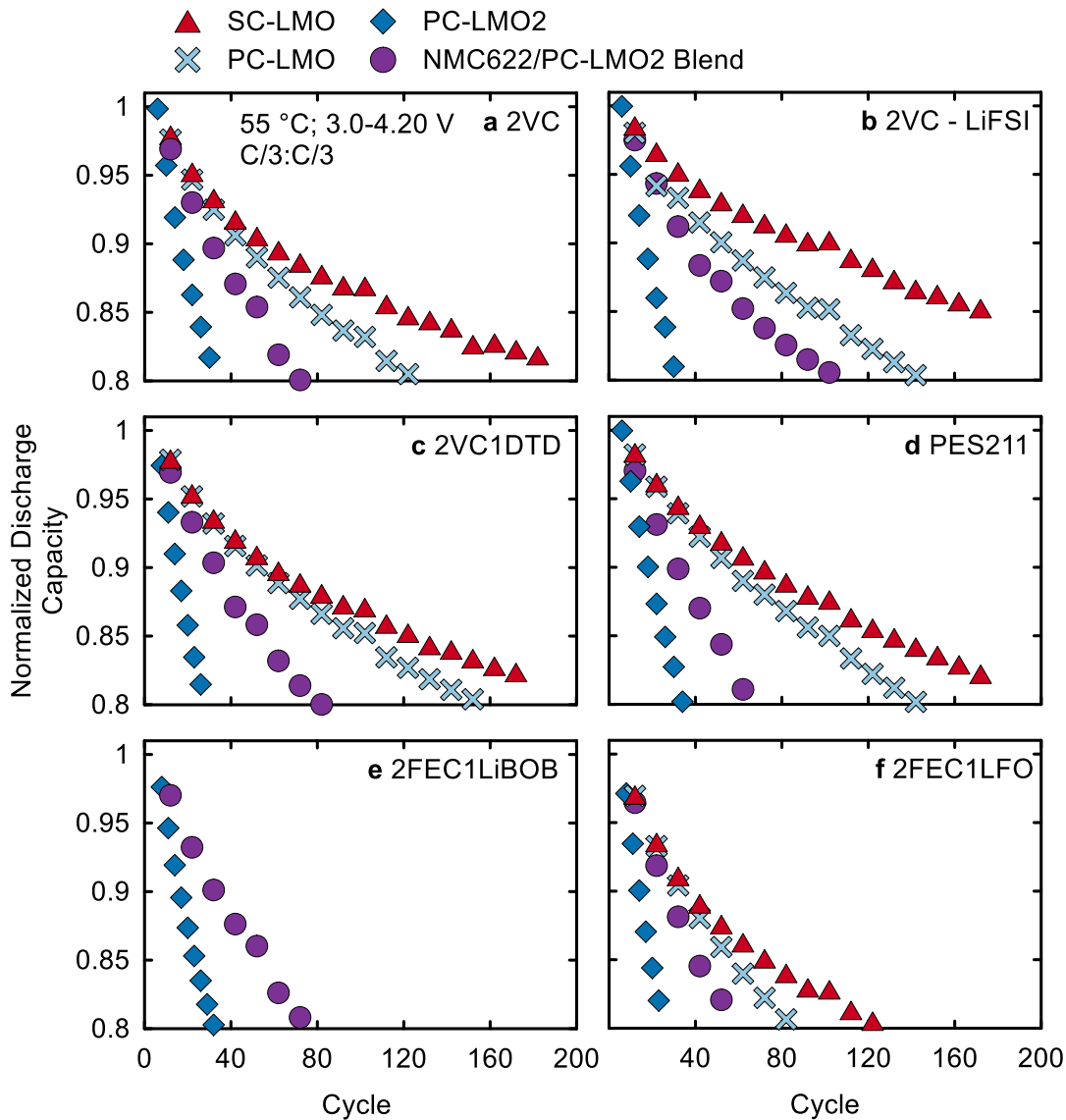
Figure 5.2. Normalized discharge capacity versus cycle number for the LMO/AG pouch cells with (a) 2VC; (b) 2VC-LiFSI; (c) 2VC1DTD; (d) PES211; (e) 2FEC1LiBOB; and (f) 2FEC1LFO electrolytes. Cycling was done at 55 °C at C/3:C/3 and 3.0-4.20 V.

Figure 5.3 shows the normalized discharge capacity versus cycle number at 70 °C, and Figures A20-21 show the absolute capacity and normalized ΔV growth plots. At 70 °C, the capacity retention quickly deteriorates for all cell types and electrolyte formulations and the trends observed at 40 °C (Figures A15-17) and 55 °C (Figure 5.2) are more striking at 70 °C. The synergy of NMC-LMO blending is quite dramatic at this temperature. For example, Figure 5.3a shows that PC-LMO2 reached 60 % retention in a mere 20 cycles, while NMC622/PC-LMO2 cell hit 60 % retention in 160 cycles. Similar improvements can be seen with other electrolyte formulations as well. The impact of electrolyte formulation on the perceived synergy between NMC and LMO is once again very clear in Figure 5.3.
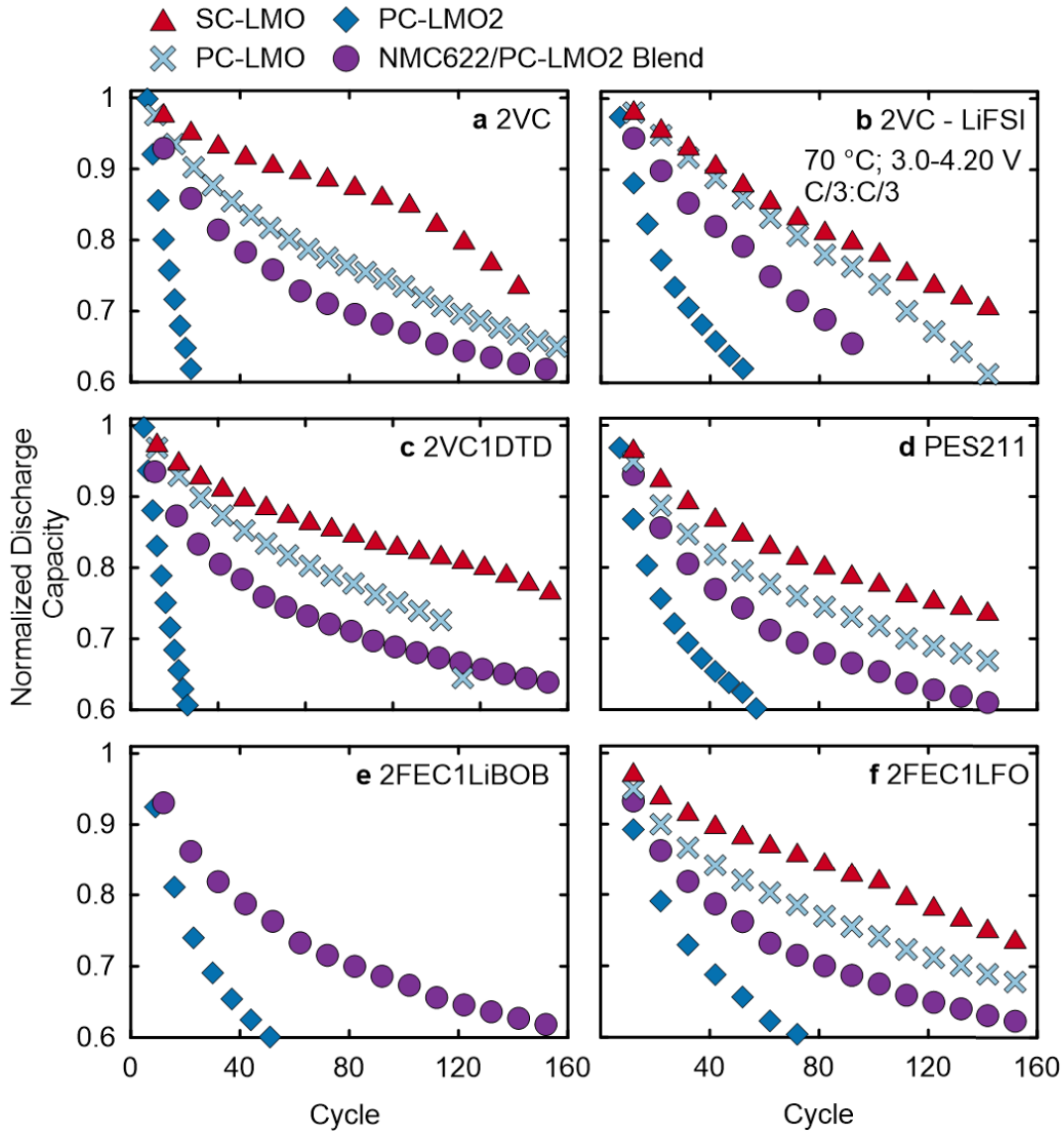
Figure 5.3. Normalized discharge capacity versus cycle number for the LMO/AG pouch cells with (a) 2VC; (b) 2VC-LiFSI; (c) 2VC1DTD; (d) PES211; (e) 2FEC1LiBOB; and (f) 2FEC1LFO electrolytes. Cycling was done at 70°C at C/3:C/3 and 3.0-4.20 V.

To summarize the cycling performance of the different LMO/AG cells, the number of cycles achieved before reaching 80 % capacity retention was tabulated. Figure 5.4 shows the number of cycles to reach 80 % retention for all cells cycled at C/3:C/3 at different temperatures. At RT, PC-LMO and SC-LMO cells with

2VC1DTD or PES211 additives reached ~80 % retention after roughly 2250 cycles. PC-LMO2 cells had rapid capacity fade compared to PC-LMO (despite similar morphology and particle size) even at RT and none of the PC-LMO2 cells achieved more than 550 cycles before reaching 80 % capacity. The rapid failure of PC-LMO2 is attributed to the smaller Li excess, x, in $Li_{1+x}Mn_{2-x}O_4$ (see Table 5.1). By *decreasing* the Li excess in LMO materials, the specific capacity *increases* at the expense of cycle life[155,156]. Gao et al[156] and Schlueter et al[157] showed that increasing the Li excess suppresses the phase transitions in LMO materials cycled past 4.0 and 4.15 V vs Li/Li^{+}, which is consistent with trends in cycle stability shown in Figure 5.4.

Blending NMC622 with PC-LMO2 in a 25:75 weight ratio improved the capacity retention of PC-LMO2, but the blended cells were still far less competitive compared to PC-LMO and SC-LMO. The 2VC-LiFSI electrolyte appeared to be incompatible with LMO cells at RT as evident in the rapid capacity loss and ΔV growth in Figure A14b which could be due to some Li plating at RT. At 40 °C, the capacity retention was worse than RT as expected, but SC-LMO cells remained competitive especially with LiFSI salt and reached 80 % retention in 1000 cycles. Figure A.17 shows that SC-LMO cells had a ΔV growth of ~20-25 % at 80 % capacity for all electrolytes, apart from 2VC-LiFSI which had a 50 % increase in ΔV after 1000 cycles.

The SC-LMO material stood out with the best performance compared to the others. Generally, VC-containing electrolytes showed superior capacity retention

at all temperatures for the various LMO types here, with 2VC1DTD cells generally outperforming VC only. FEC-containing blends were less competitive. At temperatures greater than 40 °C, all LMO cells quickly fail and none of the cells tested at 55 or 70 °C could sustain 800 cycles before reaching 80 % capacity.
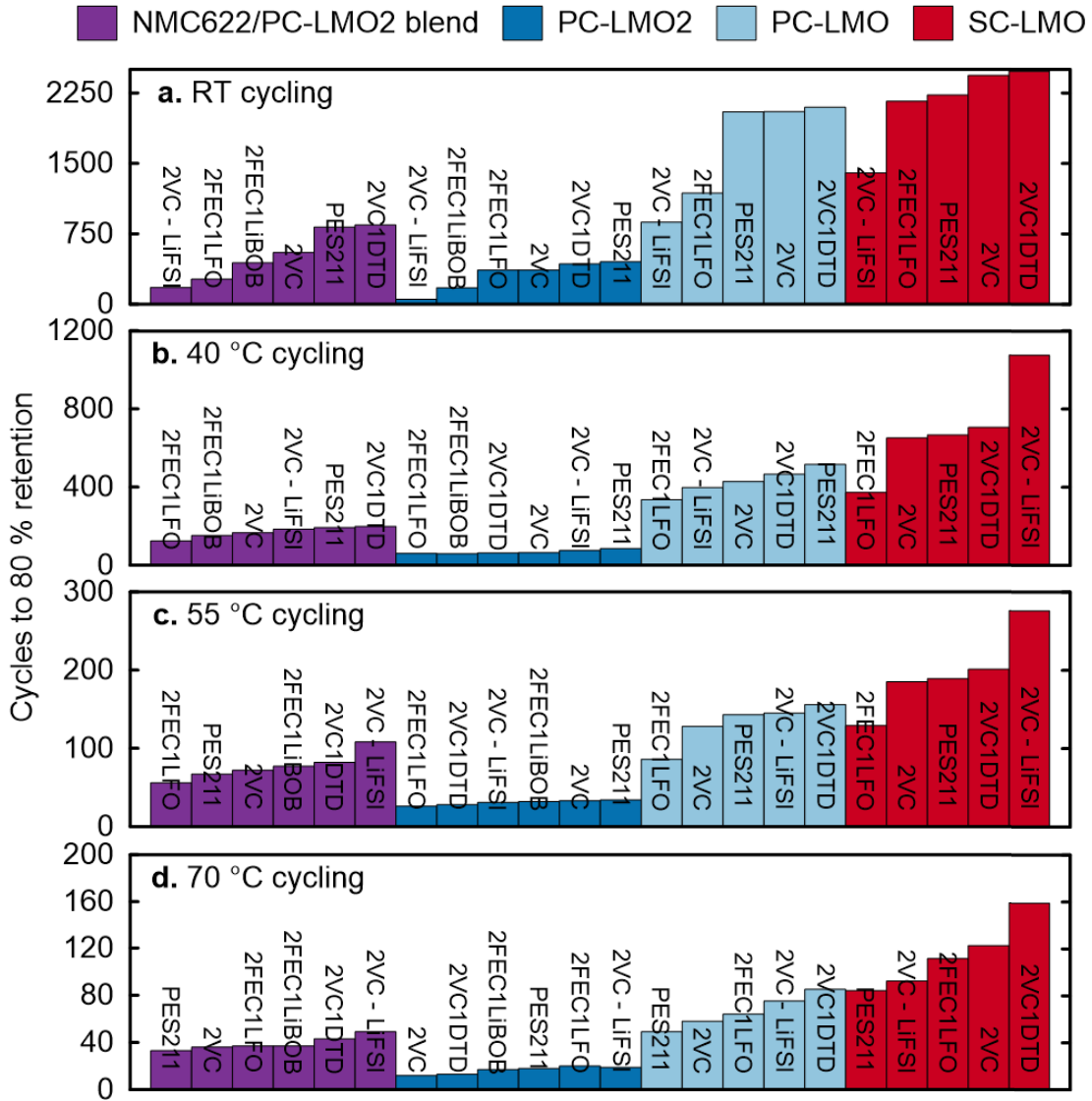
Figure 5.4. Number of cycles to reach 80 % capacity retention for the LMO/AG pouch cells tested in this work at (a) RT; (b) 40 °C; (c) 55 °C; and (d) 70 °C. All cycling was at C/3:C/3 and 3.0-4.20 V.

A notable observation in Figures 5.2-3 is that the extent of synergy between NMC and LMO in the blended cells depends on the choice of electrolyte. The synergy between NMC and LMO is well-known, but the impact of electrolytes on this synergy has not been explored. To quantify the extent of the synergy between NMC and LMO, we calculated a "synergy factor" value for NMC622/PC-LMO2 cells cycled at various temperatures with different electrolytes according to this simple ratio:

$$\text{Synergy factor} = \frac{0.75 * \text{PC-LMO2 cap. loss at cycle x}}{\text{NMC622/PC-LMO2 cap. loss at cycle x}} \qquad (5.1)$$

A synergy factor of 1 means that there is no synergy between NMC and LMO in the blended cells and that the capacity retention boost is simply due to having a smaller LMO active fraction in the positive electrode, while synergy factors >1 imply a favorable cross-talk between NMC and LMO in the blended cells. The synergy factor assumes that pure NMC622 would show no capacity fade over the charge-discharge cycling window.

Figure 5.5 shows the synergy factor versus cycling temperature for NMC622/PC-LMO2 cells with different electrolyte formulations. Generally, one can see that the synergy factor is more significant at higher temperatures except for 2FEC1LFO at 70 °C. Additionally, VC-containing electrolytes showed greater synergy than the other formulations. PES211 electrolyte showed the same synergy factor at 40-70 °C, but no synergy at RT when the cycling experiment was concluded. PES211 is known to cause high negative electrode charge transfer impedance which may have caused slight Li plating for the RT experiments[126].

Additionally, 2VC1DTD electrolyte had the largest synergy factor at 40-70 °C compared to the other LiPF$_6$-containing electrolytes. Comparing 2VC and 2VC-LiFSI electrolytes, we saw that LiFSI was beneficial at 55 °C, but was worse compared to LiPF$_6$ at 40 °C. However, LiFSI introduces safety issues at high voltages due to the corrosion of Al foil, which will be discussed later along with strategies to mitigate Al corrosion in LiFSI electrolytes. XRF analysis on the cells shown in Figure 5.4 can shed some light into the differences in degradation for each electrolyte, if any, and its impact of NMC-LMO synergy.
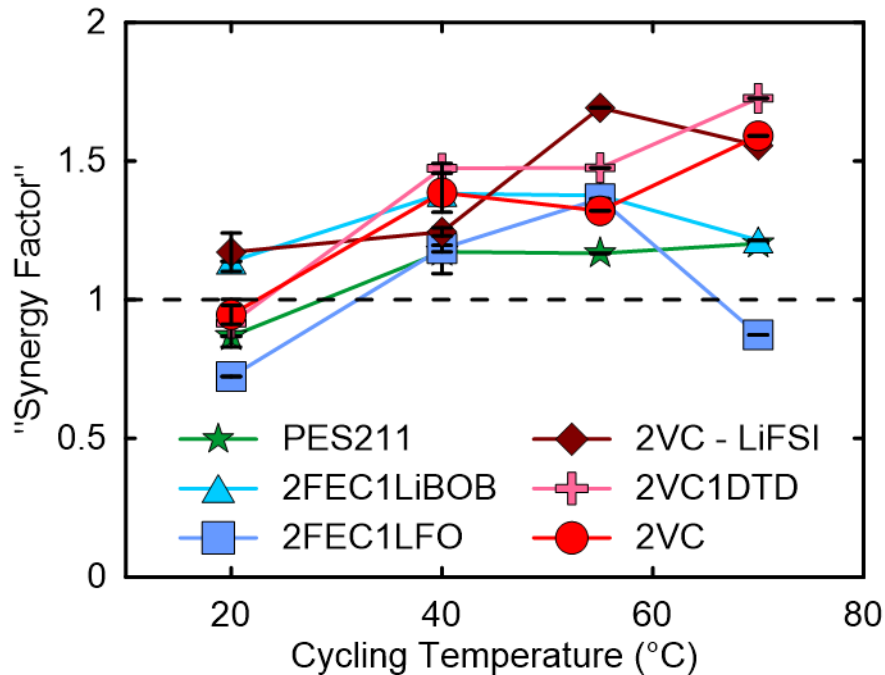
Figure 5.5. Synergy factor for NMC622/PC-LMO2 cells versus cycling temperature (°C) for different electrolyte blends.

5.3. XRF on Aged Negative Electrodes

In this section, XRF is used to study the impact of Li excess, particle size, temperature, electrolyte, and NMC blending on Mn deposition on the negative electrode. Figure 5.6 shows the Mn loading on the negative electrode (μg cm^{-2}) after 55 °C and 70 °C cycling for all LMO/AG cell types. The SC-LMO cell had smaller Mn loading on the negative electrode at 55 and 70 °C compared to PC-LMO regardless of the electrolyte. Additionally, the different electrolyte additives in LiPF$_6$-containing electrolytes did not significantly change the Mn loading in many cells despite a difference in capacity retention (see Figure 5.4). Moreover, PC-LMO2 cells had a nearly 2-fold increase in Mn loading compared to PC-LMO and blending NMC622 greatly reduced the amount of Mn on the negative electrode. Notably, using LiFSI instead of LiPF$_6$ increased the Mn loading for all cells except NMC622/PC-LMO2 and SC-LMO.
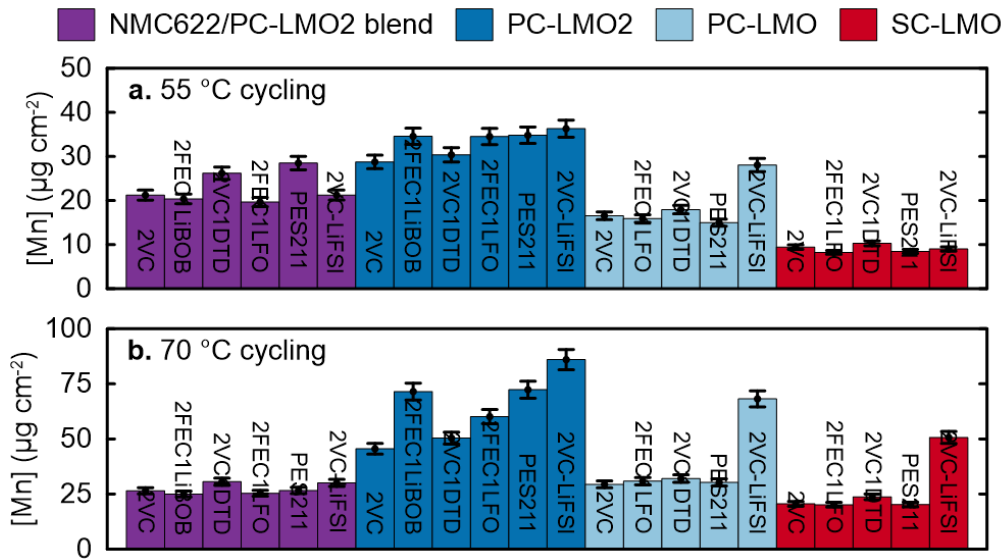
Figure 5.6. Mn loading deposited on the negative electrode (μg cm^{-2}) for LMO/AG pouch cells cycled at (a) 55 and (b) 70 °C with different electrolyte blends.

XRF was also performed on LMO/AG cells cycled at 40 °C. One of each pair cell at 40 °C was taken off cycling earlier, when possible, to examine the time-dependency of Mn deposition. Figure 5.7 shows the Mn loading versus cycle number after cycling at 40 °C with different electrolytes.
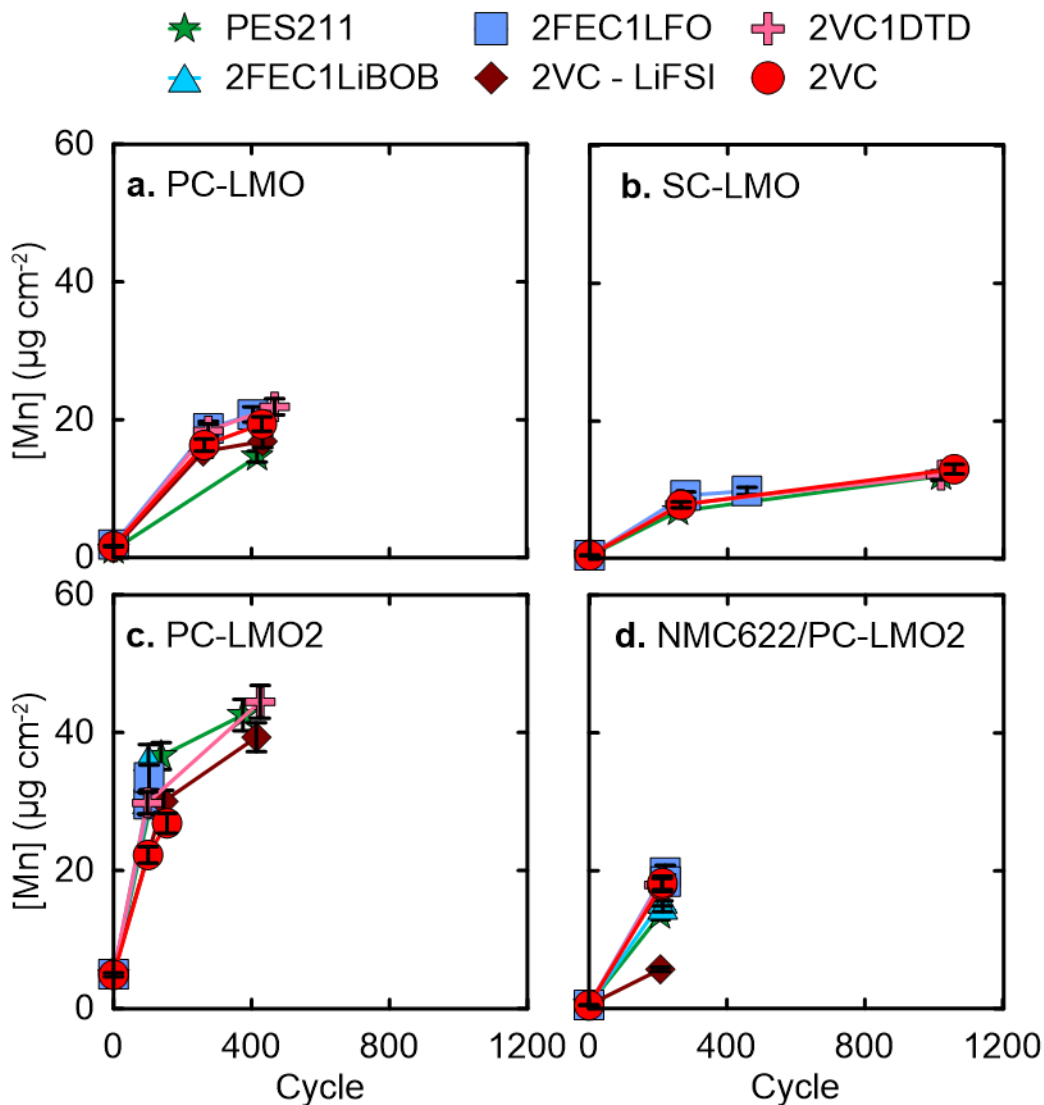
Figure 5.7. Mn loading deposited on the negative electrode (μg cm^{-2}) versus cycle number for (a) PC-LMO; (b) SC-LMO; (c) PC-LMO2; and NMC622/PC-LMO2 pouch cells cycled at 40 °C with different electrolyte blends.

In general, most of the Mn deposition occurs during the early cycles of the cell. The Mn loading for all SC-LMO cells increased from ~0.5 μg cm^{-2} to 7-10 μg cm^{-2} between the formation cycle (cycle 0) and the 300th cycle, while Mn loading increased only by an additional ~3 μg cm^{-2} between cycles 300 and 1000. Similar trends can be seen for PC-LMO and PC-LMO2 where the bulk of Mn deposition occurred during the early cycles (NMC622/PC-LMO2 pairs cells stopped cycling at the same time). In Figure 5.7 we see that each LMO/AG cell type had a very similar Mn loading regardless of the electrolyte used, despite differences in capacity retention as shown in Figure 5.4. While it may seem odd that some Mn loadings for 40 °C cells are similar to, or greater than, some of the equivalent 55 °C cells in Figure 5.6, it is important to note that the 40 °C cells cycled for much longer times than the 55 °C ones (Figure 5.4).

Figure 5.8 shows the Mn loading versus capacity loss and cycle number for LMO/AG cells after cycling at 40, 55, and 70 °C. There could be some correlation between capacity loss and Mn loading on the negative electrode in Figure 5.9, but the Mn loading for each cell type is clustered despite some differences in capacity loss within each cell type (see NMC622/PC-LMO2, for example). Therefore, it is difficult to be establish a strong correlation between capacity loss and Mn dissolution. Looking at Mn loading versus cycle number, one can also see no correlation, where each group of LMO cells had a similar Mn loading despite differences in cycle number (and capacity loss). This is consistent with Figure 5.7 where the bulk of Mn deposition appear to occur during early stages of cell life.
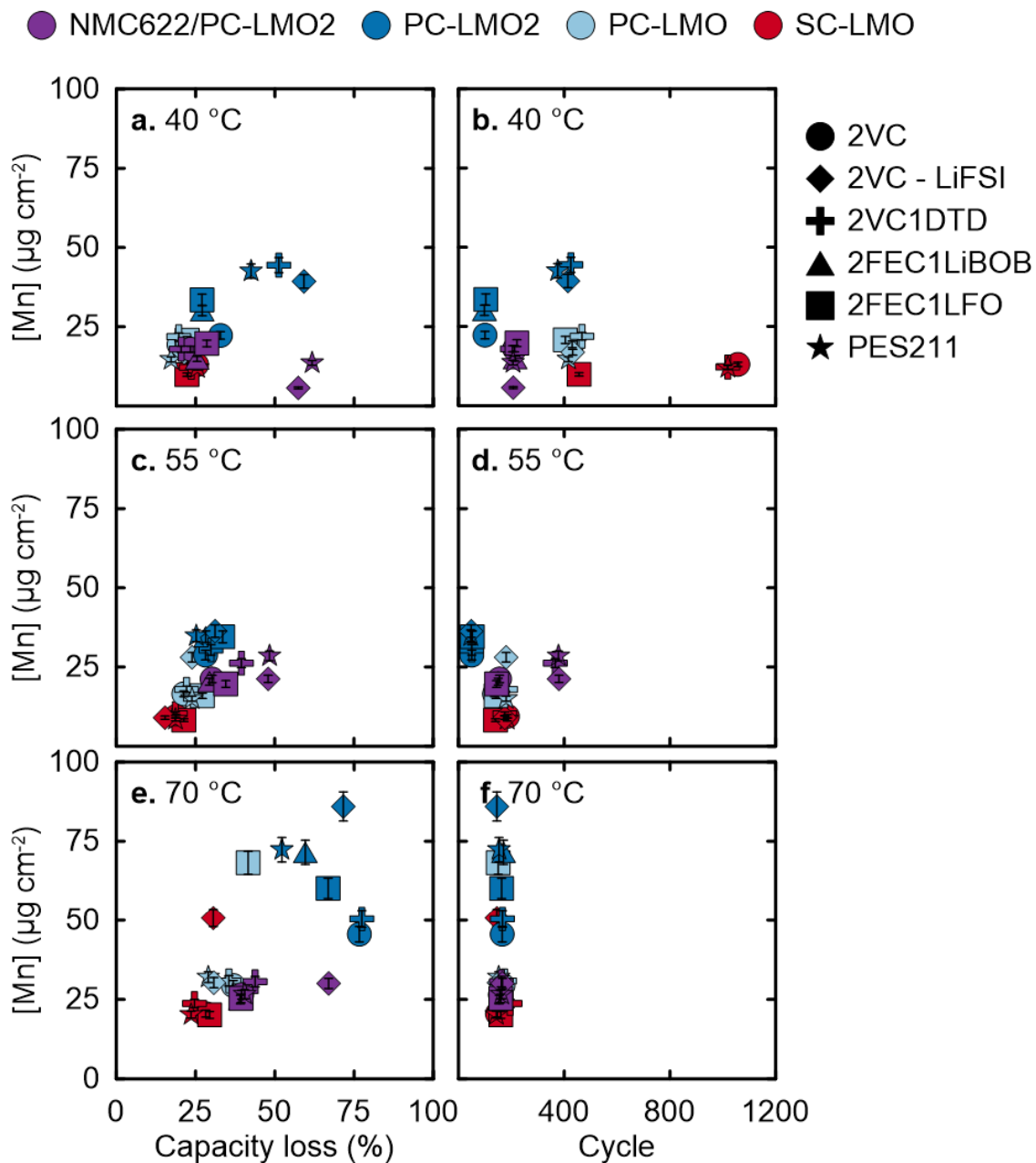
Figure 5.8. Mn loading on the negative electrode versus capacity loss (%) or cycle number for LMO/AG cells cycled with different electrolytes at (a-b) 40 °C; (c-d) 55 °C; and (e-f) 70 °C.

This section shows that Mn deposition is not linear with cycle number and that it plateaus as the cells ages. The rate of Mn dissolution and deposition also appears to depend on properties of the positive electrode (i.e., Li excess, particle size, NMC blending) and less on the electrolyte choice, despite differences in capacity retention for the electrolyte blends tested here. One can see that a large Li excess (see SC-LMO and PC-LMO) results in decreased Mn deposition. As the positive electrode loses more Mn, the LMO particle surface will become Mn-deficient (i.e., greater Li excess) thus hindering further Mn dissolution[143,153], consistent with the observations in Figure 5.8. It is unclear at what cycle number does Mn dissolution plateaus, so a systematic study of Mn loadings as a function of cycle number is necessary and will be discussed later.

5.4. UHPC and DCA Results

To gain some insight into the cell failure mechanisms in LMO/AG, UHPC cycling and DCA were carried out. Figure 5.9 shows the CIE/hr, fractional fade, and fractional slippage per hour for all LMO/AG cells. SC-LMO and PC-LMO cells had a similar CIE, fade, and slippage rates, and the choice of electrolyte had a significant impact here. For example, all VC-containing electrolytes had a lower CIE compared to 2FEC1LFO and PES211 for both cell types. And while the use of LiFSI reduced the fade rate in SC-LMO and PC-LMO, it resulted in a greater slippage compared to $LiPF_6$. Additionally, PC-LMO2 cells had the highest CIE and fade rates, with 2FEC1LFO having the worst performance of all electrolytes. However, NMC622/PC-LMO2 cells had a remarkably improved CIE and fade relative to PC-LMO2, highlighting the importance of NMC-blended positive

electrodes in improving the lifetime of LMO cells. PC-LMO2 and NMC622/PC-LMO2 cells had a negative slippage rate due to the *decreasing* charge endpoint capacity. Typically, charge endpoint capacity increases due to some electrolyte oxidation reactions on charge as discussed in Chapter 1, so the observed decrease in charge endpoint capacity suggests that a more severe capacity fade mode is taking place. While SC-LMO and PC-LMO cells had the lowest CIE/hr, the values shown in Figure 5.9 are still quite high compared to an NMC/Graphite cell where CIE/hr can be nearly half of that measured for the best LMO cells here.
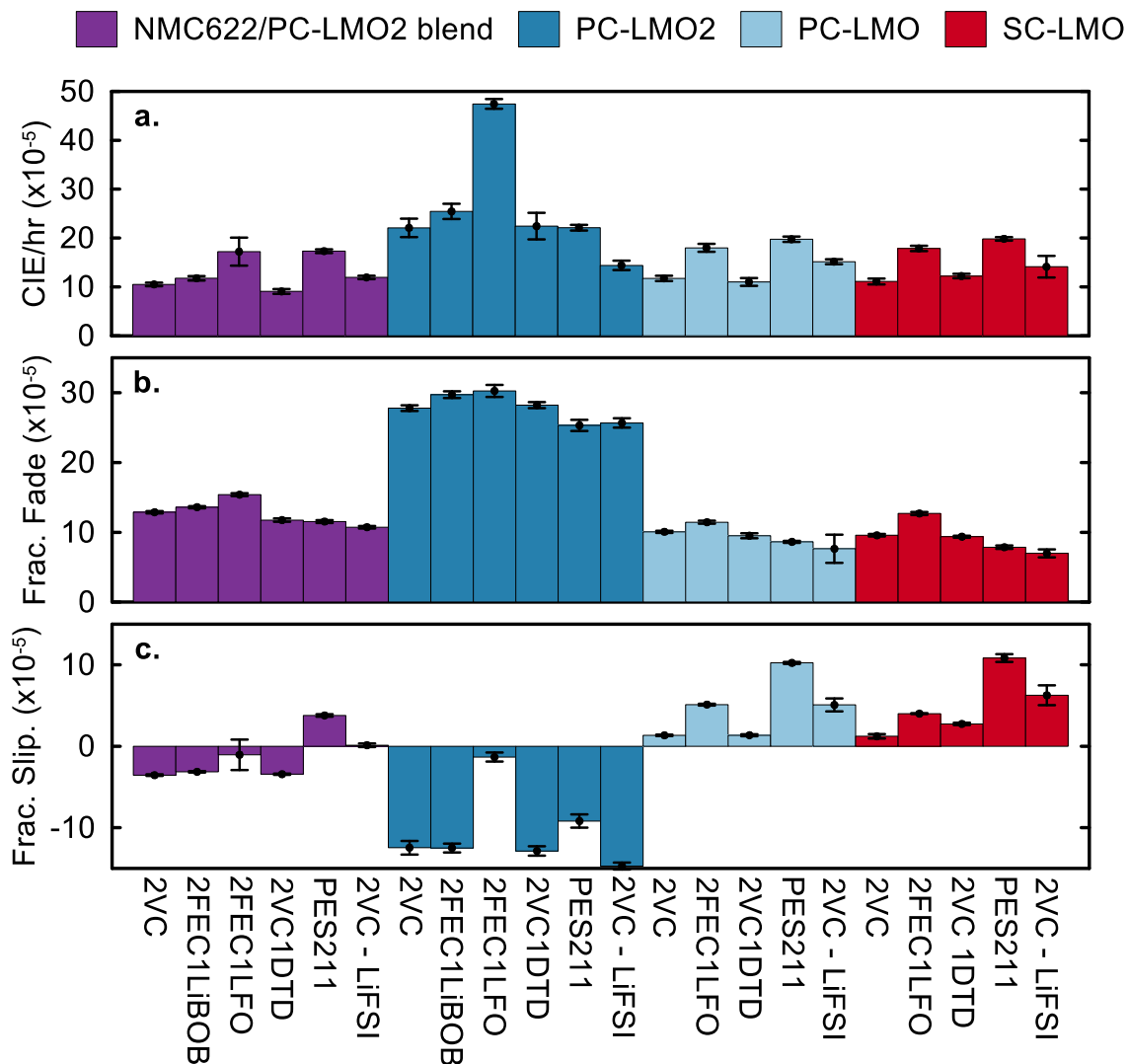
Figure 5.9. (a) CIE per hour; (b) fractional fade per hour; and (c) fractional slippage per hour for LMO/AG pouch cells with different electrolyte blends. All UHPC cycling was at 40 °C at C/20:C/20 and 3.0-4.20 V.

The decreasing charge endpoint capacity seen for PC-LMO2 and the blended cells in Figure 5.9 can be attributed to severe decrease in positive electrode active mass with each cycle. To examine the change in positive electrode mass before and after cycling, DCA was performed on 2VC1DTD and 2FEC1LFO cells from Figure 5.9. These two electrolytes were chosen since

2VC1DTD generally performed very well, while 2FEC1LFO performed poorly in many cases (see Figures 5.4).

Figure 5.10 shows full cell, positive electrode, and negative electrode voltage versus capacity curves from DCA on 2VC1DTD cells. Figure A.22 shows the measured and calculated dV/dQ curves for cells with 2VC1DTD electrolyte. The black lines show the voltage curves for cycle 1 and the colored lines show the voltage curves for cycle 20. In all cells, some amount of shift loss (i.e., Li inventory loss) can be seen after 20 cycles. Shift loss here is taken as the difference between the relative electrode slippage at cycle 20 and cycle 1. In addition to shift loss, some cells show shrinking of the positive and negative electrode voltage curves after 20 cycles which represent electrode mass loss. All cells in Figure 5.10 show shrinking of the positive electrode voltage curve as expected since these cells suffer from Mn dissolution, which can be very severe for PC-LMO2 as evident in Figure 5.10c. In addition, PC-LMO2 and NMC622/PC-LMO2 cells in Figure 5.10c-d show some negative electrode mass loss. For competitive NMC532 cells with the same graphite electrode as the cells in Figure 5.10, negative electrode mass loss was not seen after 1 year of cycling at 40 °C and 4.30 V UCV[17], so this might be a consequence of Mn deposition which will be discussed below.
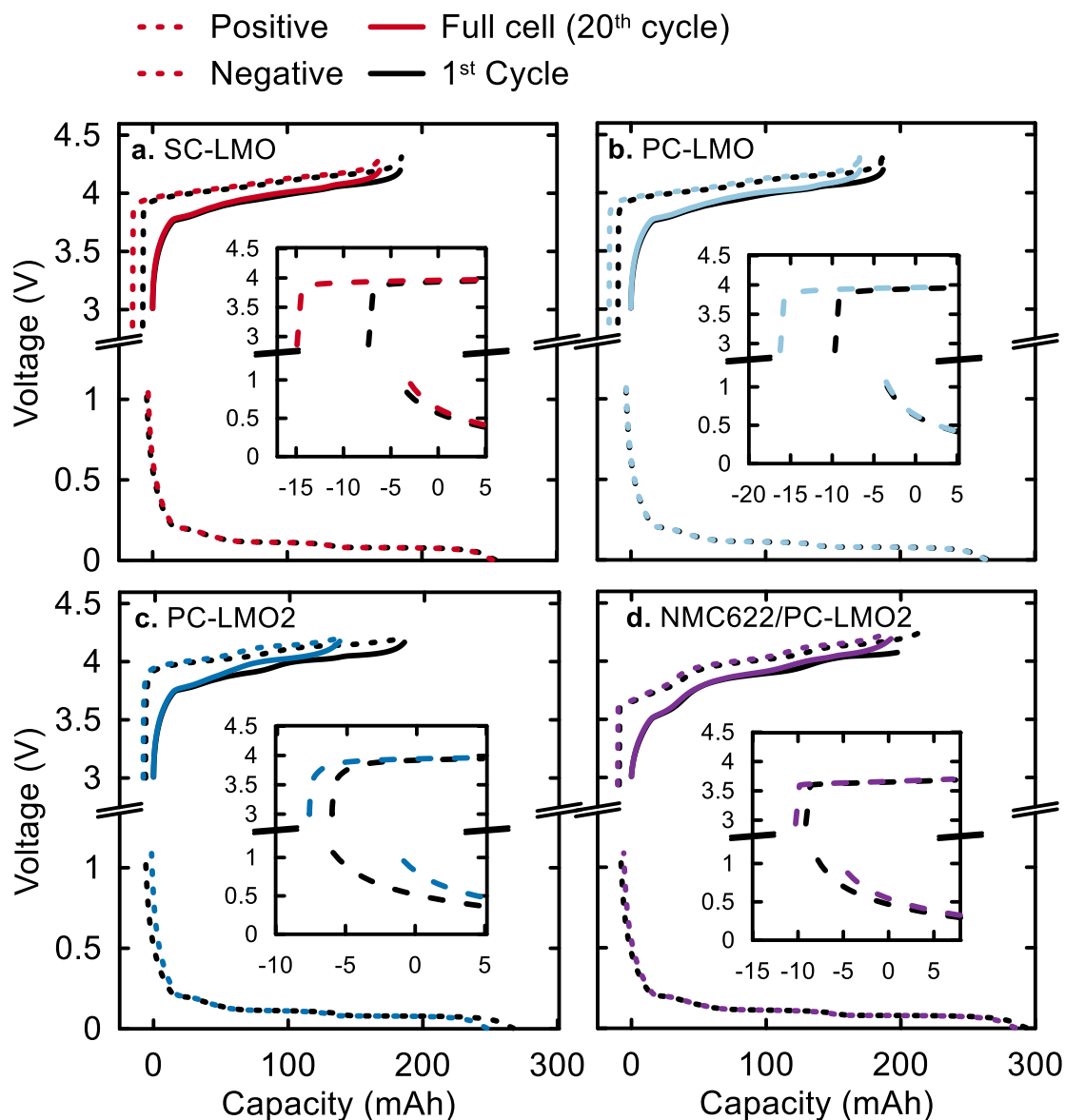
Figure 5.10. Full cell, positive electrode, and negative electrode voltage (V) versus capacity (mAh) profiles obtained from dV/dQ fitting for (a) SC-LMO; (b) PC-LMO; (c) PC-LMO2; and (d) NMC622/PC-LMO2 cells. Results for the 1st cycle are shown in black in all panels and 20th cycle is shown in color, and the full cell voltage curve is shown in solid lines. Cycling was done at 40 °C with C/20:C/20 and 3.0-4.20 V with 2VC1DTD electrolyte. Inset shows the difference in relative electrode slippage between cycle 1 and 20.

To understand the changes seen in the voltage curves in Figure 5.10, one must realize how the positive and negative electrode voltages curves are transformed in DCA due to electrode mass loss and Li inventory loss. Figure 5.11 shows calculated voltage versus capacity curves for a full cell, positive electrode and a negative electrode before and after capacity loss in dashed and solid lines, respectively. In the event of positive mass loss only, the positive electrode voltage curve will shrink as shown in Figures 5.11a-b. If the mass loss occurs at low SOC, the positive electrode will attain less capacity on charge, and the opposite will happen if the positive mass loss occurs at high SOC. In $Li_{1+x}Mn_{2-x}O_4$, the positive electrode will have more Mn^{3+} at low SOCs. Previous reports suggest that Mn^{3+} is likely to undergo disproportionation into Mn^{2+} (which is soluble in organic carbonates) and Mn^{4+}, resulting in Mn dissolution[143]. Therefore, positive mass loss at low SOC is not unexpected.

The full cell in both positive electrode mass loss scenarios can encounter Li inventory loss as well, which will shift the negative electrode along the x-axis as shown in Figures 5.11c-d. This can yield full cells where the cell capacity is limited by that of the negative electrode. In Figure 5.11c, the total capacity loss can be described as the sum of positive mass loss (see shrinking of the positive in Figure 5.11c) and Li inventory loss (see shift of the negative in Figure 5.11c); while the capacity loss for the cell in Figure 5.11d is just due Li inventory loss, even though positive mass loss took place. This was observed by Gauthier et al in NMC622/NG cells[43]. In Figure 5.10, we see that the voltage curves at cycle 20 for all cells closely match the calculated scenario in Figure 5.11c, so capacity loss can

164

be taken as the sum of the positive mass loss and shift loss for these cells. It is

important to also note that if negative electrode mass loss occurs at high SOC (or

non-zero SOC), it will have the same effect on the negative electrode voltage curve

as shift loss so it would be indistinguishable in DCA, but mass loss at low SOC will

decrease the negative electrode capacity on charge (similar to the positive

electrode in Figure 5.11a).
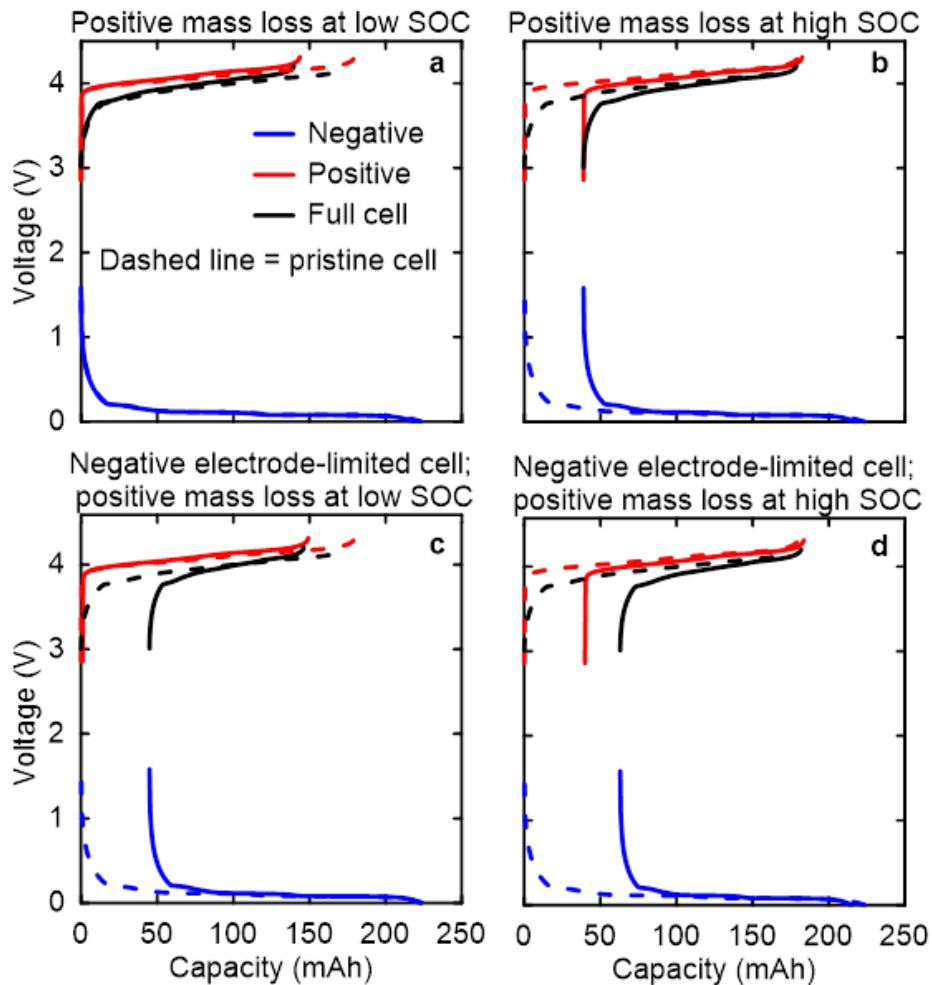
Figure 5.11. Calculated voltage versus capacity curves showing positive electrode mass loss at (a) low SOC and (b) high SOC, and (c-d) the impact of Li inventory loss in both scenarios.

Figure 5.12 shows capacity loss from positive electrode mass loss (mAh), negative electrode mass loss (%), shift loss (mAh), and sum of shift loss and positive electrode capacity loss versus the measured capacity loss during UHPC cycling of cells with 2FEC1LFO or 2VC1DTD electrolytes. Error bars represent the range of two pair cells. Figure 5.12 shows that positive electrode mass loss in SC-LMO contributed to ~5-6 mAh of capacity loss, and about ~6-7 mAh for PC-LMO. Cells with PC-LMO2 and NMC622/PC-LMO2 lost a staggering 35-45 mAh and 22-28 mAh of positive electrode capacity, respectively. In addition to positive mass loss, PC-LMO2-containing cells also showed negative electrode mass loss which was 6-8 % for PC-LMO2 and ~4 % for NMC622/PC-LMO2. A larger portion of the capacity loss in SC-LMO and PC-LMO cells came from shift loss (8-10 mAh), while 5-7 mAh came from positive mass loss. On the other hand, capacity loss in PC-LMO2-containing cells was dominated by positive mass loss. In these cells, shift loss was on the order of 8-12 mAh for 2FEC1LFO and 2-4 mAh for 2VC1DTD, where blending NMC622 greatly reduced shift loss. The NMC622/PC-LMO2 cells had less shift loss compared to SC-LMO cells, but they had greater capacity loss overall due to the contributions of positive mass loss. Figure 5.12 suggests that when a poor LMO material such as PC-LMO2 is used, capacity loss is dominated by degradation of the positive electrode, while Li inventory loss dominates the capacity loss in cells with more stable materials such as SC-LMO or PC-LMO. Finally, Figures 5.12g-h show a good agreement between the measured and calculated capacity loss from DCA.
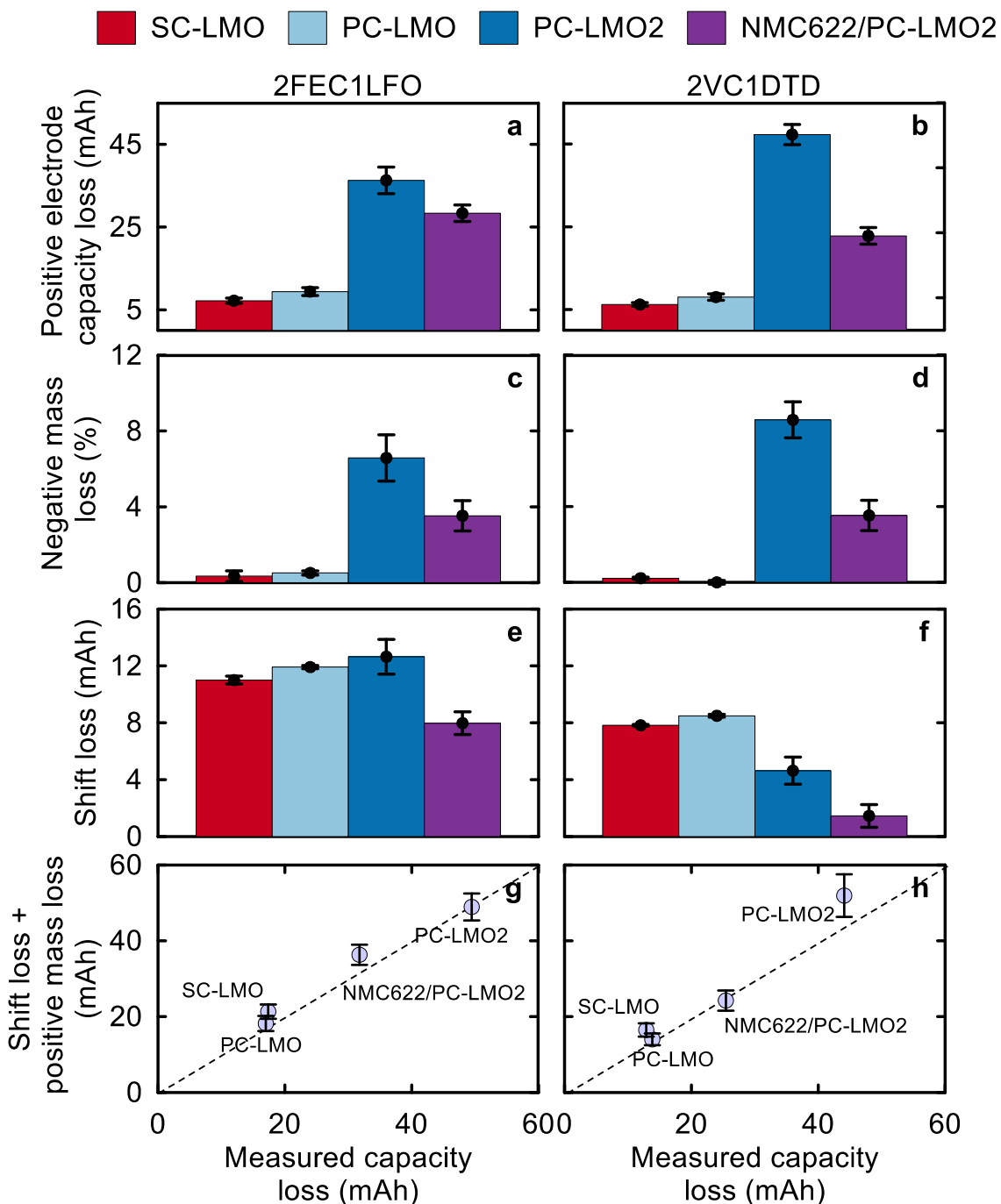
Figure 5.12. DCA summary for LMO/AG pouch cells showing (a-b) positive electrode capacity loss (mAh); (c-d) negative mass loss (%); (e-f) shift loss (mAh); and (g-h) the sum of shift loss and positive mass loss (mAh) versus measured capacity loss (mAh). Cycling was done at 40 °C and C/20:C/20 between 3.0-4.20 V with 2FEC1LFO or 2VC1DTD electrolyte.

Negative electrode mass loss is usually not seen in NMC/Graphite cells under typical operating conditions, but it was clear in PC-LMO2-containing cells. Electrode mass loss is attributed to active materials that are no longer electrochemically active, which can occur when particles are disconnected from the current collector due to substantial volume expansion and/or cracking. However, the Kaijin AML400 negative electrode material in this work is known to have remarkable performance and did not show any negative electrode mass loss after a year of cycling with a NMC532 positive electrode and 2VC1DTD electrolyte[17]. Therefore, the observed negative electrode mass loss must be caused by reactions initiated by the degradation of the LMO positive electrode.

All LMO/AG cells in this work have substantial Mn loading on the negative electrode, especially the PC-LMO2 cells. Numerous reports suggest that Mn on the negative electrode results in SEI thickening, increase in parasitic reactions, and/or SEI decomposition[54]. Zhou et al developed a mathematical model to study SEI formation dynamics under various conditions, one being Mn dissolution[158]. In their study, Zhou et al demonstrated that Mn dissolution gradually reduced the negative electrode porosity with cycling due to the ability of Mn to promote SEI formation and lower the cell's capacity[158]. In addition, Ochida et al showed using cyclic voltammetry with a highly ordered pyrolytic graphite working electrode that the Li intercalation/de-intercalation currents substantially decrease with cycle number when Mn ions are present in the electrolyte solution[159]. This is consistent with our observation in Figure 5.12 of increased negative electrode active mass loss for cells with substantial positive mass loss and more Mn deposition as shown

previously. While the role of additives on Mn dissolution is not clear yet, we can say with certainty that Mn deposition on the negative electrode can contribute to negative electrode active mass loss.

5.5.   Chemical and Physical Changes as a Function of Cycle Number

In order to probe the plateau in Mn dissolution for LMO/AG, we cycled cells with 2VC1DTD electrolyte at 70 °C for 20, 40, 80, and 100 cycles at C/3:C/3 and 3.0-4.20 V. After cycling, NMR and XRF were carried out to quantify salt concentration changes and the Mn loading on the negative electrode. These cells had an additional 1 mL of 2VC1DTD electrolyte (total of 2 mL) for ease of electrolyte extraction. Figure 5.13 shows capacity loss (%), ΔV growth (%), Mn loading on the negative electrode (μg cm^{-2}), and [PF$_6^-$] (mol kg^{-1}) versus cycle number for all LMO/AG cells cycled at 70 °C. Figure 5.13a summarizes the impact of positive electrode morphology and composition on capacity loss, which was already discussed above.

Figure 5.13c shows that the bulk of Mn deposition occurs between cycle 0 (formation, 40 °C) and cycle 25. PC-LMO and NMC622/PC-LMO2 cells show a plateau in Mn loading around ~30 μg cm^{-2} and 20 μg cm^{-2}, respectively, while SC-LMO and PC-LMO2 show a slow increase in Mn loading past the initial jump at cycle 25. The synergy between NMC622 and LMO is incredible here, where the Mn loading in the NMC622/PC-LMO2 was almost an order of magnitude less than PC-LMO2 alone at cycle 25 (~7 vs 50 μg cm^{-2}), despite the positive electrode being 75 % PC-LMO2 in the blended case. This phenomenal ability of NMC622 to lower

Mn deposition might explain why some NMC cells show very minimal transition metal dissolution and deposition after months or even years of cycling[56,109,110]. The non-linear trend relationship between Mn dissolution and cycle number is consistent with the formation a Mn-deficient surface as x in $Li_{1+x}Mn_{2-x}O_4$ increases, which slows further Mn dissolution during cycling[153].

Looking at salt consumption, we see a dramatic decrease in [PF_6^-] after 100 cycles for all cell types (Figure 5.13d). PC-LMO2 and NMC622/PC-LMO2 showed an initial increase in [PF_6^-] after formation (cycle 0) due to solvent consumption, while SC-LMO and PC-LMO showed an initial [PF_6^-] similar to the initial concentration in the electrolyte as measured by NMR (dashed line). SC-LMO and PC-LMO could have still lost both salt and solvent during formation, but the overall [PF_6^-] was similar to the initial as-prepared electrolyte. After 100 cycles, the final [PF_6^-] was 0.9-1.1 m which is significantly less than the initial ~1.33 m in the fresh electrolyte. This rapid change in salt concentration indicates an extremely high rate of parasitic reactions in LMO/AG cells cycled at 70 °C.
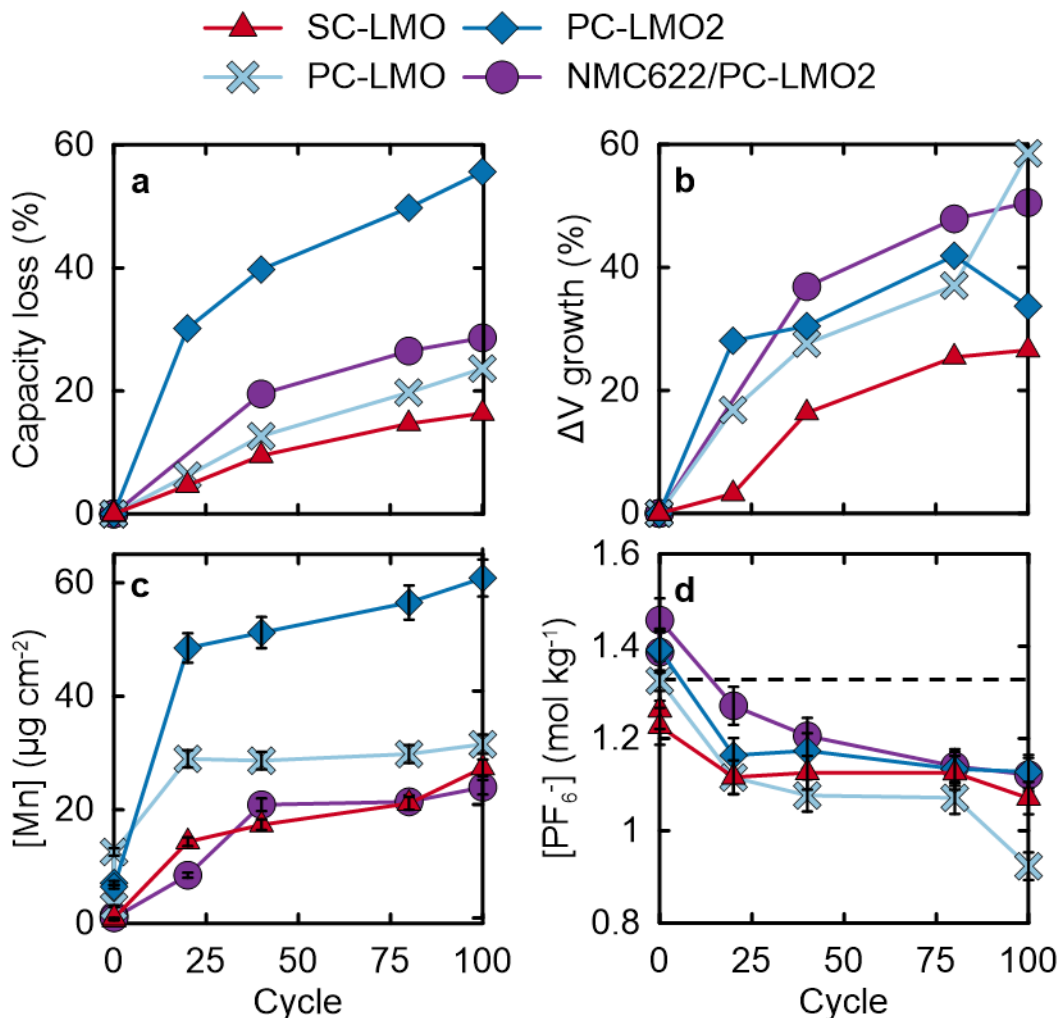
Figure 5.13. (a) capacity loss (%); (b) ΔV growth (%); (c) Mn on the negative electrode (μg cm^{-2}); (d) [PF_6^-] in electrolyte (mol kg^{-1}) as a function of cycle number for LMO/AG pouch cells cycled at 70 °C. The dashed lines represent the initial salt concentration in the electrolyte as measured by NMR. All cycling was at C/3:C/3 and 3.0-4.20 V. Cycle 0 is the C/20:C/20 formation cycle at 40 °C.

Cells in Figure 5.13 did a formation cycle (i.e., cycle 0) at 40 °C so it is unclear if Mn dissolution happens mostly during formation, then spikes during early 70 °C cycles. To examine this, XRF was done on LMO/AG cells at different stages during the initial formation charge, from 1.5 V to 4.20 V. Figure 5.14 shows the Mn loading on the negative electrode and capacity attained during charge versus

formation UCV for SC-LMO and PC-LMO2 with 2VC1DTD electrolyte formed at 40 °C or 70 °C. These two cell types were chosen because SC-LMO had the least amount of Mn on the negative electrode, while PC-LMO2 had severe Mn deposition as shown above. The data point around ~300 mV is for cells that underwent XRF analysis after filling with electrolyte and resting at room temperature for 12 hours at OCV, and the 1.5 V data points are for cells that underwent XRF after a 24 hour hold at 1.5 V (i.e., jellyroll wetting step) prior to disassembly for XRF.

Figure 5.14 shows that Mn was not detected on the negative electrode until 3.20 V, which is near the onset of SEI formation in typical Li-ion cells. At 3.20 V vs. graphite, there is very little Li intercalation in the graphite (see Figures 5.14c-d), but electrolyte reduction and SEI formation occurs. With increasing UCV, the Mn loading on the negative did not increase significantly for PC-LMO2 and SC-LMO cells at 40 °C, and the bulk of Mn deposition during the first formation charge was around 3.20 V. At 70 °C, we see a different story where Mn loading on the negative electrode continuously increases with formation UCV rather than remaining constant after 3.20 V as was seen at 40 °C. For PC-LMO2 and SC-LMO, the maximum Mn loading at 4.20 V and 70 °C is ~17 and 5 μg cm^{-2}. Surprisingly, Figure 5.14b shows a significant amount of Mn was found on the negative electrode of SC-LMO and PC-LMO2 after wetting at 70 °C (i.e., 24-hour hold at 1.5 V), which highlights the poor high temperature stability of LMO materials in contact with electrolyte.
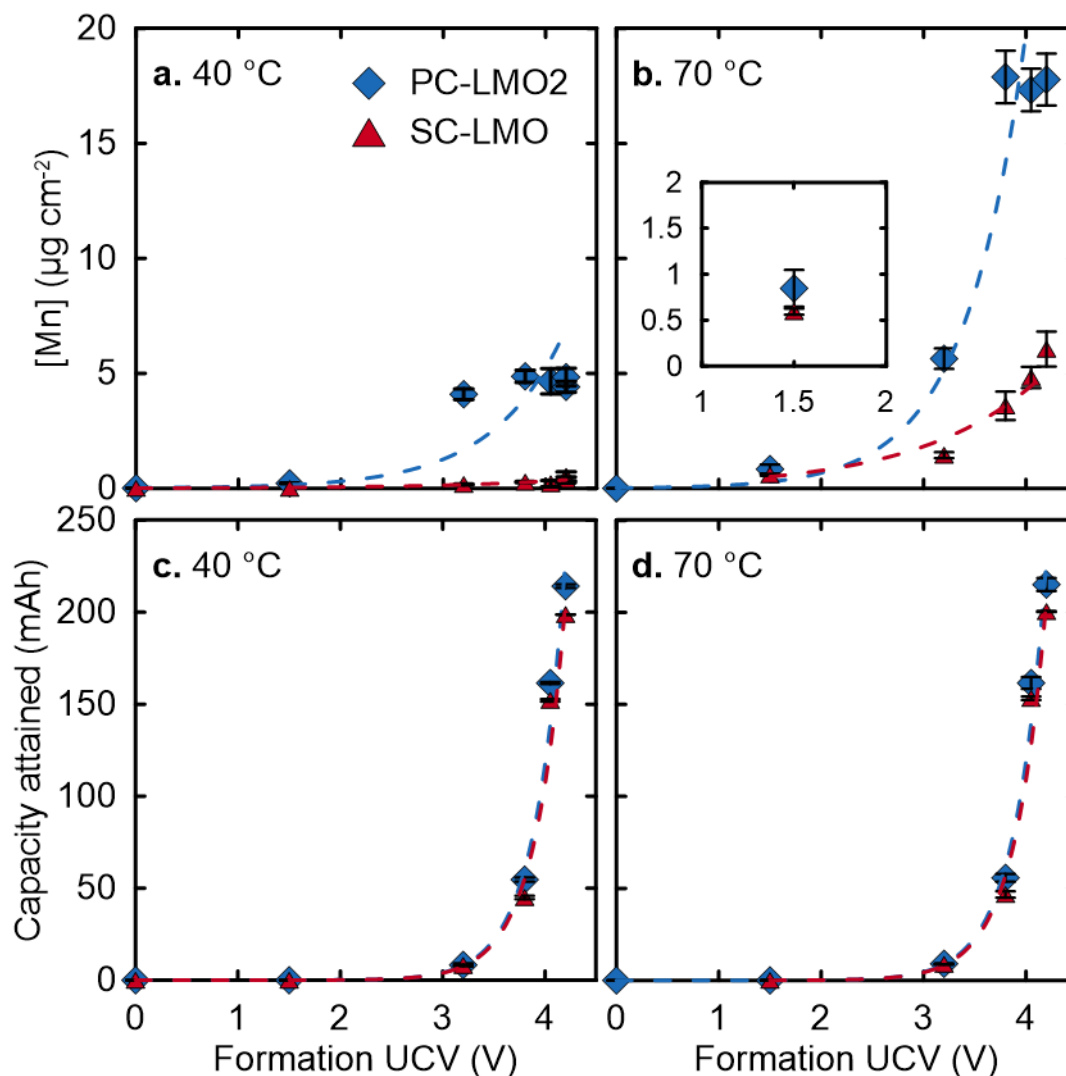
Figure 5.14. (a-b) Mn loading on the negative electrode (µg cm^{-2}); and (c-d) capacity attained on charge as a function of formation UCV (V) for SC-LMO and PC-LMO2 pouch cells formed at 40 and 70 °C.

In all cases, a significant amount of Mn was found after formation, and the Mn loading depended on the LMO composition and morphology as discussed above. PC-LMO2 cells had around ~5 µg cm^{-2} of Mn on the negative electrode after formation at 40 °C alone (for reference, NMC and LFP cells after extensive long-term cycling and/or storage would typically have < 5 µg cm^{-2} of TM

deposition[55,56,109,110]). After 70 °C formation, PC-LMO2 cells had ~17 μg cm^{-2} of Mn which is around a third of the total Mn loading seen in the same cells after 100 cycles at 70 °C.

Figure 5.14 proposes an interesting question: if one can charge and hold the cell at 3.0 V to reduce film-forming additives and solvent (i.e., SEI formation) without any lithium deintercalation from the positive electrode, can we generate a robust, Mn-poor SEI layer that can slow down further Mn dissolution? If a cell can be held for a long period of time (i.e., 24 hours) during formation at 3.0 V vs. graphite, SEI formation can take place since EC and film-forming additive such as VC are reduced at lower potentials. The 3.0 V hold can be followed by a formation cycle at lower temperature where further Mn dissolution will be slow, thus creating a well-passivated initial SEI layer with smaller Mn loadings, if any. Testing this hypothesis will shed light on the role of Mn on SEI formation and capacity retention and requires numerous additional experiments.

5.6.   Electrode/Electrolyte Reactivity

We demonstrated in the previous sections that parasitic reactions in LMO/AG cells result in salt consumption as well as Mn dissolution and deposition on the negative electrode. In this section, we probe the reactivity of the positive and negative electrodes with electrolyte to understand the contribution of each electrode to parasitic reactions using electrode pouch bags (see Section 2.12). LMO/AG pouch cells underwent a formation cycle at 40 °C and were charged to 4.20 V before being dissembled in an Ar-filled glovebox to harvest the positive and

174

negative electrodes. First, we measured the parasitic heat flow resulting from reactions between the lithiated graphite and the electrolyte using IMC.

Figure 5.15 shows the parasitic heat flow (μW/g$_{graphite}$) versus time for lithiated graphite electrode pouch bags made from different LMO/AG pouch cells with 2VC electrolyte after formation, and the heat flow value after 120 hours versus Mn loading on the negative electrode after one formation cycle. The negative electrode pouch bags were stored for 1 month at 60 °C prior to the calorimetry test to monitor gas production. Figure 5.15a shows that PC-LMO2 negative electrode had the largest parasitic heat flow of ~17.5 μW/g$_{graphite}$, followed by PC-LMO (~13 μW/g$_{graphite}$), and NMC622/PC-LMO2 and SC-LMO (~11-12 μW/g$_{graphite}$). This result is striking since all lithiated graphite pouch bags shown in Figure 5.15a have an identical Kaijin AML400 artificial graphite electrode, with the choice of positive electrode (and Mn dissolution) being the only difference in these cells.
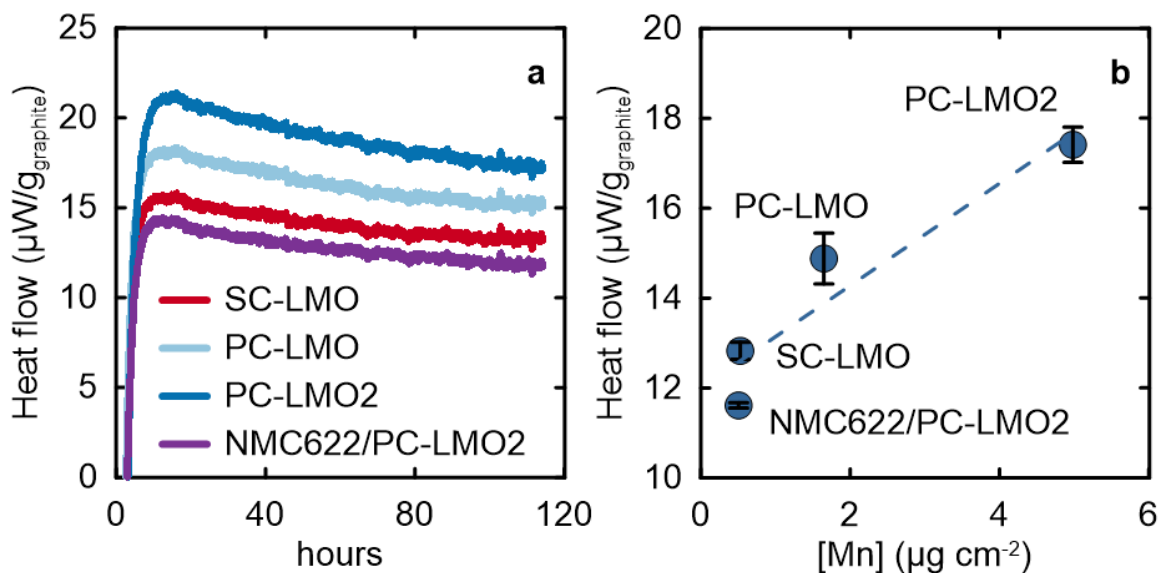
Figure 5.15. (a) heat flow (μW/g$_{graphite}$) versus time (hours) for negative electrode pouch bags; (b) heat flow (μW/g$_{graphite}$) versus Mn loading on the negative electrode (μg cm^{-2}) of different LMO/AG cell types.

We also see a strong correlation between negative electrode heat flow and Mn loading in Figure 5.15b. Negative electrodes from SC-LMO and NMC622/PC-LMO2 cells had the smallest heat flow and Mn loading, followed by PC-LMO and PC-LMO2. The correlation between heat flow and Mn loading on the negative electrode suggests that the Mn deposition is responsible for accelerating the parasitic heat flow from reactions between negative electrode and the electrolyte. Interestingly, negative electrodes from SC-LMO and NMC622/PC-LMO2 showed differences in heat flow despite having the same Mn loading after formation. This suggests that the *accelerated* SEI growth due to Mn deposition may only take place after a certain Mn threshold, however, this requires additional experiments to verify.

176

The volume of gas in the pouch bags was monitored periodically over 60 days of storage at 60 °C. Figure 5.16 shows gas volume (mL) versus storage time at 60 °C. The lithiated graphite generated a lot of gas as expected based on previous work[78,82]. The differences in negative electrode gas volume in Figure 5.16a are consistent with the Mn loadings and the parasitic heat flow values in Figure 5.15. The graphite electrode from the PC-LMO2 cells had the largest gas volume (0.85 mL) followed by PC-LMO (0.4 mL), NMC622/PC-LMO2 (0.3 mL), and SC-LMO (0.2 mL). Two of the delithiated LMO electrodes generated a considerable amount of gas suggesting that the delithiated cathode can be reactive in this case as well, unlike previous reports using NMC or LFP cells[78,82]. The PC-LMO2 positive electrode generated about 0.6 mL of gas after 60 days, and the addition of NMC622 remarkably decreased the gas volume to 0.2 mL over the same time. SC-LMO and PC-LMO, however, had no significant gas generation after 60 days at 60 °C. Once again, we see that LMO materials with large Li excess are less reactive and therefore have better lifetime compared to the higher specific capacity materials with lower Li excess.
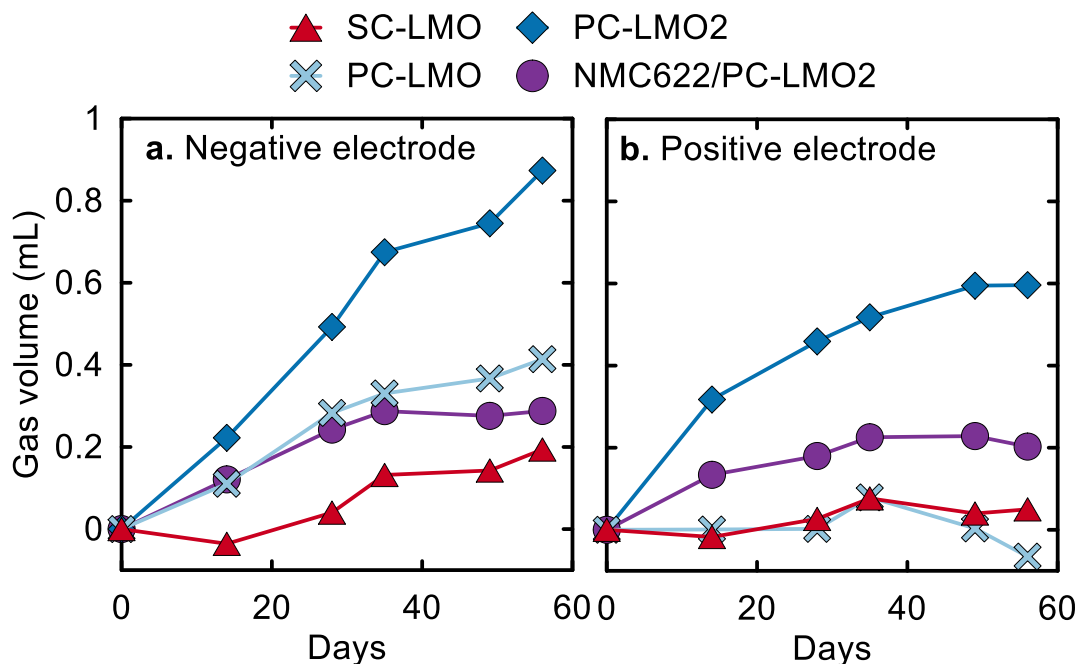
Figure 5.16. Gas volume (mL) versus days of storage at 60 °C for (a) negative electrode pouch bags and (b) positive electrode pouch bags assembled from LMO/AG pouch cells after formation.

5.7. Impact of Mixed Salts on Metal Dissolution and OCV Storage

As seen in Figure 5.4, the use of LiFSI as the sole salt results in improved capacity retention compared to LiPF$_6$ for cells cycled at 40 and 55 °C. However, it is well known that LiFSI can corrode Al foil used in the positive electrode at high potentials[152,160] which can present a serious safety risk that outweighs the improved capacity retention. At 40 and 55 °C, LiFSI outperformed LiPF$_6$ for most of the cells we tested, but it performed very poorly at 70 °C. This suggests that Al corrosion is very slow at 40 °C and 4.20 V UCV (or does not take place under these conditions), or that 70 °C cycling results in a lower threshold potential for Al corrosion. To confirm the presence of Al corrosion at 70 °C, SC-LMO and PC-LMO

178

cells with 2VC-LiFSI electrolyte were cycled for 20, 40, and 80 cycles at 70 °C. Figure 5.17 shows the Al map obtained from XRF of the negative electrode after cycling. We clearly see Al deposits on the negative electrode after only 20 cycles at 70 °C and 4.20 V for SC-LMO and PC-LMO. It is worth noting that XRF done at lower temperatures with LiFSI-containing cells did not show significant Al on the negative electrode at the time our tests concluded (data not shown here). Therefore, LiFSI alone will not be suitable for long-term cycling in LMO cells, even at lower temperature since the risk of Al corrosion might still persist.
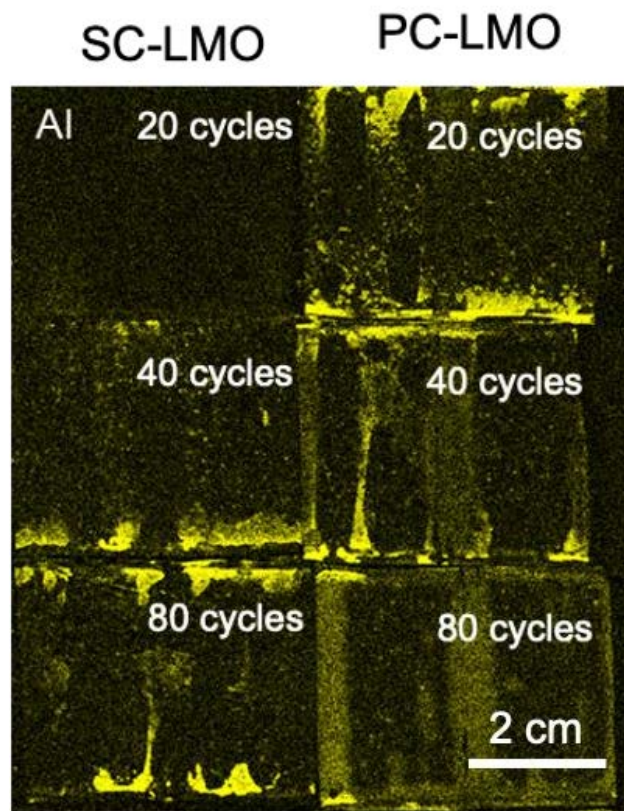
Figure 5.17. Al XRF maps of negative electrodes taken from SC-LMO and PC-LMO pouch cells cycled at 70 °C with 1.5 M LiFSI and 2VC.

It is important to examine ways to passivate the Al foil against LiFSI corrosion while maintaining or improving the performance of the LiFSI-containing cells. One approach is to use co-salts with LiFSI to passivate the Al foil. Additionally, we explored co-salts for $LiPF_6$ since it is known to cause Mn dissolution through electrolyte degradation and HF generation at elevated temperatures[53,73,134,161]. We used PC-LMO2 cells as a test vehicle for mixed salt electrolyte OCV storage tests at 60 °C to accelerate cell degradation[55,110]. The co-salt used with $LiPF_6$ was chosen to be $LiBF_4$[24], while LiFSI was tested with either $LiBF_4$ or LiDFOB[26]. Figure 5.18 shows voltage versus time for the 60 °C OCV storage period. The salt composition (in moles per liter) is indicated on each panel. All PC-LMO2 cells in Figure 5.18 lost a substantial amount of their capacity and the voltage dropped to ~3.95-4.0 V from 4.20 V. The differences in the $LiPF_6$-$LiBF_4$ salt mixtures were fairly small (Figure 5.18a), but in Figures 5.18b-c the addition of $LiBF_4$ or LiDFOB to LiFSI reduced the voltage drop slightly. The $1.5LiBF_4$ and $0.75LiFSI$-$0.75LiBF_4$ cells had the same voltage drop which was about 50 mV less than LiFSI only. In Moreover, using 0.25 M LiDFOB resulted in the smallest voltage drop compared to 0.5 M LiDFOB and LiFSI only.
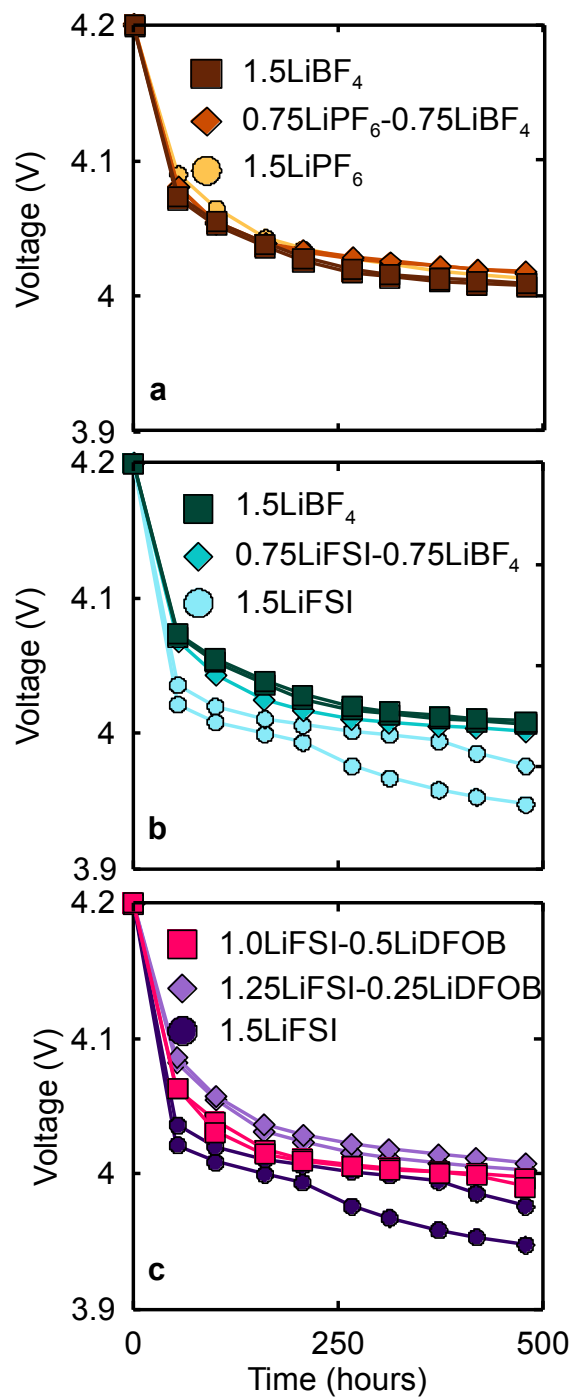
Figure 5.18. Voltage (V) versus time (hours) for PC-LMO2 pouch cells with (a) LiPF$_6$- LiBF$_4$; (b) LiBF$_4$-LiFSI or (c) LiFSI-LiDFOB salt mixtures. OCV storage was done at 60 °C.

Figure 5.19 shows the voltage drop (V), capacity loss during OCV (mAh), which is the sum of reversible and irreversible losses, and irreversible capacity loss (mAh) as a function of Mn loading on the negative electrode for PC-LMO2 cells. The salt composition is labeled for each data point.
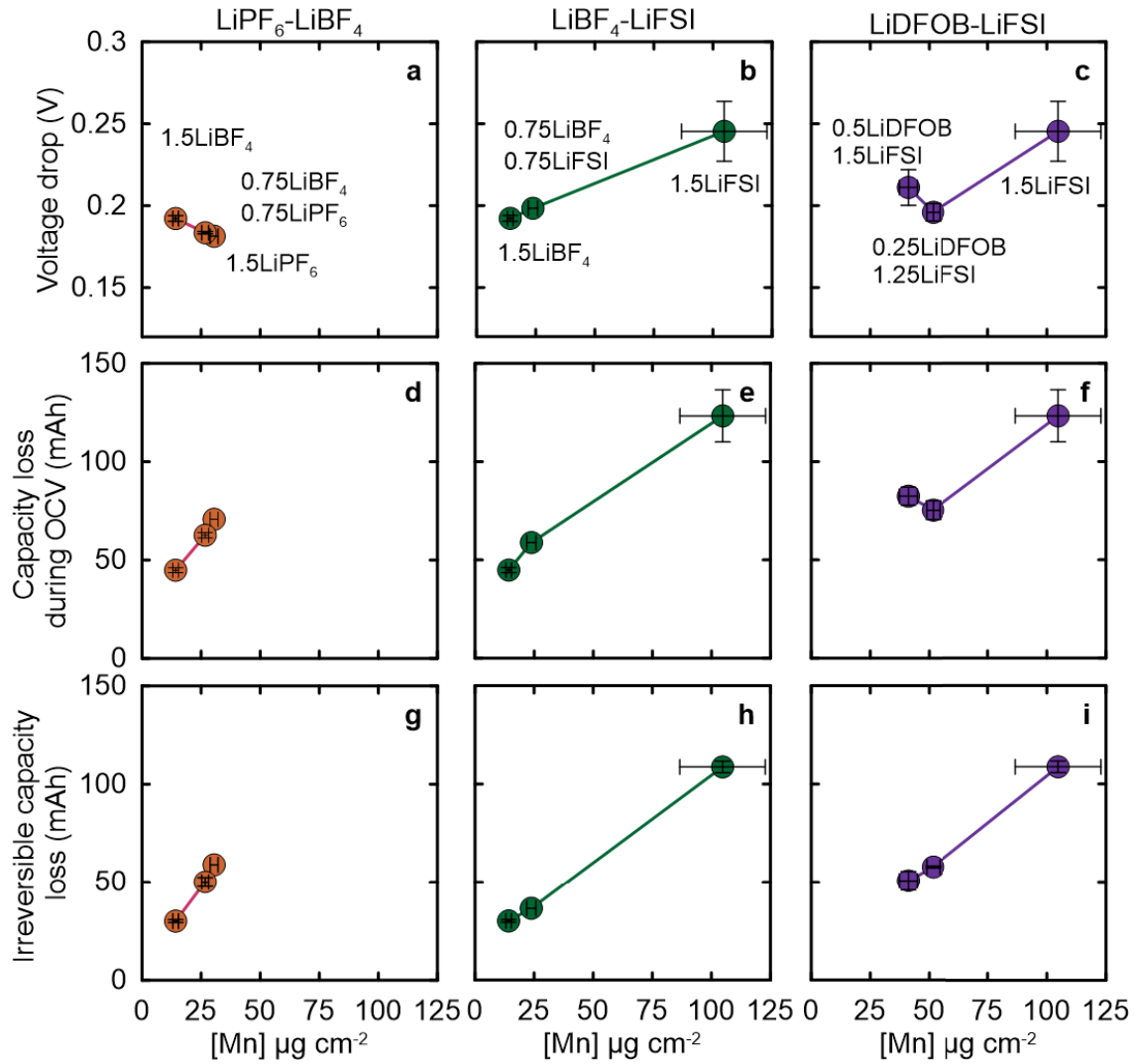
Figure 5.19. (a-c) voltage drop (V); (d-f) capacity loss during OCV (mAh); and (g-i) irreversible capacity loss (mAh) versus Mn loading on the negative electrode after storage for LiBF₄-LiPF₆, LiBF₄-LiFSI, and LiFSI-LiDFOB in PC-LMO2 pouch cells. OCV storage was done at 60 °C for 500 hours at 4.20 V.

In the $LiPF_6$-$LiBF_4$ series (left column), increasing the $LiBF_4$ content reduced the capacity lost during OCV from 75 mAh ($LiPF_6$ only) to 45 mAh ($LiBF_4$ only), as well as the irreversible capacity loss which decreased from ~60 to ~30 mAh. Moreover, replacing $LiPF_6$ with $LiBF_4$ resulted in smaller Mn loading on the negative electrode after storage, from ~30 $\mu g\ cm^{-2}$ for $LiPF_6$ only to ~12.5 $\mu g\ cm^{-2}$ for $LiBF_4$.

In the $LiBF_4$-LiFSI series (middle column), replacing LiFSI with $LiBF_4$ resulted in lower voltage drop, smaller capacity loss during OCV and smaller irreversible loss as well. Remarkably, changing the electrolyte salt from 1.5 M LiFSI to 0.75 M LiFSI + 0.75 M $LiBF_4$ lowered the irreversible capacity loss from ~110 mAh to ~30 mAh. Similarly, adding $LiBF_4$ to LiFSI dramatically lowered Mn loading on the negative electrode from 110 $\mu g\ cm^{-2}$ (LiFSI only) to ~12.5 $\mu g\ cm^{-2}$ ($LiBF_4$ only).

Finally, in the LiDFOB-LiFSI series (right column), mixing LiDFOB with LiFSI improved the storage performance as well. For example, 0.25 M LiDFOB + 1.25 M LiFSI combination lowered the irreversible loss from 110 mAh to 60 mAh, and the capacity loss during OCV improved from ~125 mAh to ~80 mAh. However, increasing the LiDFOB concentration from 0.25 to 0.50 M resulted in greater voltage drop and capacity loss. LiDFOB was also effective at lowering Mn loading on the negative electrode from 110 $\mu g\ cm^{-2}$ (LiFSI only) to ~40-50 $\mu g\ cm^{-2}$ for the two LiDFOB-containing blends. We did not investigate LiDFOB concentrations

greater than 0.5 M since LiDFOB results in a poor SEI and significant gassing from our experience.

Figure 5.20 shows the Mn loading and the Al loading on the negative electrode (μg cm^{-2}) for PC-LMO2 cells after 60 °C storage at 4.20 V for 500 hours. The impact of salt choice on Mn loadings was discussed above, so we will focus on Al deposition here. The deposited Al in the pure LiFSI cell was around 5.5 μg cm^{-2} while the LiBF$_4$-containing cells had virtually no Al deposition on the negative electrode. Similarly, the LiDFOB-LiFSI series shows that adding LiDFOB effectively suppressed Al deposition.

The LiFSI-only cells showed an enormous irreversible capacity loss of ~110 mAh after storage. In cases where Al corrosion is severe such as the LiFSI-only cells, positive electrode particles may become electrically disconnected when the current collector is corroded during 4.20 V storage at 60 °C. On the subsequent capacity check cycles, the disconnected particles cannot participate in the charge/discharge process, which would result in a low cell capacity as seen in Figure 5.19. Moreover, if the corroded current collector results in some delamination of the positive electrode, Mn dissolution may occur at a faster rate, as suggested by the concurrent increase in Mn and Al loadings for LiFSI only cells in Figure 5.20. The increased Mn deposition can result in increased negative electrode parasitic heat flow (see Figure 5.15) which would increase irreversible capacity loss for the LiFSI-only cells.
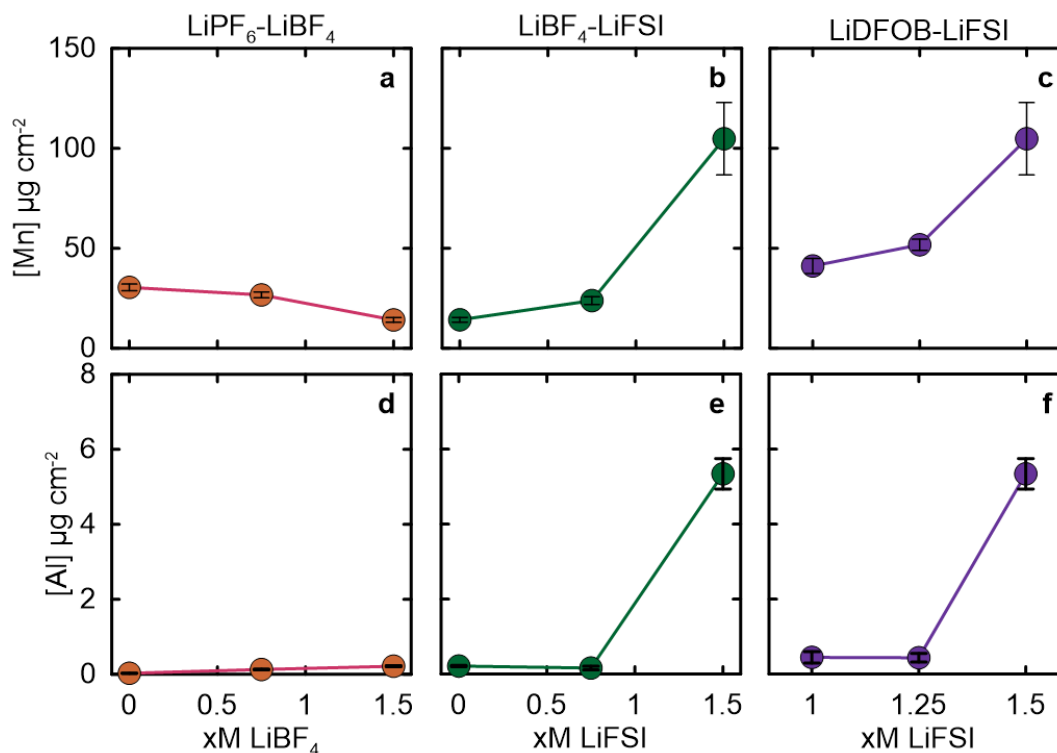
Figure 5.20. (a-c) Mn loading and (d-f) Al loading on the negative electrode (µg cm^{-2}) of PC-LMO2 pouch cells with LiBF$_4$-LiPF$_6$, LiBF$_4$-LiFSI, or LiFSI-LiDFOB salt mixtures after 500 hours of OCV storage at 60 °C at 4.20 V. Total [salt] was 1.5 M.

In addition to suppressing Al deposition, the structural integrity of the electrodes and jelly roll was maintained when LiBF$_4$ was used as co-salt for LiFSI. Figure 5.21 shows pictures of the disassembled LiBF$_4$-LiFSI series storage cells. It is clear that the negative electrode in the pure LiFSI cell was severely degraded. The separator was stuck on the negative electrode and yellow deposits were seen on the surface Additionally, lots of discolouration on the negative electrode and separator was observed. A close-up of the wound jelly roll shows signs of Al corrosion evident from the pitting on the outside of the jelly roll, along with some foil tearing along the edges of the jelly roll. Remarkably, adding LiBF$_4$ to LiFSI, or

using LiBF$_4$ as the sole salt, virtually eliminated most of the discolouration of the negative electrode seen in the pure LiFSI case, as well as prevented the separator from sticking to the electrode.
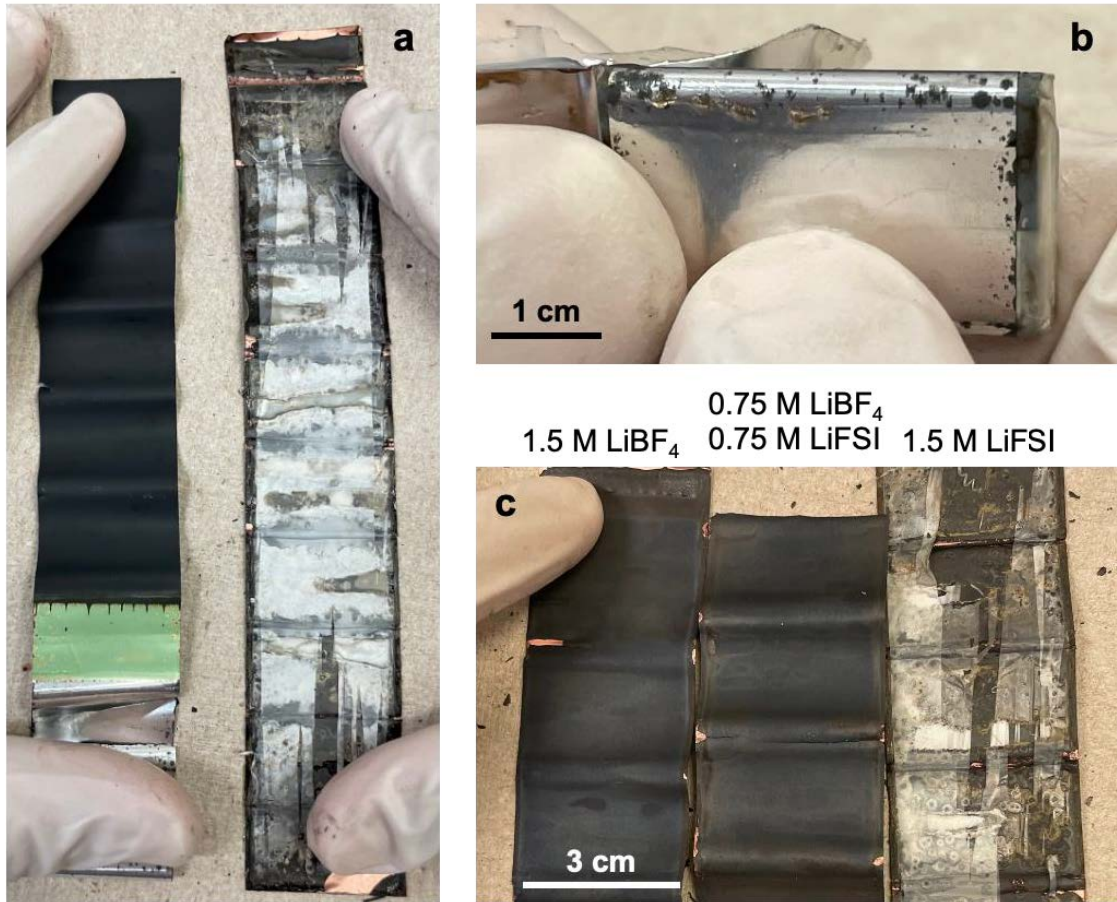
Figure 5.21. (a) pictures of a disassembled PC-LMO2 pouch cell with LiFSI only salt after 500 hours of OCV storage at 60 °C; (b) a close-up picture of the jelly roll exterior showing corrosion of Al current collector; and (c) negative electrodes from disassembled PC-LMO2 pouch cells after 500 hours of OCV storage at 60 °C with different LiBF$_4$-LiFSI salt combinations. Cells were disassembled at 2.5 V.

5.8. Conclusion

This chapter explored the impact of Li excess, particle size, and NMC blending on cycle life performance of LMO/AG pouch cells with 5-6 different electrolyte blends and various salt combinations. Cycling experiments were done at RT, 40, 55, and 70 °C. We showed that SC-LMO cells with large primary particle size (~6-10 μm) and VC-containing electrolytes can have 2200+ cycles at RT and 800+ at 40 °C with C/3:C3 charge/discharge rates. However, the performance of all LMO/AG cells quickly deteriorated at more elevated temperatures. The biggest performance penalty was a result of decreasing Li excess in $Li_{1+x}Mn_{2-x}O_4$ in PC-LMO2 materials compared to PC-LMO. However, the performance of PC-LMO2 was greatly improved by blending 25 % of NMC622 with PC-LMO2. The observed synergy between PC-LMO2 and NMC622 was shown to be electrolyte-dependent and more significant at elevated temperatures.

XRF was used to quantify the Mn loading on the negative electrode after cycling, where the PC-LMO2 cells had the most severe Mn dissolution compared to the other LMO types due to their smaller Li excess and particle size. The synergy between NMC622 and PC-LMO2 was evident in the Mn loading on the negative electrode which decreased significantly decreased in the blended cells compared to PC-LMO2 only. The Mn loading was independent of the electrolyte used and no strong correlation between the capacity loss of a given electrolyte and Mn loading could be made. It was clear that the Mn loading depends on the morphology and Li excess of the LMO positive electrode as well as the cycling temperature. Mn deposition on the negative electrode appeared to primarily occur during the early

cycles of the cell and slowly increase with subsequent cycles. It is unclear if all Mn dissolution occurs at once then gradually deposits on the negative electrode, or if the dissolution and deposition is continuously occurring. This will require further work to understand.

Finally, DCA was used to quantify shift loss and electrode active material loss. We saw severe active mass loss for PC-LMO2, followed by NMC622/PC-LMO2, PC-LMO, SC-LMO, which correlated well with the Mn loading on the negative electrode. Cells with large Mn loading had more negative electrode active mass loss which we attributed to the ability of Mn to thicken the SEI[54,158]. In cells with PC-LMO2, the main capacity loss route was positive electrode mass loss, while cells with the more stable SC-LMO and PC-LMO lost more capacity due to Li inventory loss during UHPC cycling.

In addition, we investigated the degradation of LMO/AG cells cycled at 70 °C using XRF and NMR and probed the electrode/electrolyte reactivity with IMC and pouch bag studies. Dual salt electrolytes to control Mn dissolution and Al corrosion (in LiFSI electrolytes) during high-temperature storage at 60 °C were also investigated. We concluded the following:

1. LiFSI improves capacity retention compared to $LiPF_6$ but Al corrosion at high temperatures makes it incompatible with LMO/AG cells;

2. Mn deposition on the negative electrode occurs primarily during the early cycles of LMO/AG cells at 70 °C (up to cycle 25) and slows down as the

cells age. Further work is needed explore the rate of Mn deposition in those earlier cycles;

3. LMO/AG cells suffers from severe PF_6^- consumption (~0.1-0.30) after 100 cycles at 70 °C:

4. Most of the Mn deposition during formation at 40 °C occurs at ~3.20 V, which is near the onset of SEI formation;

5. Increasing Mn content on the negative electrode after formation results in greater negative electrode heat flow in pouch bag studies;

6. Negative electrode pouch bags stored at 60 °C for 60 days generate a substantial amount of gas consistent with the Mn content on the electrode, and only the LMO positive electrodes with low Li excess were reactive with the electrolyte;

7. Using $LiBF_4$ in combination with $LiPF_6$ lowers Mn deposition after 500 hours of OCV storage at 60 °C in PC-LMO2 pouch cells and improves the storage performance

8. Using $LiBF_4$ or LiDFOB in combination with LiFSI lowered Mn deposition after 500 hours of OCV storage at 60 °C in PC-LMO2 pouch cells, suppressed Al corrosion, and also improved the storage performance compared to LiFSI alone.

SC-LMO materials with primary particle size of 6-10 μm and a composition of $Li_{1.125}Mn_{1.875}O_4$ had superior cycle life performance at all temperatures tested (RT to 70 °C) compared to the three other types of LMO positive electrodes used.

LiFSI salt resulted in improved capacity retention in SC-LMO at 40 °C, but 55 and 70 °C cycling showed severe Al corrosion which could present a safety concern in long-term cycling even at lower temperatures. However, co-salts such as LiBF$_4$ and LiDFOB were effective in suppressing Al corrosion during 60 °C storage tests in PC-LMO2, so their efficacy at suppressing Al corrosion during long-term cycling will be explored in upcoming work. Moreover, 2VC1DTD and PES211 electrolytes had superior capacity retention compared to other blends in SC-LMO and PC-LMO cells so we believe these electrolyte blends are useful in LMO/AG cells.

This work shows that competitive LMO cell design should utilize SC LMO particles with 2VC1DTD or PES211 electrolytes. Additionally, blending NMC with SC LMO would prolong the cell lifetime even further due to the synergy between NMC and LMO. Decreasing the Li excess will increase the specific capacity of the LMO material, but at a lifetime penalty as shown in this work. Therefore, Li excess should be carefully tailored to strike a balance between energy density and lifetime for a given application. In cases where Li excess must be very small, then a composite NMC/LMO positive electrode with PES211 electrolyte will be useful to improve cell lifetime.

The next chapter will focus on SC LMO/AG pouch cells with larger particle size compared to our SC-LMO used in this work, as well as blending NMC with SC-LMO to utilize the synergy between NMC and LMO in a superior LMO material. Additionally, more work on optimizing solvent composition and salt mixtures will be carried out to further understand the impact mixed salts have on capacity retention.

Chapter 6. Single-Crystal LMO Blended Cells with Larger Particle Size

The results shown in this chapter are part of a manuscript that is in-progress. A. Eldesoky conceived and planned all experiments presented here, completed the data analysis with supervision from J. R. Dahn. A. Eldesoky carried out all XRF measurements according to the method developed for this thesis and published in *A. Eldesoky et al* 2020 *J. Electrochem. Soc.* **167** *130539*. N. Kowalski and H. Ni prepared the electrolyte recipes and filled the cells. A. Dutta measured the lattice parameters for the LMO materials used here.

6.1. Introduction

In Chapter 5, we examined the performance and degradation of various LMO/Graphite cell designs and found that SC LMO material with an average composition of $Li_{1.125}Mn_{1.875}O_4$ performed significantly better during galvanostatic cycling in at temperatures ranging from RT to 70 °C. The SC LMO cells also had less Mn dissolution and lower parasitic heat flow resulting from electrolyte reactivity with the lithiated negative electrode and electrolyte after formation. We saw that SC LMO outperformed the PC counterpart with a similar Li excess which we attributed to the larger primary particle size in the SC morphology. In this chapter, we will explore the impact of increasing the particle size of SC LMO from a D50 of 10.42 μm to 13.82 μm with a similar Li excess. Moreover, the SC LMO materials with the larger particle size will be blended with NMC622 to explore the impact of the NMC/LMO synergy on the performance of this material.

XRF will be used to study Mn dissolution after various electrochemical tests in the new SC LMO cells with and without NMC622 blending, which will be compared to the SC LMO material introduced in Chapter 5. The role of mixed salt electrolytes in improving the capacity retention and degradation of SC LMO cells will be also discussed.

The cell specifications are shown in Table 6.1. The electrolyte compositions are shown in Table 6.2. Since $LiBF_4$ can lower the electrolyte conductivity, the base solvent for the mixed salt electrolyte was changed to EC:DMC (15:85) from EC:EMC:DMC (25:5:70) to achieve a lower viscosity[162]. For mixed salt electrolytes, the VC loading increased from 2 % to 3 % to ensure a well-passivated SEI is formed since $LiBF_4$ does not passivate the SEI as effectively as $LiPF_6$[124,163].

Table 6.1. List of LMO/Graphite cell types used in this chapter.

Positive electrode	Li excess (x in Li$_{1+x}$Mn$_{2-x}$O$_4$)	D50 (μm)	*a* lattice parameter (Å)	LMO Capacity (mAh g^{-1})	Loading (mg cm^{-2})	Negative electrode	Loading (mg cm^{-2})
SC-LMO	0.125 ± 0.029	10.42	8.1994	105	22.7		8.5
SC-LMO2	0.125 ± 0.031	13.80	8.1998	105	22.7	Kaijin AML400	8.2
SC-LMO2B 25 % NMC622 + 75 % SC-LMO2	-		-	-	22.4		8.8

Table 6.2. List of electrolytes used in this chapter.

Name	Salt	Solvent (wt. ratio)	Additive (wt.%)
2VC1DTD	1.5 M LiPF$_6$	EC:EMC:DMC (25:5:70)	2 % VC 1 % DTD
2VC			2 % VC
2FEC1LFO			2 % FEC 1 % LFO
PES211			2 % PES 1 % MMDS 1 % TTSPi
1.5LiPF$_6$	1.5 M LiPF$_6$	EC:DMC (15:85)	3 % VC 1 % DTD
0.5LiPF$_6$-1.0LiFSI	0.5 M LiPF$_6$ + 1.0 M LiFSI		
0.25LiPF$_6$-1.25LiFSI	0.25 M LiPF$_6$ + 1.25 M LiFSI		
1.5LiBF$_4$	1.5 M LiBF$_4$		
1LiBF$_4$-0.5LiFSI	1.0 M LiBF$_4$ + 0.5 M LiFSI		
0.5LiBF$_4$-1.0LiFSI	0.5 M LiBF$_4$ + 1.0 M LiFSI		
1.25LiFSI-0.25LiDFOB	1.25 M LiFSI + 0.25 M LiDFOB		
1.375LiFSI-0.125LiDFOB	1.375 M LiFSI + 0.125 M LiDFOB		

Figure 6.1 shows top-down SEM images of LMO positive electrodes from the three cells studied here, and the N_2 BET surface area before and after calendaring for the LMO materials. Figure 6.1a shows the SC-LMO material discussed in Chapter 5. Figure 6.1b shows the SC-LMO2 materials with a D50 of 13.8 μm (versus 10.42 for SC-LMO) where primary particle size ranges from 10-13 μm in the top-down SEM view. For SC-LMO2B in Figure 6.1c, the NMC622 particles can be seen dispersed in the electrode. The SC-LMO2 particles in Figure 6.1b-c show some cracking. Commercial electrodes are typically calendared under high pressure (>300 MPa) to increase the electrode density, so it is possible that the SC-LMO2 particles cracked during the calendaring process. The specific surface area of SC-LMO increased from 0.38 m^2 g^{-1} for the pristine powder to 1.02 ± 0.19 m^2 g^{-1} for material scraped from the electrode, while the specific area of SC-LMO2 increased from 0.21 m^2 g^{-1} for the pristine powder to 0.81 ± 0.08 m^2 g^{-1} for material scraped from the electrode. The electrodes contain about 2 % by weight Super S carbon black (approx. 60 m^2 g^{-1}) and this could account for the surface area increase of the powder scraped from the electrodes. Therefore, it is not possible to conclude from the surface area measurements that calendaring increased the specific surface area of the SC-LMO2 particles. The SEM images, however, do suggest an increase in specific surface area.
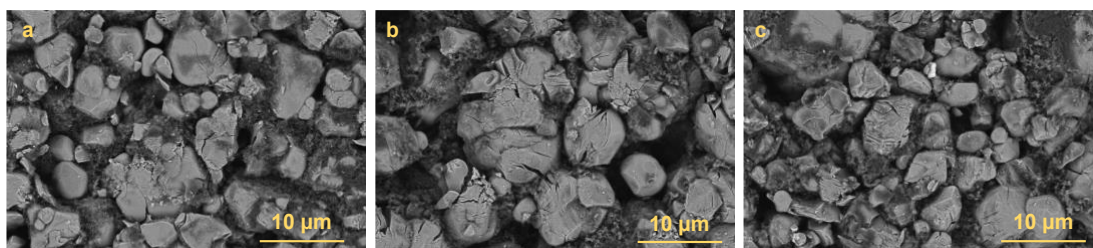
LMO type	Pristine material BET (m^2 g^{-1})	Calendared material BET (m^2 g^{-1})
SC-LMO	0.38	1.02 ± 0.19
SC-LMO2	0.21	0.81 ± 0.08

Figure 6.1. SEM images of SC-LMO, SC-LMO2, and SC-LMO2B positive electrodes taken from pouch cells, and BET surface area before and after calendaring.

6.2. Galvanostatic Cycling and XRF Analysis at Different Temperatures

6.2.1. Long-term Cycling Results

Galvanostatic charge/discharge cycling was done to probe the cycle life of SC-LMO2 and the NMC-blended SC-LMO2B cells compared to SC-LMO at various temperatures. Four of the electrolyte blends used in Chapter 5 were used again here to test the impact of electrolyte additives on lifetime. Due to the concerns with LiFSI discussed in Chapter 5, it was not used again as a standalone salt in this chapter. Figure 6.2 shows the number of cycles sustained before reaching 80 % capacity for the three types of SC LMO cells in this chapter. For cells cycled at RT, we report the number of cycles to 90 % capacity since not all cell reached 80 % capacity at the time of writing. All cycling was done at C/3:C/3 rates in the 3.0-4.20 V range. The raw cycling data for the cells in Figure 6.2 can be found in Figures A.23-A.31 and some will be discussed in the main body of this chapter.

The use of blended SC-LMO2B positive electrodes improved the capacity retention over SC-LMO2 at all temperatures and with all electrolyte formulations. The larger particle size of SC-LMO2 did not universally improve capacity retention at all temperatures for the different electrolyte blends used. At RT, the best capacity retention was in the 2VC cells where SC-LMO reached 90 % retention at cycle ~800 while SC-LMO2 reached 90 % at cycle ~1200. The SC-LMO cells with 2VC1DTD reached 90 % at cycle ~450 compared to cycle ~800 for SC-LMO2. The smallest improvements at RT were seen in PES211 and 2FEC1LFO electrolytes. At 40 °C, the SC-LMO2 cells with 2VC and 2FEC1LFO slightly outperformed the SC-LMO counterparts. Overall, the use of SC-LMO2 introduced a small improvement over SC-LMO at 40 °C and RT, while the blended SC-LMO2B cells were significantly better than both SC-LMO2 and SC-LMO.

At 55 °C, the SC-LMO2 cell with 2VC1DTD and PES211 electrolytes showed improved capacity retention compared to SC-LMO. For example, SC-LMO2 cells with 2VC1DTD took ~300 cycles to reach 80 % capacity compared to ~200 for SC-LMO counterpart. The SC-LMO2 cells with PES211 only achieved 30 more cycles compared to SC-LMO at 55 °C. On the other hand, SC-LMO2 cells performed worse than SC-LMO at 70 °C. The blended SC-LMO2B also performed worse than SC-LMO except for the 2VC1DTD cell which had 50 more compared to the SC-LMO counterpart. The really poor 70 °C performance for SC-LMO2 and SC-LMO2B could be due to the observed particle cracking in Figure 6.1 which can increase parasitic reaction rate at high temperatures. SC-LMO and SC-LMO2 had a similar Li excess (see Table 6.1) and the only difference was in the D50 particle

size. The cracking observed in the larger SC-LMO2 material could contribute to the lack of significant retention boost at all temperatures except RT seen in Figure 6.2, although more work is needed to confirm is this is indeed the reason behind the poor high temperature performance. The particles cracking can be alleviated by calendaring the electrode at lower pressures (which will also result in a lower density) or by using dopants that can improve the particle durability[164].
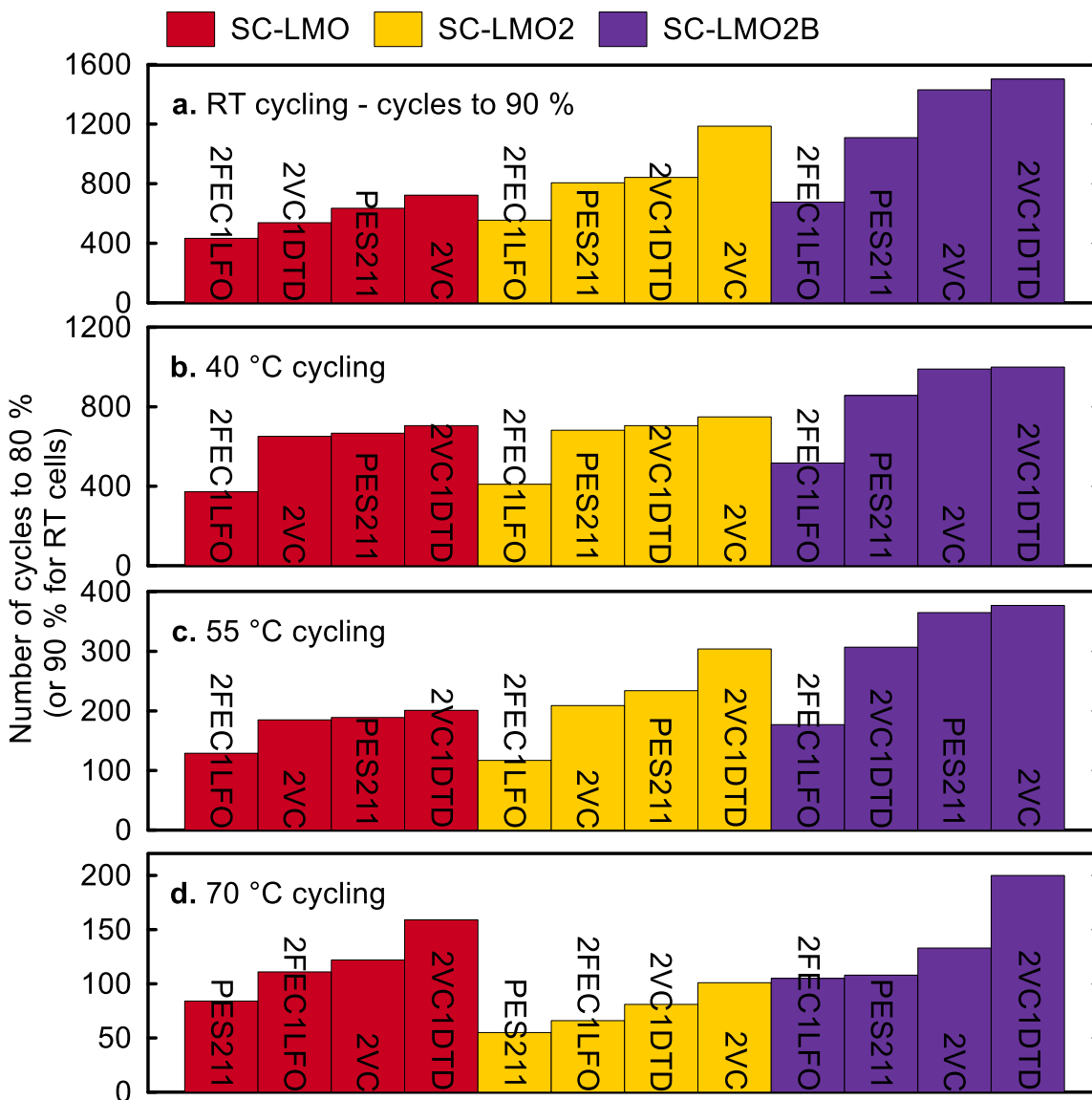
Figure 6.2. Number of cycles to 80 % capacity for SC-LMO, SC-LMO2, and SC-LMO2B pouch cells cycled at (a) RT; (b) 40 °C; (c) 55 °C; and (d) 70 °C with four different electrolytes. Most of the RT cells did not reach 80% at the time of writing, so number of cycles to 90 % capacity is shown instead. All cycling was done at C/3:C/3 and 3.0-4.20 V.

While some improvements were seen in RT and 40 °C cycling, Figure 6.2 only captures the number of cycles to reach 90 % capacity and not the capacity fade trajectory. Figure 6.3 shows the normalized discharge capacity versus cycle number for all the RT cells in Figure 6.2. Here, we see that there is indeed an early improvement in capacity retention, but all SC-LMO2 cells are tracking towards a similar (or worse) capacity retention at end of life compared to SC-LMO. Based on the capacity fade trajectory for SC-LMO2 cells, these cells can deliver slightly greater energy output but are likely to have very similar cycle life compared to SC-LMO.
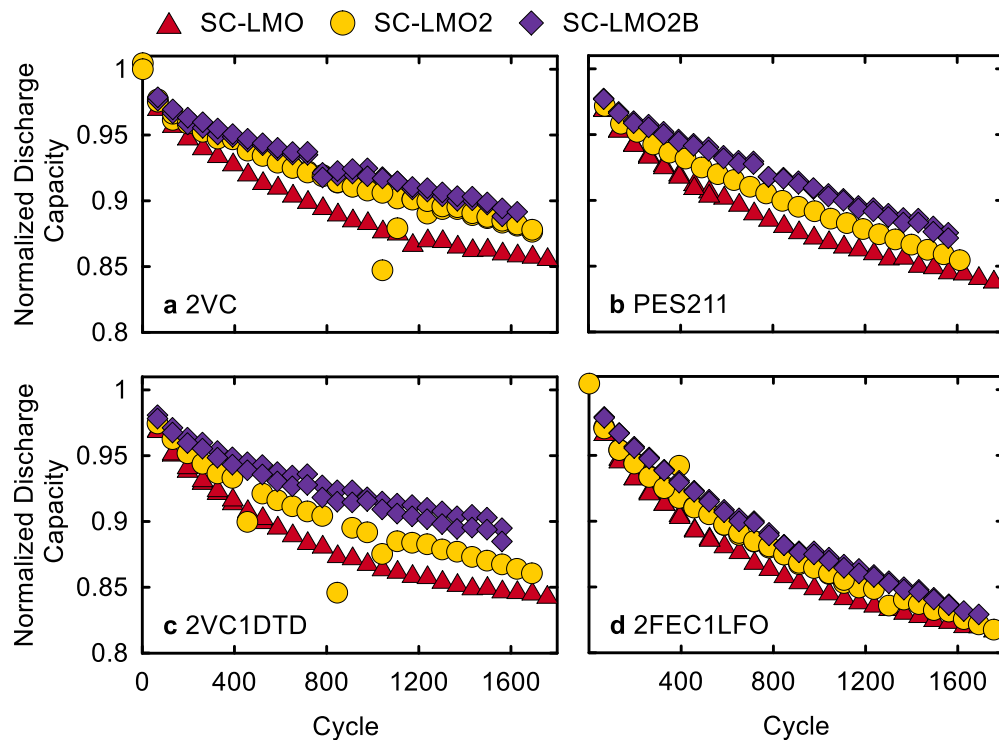
Figure 6.3. Normalized discharge capacity versus cycle number for SC-LMO, SC-LMO2, and SC-LMO2B pouch cells cycled at RT with (a) 2VC; (b) PES211; (c) 2VC1DTD; or (d) 2FEC1LFO electrolytes. All cycling was done at C/3:C/3 and 3.0-4.20 V.

Figure 6.4 shows the normalized discharge capacity versus cycle number for all the 40 °C cells shown in Figure 6.2. It is clear that SC-LMO2B cells had the best capacity retention regardless of the electrolyte used. As shown in Figure 6.2, SC-LMO2B cells with 2VC and 2FEC1LFO had longer cycle life compared to SC-LMO, although the difference is very small for 2FEC1LFO cells. Based on the D50 particle size, SC-LMO2 cell were expected to have significantly better cycle life compared to SC-LMO. However, the improvements over SC-LMO were fairly small in the long-term cycling experiments.
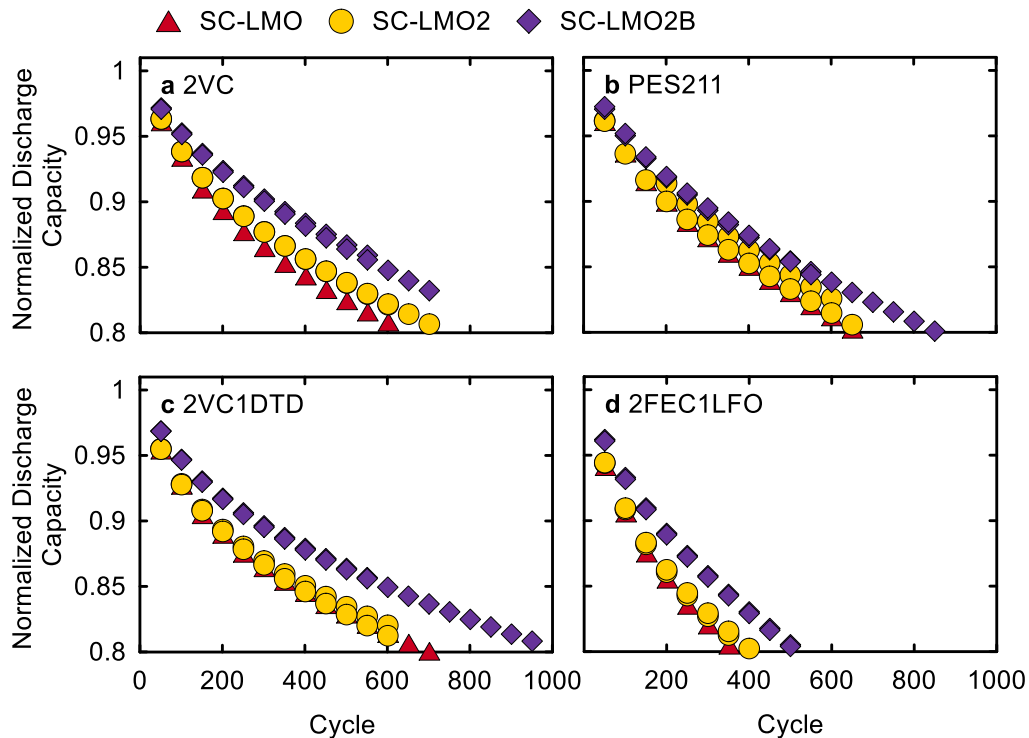
Figure 6.4. Normalized discharge capacity versus cycle number for SC-LMO, SC-LMO2, and SC-LMO2B pouch cells cycled at 40 °C with (a) 2VC; (b) PES211; (c) 2VC1DTD; or (d) 2FEC1LFO electrolytes. All cycling was done at C/3:C/3 and 3.0-4.20 V.

Looking at the cell's ΔV growth during long-term cycling can help explain some of the cycle life trends seen above. Figure 6.5 shows the normalized ΔV versus cycle number at 40 °C, where SC-LMO2 and SC-LMO2B had greater ΔV growth compared to SC-LMO. This increase in ΔV for SC-LMO2 and SC-LMO2B cells may be a product of the large particle size compared to SC-LMO and/or the mechanical damage observed in Figure 6.1, although the exact cause is not yet clear to us. Similar trends can be seen at 55 °C and 70 °C (Figure A.28 and A.31).The fractional increase in ΔV for SC-LMO2 and SC-LMO2B in Figure 6.5 is on the same order of magnitude as NMC811 cells cycled to 4.20 V for ~2000 cycles at 40 °C (see Figure 4.16), which highlights the poor performance of LMO cells.
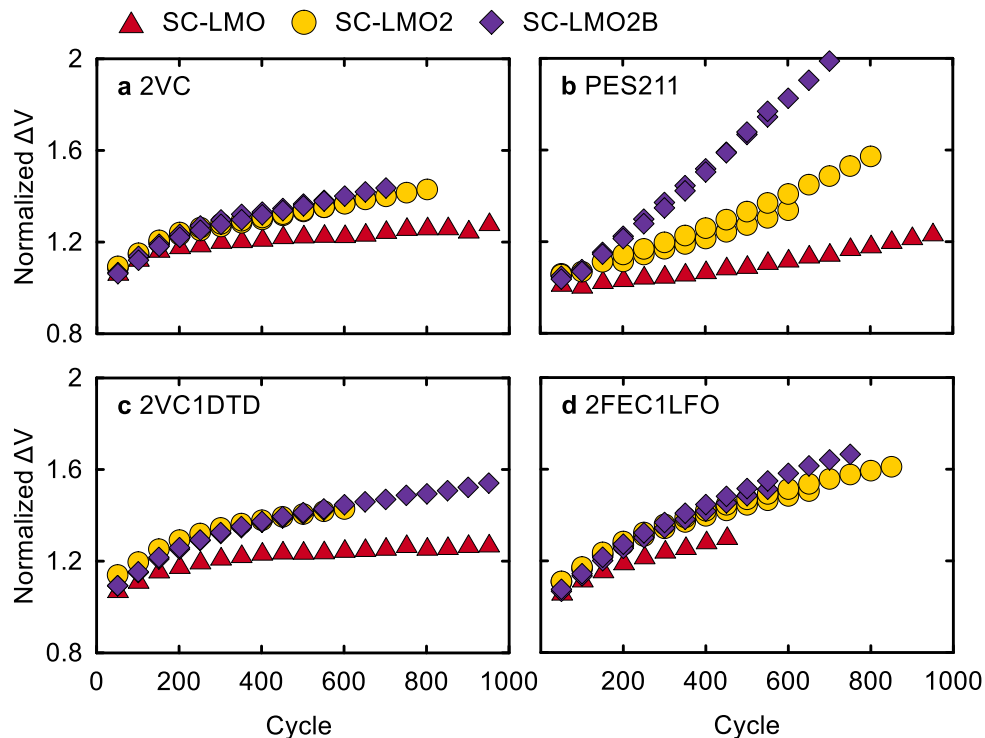
Figure 6.5. Normalized ΔV vs. cycle number for SC-LMO, SC-LMO2, and SC-LMO2B pouch cells cycled at 40 °C with (a) 2VC; (b) PES211; (c) 2VC1DTD; or (d) 2FEC1LFO electrolytes. All cycling was done at C/3:C/3 and 3.0-4.20 V.

6.2.2. Probing NMC/LMO Synergy

The improvement in capacity retention seen in SC-LMO2B compared to SC-LMO2 in could simply be due to having a smaller LMO fraction in the positive electrode compared to the LMO-only SC-LMO2 cells. By looking at the "synergy factor" introduced in Chapter 5, we can determine if NMC blending introduced any benefit to the SC-LMO2B cells. Figure 6.6 shows the synergy factor as a function of cycling temperature for SC-LMO2B cells. We only observed synergy between NMC622 and SC-LMO2 at 70 °C and for 2VC electrolyte at 55 °C. The trend of increasing synergy with cycling temperature is similar to what was observed in Figure 5.5 for VC-containing electrolytes.
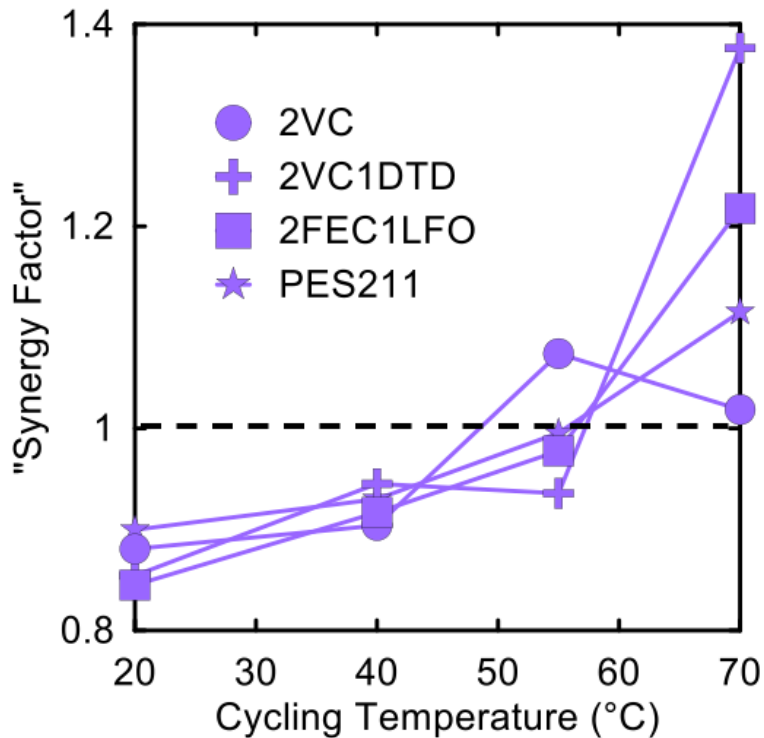
Figure 6.6. Synergy factor versus cycling temperature (°C) for SC-LMO2B pouch cells with four different electrolytes. All cycling was done at C/3:C/3 and 3.0-4.20 V.

We can attempt to rationalize the absence of synergy at lower temperatures by understanding the changes to the LMO surface during charge/discharge cycling. When $Li_{1+x}Mn_{2-x}O_4$ loses surface Mn, it will become more Li rich. Indeed, we have demonstrated in Chapter 5 that higher Li excess results in less Mn dissolution and better cycle life. In previous work looking at the NMC/LMO synergy, Smith et al showed that the formation of a Li-rich surface in LMO (due to Mn dissolution) is hindered in the presence of NMC[153]. With increasing temperature, we expect Mn dissolution to significantly increase. Therefore, the role that NMC plays in stabilizing LMO (which remains unclear in the literature) will become more pronounced at higher temperatures which is consistent with increase in the synergy factor with temperature seen in Figure 6.6. The absence of any synergy at low temperatures may be due to the relative stability of SC-LMO2 in long-term cycling below 55 °C.

6.2.3. XRF Analysis After Long-term Cycling

One advantage of SC LMO is reducing the rate of Mn dissolution compared to PC LMO as discussed in Chapter 5. So far, SC-LMO2 material has provided a capacity retention boost at RT and 40 °C. Since SC-LMO2 has a larger particle size, we expected Mn dissolution to be less severe compared to SC-LMO. Figure 6.7 shows Mn loading on the negative electrode versus capacity loss or cycle number for all three SC LMO cell types after cycling at 40 °C. The error bars are based on the relative error in the slope of the calibration curve used to convert the XRF signal count to a mass loading, unless otherwise specified.

The negative electrodes from all SC LMO cells (including the blended SC-LMO2B) had very similar Mn loading despite differences in the electrolyte additive, cycle number, capacity loss, an NMC622 blending. The Mn loading appears to taper off as the cell ages. Based on the results shown in Chapter 5, it is not surprising to see that the electrolyte additives do not play a role in regulating Mn dissolution. Previous work on LFP cells showed that the use of electrolyte additives, which can alter the properties and passivation of the SEI, can reduce TM dissolution and that VC-containing blends were more effective than FEC-containing ones[165,166]. This can be attributed to the suppression of oxidation reactions mediated by lithium alkoxide formation when VC is used[167] since electrolyte oxidation was shown to produce by-products that can form soluble TM complexes[168]. However, the Mn dissolution in our case seems to depend on the positive electrode properties (similar to the observations in Chapter 5), rather than the additive choice.

The absence of any differences between SC-LMO and SC-LMO2 in Figure 6.7 could be a result of the particle cracking seen in Figure 6.1 which may have increased Mn dissolution to the same rate as SC-LMO. Figure 6.6 showed that there is no synergy between SC-LMO2 and NMC622 at 40 °C. SC-LMO2B cells had a smaller LMO fraction so the Mn loading should have been proportionally smaller (NMC622 is robust against Mn dissolution at the cycling conditions used here[110]), surprisingly SC-LMO2B had the same Mn loading as SC-LMO2 cells and it is unclear why. Figure 6.7 shows that there is no strong correlation between Mn loading and capacity loss for all cells tested here.
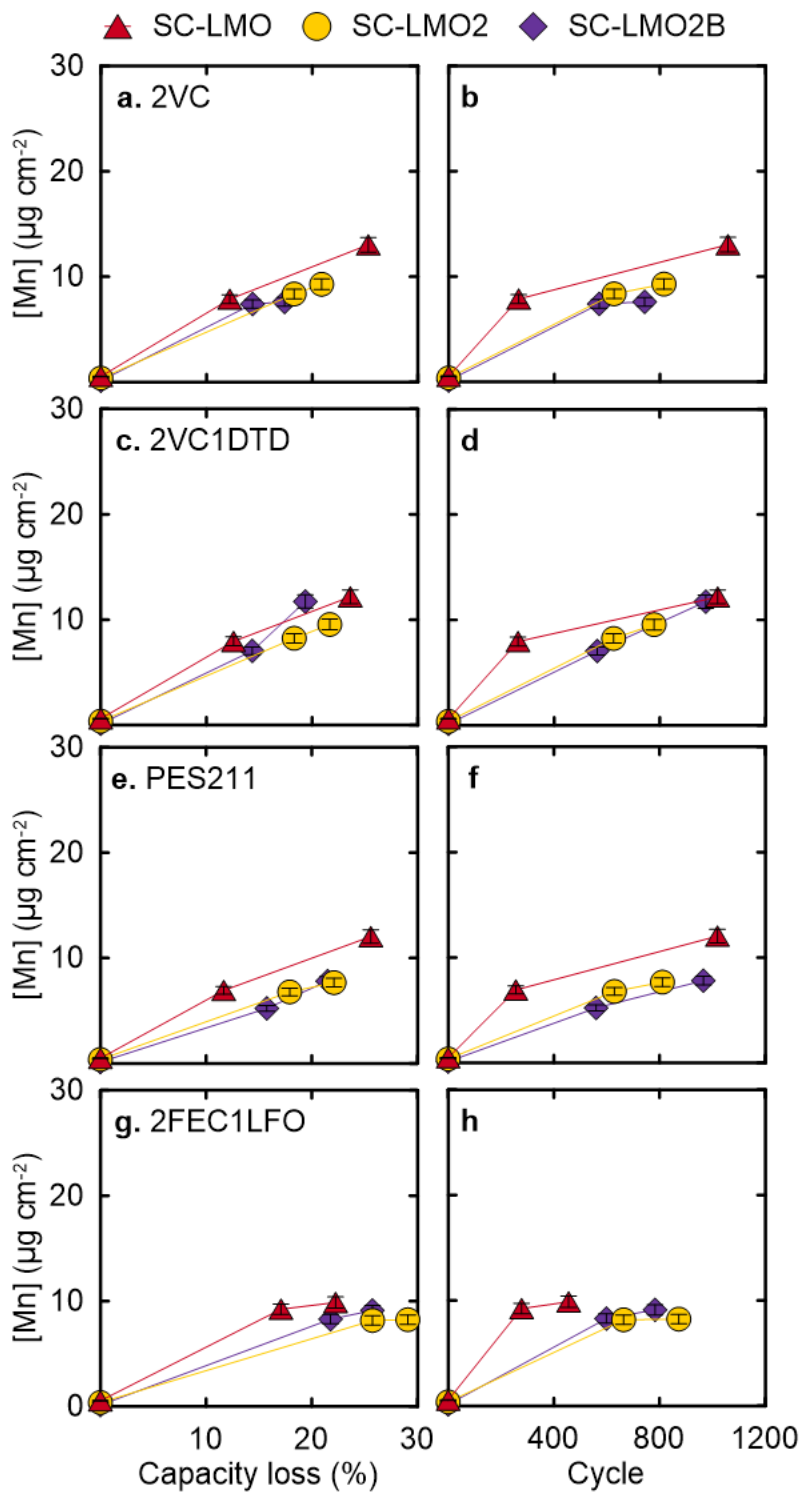
Figure 6.7. Mn loading on the negative electrode (µg cm^{-2}) versus capacity loss (%) or cycle number for SC-LMO, SC-LMO2, and SC-LMO2B cells after 40 °C cycling with (a-b) 2VC; (c-d) 2VC1DTD; (e-f) PES211; or (g-h) 2FEC1LFO electrolytes. All cycling was done at C/3:C/3 and 3.0-4.20 V.

Figure 6.8 shows the Mn loading versus capacity loss or cycle number for all SC LMO cells after cycling at 55 °C or 70 °C. We see that all SC LMO cell types have a similar Mn loading after 55 °C cycling regardless of the additives or amount of capacity loss. At 70 °C, we start to see that SC-LMO2B had the smallest Mn loading followed by SC-LMO and SC-LMO2. However, the difference between SC-LMO2 and SC-LMO2B is roughly proportional to the decrease in LMO fraction in SC-LMO2B and no synergies were seen here, in contrast with Figure 5.12 in Chapter 5, for example. There is also no clear correlation between Mn loading and capacity loss which is largely influenced by the positive electrode only.
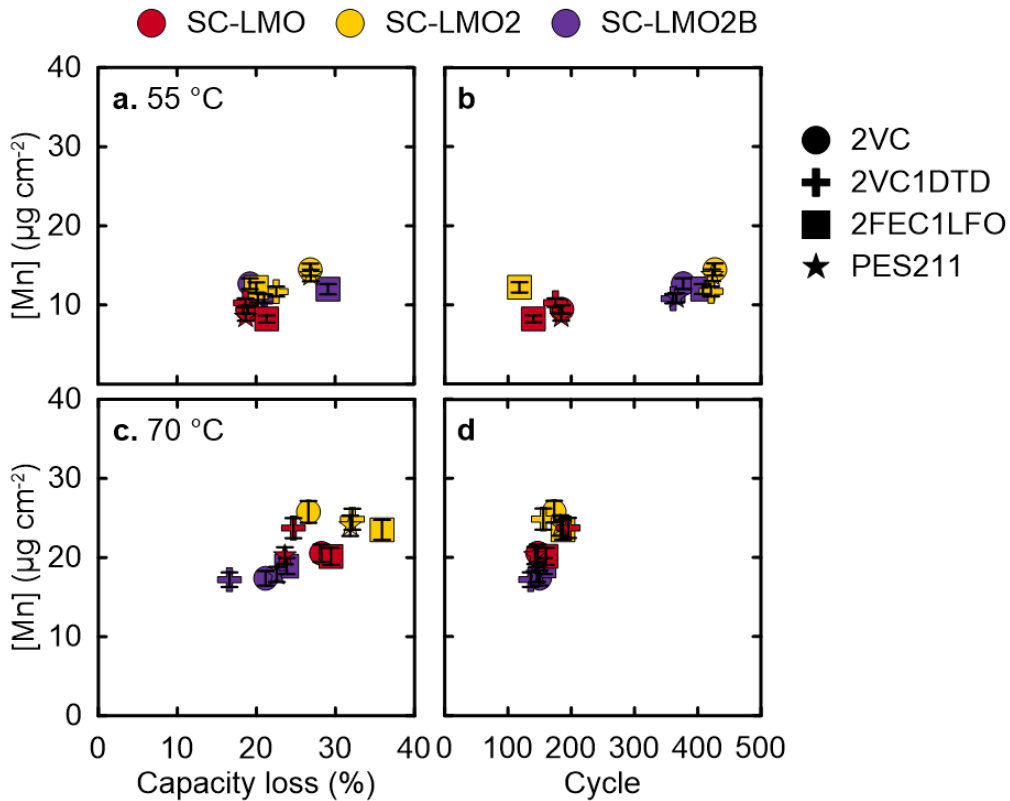
Figure 6.8. Mn loading on the negative electrode ($\mu g \ cm^{-2}$) versus capacity loss (%) or cycle number for SC-LMO, SC-LMO2, and SC-LMO2B cells after (a-b) 55 °C cycling or (c-d) 70 °C cycling with four different electrolytes. All cycling was done at C/3:C/3 and 3.0-4.20 V.

The results in Figures 6.7-6.8 are consistent with Figure 5.8 in Chapter 5. The properties of the positive electrode (Li excess, particle size, morphology, etc.) dictate the rate and severity of Mn dissolution. The properties of the electrolyte, however, dictate the capacity retention which is primary governed by Li loss at the negative electrode. Therefore, a correlation between capacity loss and Mn loading in cells with different electrolytes, but same positive electrode, is difficult to establish. There is certainly a correlation between the capacity retention of different LMO types and Mn dissolution as discussed in Chapter. So far, we saw small differences in capacity retention between the three different SC LMO cell types used in this chapter, along with small differences in Mn loading.

6.3. UHPC Cycling Results

UHPC was used to measure small changes in CE, capacity loss, and charge endpoint slippage for the three SC LMO cell types. Figure 6.9 shows the CE versus cycle number for SC LMO cells with four different additives. All cycling was done at 40 °C with a C/20:C/20 charge:discharge rate in the 3.0-4.20 V range. The cells with 2VC and 2VC1DTD electrolytes had higher CE after 20 cycles compared to the 2FEC1LFO and PES211 cells. In all cases except 2FEC1LFO, the SC-LMO2B cells had the highest CE followed by SC-LMO2 and SC-LMO. PES211 cells had the lowest CE. In long-term cycling at 40 °C, PES211 was one of the least competitive blends in SC-LMO2 and SC-LMO2B cells which is consistent with the CE trends in Figure 6.9.
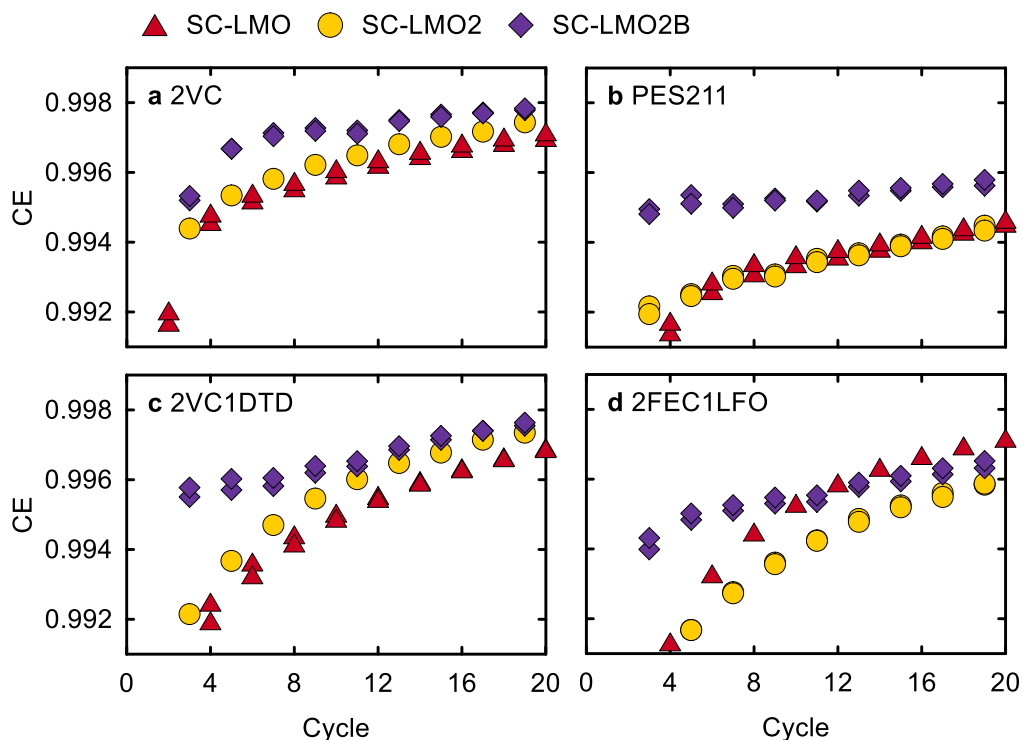
Figure 6.9. CE versus cycle number for SC-LMO, SC-LMO2, and SC-LMO2B pouch cells cycled at 40 °C with (a) 2VC; (b) PES211; (c) 2VC1DTD; or (d) 2FEC1LFO electrolytes. All cycling was done at C/20:C/20 and 3.0-4.20 V.

Figure 6.10 shows the discharge capacity loss versus cycle number for the cells in Figure 6.9. As expected, based on the CE data, the SC-LMO2B cells have the smallest capacity loss followed by SC-LMO2 and SC-LMO. The performance of all additives was very similar except for 2FEC1LFO cells which had the highest capacity loss for all cell types. Even though the SC-LMO2B cells had the lowest capacity fade, these cells lost 4-6 % capacity after only 20 cycles at C/20 (~800 hours of testing) at 40 °C which is a tremendous amount of fade over such a short period of time. For reference, the NMC811/AGC cells in Figure A.7 lost around < 2 % capacity over the same period of time and testing conditions. Despite the really poor CE, PES211 cells show similar capacity fade compared to

VC-containing cells. To explain the discrepancy between CE and capacity fade, it is important to look at the charge endpoint slippage for these cells.
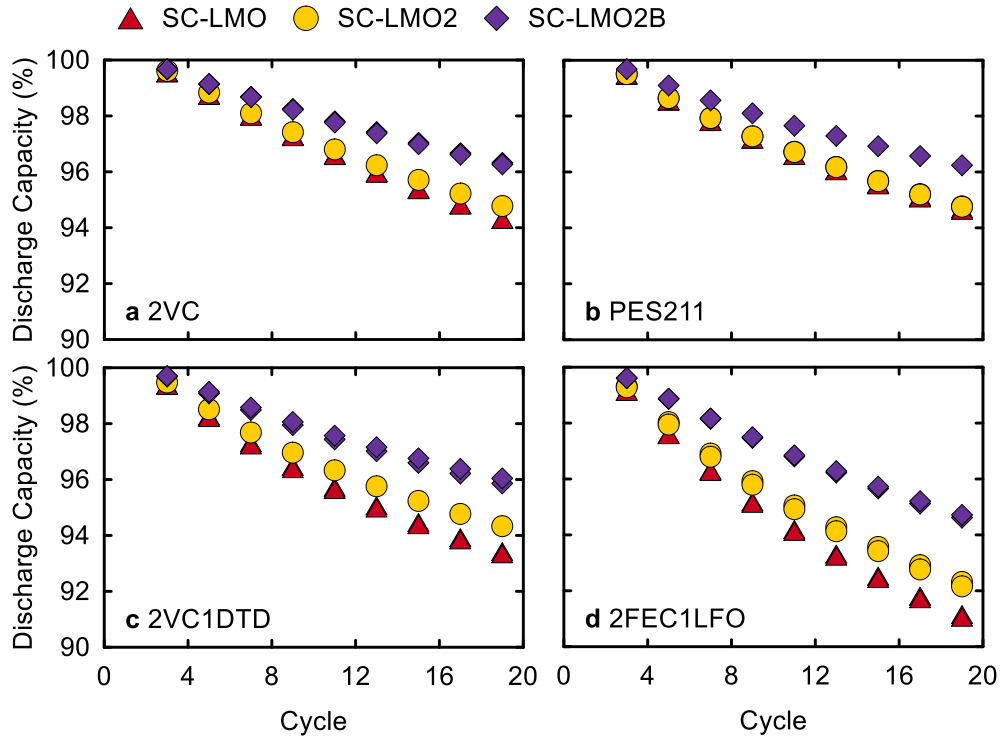
Figure 6.10. Discharge capacity (%) versus cycle number for SC-LMO, SC-LMO2, and SC-LMO2B pouch cells cycled at 40 °C with (a) 2VC; (b) PES211; (c) 2VC1DTD; or (d) 2FEC1LFO electrolytes. All cycling was done at C/20:C/20 and 3.0-4.20 V.

Figure 6.11 shows the charge endpoint slippage versus cycle number for the three SC LMO cell types. The charge endpoint slippage for all cells was in the 2-6 mAh range, except for PES211. The cells with PES211 had a very large charge slippage in the 8-10 mAh range after 20 cycles.
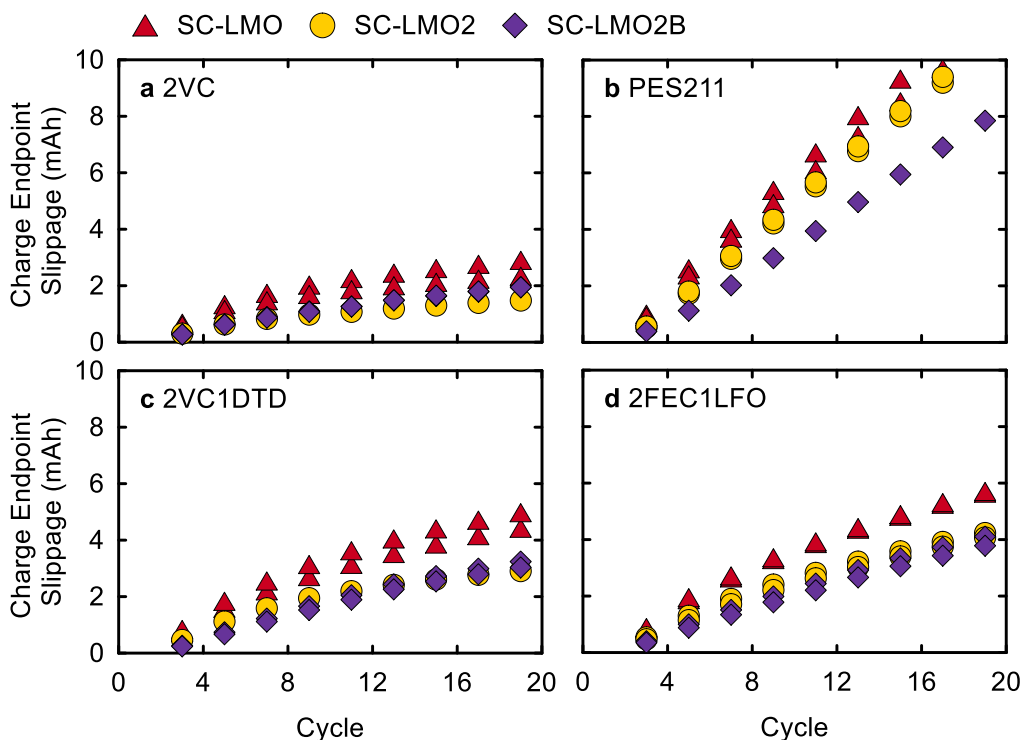
Figure 6.11. Charge endpoint slippage (mAh) vs. cycle number for SC-LMO, SC-LMO2, and SC-LMO2B pouch cells cycled at 40 °C with (a) 2VC; (b) PES211; (c) 2VC1DTD; or (d) 2FEC1LFO electrolytes. All cycling was done at C/20:C/20 and 3.0-4.20 V.

To summarize the UHPC results shown above, we calculated the CIE per hour, fractional fade per hour, and fractional slippage per hour as described by Ma et al[124]. All UHPC cells underwent XRF analysis to probe any correlation between CIE, fade, or slippage and Mn dissolution. The error bars in the Mn loading are based on the propagation of the relative error in the slope of the calibration curve used to convert the XRF signal count to a mass loading and the relative error from duplicate cells. Figure 6.12 shows the fractional fade per hour, fractional slippage per hour, ΔV growth, and CIE per hour as a function of Mn loading after 20 cycles. All cycling was at 40 °C with a C/20:C/20 charge:discharge in the 3.0-4.20 V range.

Overall, SC-LMO2B had the smallest Mn loading followed by SC-LMO2 and SC-LMO which were both similar.

Figure 6.12a shows a correlation between fractional fade rate and Mn loading. Mn deposition on the negative electrode is believed to directly contribute to SEI growthl[54], which is consistent with the observed correlation between fade and Mn loading. Numerous reports claim that Mn deposition results in increase SEI thickness or poor Li$^+$ diffusion kinetics in the negative electrode[53,54,149], both of which should have resulted in an increase in ΔV but Figure 6.12b shows that there is no correlation between ΔV and Mn loading. If Mn in the electrolyte can destabilize PF$_6^-$ anion as hypothesized by Wang et al[150], then the counter Li$^+$ could have contributed to the cell's Li inventory as result of electrolyte oxidation and resulted in increased charge endpoint slippage. It can be seen in Figure 6.12c that the PES211 and 2FEC1LFO electrolyte show a correlation between charge endpoint slippage and Mn loading, however, this was not the case for all electrolyte additives.
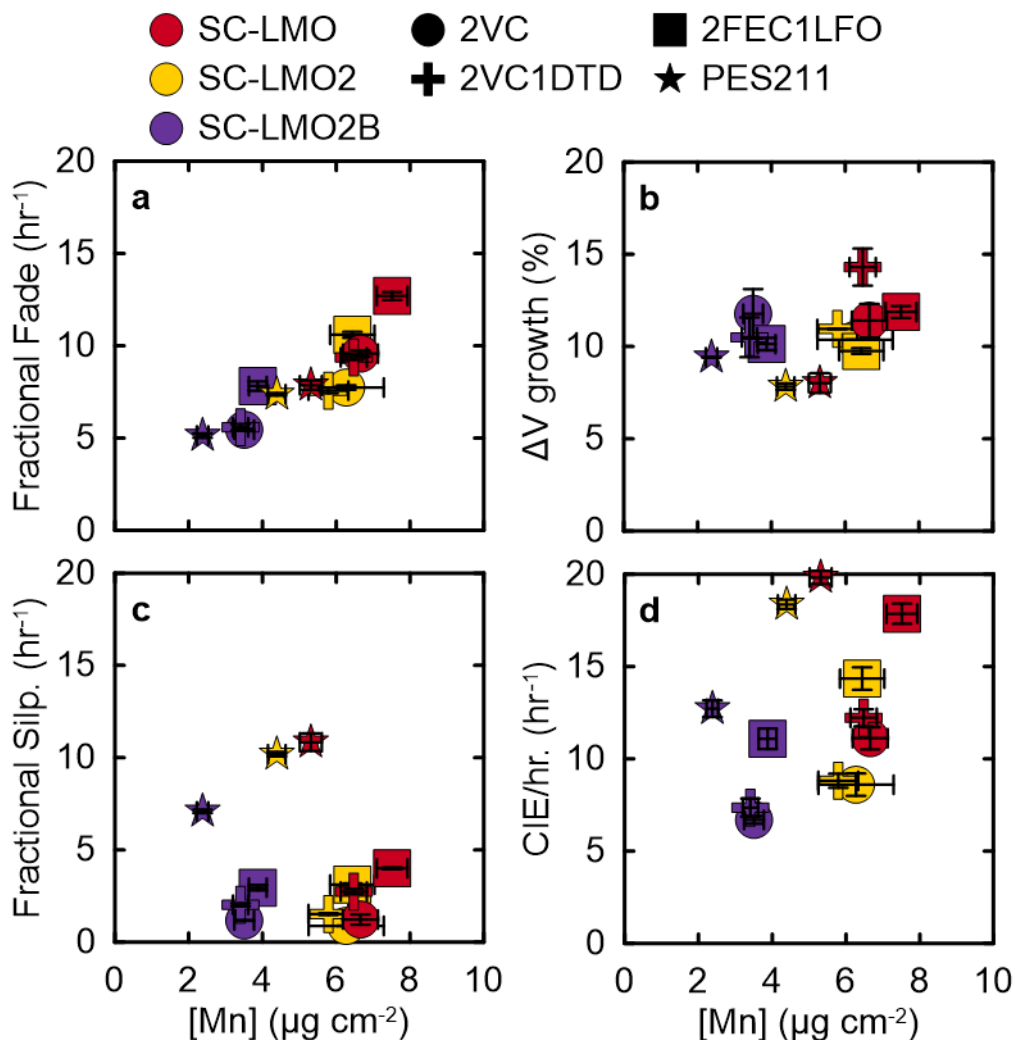
Figure 6.12. (a) fractional fade (hr^{-1}); (b) ΔV growth (%); (c) fractional slippage (hr^{-1}); and (d) CIE/hr (hr^{-1}) versus Mn loading on the negative electrode (μg cm^{-2}) for SC-LMO, SC-LMO2, and SC-LMO2B cells after 20 cycles at 40 °C. All cycling was done at C/20:C/20 and 3.0-4.20 V with four different electrolytes.

6.4. Changes in FCE, Gassing, and R$_{CT}$ with Salt Composition

Since SC-LMO2 resulted in improved capacity retention at RT and 40 °C, as well as lower CIE in UHPC cycling, we set out to further improve the cycle life of SC-LMO2 and SC-LMO2B cells by examining different electrolyte salts.

213

Recall from Chapter 5 that the use of LiFSI as the salt resulted in improved capacity retention at 40 °C. However, when LiFSI-containing cells were cycled at 70 °C and a 4.20 V UCV, severe corrosion of the Al current collector took place. Han et al demonstrated that chloride impurities present from the synthesis of LiFSI are responsible for the Al corrosion observed at high potentials, which is hindered in high-purity LiFSI salts[151], and previous work on mixed salt electrolytes showed that LiBOB and LiDFOB can effectively passivate the Al current collector in the presence of LiFSI[26,169]. Therefore, co-salts that can passivate the Al foil must be used with LiFSI in order to prevent Al corrosion and potentially retain the benefits that LiFSI brings to cell lifetime.

Figure 6.13 shows the FCE, gas volume, and R_{CT} after formation for SC-LMO2B and SC-LMO cells with mixed salt electrolytes. The solvent was EC:DMC (15:85) instead of EC:EMC:DMC (25:5:70) to improve the electrolyte viscosity since $LiBF_4$ decreases the ionic conductivity[162]. The additive loading was 3 % VC + 1 % DTD instead of 2 % VC + 1 % DTD to ensure a well-passivated SEI is formed since $LiBF_4$ does not passivate the SEI as effectively as $LiPF_6$ and due to the lower EC content in the mixed salt electrolytes[124,163]. In Figure 6.13, $LiPF_6$, $LiBF_4$, and LiDFOB are used as co-salts with LiFSI. The dashed line shows results for equivalent SC-LMO2B and SC-LMO2 cells with EC:EMC:DMC (25:5:70), 1.5 M $LiPF_6$ and 2VC1DTD for comparison.

In the $LiBF_4$-LiFSI series, adding $LiBF_4$ resulted in lower FCE, more gassing, and higher R_{CT} which was expected for $LiBF_4$ based on previous work in the

literature[163]. The reduction in FCE from 0.5LiBF$_4$-1LiFSI to 1.5LiBF$_4$ for SC-LMO2B was around 2 % and the increase in gassing was ~0.3 mL. The R$_{CT}$ increased nearly 3-fold going from 0.5LiBF$_4$-1LiFSI to 1.5LiBF$_4$. The same trends are observed for both SC-LMO2 and SC-LMO2B cells. All the cells in the LiBF$_4$-LiFSI series had lower FCE, more gas, and higher R$_{CT}$ compared to the data shown by the dashed line.

In the LiPF$_6$-LiFSI series, the changes in FCE, gassing, and R$_{CT}$ going from 1.5LiPF$_6$ to 0.5LiPF$_6$-1LiFSI were very small. For example, in SC-LMO2B, as the composition changed from 1.5LiPF$_6$ to 0.25LiPF$_6$-1.25LiFSI, the FCE went down to 0.89, gassing increased to ~0.8 mL, and the R$_{CT}$ nearly doubled. The 0.5LiPF$_6$-1LiFSI cells had a high FCE, smallest gas volume, and lowest R$_{CT}$ in the series. Compared to the baseline cell in the dashed line, changing the solvent from EC:EMC:DMC (25:5:70) to EC:DMC (15:85), and increasing the VC loading from 2 % to 3 %, resulted in a ~0.4 % reduction in FCE, a 0.1 mL increase in gassing, and a minor R$_{CT}$ increase. Similar trends can be seen for SC-LMO2 cells as well.

In the LiDFOB-LiFSI series, the 0.125LiDFOB-1.375LiFSI composition had higher FCE, less gassing, and similar R$_{CT}$ compared to the 0.25LiDFOB-1.25LiFSI mixture. The 0.125LiDFOB-1.375LiFSI composition had a FCE around 90 %, about 0.4 mL of formation gas (less than 2VC1DTD cell in the dashed line), and a slightly lower R$_{CT}$ comparable to 2VC1DTD cells. LiDFOB is expected to generate ~2 moles of CO_2 for each mole of LiDFOB that undergoes oxidative decomposition on the positive electrode, so the spike in gassing for the 0.25LiDFOB-1.25LiFSI composition was expected[170].
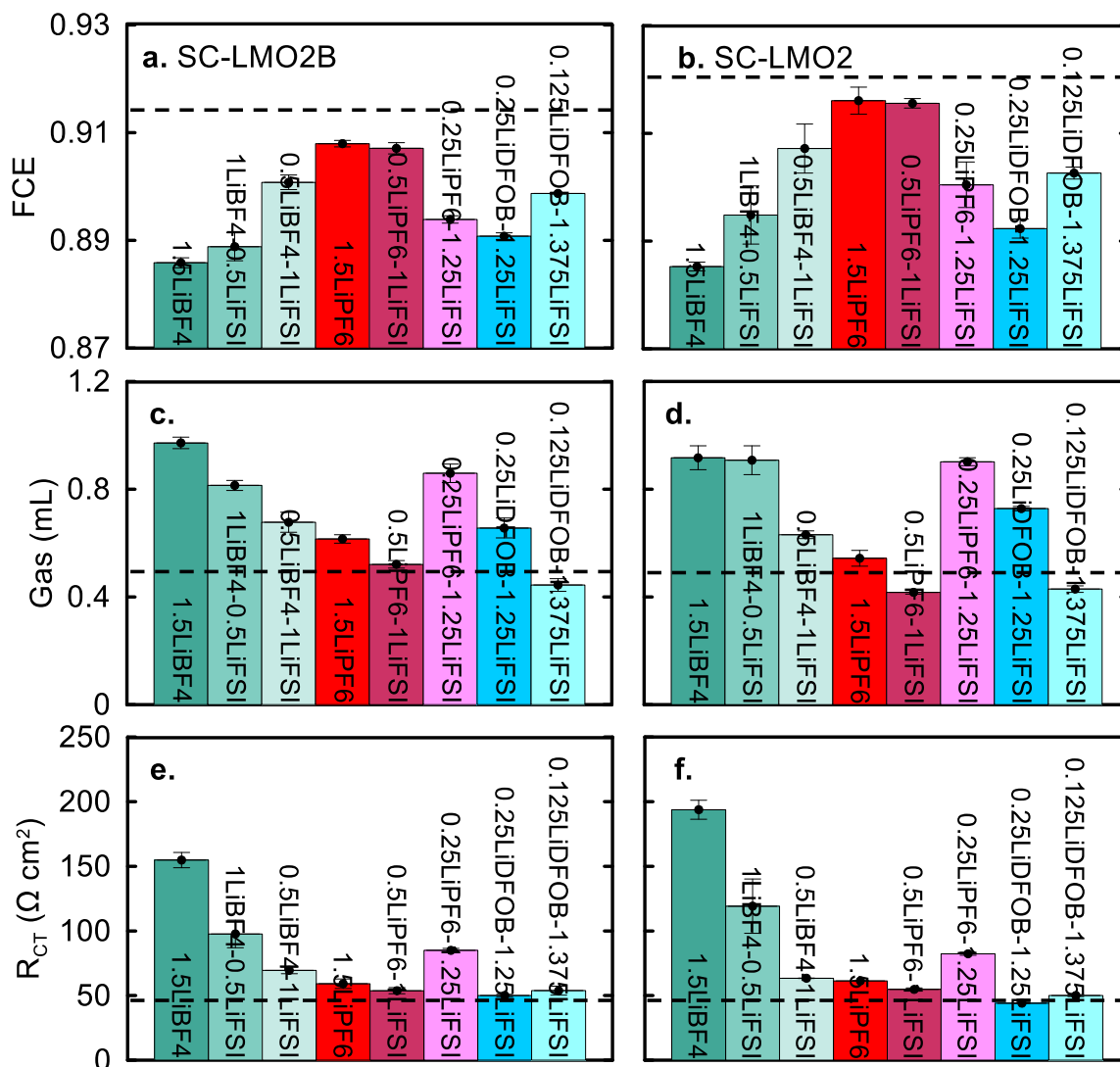
Figure 6.13. (a-b) FCE; (c-d) gas volume after formation (mL); and (e-f) R_{CT} after formation (Ω cm^2) for SC-LMO2B and SC-LMO2 pouch cells with different salt mixtures. The solvent was EC:DMC (15:85) with 3VC1DTD additive blend. Formation was done between 3.0-4.20 V at 40 °C and C/20:C/20. Dashed lines show data for equivalent cells with EC:EMC:DMC (25:5:70), 1.5 M LiPF$_6$ and 2VC1DTD electrolyte.

6.5. Galvanostatic Cycling at 40 °C and 55 °C

6.5.1. Long-term Cycling Results

To evaluate the impact of the different salt compositions on cell lifetime, long-term cycling at 40 °C and 55 °C was done followed by XRF analysis to quantify Mn and Al on the negative electrode, if any. Figure 6.14 shows the discharge capacity, normalized discharge capacity, and normalized ΔV for SC-LMO2 cells with different salt compositions. All cycling was done at 40 °C with C/3:C/3 charge:discharge in the 3.0-4.20 V range. The first column is the LiPF$_6$-LiFSI series, followed by the LiBF$_4$-LiFSI series and the LiDFOB-LiFSI series. The dashed line shows the number of cycles to 80 % capacity for a baseline SC-LMO2 cell with EC:EMC:DMC (25:5:70), 1.5 M LiPF$_6$, and 2VC1DTD (see Figure 6.2). This baseline cell had a different electrolyte (as indicated in the figure caption) from the "1.5LiPF$_6$" cells which had EC:DMC (15:85) and 3VC1DTD and is called 1.5LiPF$_6$ to distinguish it from the other cells in the mixed salt electrolyte series.

The ΔV growth for all SC-LMO2 cells was similarly large: ~75 % growth in about 1500 cycles, with the exception of 0.125LiDFOB-1.375LiFSI which had ~50 % ΔV growth. The 0.25LiPF$_6$-1.25LiFSI and 1.5LiPF$_6$ cells had the same capacity retention which was similar to the baseline shown in the dashed line: ~700 cycles to 80 % retention. The 0.5LiPF$_6$-1LiFSI mixture had a significantly improved retention which pushed the cycle life from ~700 to ~1100 cycles. For the LiBF$_4$-LiFSI series, all cells showed a capacity retention improvement over the

baseline and the 1.5LiPF$_6$ cells. There were no significant differences among the different LiBF$_4$-LiFSI cells, though. The LiBF$_4$-LiFSI cells reached 80 % retention at ~1000 cycles, just slightly less than the 0.5LiPF$_6$-1LiFSI cells, and they all showed a similar rate of ΔV growth. Finally, both mixtures in the LiDFOB-LiFSI series also showed a significant improvement over the baseline and the 1.5LiPF$_6$ cells. The 0.25LiDFOB-1.25LiFSI cells reached 80 % capacity after ~1050 cycles, while the 0.125LiDFOB-1.375LiFSI cells reached 80 % at ~1250 cycles.
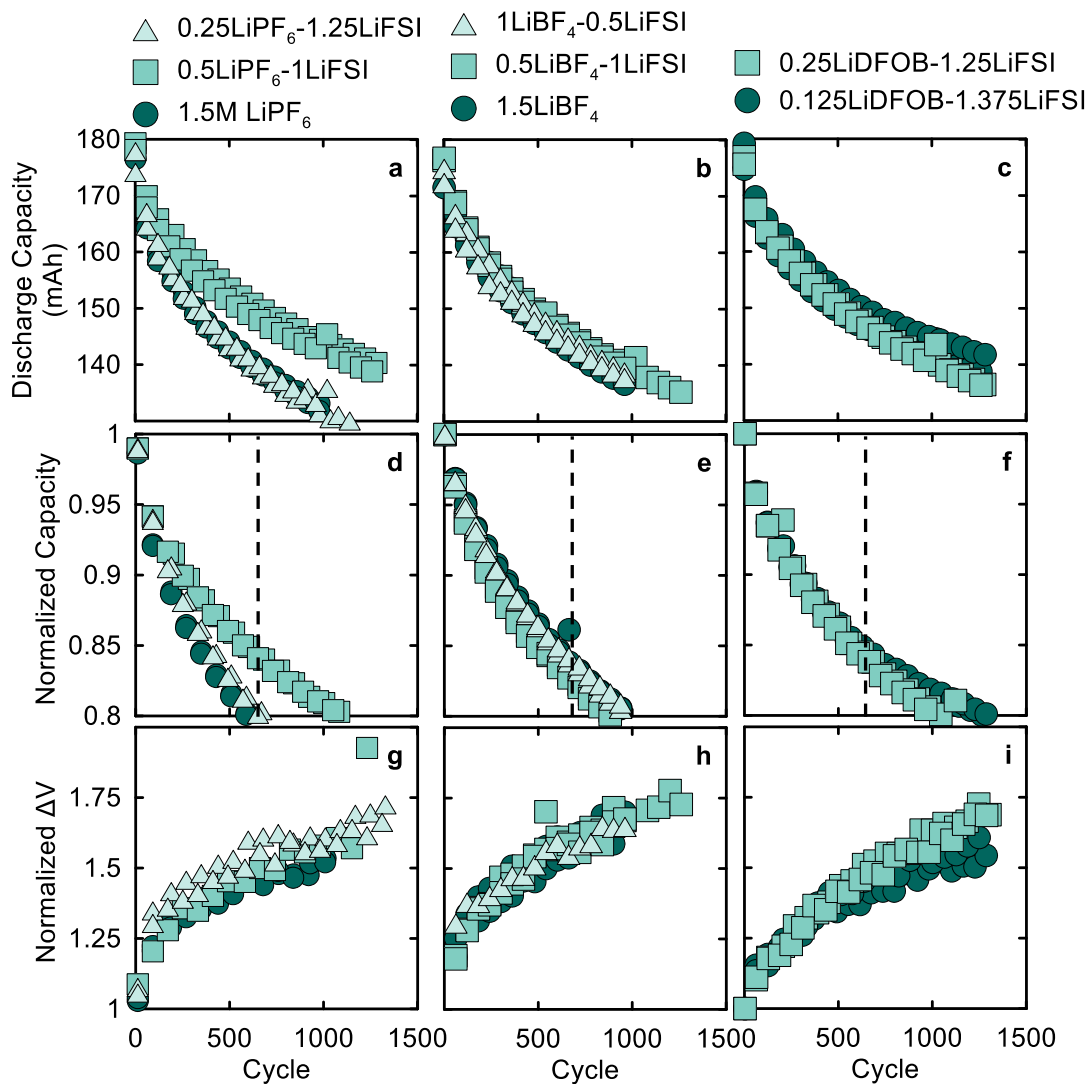
Figure 6.14. Discharge capacity (mAh), normalized discharge capacity, and normalized ΔV versus cycle number for the SC-LMO2 pouch cells cycled at 40 °C. Solvent was EC:DMC (15:85) with 3VC1DTD additive, and salt(s) as indicated above each column. Cycling was done at C/3:C/3 and 3.0-4.20 V. Dashed line shows the number of cycles to 80 % capacity for SC-LMO2 cell with EC:DMC:DMC (25:5:70), 1.5 M LiPF$_6$, and 2VC1DTD electrolyte.

Figure 6.15 shows the discharge capacity, normalized discharge capacity, and normalized ΔV growth for SC-LMO2B cells with different salt mixtures. As in Figure 6.13, the dashed line here represents number of cycles to 80 % retention for a SC-LMO2B cell with EC:EMC:DMC (25:5:70), 1.5 M $LiPF_6$, and 2VC1DTD electrolyte. Similar to the SC-LMO2 cells in Figure 6.14, we see improvements over the baseline with at least one salt mixture for each series. The 1.5$LiPF_6$ and 0.25$LiPF_6$-LiFSI cells had worse retention compared to the baseline. The cycle life for these cells was around 750 compared to ~1000 for the 2VC1DTD cell. However, the 0.5$LiPF_6$-1LiFSI mixture reached 85 % retention at ~1000 cycles and can possibly reach 80 % somewhere between 1500-2000 cycles, which will be a tremendous improvement over the 2VC1DTD cells, but their cycling was terminated for XRF analysis. Similarly, for the $LiBF_4$-LiFSI series, all cells reached 80 % capacity at around ~1100+ cycles compared to 1000 cycles for the baseline and ~750 for 1.5$LiPF_6$. Finally, the 0.25LiDFOB-1.25LiFSI and 0.125LiDFOB-1.375LiFSI cells reached 80 % and 85 % capacity, respectively, at cycle ~1200. The 0.125LiDFOB-1.375LiFSI cells are likely to reach 80 % in the 1500-2000 range similar to the 0.5$LiPF_6$-1LiFSI cells.
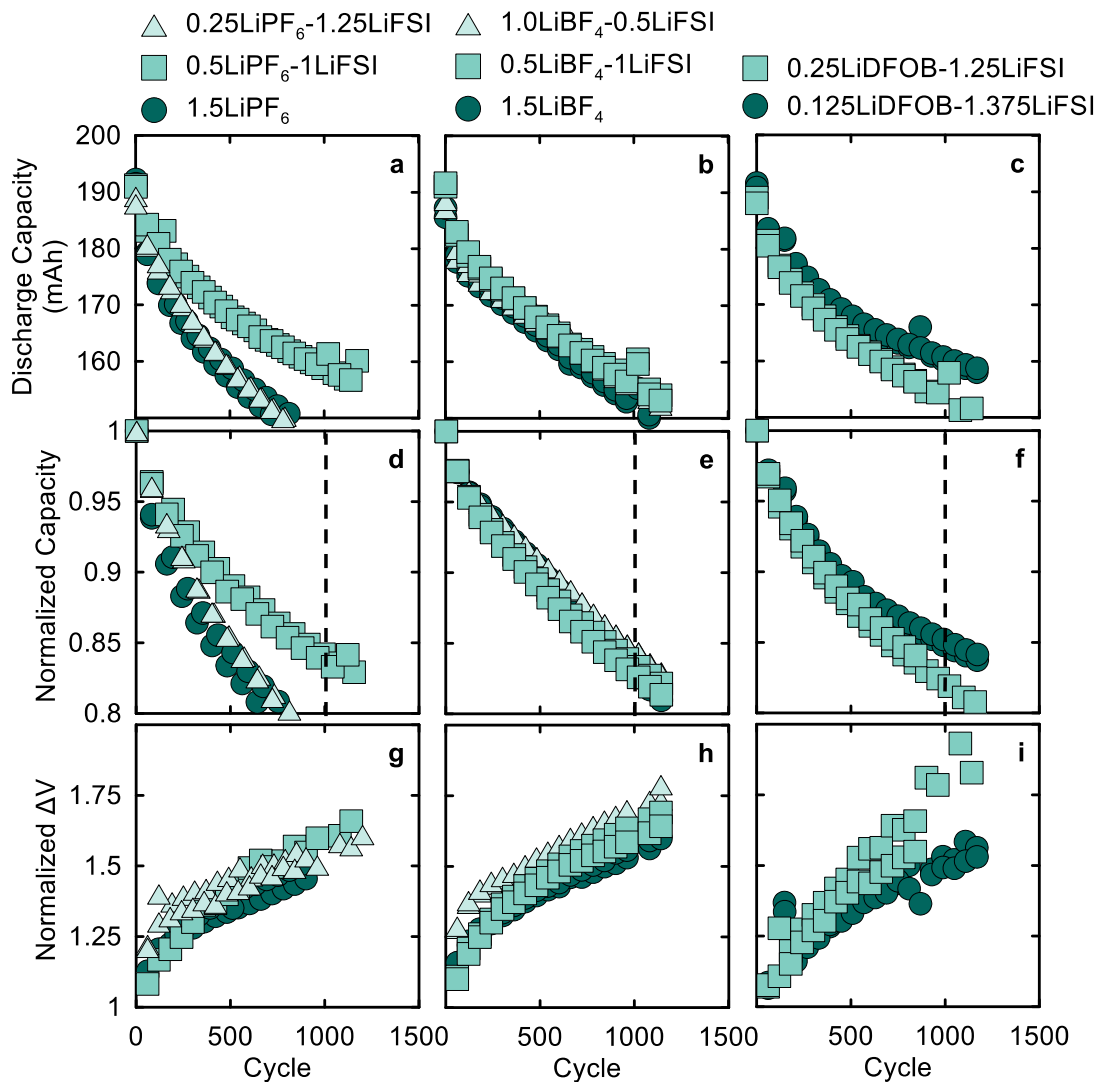
Figure 6.15. Discharge capacity (mAh), normalized discharge capacity, and normalized ΔV versus cycle number for the SC-LMO2B pouch cells cycled at 40 °C. Solvent was EC:DMC (15:85) with 3VC1DTD additive, and salt(s) as indicated above each column. Cycling was done at C/3:C/3 and 3.0-4.20 V. Dashed line shows the number of cycles to 80 % capacity for SC-LMO2B cell with EC:DMC:DMC (25:5:70), 1.5 M LiPF$_6$, and 2VC1DTD electrolyte.

Mixing LiFSI with LiPF$_6$, LiBF$_4$, or LiDFOB showed a lifetime improvement over LiPF$_6$ at 40 °C. It is unclear if the use of LiFSI co-salts can improve the lifetime compared to LiFSI only cells. However, the issues associated with LiFSI makes it impractical in LMO cells, so it was not considered as a baseline here. The ability of these salt mixtures to suppress Mn dissolution or Al corrosion will be discussed later.   Seeing the benefits of LiFSI co-salts at 40 °C, we sought to probe the cell lifetime at 55 °C for the same salt mixtures discussed above in SC-LMO2 and SC-LMO2B cells. Figure 6.16 shows the discharge capacity, normalized discharge capacity, normalized ΔV growth for SC-LMO2 cells cycled at 55 °C. The dashed line shows the cycles to 80 % for a baseline 2VC1DTD cell as shown in Figure 6.2. Unfortunately, the cycling terminated early for many 55 °C cells before reaching 80 % capacity due to a power failure that resulted in the cells sitting idle at ambient temperature without charge/discharging cycling for about 500 hours.

A notable difference at 55 °C compared to 40 °C is that there are minimal differences within each salt series. The LiBF$_4$-LiFSI series clearly performed worse than the 2VC1DTD baseline at 55 °C, which can be attributed to the poor passivation of LiBF$_4$ [24,163] which will be worse during high temperature operation. The cells in the LiPF$_6$-LiFSI series were on a trajectory to surpass the cycle life of the 2VC1DTD cell slightly, possibly by 50 cycles or so. The biggest notable improvement was in the 0.125LiDFOB-1.375LiFSI cell which reached 80 % capacity at cycle 400 compared to 300 for the 2VC1DTD baseline. The 0.125LiDFOB-1.375LiFSI cell showed ~50 % ΔV growth over 400 cycles, while the LiPF$_6$-LiFSI and LiBF$_4$-LiFSI cells showed the same growth over ~200 cycles. It is

important to note that the differences between 1.5LiPF$_6$ and the LiDFOB-LiFSI

cells (as well as other LiPF$_6$-LiFSI mixtures) are very small, so the changes to

solvent and additive composition could be contributing to the lifetime boost seen

at 55 °C as well.
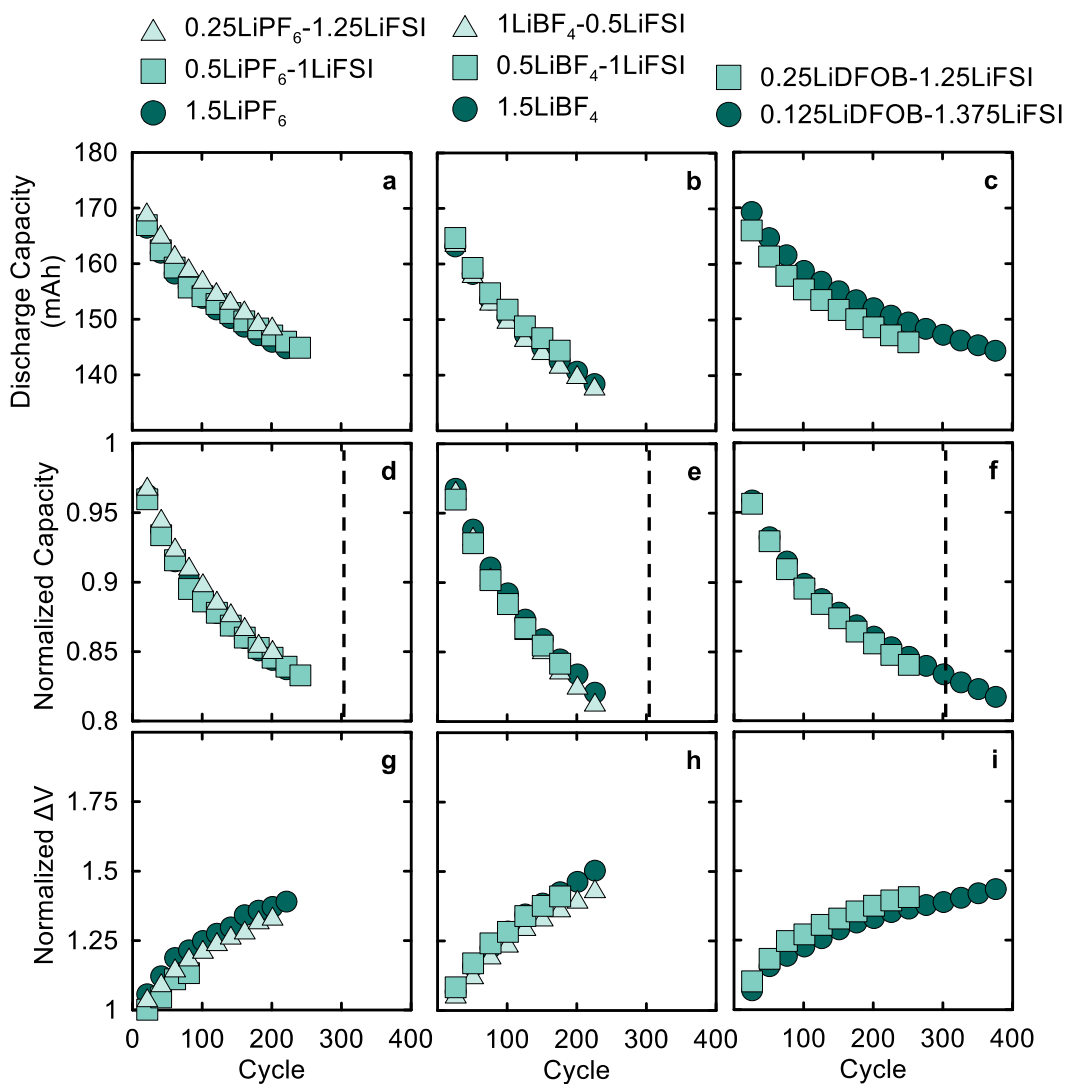
Figure 6.16. Discharge capacity (mAh), normalized discharge capacity, and normalized ΔV versus cycle number for the SC-LMO2 pouch cells cycled at 55 °C. Solvent was EC:DMC (15:85) with 3VC1DTD additive, and salt(s) as indicated above each column. Cycling was done at C/3:C/3 and 3.0-4.20 V. Dashed line shows the number of cycles to 80 % capacity for SC-LMO2 cell with EC:DMC:DMC (25:5:70), 1.5 M LiPF$_6$, and 2VC1DTD electrolyte.

Figure 6.17 shows the cycling results for SC-LMO2B at 55 °C. Here, the baseline was taken to be 2VC electrolyte, not 2VC1DTD, since 2VC significantly outperformed 2VC1DTD at 55 °C for SC-LMO2B (see Figure 6.2). Similar, to Figure 6.16, the $LiBF_4$-LiFSI cells did not show a significant improvement over baseline, and no major differences were seen within each salt series. The $LiPF_6$-LiFSI and LiDFOB-LiFSI salt mixtures are showing improved retention compared to the baseline. The LiDFOB-LiFSI cells reached 90 % capacity at cycle ~250 compared to ~190 for the $LiPF_6$-LiFSI cells, Overall, the SC-LMO2 and SC-LMO2B cells had poor performance at 55 °C but the choice of salt/electrolyte can introduce some small improvements.
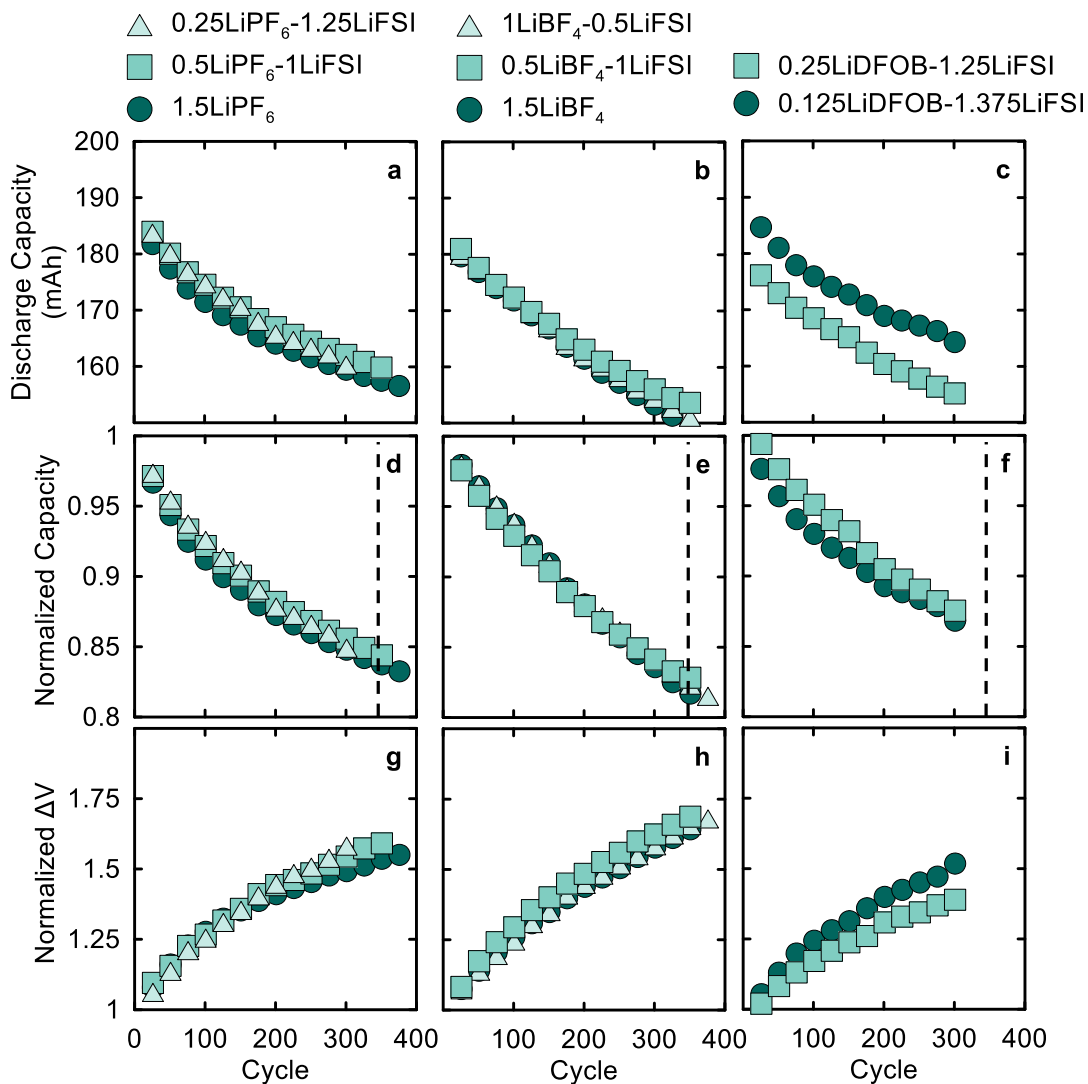
Figure 6.17. Discharge capacity (mAh), normalized discharge capacity, and normalized ΔV versus cycle number for the SC-LMO2B pouch cells cycled at 55 °C. Solvent was EC:DMC (15:85) with 3VC1DTD additive, and salt(s) as indicated above each column. Cycling was done at C/3:C/3 and 3.0-4.20 V. Dashed line shows the number of cycles to 80 % capacity for SC-LMO2B cell with EC:DMC:DMC (25:5:70), 1.5 M LiPF$_6$, and 2VC electrolyte. 2VC electrolyte was used as the baseline here because it significantly outperformed 2VC1DTD.

6.5.2. *XRF Analysis After Cycling*

After cycling at 40 °C and 55 °C, the negative electrodes from SC-LMO2 and SC-LMO2B cells underwent XRF analysis to quantify Mn on the negative electrode and look for signs of Al corrosion, if any, for the different salt mixtures. The Mn loading for the mixed salt cells will be compared to the equivalent 2VC1DTD cells which had EC:EMC:DMC (25:5:70), 1.5 M $LiPF_6$, and 2 % VC plus 1 % DTD as the electrolyte.

Figure 6.18 shows the Mn loading, Al loading, and capacity loss at the end of cycling for SC-LMO2B cells cycled at 40 °C. The cycle number achieved prior to XRF analysis is indicated for each of the pair cells. The dashed line in Figure 6.17a shows the Mn content for SC-LMO2B cell with 2VC1DTD, and the dashed line in Figure 6.17b shows the background Al levels measured on a pristine graphite electrode. Figure 6.17a shows that all cells had a significantly lower Mn loading compared to the baseline 2VC1DTD cell. Comparing the 1.5$LiPF_6$ cells to the baseline, we can see a ~4 $\mu g\ cm^{-2}$ reduction in Mn loading, which can be attributed to the increased VC content (3 % in 1.5$LiPF_6$ versus 2 % in the baseline) or the different solvent composition (EC:DMC 15:85 versus EC:EMC:DMC 25:5:70).

Figure 6.18. (a) Mn loading (μg cm^{-2}); (b) Al loading (μg cm^{-2}); and (c) capacity loss for SC-LMO2B cells cycled at 40 °C with different salt mixtures. The cycle number prior to XRF analysis is indicated for each cell. The dashed line in panel (a) show the Mn loading for SC-LMO2B cell with 2VC1DTD electrolyte. The dashed line in panel (b) represents the background Al levels in the XRF analysis. Pairs cells are shown for each electrolyte.

The EMC-free electrolyte will not be prone to alkyl carbonate transesterification, as opposed to EC:EMC:DMC. The transesterification reaction can generate diethyl carbonate (DEC), as well as DMC, which is initiated by the presence of lithium alkoxides (LiOR) species in the electrolyte[171]. The LiOR species are generated due to reactions between the electrolyte and lithiated graphite and can contribute to dimerization reactions between EC and linear alkyl carbonates as well[110,171]. Jarry et al showed that the electrochemical oxidation of DEC at the positive electrode surface results in the generation a soluble Ni or Mn bidentate complexes which can then migrate to the negative electrode where the Ni/Mn are deposited[168]. Therefore, it is possible that the reduction in Mn loading between the EC:EMC:DMC (25:5:70) cell and the EC:DMC (15:85) is due the suppression of alkyl carbonate transesterification which would produce DEC. Thompson et al quantified transesterification and TM dissolution in NMC532 and NMC622 and found that both the fraction of transesterification and TM dissolution increased with temperature and UCV[110]. However, more detailed studies of Mn loading as a function of solvent composition are needed to establish a correlation, if any.

For all SC-LMO2B cells, no Ni or Co from the NMC622 component was detected in our XRF analysis. In general, the Mn loading ranks as follows: $LiPF_6$-LiFSI series > LiDFOB-LiFSI series > $LiBF_4$-LiFSI series and no significant levels of Al were detected for any cell. For the $LiBF_4$-LiFSI series, the Mn loading increased slightly from ~4 $\mu g\ cm^{-2}$ to 5 $\mu g\ cm^{-2}$ with increasing LiFSI content. The $1LiBF_4$-0.5LiFSI cells had the best capacity retention and about 4.5 $\mu g\ cm^{-2}$. The

0.5LiBF$_4$-LiFSI cells had a slightly higher Al levels compared to the other cells in the series, but it did not result in any additional cell degradation according to Figure 6.17c. The B-F bonds in LiBF$_4$ are stronger than P-F bonds in LiPF$_6$, thus they are less prone to hydrolysis and are more thermally stable than LiPF$_6$[172]. The increase in Mn content in the LiPF$_6$ cells compared to the LiBF$_4$ cells might be attributed to the generation of difluoro phosphoric acid, HF, and other electrolyte LiPF$_6$-mediated electrolyte degradation products, all of which are thought to be a driver of TM dissolution in various Li-ion cell chemistries[36,53,54,106,173].

The LiPF$_6$-LiFSI series showed more Mn than the LiBF$_4$-LiFSI series, and 0.5LiPF$_6$-1LiFSI had the highest Mn content at ~8 μg cm^{-2}. To further complicate the impact of Mn dissolution on capacity loss, the 0.5LiPF$_6$-1LiFSI cells had the best retention but highest Mn loading despite cycling for a similar period of time as the 0.25LiPF$_6$-1.25LiFSI cell with 1235 cycles. These two cell types cycled for ~6800 hours, keeping in mind that 0.25LiPF$_6$-1.25LiFSI cells will complete a C/3:C/3 in under 6 hours as the cell loses more capacity so they will complete more cycles in the same period of time. This suggests that there could a more complex interplay between salt LiPF$_6$/LiFSI ratio and Mn dissolution which requires further work to understand.

Finally, looking at the LiDFOB-LiFSI series, the Mn loadings were comparable to the 0.25LiPF$_6$-LiFSI cells, but slightly less than the other cells in the LiPF$_6$ series. Overall, the LiDFOB-LIFSI cells with similar cycle number ~1180 had similar Mn loadings, despite the improved capacity retention seen in the 0.125LiDFOB-1.375LiFSI mixture. For the 0.25LiDFOB-1.25LiFSI cells, going from

229

871 cycles to 1187 increased capacity loss by about 10 % and increased the Mn loading by about ~1 μg cm^{-2}.

Similar trends can be seen in the SC-LMO2 cells compared to SC-LMO2B. Figure 6.19 shows the Mn loading, Al loading, and capacity loss at the end of cycling for SC-LMO2 cells cycled at 40 °C. Overall, the Al levels were similar to the background, so it is likely that no severe Al corrosion took place that resulted in Al deposition on the negative electrode. Once again, the LiBF$_4$-LiFSI mixtures were more effective at reducing Mn dissolution compared to LiPF$_6$-LIFSI and LiDFOB-LiFSI. The Mn levels for SC-LMO2 cells were slightly larger than SC-LMO2B since SC-LMO2B has a smaller LMO fraction. We see that the mixed salt electrolyte with EC:DMC 15:85 had lower Mn levels compared to the 2VC1DTD baseline. The outliers here are the 0.5LiPF$_6$-1LiFSI cells; however, they had about 500 cycles more than the baseline which can explain the larger Mn loading. Figure 6.19a shows again that the 0.5LiPF$_6$-1LiFSI mixture has the highest Mn loading despite having the best capacity retention for the LiPF$_6$-LiFSI series in Figure 6.19c. In SC-LMO2, 0.125LiDFOB-1.375LIFSI had the best capacity retention as seen in Figure 6.18c, but about a ~1-1.5 μg cm^{-2} more Mn compared to 0.25LiDFOB-1.25LiFSI.
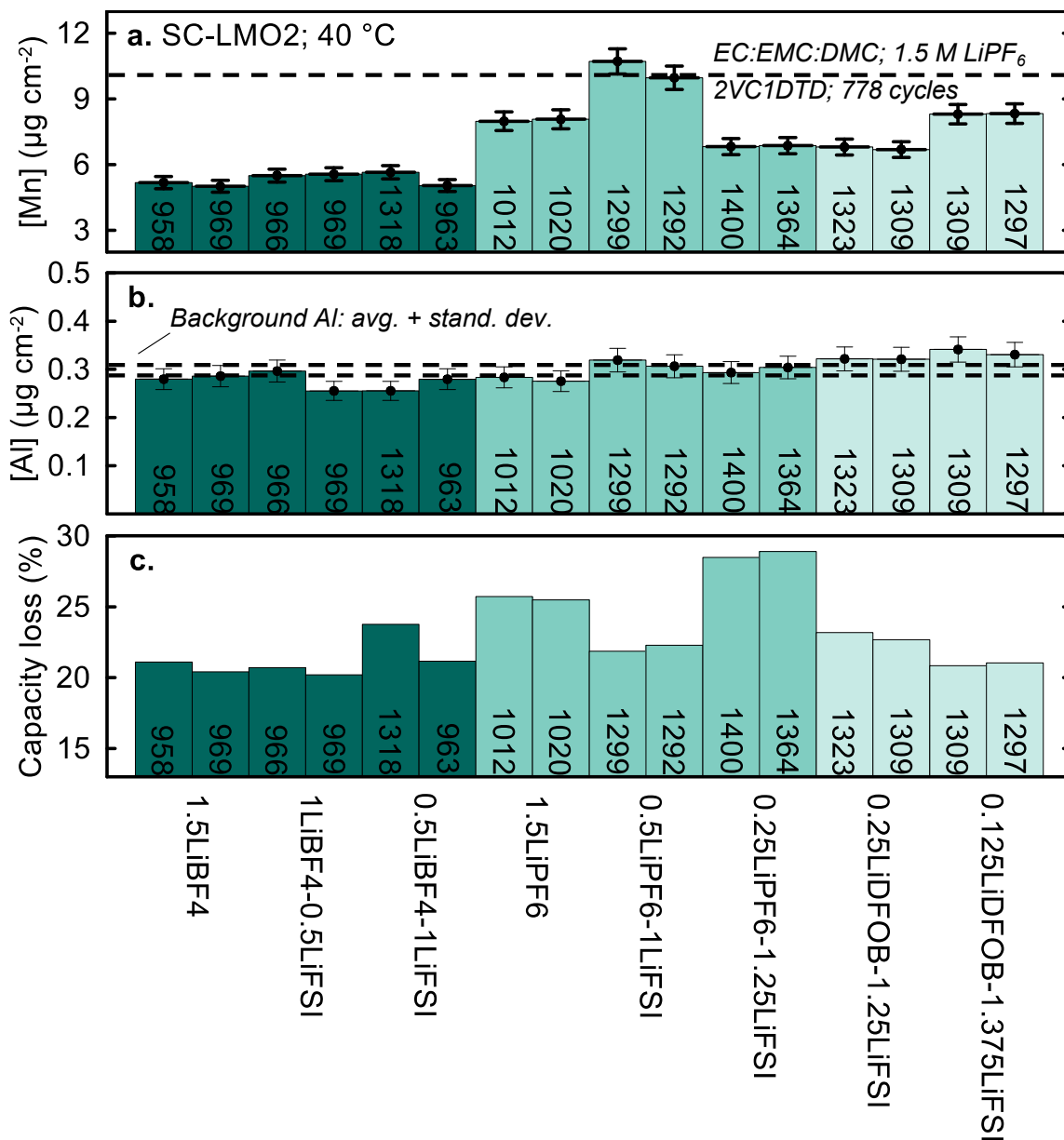
Figure 6.19. (a) Mn loading (μg cm^{-2}); (b) Al loading (μg cm^{-2}); and (c) capacity loss for SC-LMO2 cells cycled at 40 °C with different salt mixtures. The cycle number prior to XRF analysis is indicated for each cell. The dashed line in panel (a) show the Mn loading for SC-LMO2 cell with 2VC1DTD electrolyte. The dashed line in panel (b) represents the background Al levels in the XRF analysis. Pairs cells are shown for each electrolyte.

231

After 55 °C cycling, SC-LMO2B and SC-LMO2 cells underwent XRF analysis to probe the impact of temperature on Mn dissolution. Figure 6.20 shows the Mn loading, Al loading, and capacity loss at the end of cycling for SC-LMO2B cells cycled at 55 °C. Similar to the 40 °C results, we see a reduction in Mn with EC:DMC 15:85 compared to EC:EMC:DMC 25:5:70 as the solvent. Figure 6.19a shows that Mn loading increases from ~4.5 μg cm^{-2} to 6 μg cm^{-2} as the LiFSI content increases in the LiBF$_4$-LiFSI series. This is similar to the Mn loading for the equivalent 40 °C cells in Figure 6.18, but with roughly one third the number of cycles. In fact, all the mixed salt cells show a similar level of Mn at 55 °C compared to 40 °C, but after significantly fewer cycles. Overall, the trends at 55 °C are similar to the ones at 40 °C in Figure 6.18.
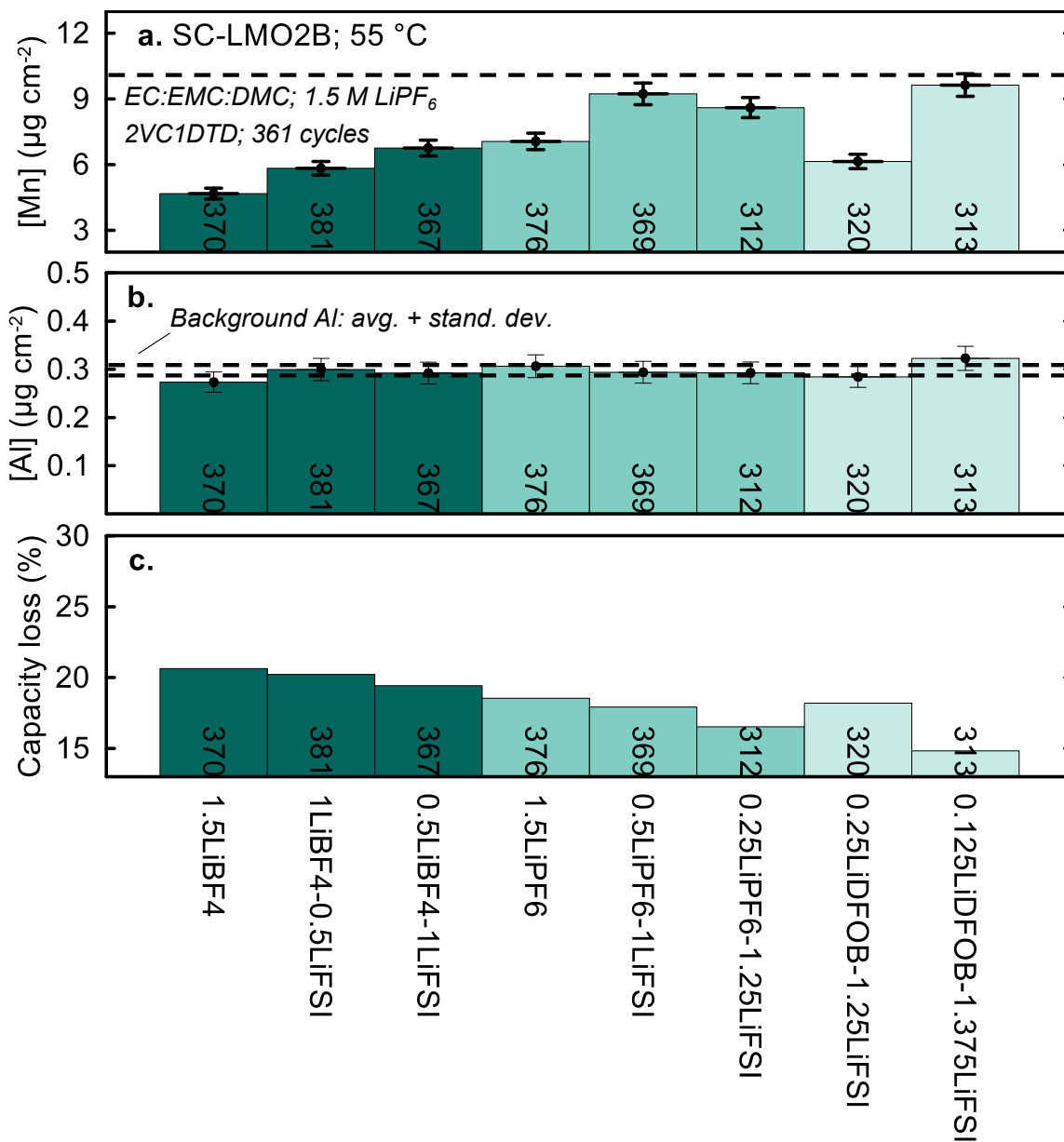
Figure 6.20. (a) Mn loading (μg cm⁻²); (b) Al loading (μg cm⁻²); and (c) capacity loss for SC-LMO2B cells cycled at 55 °C with different salt mixtures. The cycle number prior to XRF analysis is indicated for each cell. The dashed line in panel (a) show the Mn loading for SC-LMO2B cell with 2VC1DTD electrolyte. The dashed line in panel (b) represents the background Al levels in the XRF analysis.

Figure 6.21 shows the Mn loading, Al loading, and capacity loss at the end of cycling for SC-LMO2 cells cycled at 55 °C. The Mn loadings for SC-LMO2 cells are greater than the equivalent SC-LMO2B cells in Figure 6.19, especially considering that these cells generally cycled for less time compared to SC-LMO2B. Once again, we see similar changes in Mn loading as a function of salt composition as discussed above. The only difference in Figure 6.21 is that the highest Mn loading in the $LiPF_6$-LiFSI series was seen in the $0.25LiPF_6$-$1.25LiFSI$ cell, which was around 1 $\mu g\ cm^{-2}$ greater than $0.5LiPF_6$-$1LiFSI$. However, since duplicate cells were not possible at this temperature due to limited channel availability, more work is needed to confirm if this points to a difference in cell degradation or simply cell to cell variation.
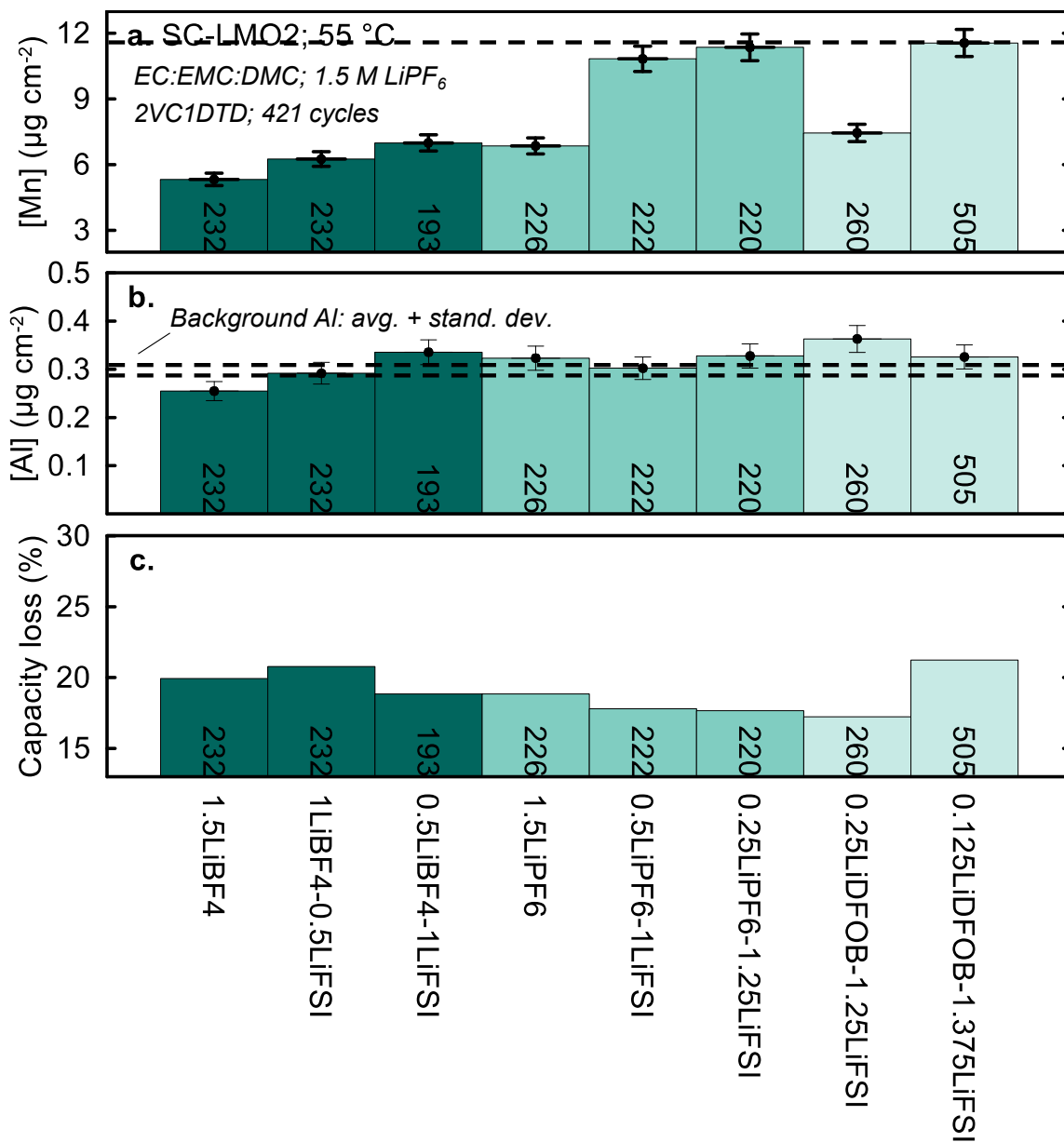
Figure 6.21. (a) Mn loading (μg cm^{-2}); (b) Al loading (μg cm^{-2}); and (c) capacity loss for SC-LMO2 cells cycled at 55 °C with different salt mixtures. The cycle number prior to XRF analysis is indicated for each cell. The dashed line in panel (a) show t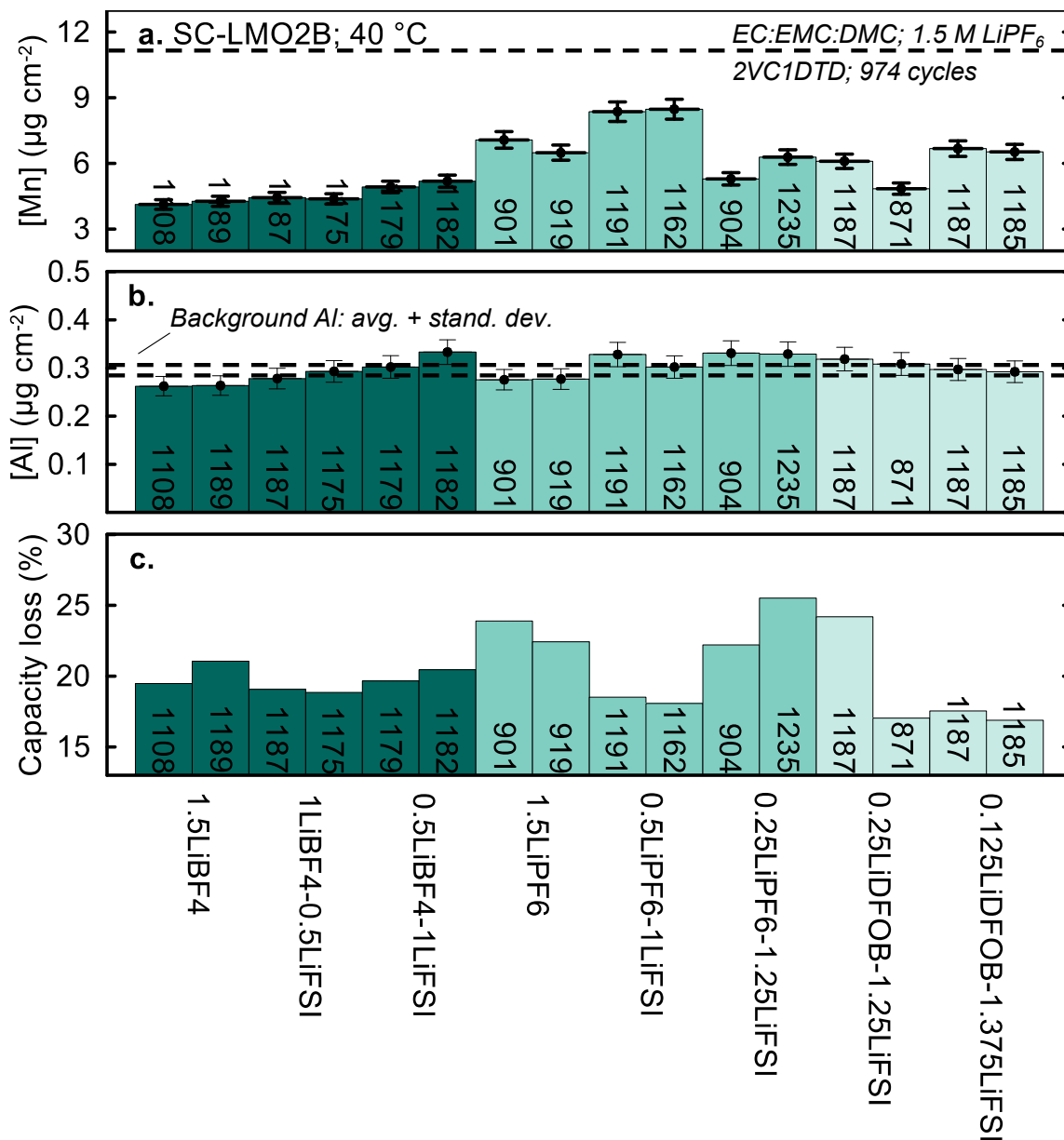he Mn loading for SC-LMO2 cell with 2VC1DTD electrolyte. The dashed line in panel (b) represents the background Al levels in the XRF analysis.

6.5.3. In-operando Gas Volume Measurements

The salt composition can greatly influence capacity loss and Mn dissolution in LMO cells as seen above. However, the utility of the electrolyte system will be under scrutiny if it results in severe gas generation and cell volume expansion during operation. Therefore, *in-operando* gas volume measurements were done to look at gas generation during cell operation. Unfortunately, due to a combination of limited channels and unplanned power failures, no data was collected for the $LiPF_6$-LiFSI series. However, visual inspection of these cells showed no noticeable amount of gas during cycling as noted prior to disassembly for XRF. Cells were cycled between 3.0-4.20 V and held at 4.20 V for 24 hours to accelerate degradation for the *in-operando* gas volume measurements.

Figure 6.22 shows the gas volume during cycling at 40 °C for SC-LMO2 cells with different $LiBF_4$-LiFSI mixtures and 0.125LiDFOB-1.375LiFSi as well as the voltage versus time profile. Figure 6.22b shows the impact of increasing LiBF4 content on gassing. As expected, due to the poor ability of $LiBF_4$ to passivate the SEI, increasing the $LiBF_4$ content resulted in an increase in the gas volume at 40 °C, which went from ~0.2 mL after 250 hours of cycle-hold testing for $0.5LiBF_4$-1LiFSI to ~0.45 mL for $1.5LiBF_4$. The capacity loss and Mn loading for the $LiBF_4$-LiFSI series cells at 40 °C were similar regardless of the $LiBF_4$ content, therefore $0.5LiBF_4$-1LiFSI is the more practical combination due to the lower gassing.

Figure 6.22c shows the main problem associated with LiDFOB which is the tremendous amount of gas generation, since its oxidative decomposition produces 2 moles of CO_2 for each mole of salt[170]. After only 250 hours at 40 °C, the 0.125LiDFOB-1.375LiFSI cells showed about 2 mL of gas generation despite the competitive capacity retention and Mn loading. More studies using a small LiDFOB fraction, or additives that can suppress gas generation, will be of value if LiDFOB-LiFSI mixtures are to be used in LMO/Graphite cells.
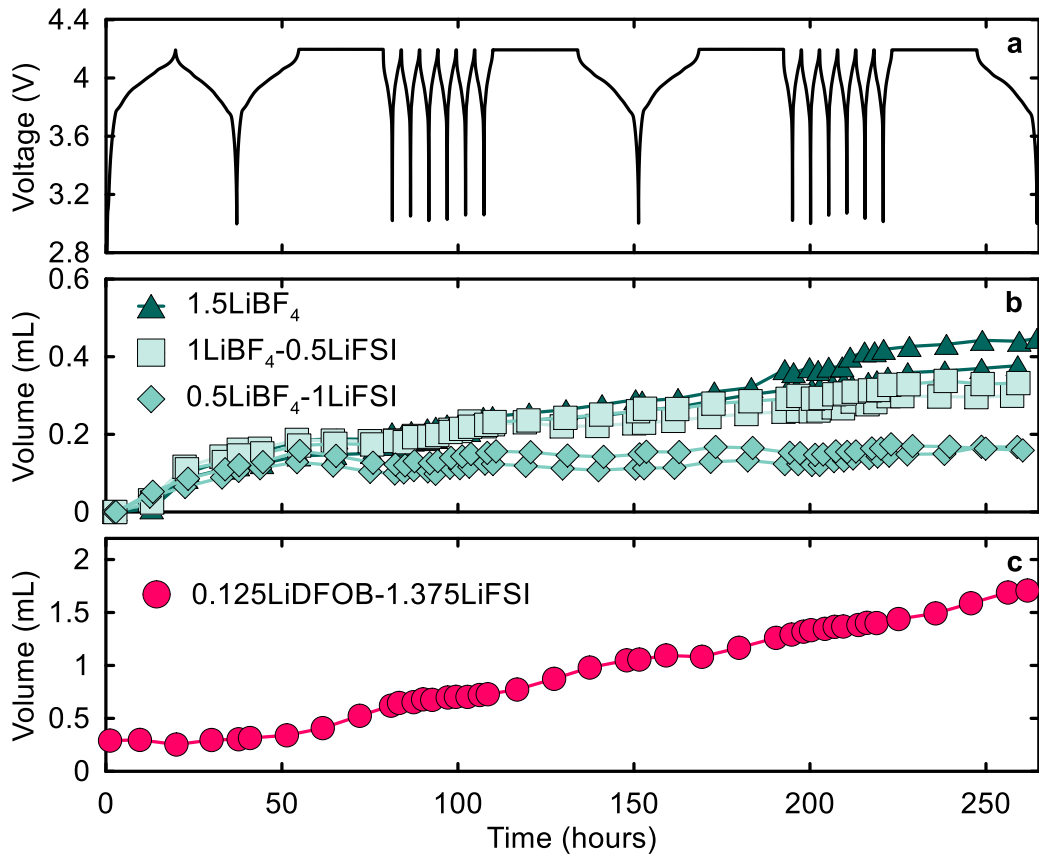
Figure 6.22. (a) voltage (V) versus time (hours); and cell volume after formation (mL) versus time (hours) for SC-LMO2 cells with (b) LiBF4-LiFSI salt blends or (c) 0.125LiDFOB-1.375LiFSI. The first formation cycle was done at C/20:C/20 and subsequent cycles were done at C/3:C/3. Voltage range was 3.0-4.20 V. The *in-operando* gas measurement was done at 40 °C.

6.6. Conclusion

In this chapter, the performance and degradation of different SC LMO pouch cells was studied. The main findings of this chapter can be summarized as follows:

1. Initial screening of the cell performance using common electrolyte formulations previously used in Chapter 5 showed that VC-containing electrolytes generally outperformed PES211 and 2FEC1LFO;

2. SC-LMO2 cells with a larger D50 particle size compared to SC-LMO show improved capacity retention during long-term cycling at RT and 40 °C, but not at 55 °C and 70 °C. The reason behind the poor high-temperature performance is unclear but can likely be attributed, at least partially, to the observed particle cracking in pristine SC-LMO2 positive electrodes. The larger particles in the SC-LMO2 appear to be more prone to cracking during electrode calendaring, so more work to optimize the electrode fabrication process and/or particle size is necessary here;

3. The blended SC-LMO2B pouch cells, which had a 25 % NMC622/75 % SC-LMO2 positive electrode, did not show signs of NMC/LMO synergy seen in Chapter 5 for PC-LMO2 material. With the exception of capacity retention at 70 °C, blending NMC622 did not appear to improve capacity retention at lower temperatures in any way that points to a favourable synergy between the two materials. NMC blending has been shown to hinder the degradation of LMO materials[153], so it is possible that the SC-LMO2 materials were relatively stable at temperatures below 70 °C which resulted in no noticeable synergy at lower temperatures;

4. UHPC cycling at 40 °C followed by XRF analysis showed a correlation between fade rate and Mn loading on the negative electrode, and a correlation between slippage and Mn loading for PES211 and 2FEC1LFO containing cells;

5. Mixed salt electrolytes were studied to probe the impact of salt choice on SC-LMO2 and SC-LMO2B cell lifetime. We showed the increasing the $LiBF_4$ content in $LiBF_4$-LiFSI mixtures results in more gassing after formation, lower FCE, and higher R_{CT}. For the $LiPF_6$-LiFSI series, using a $0.5LiPF_6$-1LiFSI composition resulted in high FCE, lowest gassing, and comparable R_{CT} to $1.5LiPF_6$. Increasing the LiDFOB content in the LiDFOB-LiFSI series resulted in more gassing and lower FCE, but RCT was unchanged and similar to $1.5LiPF_6$;

6. Long-term cycling at 40 °C shows that $0.5LiPF_6$-1LiFSI had the best capacity retention compared to $1.5LiPF_6$ and $0.25LiPF_6$-1.25LiFSI, which also outperformed the 2VC1DTD baseline cell. All the $LiBF_4$-LiFSI series cell performed similarly well and had better capacity retention compared to the baseline. For the LiDFOB-LiFSI series, 0.125LiDFOB-1.375LiFSI stood out compared to 0.25LiDFOB-1.25LiFSI and also outperformed the baseline cell;

7. Long-term cycling at 55 °C shows very small differences within each salt series. The $LiBF_4$-LiFSI cells did not outperform the baseline by a significant margin. However, the $LiPF_6$-LFSI series and LiDFOB-LiFSI series showed improved capacity retention compared to the baseline;

8. XRF on mixed salt cells after 40 °C and 55 °C cycling showed that $1.5LiPF_6$ (which used EC:DMC 15:85 as the solvent) had significantly less Mn compared to the baseline (which used EC:EMC:DMC 25:5:70 as the solvent and 1.5 M $LiPF_6$). This can be attributed to the lack of transesterification in the EC:DMC 15:85 blend which prevents the generation of DEC, or possibly the increased VC loading in the mixed salt cells. Previous reports showed that transesterification and TM dissolution increased at elevated temperatures and UCVs[110], and that DEC can result in the formation of soluble Ni or Mn bidentate complexes[168]. However, more work is needed to establish a correlation between transesterification, solvent composition, and Mn dissolution to validate this claim;

9. XRF analysis showed that, in general, $LiBF_4$-LiFSI cells had a low Mn loading, especially compared to $LiPF_6$-LiFSI, which points to the detrimental role $LiPF_6$ plays in the cell due to the salt hydrolysis at elevated temperatures and subsequent $LiPF_6$-mediated electrolyte or electrode degradation;

10. Overall, none of the mixed salt cells showed signs of significant Al corrosion due to the use of LiFSI when the cells were operated at 40 °C and 55 °C and 4.20 V UCV;

11. Despite the good capacity retention and low Mn dissolution using the LiDFOB-LiFSI salt mixtures, gas generation during cycle-hold testing at 40 °C showed that even just 0.125 M of LiDFOB results in 2 mL of gas after formation in 250 hours of testing. $LiBF_4$-LiFSI cells showed that increasing

the LiBF$_4$ content resulted in more gassing but was less than 0.5 mL for 1.5LiBF$_4$ cells. Overall, the LiPF$_6$-LiFSI visually did not show severe gassing after 40 °C and 55 °C cycling prior to disassembly for XRF, so they were omitted from the *in-operando* gas measurements due to limited channel availability. The severe gassing behavior of LiDFOB may make it difficult to use in practical cell designs without the use of gas-suppressing additives.

This chapter can serve as a guide for the use of mixed salt electrolyte in LMO/AG cells, where three salt mixtures proved to be very useful in LMO/AG cells. The best 0.5LiPF$_6$-1LiFSI had the best capacity retention in the LiFSI-LPF$_6$ series, as well as acceptable formation gassing, FCE, and R$_{CT}$. In the LiBF$_4$-LiFSI cells, the 0.5LiBF$_4$-1LiFSI mixture showed competitive capacity retention and great reduction in Mn dissolution compared to 0.5LiPF$_6$-1LiFSI. The best capacity retention was seen in the 0.125LiDFOB-1.375LiFSI electrolyte, however, it produced a lot of gas with 3VC1DTD so exploring gas-supressing additive blends will be very important.

Chapter 7. Cycling and Storage Performance of LFP/Graphite Cells with Mixed Salt Electrolytes

The results shown in this chapter are part of a manuscript that is in-progress. A. Eldesoky conceived and planned all experiments presented here, completed the data analysis with supervision from J. R. Dahn. A. Eldesoky carried out all XRF measurements according to the method developed for this thesis and published in *A. Eldesoky et al* 2020 *J. Electrochem. Soc. 167 130539*. H. Ni prepared the electrolyte recipes and filled the cells.

7.1. Introduction

LFP positive electrode materials provide a cheap, but lower energy, alternative to the layered oxide class of materials. The low cost of this material and abundance of iron has reignited interest in LFP from various automakers[174]. Previous work from our group showed that the lifetime of LFP/AG cells is considerably worse than a comparable NMC532 cell cycled to 4.30 V UCV, which is striking since LFP operates at a maximum voltage of 3.65 V and one would expect it to have a significantly lower rate of parasitic reactions based on the low UCV[175]. Therefore, it is important to probe different ways to improve the lifetime of LFP cells and understand their failure mechanism.

Numerous reports have shown that LFP cells suffer from severe Li inventory loss at elevated temperatures during cycling and/or storage[176–178]. Another contributor to capacity fade in LFP/Graphite cells is the dissolution of Fe and deposition on the negative electrode. Li et al used XPS to show that Fe dissolved

during 60 °C storage is embedded within the SEI layer and significantly contributes to increased rate of SEI growth[179]. Numerous works in the literature also point to Fe dissolution as a major contributor to capacity loss[176,180,181]. It has been shown that the hydrolysis of $LiPF_6$ and subsequent generation of acidic species is responsible for Fe dissolution in LFP cells[180,182,183]. This has been corroborated by various studies that showed a strong correlation between Fe/TM dissolution and water content in the cell[161,175,184]. Therefore, studying the impact of salt choice on LFP cells lifetime and Fe dissolution is critical to improving cell lifetime and storage performance.

Chapters 5 and 6 showed that using $LiBF_4$, LiDFOB, $LiPF_6$, and LiFSI salt mixtures can improve cell lifetime and hinder Mn dissolution at 40-60 °C. Similarly, Logan et al showed that LiFSI alone outperforms $LiPF_6$ in long-term cycling of LFP/AG cells at 20-55 °C[82], but mixtures of LiFSI and $LiBF_4$/LiDFOB were not explored in this work. In this chapter, we studied the impact of $LiBF_4$-LiFSI and LiDFOB-LiFSI salt mixtures (compared to $LiPF_6$) on the lifetime and degradation of LFP/AGC cells. The AGC material is the same as the one discussed in Chapter 3. Long-term cycling at 70 °C was used to quickly probe the impact of the salt mixture on cell lifetime, which was done at C/3:C/3 between 2.5-3.65 V. UHPC cycling was used to measure small differences in CE, fade, and slippage for the different salt mixtures, and OCV storage was used to measure self-discharge and capacity loss during storage at 60 °C. Cell specifications and electrolytes are shown in Tables 7.1-2.

Table 7.1. Cell specifications for the LFP/AGC pouch cells used in this chapter.

Neg. electrode	Loading (mg cm^{-2})	Composition	Density (g cm^{-3})	Pos. electrode	Loading (mg cm^{-2})	Composition	Density (g cm^{-3})
AGC	9.4	96:3:1 graphite:CMC/SBR:CB	1.41	LFP	18.2	96:2:2 LFP:PVDF:CB	2.31

Cu current collector thickness (µm)			8				
Al current collector thickness (µm)			16				
Nominal cell capacity (mAh)			~240 or ~550 (cylindrical cells, used in OCV storage))				
Operating range (V)			2.5-3.65				
Excess graphite capacity at 3.65 V (%)			15				

Table 7.2. List of electrolytes used in this chapter.

Name	Salt	Solvent (wt. ratio)	Additive (wt.%)
1.5LiPF$_6$	1.5 M LiPF$_6$	EC:EMC:DMC (25:5:70)	2 % VC 1 % DTD
1.5LiBF$_4$	1.5 M LiBF$_4$		
1LiBF$_4$-0.5LiFSI	1.0 M LiBF$_4$ + 0.5 M LiFSI		
0.5LiBF$_4$-1.0LiFSI	0.5 M LiBF$_4$ + 1.0 M LiFSI		
0.25LiBF$_4$-1.25LiFSI	0.25 M LiBF$_4$ + 1.25 M LiFSI		
0.125LiBF$_4$-1.375LiFSI	0.125 M LiBF$_4$ + 1.375 M LiFSI		
1.5LiFSI	1.5 M LiFSI		
1.25LiFSI-0.25LiDFOB	1.25 M LiFSI + 0.25 M LiDFOB		
1.375LiFSI-0.125LiDFOB	1.375 M LiFSI + 0.125 M LiDFOB		
1.4LiFSI-0.1LiDFOB	1.4 M LiFSI + 0.1 M LiDFOB		
1.45LiFSI-0.05LiDFOB	1.45 M LiFSI + 0.05 M LiDFOB		

7.2.   FCE, Post-formation Gassing, and R_{CT}

During the first formation charge, Li$^+$ and some electrolyte components will be irreversibly consumed to form the initial SEI layer. Figure 7.1 shows the dQ/dV versus voltage plot for the first formation charge for LFP/Graphite cells with different salt mixtures. The formation cycle was done at C/20:C/20 between 2.5-3.65 V at 40 °C. The solvent was EC:DMC:DMC (25:5:70) with 2VC1DTD additive blend. The peaks in Figure 7.1 correspond to electrolyte reduction activity. The VC reduction peak is around 2.6 V versus graphite, while the DTD reduction peaks can be seen at 2.4 V and 2.7 V versus graphite and the combination of VC and DTD yields two peaks at 2.4 and 2.65 V[185].
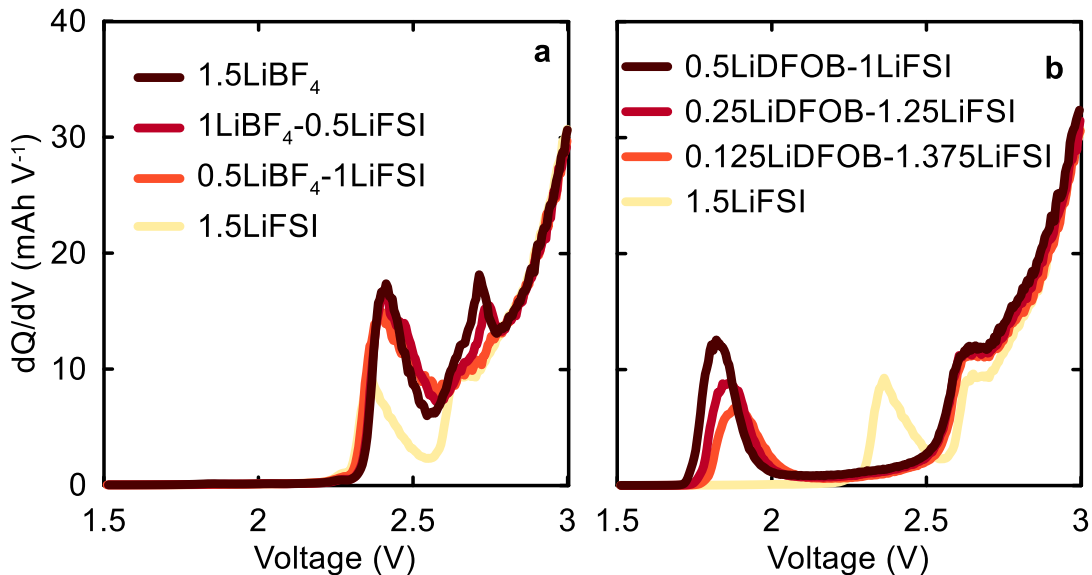
Figure 7.1. dQ/dV (mAh V^{-1}) versus voltage (V) during the formation charge for LFP/AGC pouch cells with different salt mixtures. Solvent was EC:EMC:DMC (25:5:70) with 2VC1DTD additive blend. Formation was done at 40 °C with C/20:C/20 charge:discharge rates between 2.5-3.65 V.

Figure 7.1a shows that the addition of LiBF$_4$ resulted in more electrolyte reduction compared to LiFSI only. This is consistent with previous reports showing that LiBF$_4$ does not effectively passivate the SEI[163,172], therefore more electrolyte consumption can occur in LiBF$_4$-containig cells. Figure 7.1b shows that LiDFOB is reduced around 1.8 V versus graphite and the reduction peaks shifts to higher voltage as the LiDFOB content decreases. The addition of LiDFOB suppresses the reduction peak at 2.4 V corresponding to DTD reduction, and the intensity of the VC peak at 2.6 V increases slightly compared to LiFSI only.

Figure 7.2 shows the FCE, gas after formation, and R$_{CT}$ versus LiFSI content for the LiBF$_4$-LiFSI and LiDFOB-LiFSI mixtures. The dashed line shows the results for LiPF$_6$-only cell. For the LiBF$_4$-LiFSI series, the addition of LiBF$_4$ lowers FCE from ~95 % (for 1.5LiFSI or 1.5LiPF$_6$) to 93.5 % for 1.5LiBF$_4$, along with an increase in gassing (from 0.2 mL to ~0.85 mL) and an increase in R$_{CT}$ (from 50 Ω cm^2 to 250 Ω cm^2). For the LiDFOB-LiFSI mixtures, the FCE decreases linearly as the LiDFOB content increases (95 % to 92.5 %). The 0.5LiDFOB-1LiFSI cells had 0.5 mL of gas which was reduced to ~0.2 mL with smaller LiDFOB fraction and remained constant for the rest of the cells in the series. The R$_{CT}$ was relatively unchanged regardless of the LiDFOB content and was similar to 1.5LiFSI and 1.5LiPF$_6$.
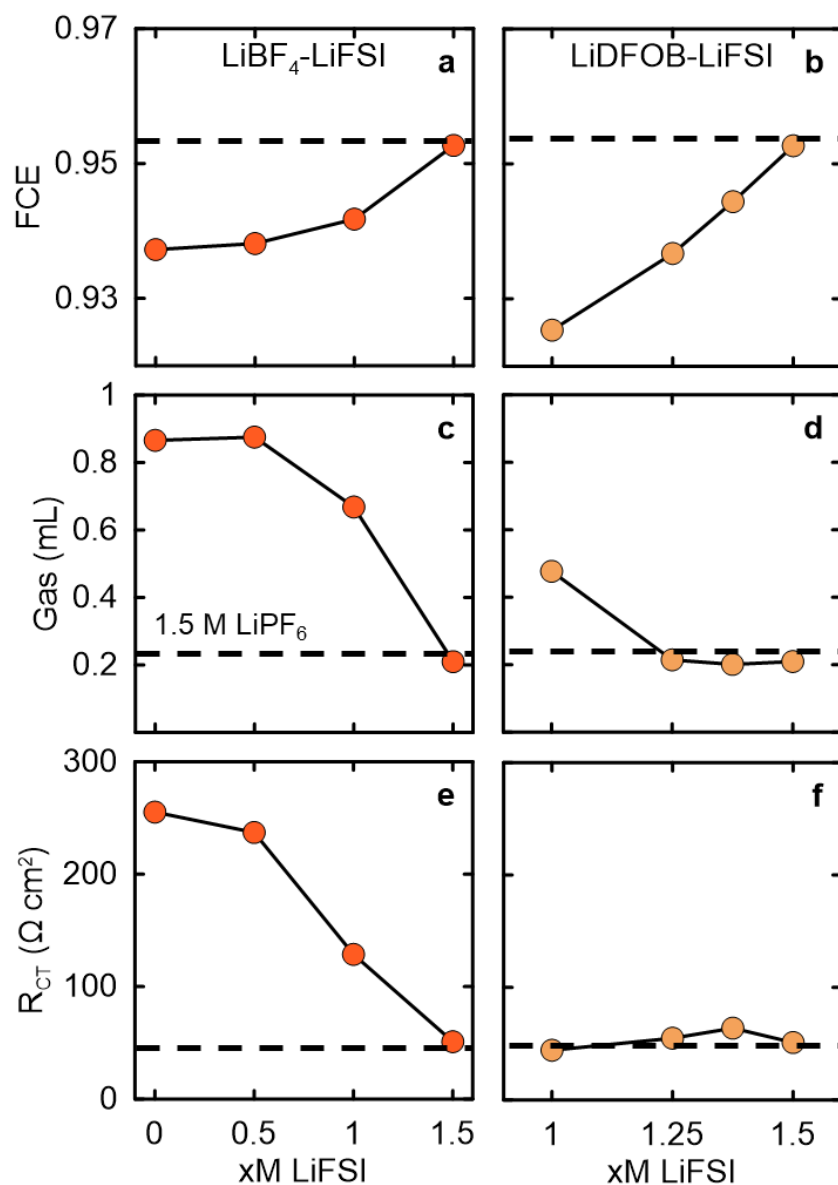
Figure 7.2. (a-b) FCE; (c-d) gas volume after formation (mL); and (e-f) R_{CT} (Ω cm^2) versus LiFSI content for LFP/AGC cells with LiBF$_4$ or LiDFOB co-salts. Solvent was EC:EMC:DMC (25:5:70) with 2VC1DTD additive blend and total salt concentration in 1.5 M. Formation was done at 40 °C with C/20:C/20 charge:discharge rates between 2.5-3.65 V. Dashed line shows post-formation results for an identical cell with 1.5 M LiPF$_6$.

7.3. Galvanostatic Cycling at 70 °C

7.3.1. Cycling Results at 70 °C

Galvanostatic cycling at 70 °C is effective in rapidly screening cell performance since the cells degrade relatively quickly at this temperature. Figure 7.3 shows the discharge capacity, normalized discharge capacity, and normalized ΔV versus cycle number for LFP/AGC cells. All cycling was done at 70 °C with C/3:C/3 charge:discharge rates between 2.5-3.65 V. The cycling results for 1.5LiPF$_6$ are shown in the dashed line. For the LiBF$_4$-LiFSI series, the 1.5LiBF$_4$ cells reached 80 % capacity after only 200 cycles. The 1LiBF$_4$-0.5LiFSI and 1.5LiFSI cells had a very similar capacity retention and are on track to reach 80 % capacity around cycle 500. The 1.5LiPF$_6$ and 0.5LiBF$_4$-1LiFSI cells had similar capacity fade as well and will reach 80 % capacity at cycle 800. In this series, LiBF$_4$-LiFSI mixtures did not significantly improve the cell performance compared to 1.5LiPF$_6$. Given the FCE, gassing, and R$_{CT}$ penalty that comes with the use of LiBF$_4$, it seems more practical to use LiPF$_6$ or a 1:1 mixture of LiPF$_6$:LiFSI which may outperform LiPF$_6$ and LiFSI alone at 70 °C according to Logan et al[82].

For the LiDFOB-LiFSI series, the 0.5LiDFOB-1LiFSI mixtures had terrible capacity retention and barely did 50 cycles at 70 °C. However, 0.25LiDFOB-1.25LiFSI, which reached 80 % capacity at cycle ~900, and 1.5LiFSI both had similar capacity fade compared to 1.5LiPF$_6$. The biggest retention boost was seen in the 0.125LiDFOB-1.375LiFSI mixture which reached 85 % capacity at cycle ~1200, significantly better than both 1.5LiFSI and 1.5LiPF$_6$.
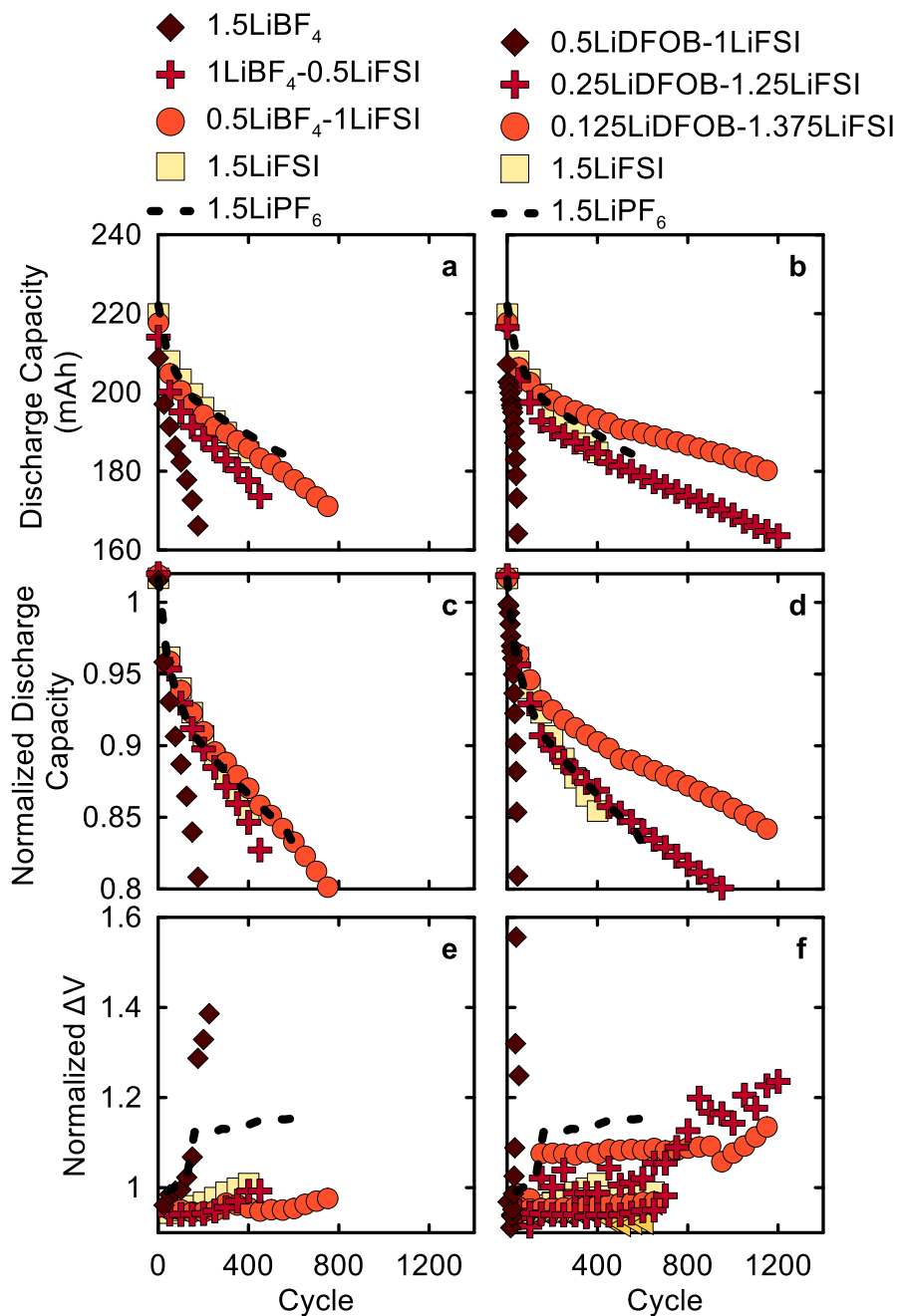
Figure 7.3. (a-b) discharge capacity (mAh); (c-d) normalized discharge capacity; and (e-f) normalized ΔV versus cycle number for LFP/AGC cells with LiBF$_4$ or LiDFOB co-salts. Solvent was EC:EMC:DMC (25:5:70) with 2VC1DTD additive blend. Cycling was done at 70 °C with C/3:C/3 charge:discharge rates between 2.5-3.65 V. Dashed line shows cycling results for an identical cell with 1.5 M LiPF$_6$.

7.3.2. XRF Analysis After Cycling

After long-term cycling, LFP/AGC cells underwent XRF analysis to quantify Fe loading on the negative electrode. Figure 7.4 shows Fe loading, Al loading, and capacity loss at the end of cycling for LFP/AGC cells with mixed salt electrolytes. The error bars are based on the relative error in the slope of the calibration curve used to convert the XRF signal count to a mass loading. The cycle number achieved prior to XRF analysis is shown for each cell. Due to a limited cell supply, duplicates were omitted for galvanostatic cycling. The machine-made pouch cells used in this thesis generally have excellent cell to cell reproducibility as shown throughout this thesis.

The $1.5LiPF_6$ cell had about 2 μg cm^{-2} of Fe after 602 cycles at 70 °C where the capacity loss was around 18 %. By switching to $1.5LiBF_4$, the Fe loading decreased to ~0.8 μg cm^{-2} but the cell lost ~30 % capacity in 234 cycles only. This significant reduction in Fe loading cannot be attributed to the reduced cycle number only, since the other cells in the $LiBF_4$-LiFSI series showed significant Fe loading reduction, even though $0.5LiBF_4$-1LiFSI cycled for 780 cycles compared to 602 for $1.5LiPF_6$. The $0.5LiBF_4$-1LiFSI cell had around 20 % capacity loss after 780 cycles, and only half the Fe loading of $1.5LiPF_6$. This can be attributed to the improved thermal and chemical stability of $LiBF_4$ compared to $LiPF_6$[172,186]. The $LiPF_6$ salt is known to undergo hydrolysis and produce acidic species in the electrolytes that can increase TM dissolution in low-voltage positive electrode materials (such as LFP) as shown by Sahore et al[161].

One striking result in Figure 7.4 is the large Fe loading seen in the 1.5LiFSI cell which was ~5.6 μg cm^{-2}. The 1.5LiFSI cell cycled 435 times and lost ~19 % capacity, similar to 1LiBF$_4$-0.5LiFSI which had only < 1 μg cm^{-2} of Fe. The 1.5LiPF$_6$ cells which had a similar capacity loss compared to 1.5LiFSI, and about 170 cycles more, but only had ~2 μg cm^{-2} of Fe. Therefore, it is clear that the use of LiFSI increases Fe loading at 70 °C, which can also be seen in the LiBF$_4$-LiFSI series cells.

In previous work by Logan et al, LFP cells cycled with 1.5 M LiFSI outperformed 0.75 M LiFSI + 0.75 M LiPF$_6$ and 1.5 M LiPF$_6$ at 20 °C, 40 °C, and 55 °C, and the use of LiFSI reduced Fe loading at these temperatures for cells with or without electrolyte additives (solvent was EC:DMC 3:7 and additive was 2VC)[82]. For example, at 55 °C, a 1.5 M LiPF$_6$ cell had ~3.2 μg cm^{-2} of Fe after ~700 cycles while the 1.5 LiFSI cell had 2.5 μg cm^{-2} after ~1200 cycles. At 70 °C, however, Logan et al showed that the 1.5 M LiFSI cell started to lose more capacity compared to the 0.75 M LiFSI + 0.75 M LiPF$_6$ one (but still outperformed LiPF$_6$ only), suggesting that the degradation route of LiFSI-only cells may be different at 70 °C. Unfortunately, the Logan et al study did not report Fe loading after 70 °C cycling. Work by Taskovic et al showed that an LFP/AGC cell cycled with EC:DMC (3:7), 1.0 M LIFSI and 2VC1DTD had 3.5 μg cm^{-2} of Fe after ~700 hours of C/3 cycling at 85 °C (~116 cycles), but no comparison to other salt mixtures was made[187]. The mechanism of Fe dissolution in LiFSI cells at elevated temperatures, which are not prone to hydrolysis like LiPF$_6$ and result in a more stable SEI[188–190],

has not been extensively discussed in the literature and should be the subject of extensive future work.

Finally, the 0.125LiDFOB-1.375LiFSI cell with 1163 cycles lost ~19 % capacity and had Fe loading around 1.8 μg cm^{-2} which increased to 4 μg cm^{-2} for 0.25LiDFOB-1.25LiFSI. The Fe loading nearly doubled with doubling the LiDFOB content. Figure 7.4a shows the remarkable role that a small amount of LiDFOB plays in suppressing Fe dissolution compared 1.5LiFSI, especially since the LiFSI cell had nearly a third of the cycle number achieved by the LiDFOB-containing cells, which is consistent with a report from Xu et al on the beneficial role of LiDFOB as an additive in LFP/Graphite cells cycled at 60 °C[191].
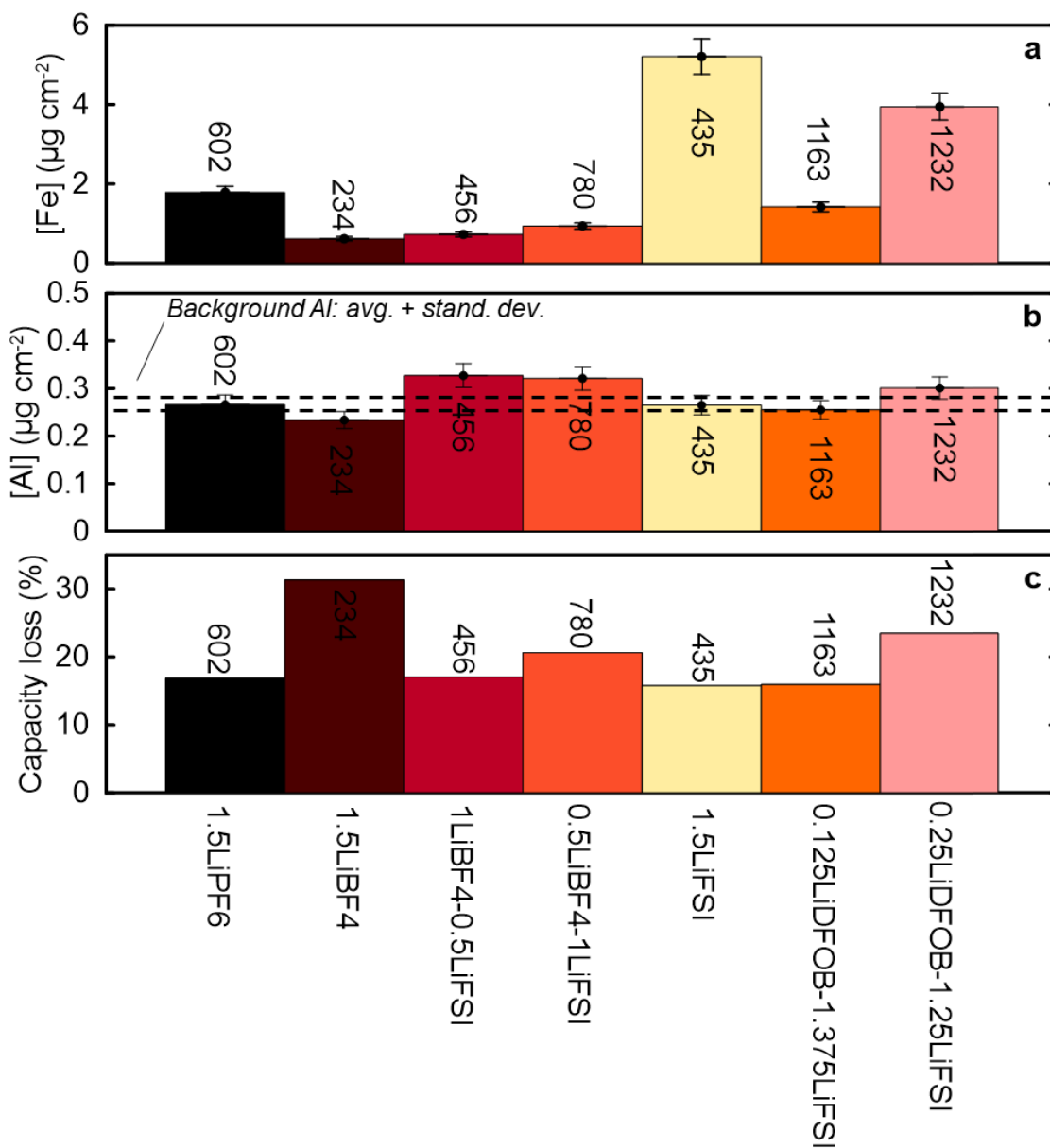
Figure 7.4. (a) Fe loading ($\mu g\ cm^{-2}$); (b) Al loading ($\mu g\ cm^{-2}$); and (c) capacity loss for LFP/AGC cells cycled at 70 °C with different salt mixtures. The cycle number prior to XRF analysis is indicated for each cell. dashed line in panel (b) represent the background Al levels in the XRF analysis. The electrolyte was EC:EMC:DMC (25:5:70), 2VC1DTD and 1.5 M of salt.

7.4. UHPC Results

Out of all the mixed salt combinations tested in Figure 7.3, 0.125LiDFOB-1.375LiFSI is the only mixture that outperformed 1.5LiFSI and 1.5LiPF$_6$ significantly in terms of capacity retention. Figure 7.3c-d show that the capacity retention improved as the LiBF$_4$ and LiDFOB content decreased for each mixed salt series, with 0.5LiBF$_4$-1LiFSI slightly outperforming 1.5LiFSI and 0.125LiDFOB-1.375LiFSI providing a significant retention boost. Therefore, we sought to explore the impact of very small LiBF$_4$ and LiDFOB concentrations on cell performance in an attempt to optimize the salt composition. Here, UHPC cycling was used to quickly probe small differences in CE, fade, and slippage for different LiBF$_4$-LiFSI and LiDFOB-LiFSI mixtures.

Figure 7.5 shows CE, normalized discharge capacity, and charge endpoint slippage versus cycle number for LFP/AGC cells. All cycling was done at 40 °C with C/20:C/20 charge:discharge rates between 2.5-3.65 V. In the LiBF$_4$-LiFSI series, 1.5LiBF$_4$ cells had the lowest CE and worst capacity fade. Cells with 1.5LiFSI and 0.125-0.25 M LiBF$_4$ are showing the highest CEs and lowest capacity fade. Looking at the charge slippage, 1.5LiFSI cells have the highest slippage which is significantly reduced by the addition 0.125-0.25 M LiBF$_4$. In the LiDFOB-LiFSI series, 0.25LiDFOB-1.25LiFSI had the lowest CE and highest charge slippage. Cells with 0.05-0.1 M LiDFOB had a similar CE, capacity loss, slippage compared to 1.5LiFSI.
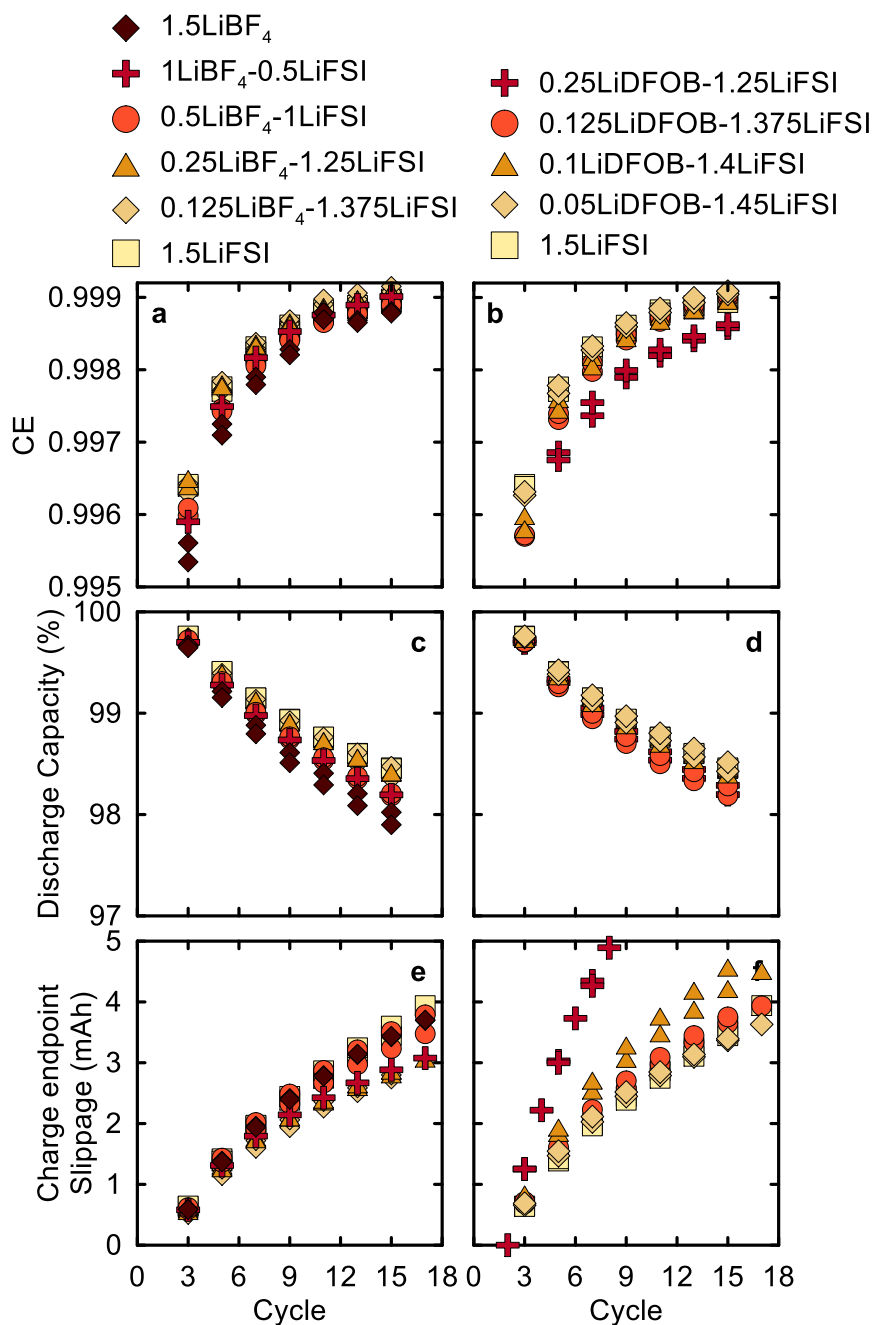
Figure 7.5. (a-b) CE; (c-d) normalized discharge capacity (%); and (e-f) charge endpoint slippage (mAh) versus cycle number for LFP/AGC cells with LiBF₄ or LiDFOB co-salts. Solvent was EC:EMC:DMC (25:5:70) with 2VC1DTD additive blend. Cycling was done at 40 °C with C/20:C/20 charge:discharge rates between 2.5-3.65 V.

To better visualize the small differences between the cells in Figure 7.5, we calculated the fractional fade, slippage, and CIE rates per hour as described by Ma et al[124]. Figure 7.6 shows the fractional fade per hour, fractional slippage per hour, and CIE per hour versus LiFSI content for the cells in Figure 7.5. As the $LiBF_4$ content increases, the fractional fade increases, with the minima being around 1.5LiFSI and 0.125$LiBF_4$-1.375LiFSI. As for the slippage, 1.5LiFSI has the largest slippage in the $LiBF_4$-LiFSI series, which decreases as $LiBF_4$ is added.

The relatively high charge slippage for LiFSI-containing LFP/Graphite cells was reported previously by Logan et al[82]. An increase in charge endpoint slippage is generally an indication of parasitic reactions occurring on the positive electrode such as Fe dissolution, the generation of decomposition products on the negative electrode which migrate to the positive electrode to react further (i.e., cross-talk reactions), or a redox shuttle type reaction where a species is oxidized on the positive electrode and reduced on the negative without irreversibly consuming Li inventory. The high charge endpoint slippage for LiFSI observed by Logan et al was responsible for large reversible capacity loss during OCV storage, but LiFSI had less irreversible loss compared to $LiPF_6$. Therefore, the high charge slippage was therefore attributed to a shuttle-type mechanism that does not consume Li inventory[82], as confirmed by recent work from our group[165,192,193].

Figure 7.6c shows that the addition of a small amount (0.125-0.25 M) of $LiBF_4$ can significantly decrease the charge endpoint slippage for LiFSI-containing cells. Due to limited cell availability, long-term cycling was not done on the 0.125-0.25 M $LiBF_4$ mixture to probe the impact of small $LiBF_4$ concentrations on

cell lifetime but will be considered in future work, especially since these cells had the lowest CIE and comparable fade rates to 1.5LiFSI. Visual inspection of the UHPC cells showed no significant gas generation after 18 C/20 cycles at 40 °C.
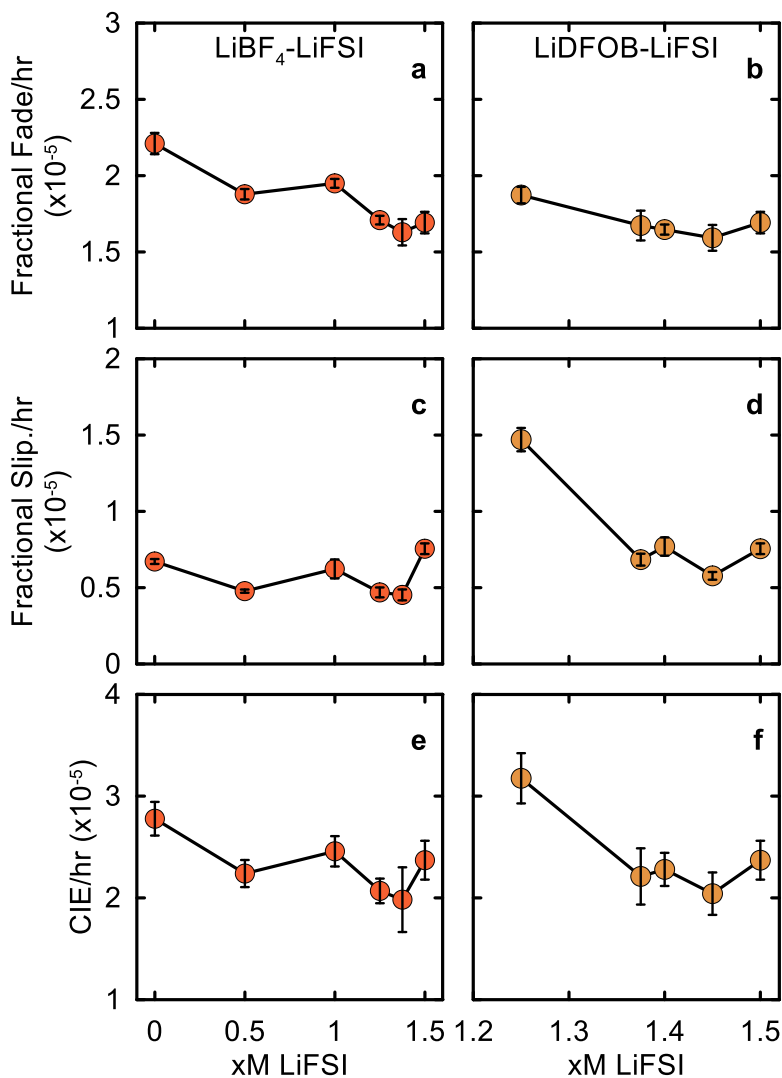
Figure 7.6. (a-b) fractional fade/hr.; (c-d) fractional slippage/hr.; and (e-f) CIE/hr. versus cycle number for LFP/AGC cells with LiBF₄ or LiDFOB co-salts. Solvent was EC:EMC:DMC (25:5:70) with 2VC1DTD additive blend. Cycling was done at 40 °C with C/20:C/20 charge:discharge rates between 2.5-3.65 V.

UHPC results for LFP/AGC cells with LiDFOB-LiFSI mixtures show that 0.05LiDFOB-1.45LiFSI had the smallest fade and slippage. The CIE for the LiFSI-LiDFOB mixtures reached a minimum at 0.05 M LiDFOB. This result suggests that 0.05 M LiDFOB can effectively lower the charge slippage associated with LiFSI and potentially lower the fade rate at 40 °C.

Comparing these results to 70 °C cycling, we can start to see some discrepancies. For example, 0.125LiDFOB-1.375LiFSI has great capacity retention at 70 °C compared to 1.5LiFSI, but the fade, slippage, and CIE are similar for both salt mixtures at 40 °C. It is possible that the 0.125LiDFOB-1.375LiFSI is more suited for high temperature applications and does not provide a significant boost at 40 °C. Long-term cycling at RT, 40 °C, and 55 °C was not done due to limited cell supply but will be important in future work to understand the impact of salt mixtures as a function of temperature.

7.5. OCV Storage

7.5.1. Storage Results

The UHPC cycling results shown above suggest that small amounts of LiBF$_4$ or LiDFOB mixed with LiFSI can reduce the charge endpoint slippage and slightly improve the fade at 40 °C. Another consequence of the larger charge endpoint slippage associated with LiFSI is rapid self-discharge during OCV storage. To probe the impact of co-salts on storage performance, OCV storage for 500 hours at 100 % SOC and 60 °C was done. The reversible and irreversible capacity losses were measured as described in Chapter 2, and XRF was used to

259

probe any differences in Fe dissolution. Due to a shortage of the pouch cells with a nominal 240 mAh capacity (used in all experiments above), cylindrical LFP/AGC cells with identical components (but a 550 mAh nominal capacity) was used in the OCV storage test. The 550 mAh cells used twice the electrolyte volume (2 mL) compared to the smaller 240 mAh cells.

Figure 7.7 shows the reversible and irreversible capacity losses and Fe loading on the negative electrode versus LiFSI content for LFP/AGC cells. In the LiBF$_4$-LiFSI series, the reversible capacity loss increases with LiFSI content from 6 to 7 mAh. This is consistent with the reduction in slippage when LiBF$_4$ is a co-salt as shown in Figure 7.6. Logan et al reported ~5 mAh reversible capacity loss after storage for LFP/Graphite cells (~240 mAh nominal capacity)[82], which is significantly more than the 7 mAh seen here for a 550 mAh cell. However, the cells used by Logan et al used only 2VC as the additive, the solvent was EC:DMC (3:7), and a different graphite material was used. Figure 7.7c shows the benefit of using LiFSI in the significant reduction of irreversible capacity loss with increasing LiFSI content. The 1.5LiBF$_4$ cells lost ~27 mAh of capacity compared to just ~18 mAh for 1.5LiFSI.

Unfortunately, the trends were less clear for the LiDFOB-LiFSI series. The highest reversible and irreversible losses were found in the 0.25LiDFOB-1.25LiFSI cells, which were ~11 mAh and ~28 mAh, respectively. The 0.125LiDFOB-1.375LiFSI cells had a significantly reduced reversible capacity loss of just ~7 mAh which is similar to 1.5LiFSI. The other two LiDFOB blends showed a slightly higher reversible loss compared to 0.125LiDFOB-1.375LiFSI and

1.5LiFSI. The main drawback of LiDFOB was seen in the irreversible capacity loss, similar to LiBF₄, where adding LiDFOB significantly increased the capacity loss relative to 1.5LiFSI.
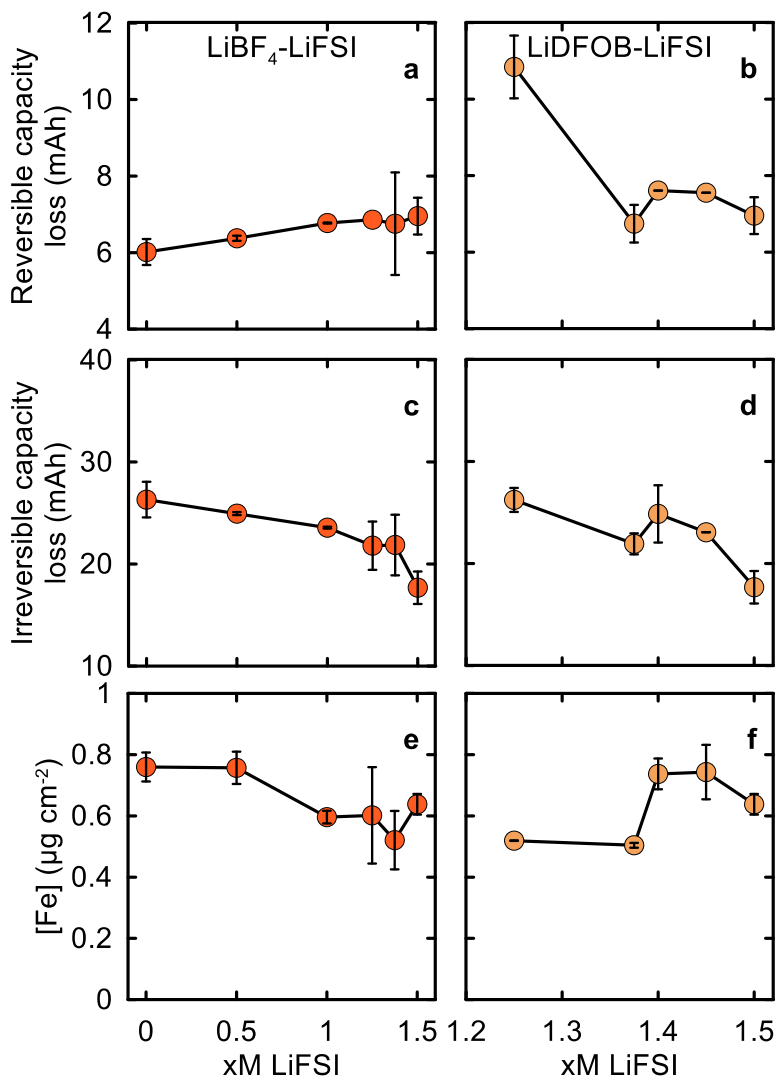
Figure 7.7. (a-b) reversible and (c-d) irreversible capacity loss (mAh) during OCV storage; and (e-f) Fe loading on the negative electrode after storage (µg cm⁻²) versus LiFSI content for LFP/AGC cells with LiBF₄ or LiDFOB co-salts. Solvent was EC:EMC:DMC (25:5:70) with 2VC1DTD additive blend. OCV storage was done at 60 °C at 3.65 V for 500 hours. The cells used in the OCV storage experiments were cylindrical LFP/AG pouch cells with a 550 mAh nominal capacity.

Lastly, we used XRF to quantify Fe on the negative electrode to probe the impact of salt choice on Fe dissolution. The cells in Figure 7.7 only underwent 500 hours of OCV storage at 60 °C, so they were not expected to have significant Fe levels. For example, work by Logan et al showed that LFP/Graphite cells with EC:DMC (3:7), 1.5 M LiFSI and 2VC will have about 2.5 μg cm^{-2} after 1150 cycles at 55 °C (roughly 6900 hours of cycling)[82]. Similarly, previous work by Eldesoky et al showed that LFP/Graphite cells with 1.5 M LiPF$_6$ and 2 % VC did not show any significant Fe levels for the first ~175 cycles at 55 °C (~1050 hours)[194].

The cells in Figure 7.7 had between 0.6-0.8 μg cm^{-2} of Fe on the negative electrode. With such small Fe loadings, it is difficult to make conclusive statements about the impact of salt on Fe dissolution, if any, since the error associated with our quantification is larger for very small Fe loadings. However, it is clear that for the first 500 hours of OCV storage at 60 °C, the salt mixtures in Figure 7.7 did not have a significant impact on the Fe dissolution in our cells.

7.5.2. Gassing After Storage

So far, a small amount of LiDFOB (0.125 M) was shown to improve the 70 °C cycling performance of LFP/AGC cells, and 0.125-0.25 M LiBF$_4$ or 0.05 M LiDFOB can be used alongside LiFSI to lower the charge endpoint slippage. However, any potential benefits from these salt mixtures may be compromised if there is severe gas generation during cell operation.

Figure 7.8 shows the gas volume and R_{CT} after formation and OCV storage at 60 °C for LFP/AGC with a nominal capacity of 550 mAh versus LiFSI content. As shown in Figure 7.2, increasing the $LiBF_4$ content increases gas generation and R_{CT} significantly in LFP/AGC cells. On the other hand, after 500 hours of storage at 60 °C, which provides sufficient time and temperatures for the SEI to mature, we see minimal changes to gas generation $LiBF_4$-LiFSI and LiDFOB-LiFSI cells. The 1.5$LiBF_4$ cells had about 2 mL of gas after formation (down to 0.25 mL for 1.5LiFSI), which was reduced to 0.5 mL after storage. The R_{CT} for 1.5$LiBF_4$ cells nearly doubled after storage which indicates the formation of a thick SEI layer that can hinder charger transfer. The only cells in the $LiBF_4$-LiFSI series which did not show a significant rise in R_{CT} were 1.5LiFSI, 0.125$LiBF_4$-1.375LiFSI, and 0.25$LiBF_4$-1.25LiFSI. All the cells in the LiDFOB-LiFSI series showed similar gassing and R_{CT} after formation and storage, which did not significantly change with the LiDFOB content. The LiDFOB-LiFSI cells in Figure 7.8 had 0.25-0.50 mL of gas after storage at 60 °C, which is close to formation gas volume but can be further reduced with the use of gas-suppressing electrolyte additives[195] that is outside the scope of this work.
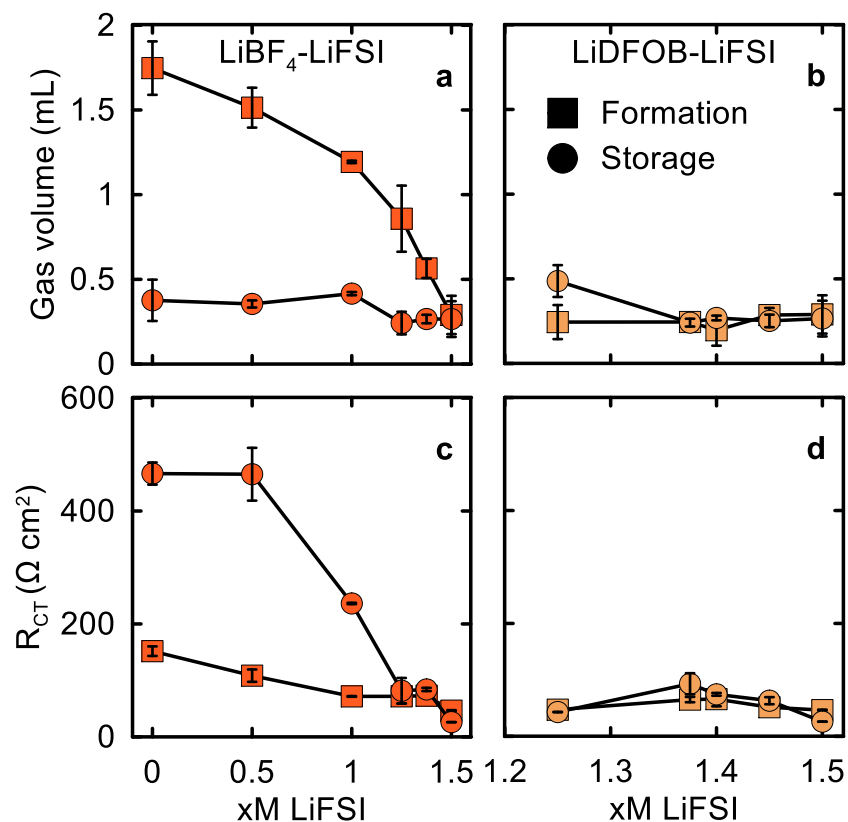
Figure 7.8. (a-b) gas volume (mL) after formation and storage; (c-d) R_{CT} (Ω cm^2) after formation and storage versus LiFSI content for LFP/AGC cells with LiBF$_4$ or LiDFOB co-salts. Solvent was EC:EMC:DMC (25:5:70) with 2VC1DTD additive blend. OCV storage was done at 60 °C at 3.65 V for 500 hours. The cells used in the OCV storage experiments were cylindrical LFP/AG pouch cells with a 550 mAh nominal capacity.

7.6. Conclusion

This chapter examined the impact of LiBF$_4$-LiFSI and LiDFOB-LiFSI salt mixtures on the 70 °C cycling performance of LFP/AGC cells. Additionally, UHPC cycling at 40 °C and OCV storage at 60 °C were used to measure small differences in CE, fade, slippage, and capacity loss during storage for a range of LiBF$_4$-LiFSI and LiDFOB-LiFSI compositions. The main findings of this chapter can be summarized as follows:

1. Addition of LiBF$_4$ and LiDFOB to LiFSI results in an FCE penalty. The use of LiBF$_4$ also increases gassing during formation and R$_{CT}$, but the impact of LiDFOB on these metrics was negligible (for concentrations less than 0.5 M);

2. At 70 °C, increasing the LiBF$_4$ content compromised the cell performance compared to LiFSI or LiPF$_6$ only. The 0.5LiBF$_4$-1LiFSI mixture was the only one to provide comparable performance to LiFSI and LiPF$_6$, but at an FCE and R$_{CT}$ penalty. The 0.125LiDFOB-1.375LiFSI mixtures resulted in a significant capacity retention boost at 70 °C compared to LiFSI or LiPF$_6$ only;

3. LiBF$_4$-containing electrolytes showed a significant reduction in Fe loading on the negative electrolyte compared 1.5LIPF$_6$ and 1.5LiFSI after 70 °C cycling. Adding LiDFOB to LiFSI also reduced the Fe loading, especially for 0.125LiDFOB-1.375LiFSI mixture. Doubling the LiDFOB content, however, nearly doubled the Fe loading. Surprisingly, 1.5LIFSI had significantly more Fe than 1.5LiPF$_6$, which points to some poorly understood interplay between LiFSI and Fe dissolution at 70 °C;

4. UHPC cycling shows the 0.125LiBF$_4$-1.375LiFSI, 0.25LiBF$_4$-1.25LiFSI, 0.05LiDFOB-1.45LiFSI mixtures can reduce charge endpoint slippage compared to LiFSI only, which in turn lowered the CIE at 40 °C. Long-term cycling using these salt mixtures is needed to probe their impact on cell lifetime and Fe dissolution;

5. OCV storage at 60 °C showed the increasing the LiFSI content in the LiBF$_4$-LiFSI cells increased the reversible capacity loss (consistent with the large charge endpoint slippage of LiFSI) but lowered the irreversible capacity loss. Small differences in the reversible loss were seen in the LiDFOB-LiFSI series, but the irreversible loss decreased significantly with increasing the LiFSI content. For both salt series, the Fe loading on the negative electrode after storage was very small and no clear dependency on salt composition was seen after only 500 hours of storage at 60 °C.

The initial screening of LiBF$_4$-LiFSI and LiDFOB-LiFSI mixed salts in LFP/AGC cells did not address the long-term cycling performance at lower temperatures. This will be important to consider in future work as some discrepancies between UHPC results at 40 °C and 70 °C cycling were seen. For example, 0.125LiDFOB-1.375LiFSI showed similar CIE and fade to 1.5LiFSI, despite having significantly better capacity retention at 70 °C which hints that some of the salt mixtures here may not be beneficial at every temperature range. Using LiBF$_4$ and LiDFOB as co-salts with LiFSI shows some promise in high temperature performance, reversible capacity loss during storage, and lowering charge endpoint slippage, so we believe the work in this chapter can serve as a starting point for additional studies on LFP/AG cells to further improve their performance by simple electrolyte engineering.

Chapter 8.   Conclusions and Future Work

8.1.   Conclusion of Thesis Findings and Contributions

Studies of Li-ion cell failure and strategies to improve cell lifetime were discussed for NMC811, LMO, and LFP cell chemistries. Throughout this thesis, XRF was used to quantify TM dissolution and deposition on the negative electrode using a procedure developed by the author, which has since been used in numerous publications from our group. The main findings and contributions of each thesis chapter are summarized below.

Chapter 3 examined the impact of DOD, C-rate, UCV, and temperature on the lifetime of NMC811/AG pouch cells, after which the cells underwent various characterization tests to study the impact of cycling conditions on the cell aging. NMC811/AG cells were cycled to 4.06 V or 4.20 V UCV, with 25, 50, 75, or 100 % DOD at C-rates of C/3, C/5, C/10, or C/50, and cycling temperatures were RT or 40 °C. After 1 year of cycling with 4.20 V UCV, XRF analysis, synchrotron CT, and cross-section SEM of the positive electrode showed no significant TM dissolution, signs of mechanical degradation, or particle microcracking regardless of C-rate or DOD.

The inverse correlation between DOD and capacity loss seen for NMC811 cells in Chapter 3 is contrary to conventional wisdom. Larger DODs result in greater Li utilization and volume change of the graphite electrode, thus increasing capacity loss for both NG and AG materials (but will be much less severe in AG). However, NMC811 is prone to oxygen release from the positive electrode at

267

around 80 % SOC, so small DODs will result in more time spent at high SOC where increased rate of parasitic reactions from the positive electrode and possibly oxygen release can take place. Indeed, NMC532 and NMC640 cells (which do not suffer from oxygen release at the UCVs chosen in Chapter 3) cycled at 1C:1C, as well as NMC640 cells cycled at C/3:C/3 with a 4.30 V UCV, showed more capacity loss at larger DODs as expected. Finally, NMC811 cells cycled to 4.20 V showed a tremendous increase in ΔV, likely a consequence of the lattice volume collapse and concomitant oxygen release, which was virtually nonexistent for the 4.06 V counterparts. Chapter 3 showed that increasing the lifetime of NMC811 cells can be achieved by limiting the SOC to ~80 % or less, where the only contributor to capacity fade is Li inventory loss. Since Li inventory loss is highly dependent on the graphite material choice, optimizing the performance of the negative electrode and keeping the SOC at or below 80 % should yield a long-lived NMC811 cell.

Chapter 4 studied the physical and electrochemical differences between five graphite materials from reputable suppliers, and their impact on the performance and lifetime of NMC811 pouch cells. We showed that N_2 BET surface area does not provide a reliable measure of the electrochemically accessible area. Chemical and electrochemical metrics such as gas generation, dQ/dV vs. V plots showing electrolyte reduction activity, formation gas composition, FCE and parasitic heat flow measurements provide a more useful measure of the accessible surface area. For example, cells with higher C_2H_4/CO_2 gas ratio after formation had a lower FCE, due to the insufficient passivation by the additives and increased consumption of EC and Li inventory. Therefore, gas composition after formation

can be a useful measure of negative electrode passivation and may be a predictor of cell performance in cases where capacity fade is only due to Li inventory loss. However, the most competitive AGC material—which had a low accessible surface, improved capacity retention compared to the AGA baseline, and high FCE—showed a large R_{CT} due to the limited redox active sites available. In fact, we saw that a correlation between high FCE and large R_{CT} in all the graphite materials in Chapter 4. Further, the AG materials in Chapter 4 had substantially smaller stack thickness growth at 40 °C as shown by *in-operando* pressure measurements. The AGB and AGC materials outperformed our baseline AGA material in long-term cycling experiments, except for 55 °C cycling at 4.20 V UCV where AGC material suffered from more rapid capacity fade compared to baseline.

The remainder of Chapter 4 focused on the pros and cons of using a simple SEI growth model to predict cell lifetime. While the commonly-used square-root time model can be used in many cases to quantify the rate of SEI growth, the complicated reactivity between the electrodes and electrolyte, negative electrode overhang, and cell failure mechanisms unique to each temperature range makes it very difficult to predict lifetime based on this simple model alone. Finally, we showed that NMC811/AGC cells will benefit from a substantial lifetime boost when operated at or below an UCV of 4.06 V, and that these cells may provide greater lifetime energy output compared to higher SOC ones. Based on Chapters 3 and 4, we believe that the limited UCV and use of competitive graphite materials such as AGC unlocks the potential for ultra-long-lived NMC811 cells for grid energy storage or long-lifetime applications.

Chapter 5 pivoted to studying the performance and degradation of LMO/AG pouch cells in an effort to increase the lifetime of this low-cost positive electrode material. This chapter explored the impact of Li excess, particle size, and NMC blending on cycle life of LMO/AG pouch cells with 5-6 different electrolyte blends. We showed that SC-LMO cells with VC-containing electrolytes can obtain 2200+ cycles at RT and 800+ at 40 °C. However, the performance of all LMO/AG cells quickly deteriorated at high temperatures. By decreasing Li excess in $Li_{1+x}Mn_{2-x}O_4$ from 0.078 ± 0.016 to 0.011 ± 0.003, PC-LMO2 materials performed significantly worse compared to PC-LMO in terms of capacity retention and Mn dissolution. The performance of PC-LMO2 was greatly improved by blending 25 % of NMC622, and the observed synergy between these materials was shown to be electrolyte-dependent and more significant at elevated temperatures.

XRF was used to quantify the Mn loading on the negative electrode after cycling, where the PC-LMO2 cells had the most severe Mn dissolution due to their smaller Li excess and particle size. The Mn loading decreased significantly in the blended cells compared to PC-LMO2 only, which highlights the ability of NMC to stabilize the LMO component in blended cells. Mn deposition appeared independent of the electrolyte additive and no strong correlation between the capacity loss and Mn loading could be made within each LMO cell group. It was clear that the Mn loading depends on the morphology and Li excess of the LMO positive electrode as well as the cycling temperature. Moreover, DCA was used to quantify shift loss and electrode active material loss. We saw severe positive electrode active mass loss for PC-LMO2, followed by NMC622/PC-LMO2,

PC-LMO, SC-LMO, which correlated well with the Mn loading on the negative electrode. We found that the high Mn loading resulted in negative electrode active mass loss which we attributed to the ability of Mn to thicken the SEI.

We performed NMR analysis on the electrolyte extracted from LMO/AG cells over the course of 100 cycles at 70 °C, where we saw severe PF_6^- consumption on the order of 0.1-0.30 m. XRF was used to show that Mn deposition occurs primarily during the early cycles of the cell at 70 °C (a third of which comes during formation alone). Using IMC, we saw that increasing the Mn loading on the negative electrode results in higher parasitic heat flow in negative electrode pouch bags, consistent with the suspected role Mn plays in the acceleration of SEI growth. Based on the results shown in Chapter 5, we found that SC-LMO with an average composition of $Li_{1.125}Mn_{1.875}O_4$ had the best capacity retention, smallest amount of Mn dissolution (and negative electrode parasitic heat flow); and that PES211 and VC-containing additive blends resulted in good cycle life performance compared to FEC-containing additive blends.

We found that LiFSI improves capacity retention compared to $LiPF_6$ at 40 °C, but Al corrosion at high temperatures makes it incompatible with LMO/AG cells. To mitigate Al corrosion, co-salts mixed with LiFSI were used in high-temperature storage at 60 °C and 4.20 V in order to passivate the Al current collector. Using $LiBF_4$ or LiDFOB as co-salts with LiFSI, Mn deposition was lowered after 500 hours of OCV storage at 60 °C in PC-LMO2 pouch cells, Al corrosion was suppressed, and the storage performance was improved compared

to LiFSI alone. After some success with mixed salt electrolyte and SC-LMO materials, we sought to use some of the successful electrolyte formulations in Chapter 5 to in SC LMO pouch cells with a large D50 particle, and to study the impact of NMC blending in SC LMO cells.

Chapter 6 looked at different SC LMO pouch cell types with or without NMC622 blending. The SC-LMO2 materials in this chapter had a D50 of ~13.8 μm compared to 10.42 μm for SC-LMO in Chapter 5. Unfortunately, SC-LMO2 cells with a larger D50 particle size suffered from particle cracking during calendaring and we suspect this is one reason why this material did not improve capacity retention compared to SC-LMO at 55 °C and 70 °C. The SC-LMO2 and blended SC-LMO2B cells outperformed SC-LMO at RT and 40 °C, and also had smaller CIE during UHPC cycling. However, SC-LMO2 and SC-LMO2B cells had greater ΔV growth during long-term cycling, which we suspect may be the consequence of electrode damage during calendaring, although this is not yet clear. Similar to Chapter 5, we saw that VC-containing electrode additives outperformed 2FEC1LFO in the SC-LMO2 and SC-LMO2B cells.

Long-term cycling at 40 °C shows that 0.5LiPF$_6$-1LiFSI had the best capacity retention compared to 1.5LiPF$_6$. The LiBF$_4$-LiFSI cells all had similar capacity retention which was also better than the baseline cell. Finally, for the LiDFOB-LiFSI mixtures, 0.125LiDFOB-1.375LiFSI cell had superior retention compared to 0.25LiDFOB-1.25LiFSI and the baseline cell. Long-term cycling at 55 °C shows very small differences within each salt series.

The choice of salt greatly influenced Mn dissolution. The 1.5LiPF$_6$ cells (which used EC:DMC 15:85 as the solvent) had significantly less Mn compared to the baseline (which used EC:EMC:DMC 25:5:70 as the solvent and 1.5 M LiPF$_6$). This can be attributed to the lack of transesterification in the EC:DMC 15:85 blend or possibly the increased VC loading in the mixed salt cells, but the impact of solvent will require further work to understand. In general, LiBF$_4$-LiFSI cells had a low Mn loading, compared to LiPF$_6$-LiFSI, which points to the detrimental role LiPF$_6$ plays in the cell due to the salt hydrolysis at elevated temperatures. None of the mixed salt cells showed significant Al corrosion due to the use of LiFSI which suggests that the co-salts were effective in suppressing Al corrosion over the duration of cycling.

The 0.125LiDFOB-1.375LiFSI salt mixture, which had excellent capacity retention, results in ~2 mL of gas generation after 250 hours of cycle-hold testing at 40 °C. Similarly, LiBF$_4$-LiFSI cells showed that increasing the LiBF$_4$ content resulted in more gassing but was less than 0.5 mL for 1.5LiBF$_4$ cells. The severe gassing behaviour of LiDFOB may make it difficult to use in practical cell designs without the use of gas-supressing additives. Based on our work with mixed salt electrolytes, 0.5LiPF$_6$-1LiFSI or 0.5LiBF$_4$-1LiFSI salt mixtures are likely to be the most attractive in LMO/AG cell chemistries, and the 0.125LiDFOB-1.375LiFSI mixture will be of great value if the gas generation can be better controlled.

Chapter 7 used some of the competitive mixed salt electrolyte systems from Chapter 6 and the best graphite material from Chapter 4 to study the degradation of LFP/AGC pouch cells cycled at 70 °C. The addition of LiBF$_4$ and LiDFOB to

LiFSI results in a FCE penalty, similar to LMO cells. The use of LiBF$_4$ also increases gassing during formation and R$_{CT}$, but the impact of LiDFOB was negligible for concentrations less than 0.5 M. Increasing the LiBF$_4$ content resulted in worse performance compared to LiFSI or LiPF$_6$ at 70 °C. The 0.5LiBF$_4$-1LiFSI mixture was the only mixture to provide comparable performance to LiFSI and LiPF$_6$, but LiBF$_4$ also introduced a FCE and R$_{CT}$ penalty. However, the 0.125LiDFOB-1.375LiFSI cell significantly outperformed both LiFSI and LiPF$_6$ at 70 °C.

XRF analysis showed that the use of LiBF$_4$ introduced a significant reduction in Fe loading compared to 1.5LiPF$_6$ and 1.5LiFSI after cycling, which was true for all cells in the LiBF$_4$-LiFSI series. Similarly, adding LiDFOB to LiFSI reduced the Fe loading, especially for the 0.125LiDFOB-1.375LiFSI mixture. Surprisingly, we saw a significant increase in Fe loading for 1.5LiFSI compared to 1.5LiPF$_6$, which points to some poorly understood interplay between LiFSI and Fe dissolution at 70 °C. Finally, UHPC cycling shows that the 0.125LiBF$_4$-1.375LiFSI, 0.25LiBF$_4$-1.25LiFSI, and 0.05LiDFOB-1.45LiFSI salt mixtures can reduce charge endpoint slippage compared to LiFSI only, which in turn lowered the CIE at 40 °C. OCV storage at 60 °C showed that increasing the LiFSI content in the LiBF$_4$-LiFSI cells increased the reversible capacity loss (consistent with the large charge endpoint slippage of LiFSI) but lowered the irreversible capacity loss. For both salt series, the Fe loading on the negative electrode after storage was very small and no clear dependency on salt composition was seen after 500 hours of storage at 60 °C.

8.2. Future Work

While the work in this thesis contributes to the body of knowledge surrounding cell failure mechanisms and lifetime improvements, it also presents many avenues for future work, some of which are discussed below.

8.2.1. LMO Lifetime and Degradation

Physical and Chemical Changes in Mixed Salt LMO Cells

In Figure 5.12, we tracked physical and chemical changes to LMO/AG cells at 70 °C as a function of cycling number for $LiPF_6$-based electrolytes. This provided insight into salt consumption and Mn dissolution as a function of cycle number. With the success seen using mixed salt electrolytes in Chapter 6, carrying out a similar experiment for different salt combinations will be important. NMR analysis of aged electrolytes can determine which salt component is more preferentially consumed during cell aging. This has been useful in previous studies of Li metal cells with dual-salt electrolyte and allowed us to understand the contributions of each salt to capacity retention[196]. Further, understanding the electrolyte changes and degradation will improve our understanding of cell failure mechanisms for different electrolyte salt systems, and may help us identify electrolyte by-products, that may prove to be critical to the longevity of the cells.

This study can be done by cycling LMO/AG for 0, 50, 100, and 200 cycles at different temperatures, then extracting the electrolyte for GCMS, NMR, and ICP-OES analysis to identify electrolyte degradation products, quantify salt consumption, and measure Mn concentration in the electrolyte, which we have

neglected in this thesis. Additionally, previous work by Nie et al showed a simple method to identify some soluble SEI components using NMR[197]. By soaking pieces of the negative electrode in D_2O, water soluble SEI components can be identified and quantified with NMR. This can be done as a function of cycle number to track SEI evolution, along with surface-sensitive techniques such as XPS to track the evolution of the water insoluble components.

"Pre-formed" Graphite and Mn-Free Initial SEI

An outstanding question in the literature and throughout this thesis is the impact of Mn on SEI growth and Li loss. Another way to probe the impact of Mn on capacity loss is using "pre-formed" graphite electrodes. In this setup, the negative electrode from, say, a NMC532/Graphite cell would be extracted after ~10-20 cycles at 40 °C (which would have little to no TMs) and used to construct an LMO/Graphite cell with a negative electrode that has a mature, TM-free, SEI layer. Previous work on LFP cells showed that dissolved Fe is embedded within the SEI[182]. If this is due to the accumulation of SEI products on Fe, will this still occur if a mature SEI is already developed prior to Fe (or Mn) deposition? While using aged electrodes to construct new cells is certainly not practical, it can provide useful insight into the role of Mn in cell degradation.

Figure 5.13 shows that the onset of Mn dissolution during formation at 40 °C or 70 °C is around 3.20 V vs. graphite. Knowing that the reduction potential of many electrolyte components is before ~3.0 V vs. graphite, it would be interesting to charge and hold the cell at 3.0 V at different temperatures to allow for SEI

formation without inducing any Mn dissolution. This approach may yield a "pre-formed" negative electrode *in-situ* instead of using aged electrodes from another cell. After inducing SEI formation without Mn dissolution, UHPC and long-term cycling can be used to probe the impact of this formation process on the cell lifetime. If the Mn deposition occurs after a mature SEI layer has formed, will Mn play a significant role in capacity loss? Or will it deposit on the mature SEI and cause more SEI growth?

Electrolyte Additives for LMO Cells with Mixed Salt Electrolytes

Chapter 6 shows that mixed salt electrolytes can prolong the lifetime of LMO/AG cells but introduce a FCE, gassing, and/or R_{CT} penalty, all of which can be modified to some extent with proper electrolyte additives. We have not extensively studied the impact of electrolyte additives on the performance of mixed salt electrolytes, but it is a very important step towards the development of these electrolyte systems. Results of some preliminary work done on SC-LMO2 cells will be discussed below to serve as a starting point for future additive development. The only salt mixture considered here was 1.0 M LiBF$_4$ + 0.5 M LiFSI but developing additives for 0.125LiDFOB-1.375LiFSI and 0.5LiBF$_4$-1LiFSI is very important especially since they turned out to be more competitive, which was yet unclear at the time this preliminary data was collected.

Figure 8.1 shows FCE, gas volume after formation, and R_{CT} for SC-LMO2 cells with 1LiBF$_4$-0.5LiFSI and different additive blends. Some of the new additives are propane sultone (PS), succinic anhydride (SA), or PES221 (2 % PES,

277

2 % DTD, 1 % TTSPi). All the new additives here have been reported in previous works by our group and others[195,198–200]. The blend used in Chapter 6 was 3VC1DTD. By switching to 2VC1PS or 2VC1DTD+1PS, the FCE increases and gassing is decreased almost 4-fold. However, the use of 2VC1PS resulted in a very large R_{CT}. The R_{CT} can be reduced by using SA in the 2VC1DTD+1SA blend, but the FCE and gassing are compromised. Lastly, PES211 and PES221 showed moderately-high FCE, very little gassing and typical R_{CT}, which makes them very promising candidates for the 1LiBF$_4$-0.5LiFSI salt mixture.
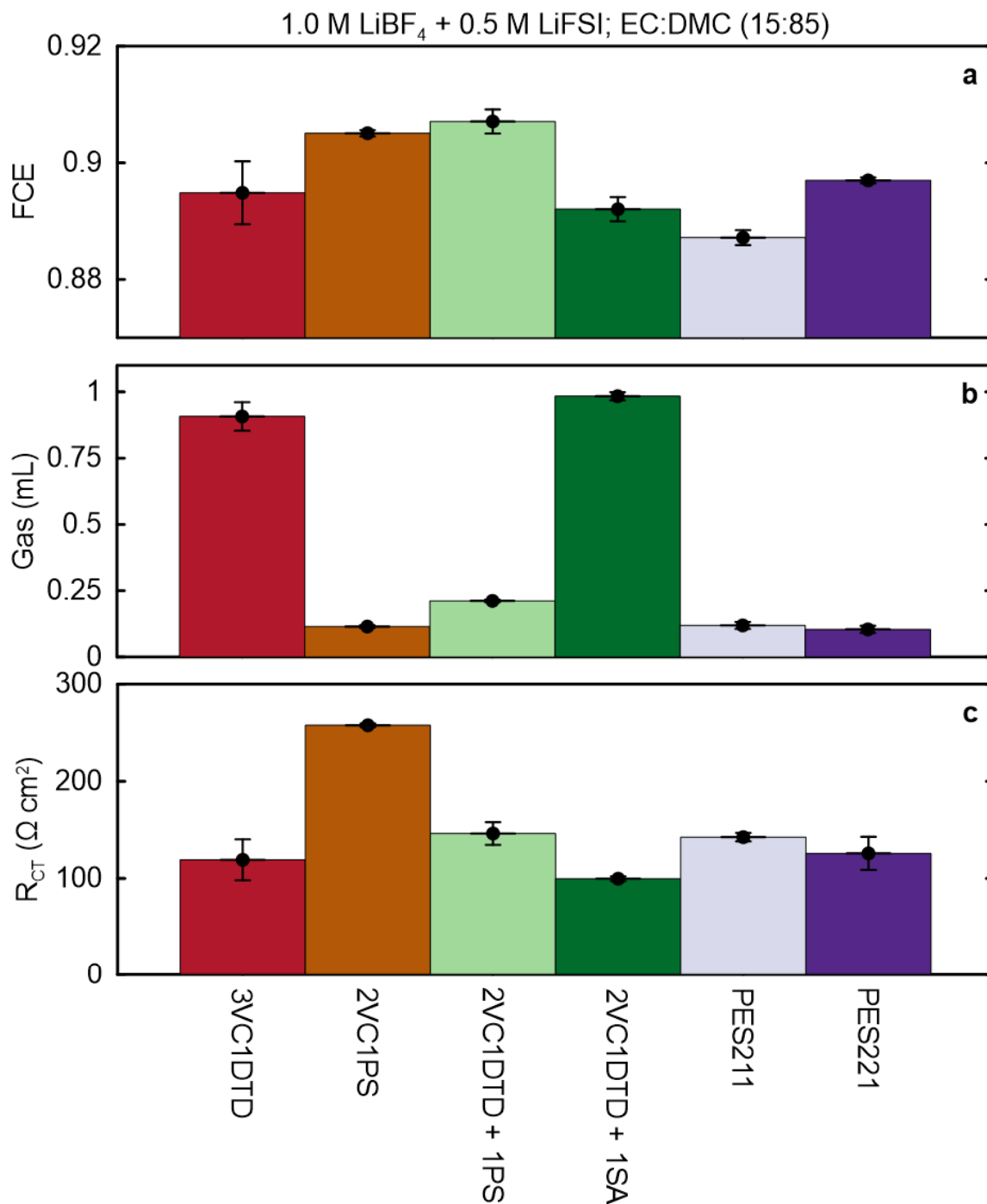
Figure 8.1. (a) FCE; (b) gas volume; and (c) R_{CT} after formation for SC-LMO2 cells with different additive blends. Electrolyte was EC:DMC (15:85) with 1.0 M LiBF$_4$ + 0.5 M LiFSI. Formation was done at 40 °C with C/20:C/20 rate between 3.0-4.20 V.

Figure 8.2 shows the discharge capacity, normalized discharge capacity and normalized ΔV for SC-LMO2 with different electrolyte additives and EC:DMC (15:85) with 1LiBF$_4$-0.5LiFSI. All cycling was done at 40 °C with C/3:C/3 rates between 3.0-4.20 V. PES221 and PES211 blends had the best capacity retention and ΔV growth, which outperformed the 3VC1DTD blend in Chapter 6. However, the other additive blends did not introduce a significant improvement over 3VC1DTD in terms of capacity retention, although some mixtures such as 2VC1DTD+1PS would be considered more competitive since they have similar capacity retention compared to 3VC1DTD but better FCE, gassing, and R$_{CT}$. Figure 8.2 clearly shows that despite the significant improvements made in LMO electrolyte design, there is still room for improvement by tuning the additive compositions, and certainly fine tuning the solvent and salt formulations as well.
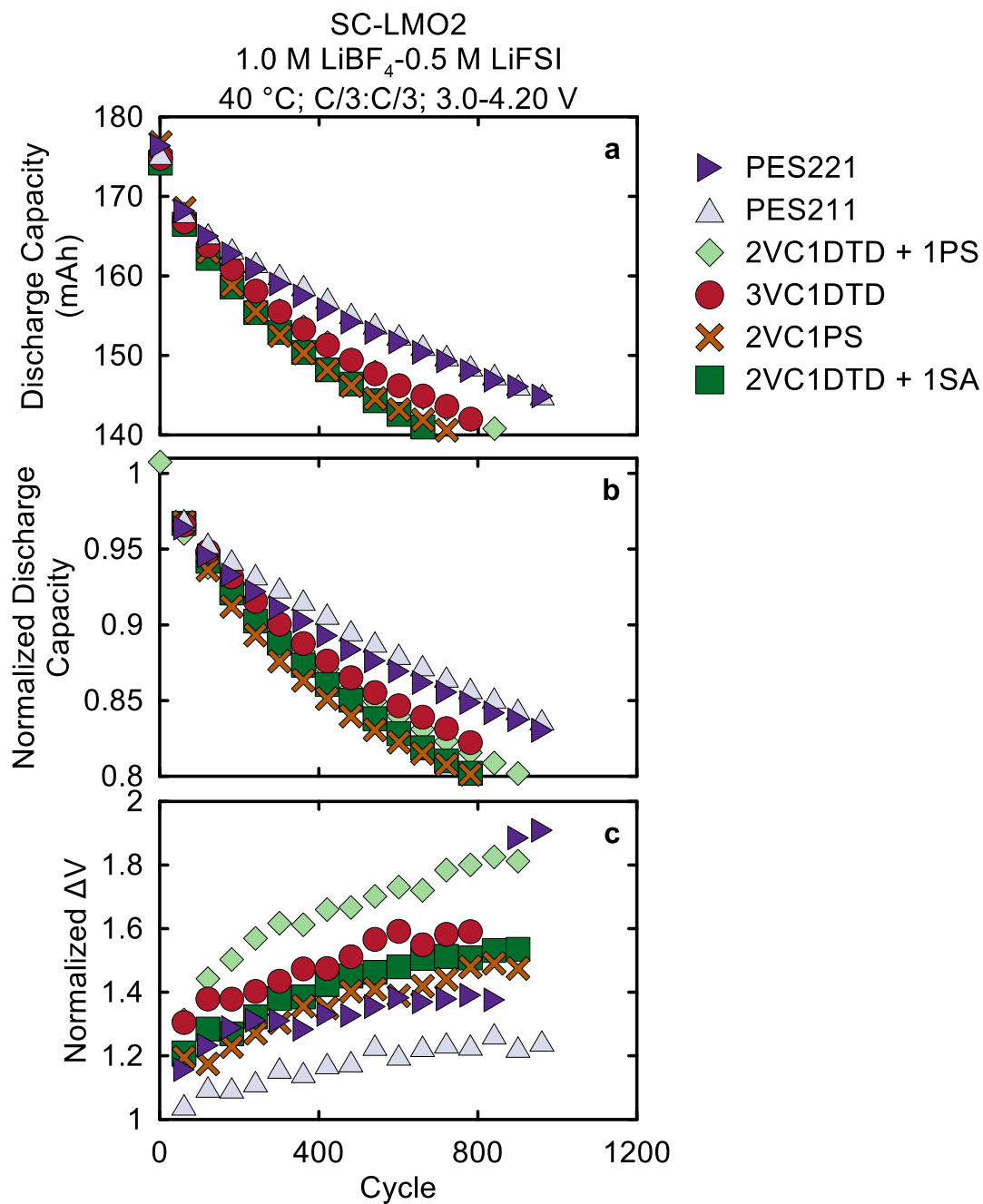
Figure 8.2. (a) discharge capacity (mAh); (b) normalized discharge capacity; and (c) normlized ΔV for SC-LMO2 cells with different additives. Electrolyte was EC:DMC (15:85) with 1.0 M LiBF$_4$ + 0.5 M LiFSI. All cycling was done at 40 °C with C/3:C/3 rate between 3.0-4.20 V.

8.2.2. *Understanding NMC/LMO Synergy*

Chapter 5 highlighted the unique synergy between LMO and NMC materials which resulted in more stable cycling and greatly reduced Mn dissolution. While this synergy in blended positive electrodes has been well-known in the industry, and even used in early EV models, it is still not clear what role NMC plays in stabilizing LMO. This is made more complicated by the fact that not all electrolyte additives had the same degree of synergy as shown in Figure 5.5. Further, the incredible reduction in Mn dissolution in the presence of NMC suggests that the existence of some interplay between the LMO and NMC, or NMC and electrolyte, that is somehow stabilizing the LMO component and hindering Mn dissolution. Probing the underlying mechanisms of this synergy is an area of research that deserves an extensive body of work.

Figure 8.3 shows a schematic representation of a simple pouch bag experiment that can be used to evaluate the role NMC plays in reducing electrode/electrolyte reactivity in blended positive electrodes. By storing lithiated and delithiated positive electrodes from LMO, NMC, and LMO/NMC in pouch bags filled with an excess (~1-2 mL) of $LiPF_6$-based electrolyte, we can monitor the reactivity between the electrodes and electrolytes at different states of charge. After assembly, the pouch bags can be stored at elevated temperature for some period of time while monitoring volume change due to gas generation. Since these pouch bags are filled with a large electrolyte volume, samples of the electrolyte can be periodically extracted for ICP-OES, GCMS, and NMR analysis. This will allow us to monitor the impact of NMC blending on Mn dissolution from the LMO

component, changes to electrolyte composition with and without NMC blending, as well as identify any degradation by-products that are unique to each positive electrode in Figure 8.3, if any. This could be coupled to IMC measurements to probe heat flow from reactions that do not produce gaseous products.
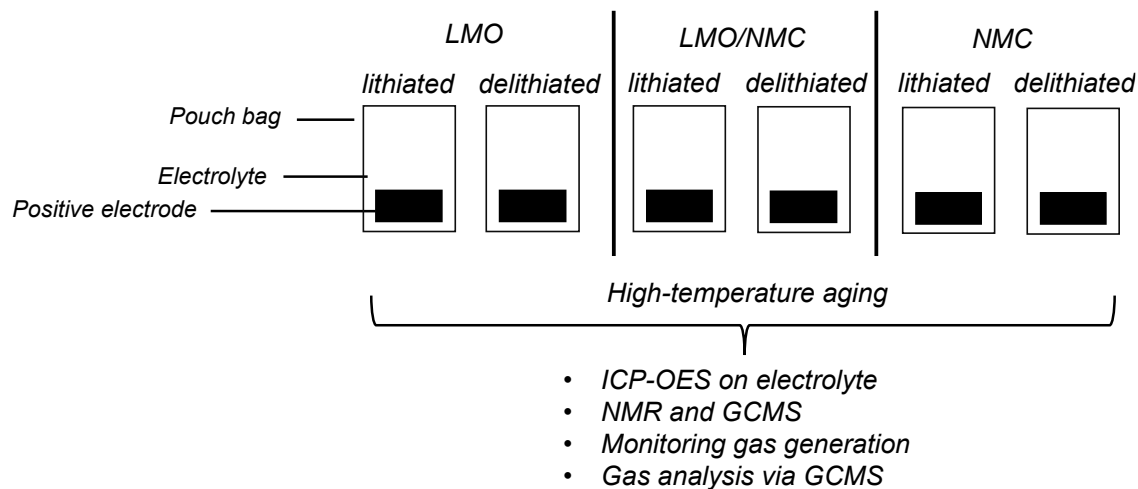
Figure 8.3. Schematic of a simple "pouch bag" study to probe Mn dissolution and electrolyte changes in LMO and LMO/NMC blended positive electrodes.

The goal of this simple test is to identify whether or not the NMC component in blended cells can somehow stabilize the electrolyte by consuming harmful by-products or acidic species that can otherwise degrade the LMO component. This can be exaggerated by introducing water to the electrolyte, which may accelerate the degradation of the LMO component, but not the delithiated NMC according to Sahore et al[161] which suggests that delithiated NMC can consume harmful $LiPF_6$ hydrolysis by-products. Mn dissolution is greatly reduced in blended positive electrodes compared to LMO only (see Figure 5.12), and the ability of NMC to stabilize the electrolyte, if true, might be one of the reasons why NMC cells

have extremely long lifetime compared to other cell chemistries. Similar studies can be done for different electrolyte salts as well.

8.2.3. High Voltage/Temperature Operation of LiFSI-Containing Cells

Figure 5.16 showed that using LiFSI at 70 °C in LMO cells with a 4.20 V UCV induced severe corrosion of the Al current collector, which is serious safety hazard. However, the use of LiFSI also improved cell lifetime at 40 °C (see Figure 5.4) and Al corrosion was not seen over the duration of our cycling experiment. Based on Figure 5.16, co-salts were used alongside LiFSI in Chapter 6 which improved capacity retention and no signs of Al corrosion were seen. Some co-salts such as $LiBF_4$ and LiDFOB lowered the FCE and increased gassing, but there were effective at suppressing Al corrosion. Therefore, knowing the changes in Al corrosion as a function of voltage in LiFSI-only electrolyte at different temperatures, and using the smallest co-salt amount needed to suppress Al corrosion, will be important in optimizing LiFSI electrolyte formulations.

Figure 8.4 shows a schematic of Al loading versus voltage (at different temperatures) and LiFSI co-salt concentration. The onset of Al corrosion can be simply identified with a simple cycling experiment: a C/20 formation cycle and a CV hold at top of charge. For example, one can prepare a set of LMO/AG (or other high voltage cells) that undergoes a typical formation with UCVs of 3.8, 3.9, 4.0…4.4 V followed by a CV hold at top of charge for 2-4 weeks, which is repeated at temperatures from RT to 85 °C. Based on this simple test, one would expect the onset of Al corrosion to change with temperature as depicted in Figure 8.6. Once

the corrosion potential is identified for different temperatures, $LiPF_6$, $LiBF_4$, or LiDFOB co-salt concentration can be varied until the smallest co-salt concentration that suppresses Al corrosion is identified (which may be different for each salt).
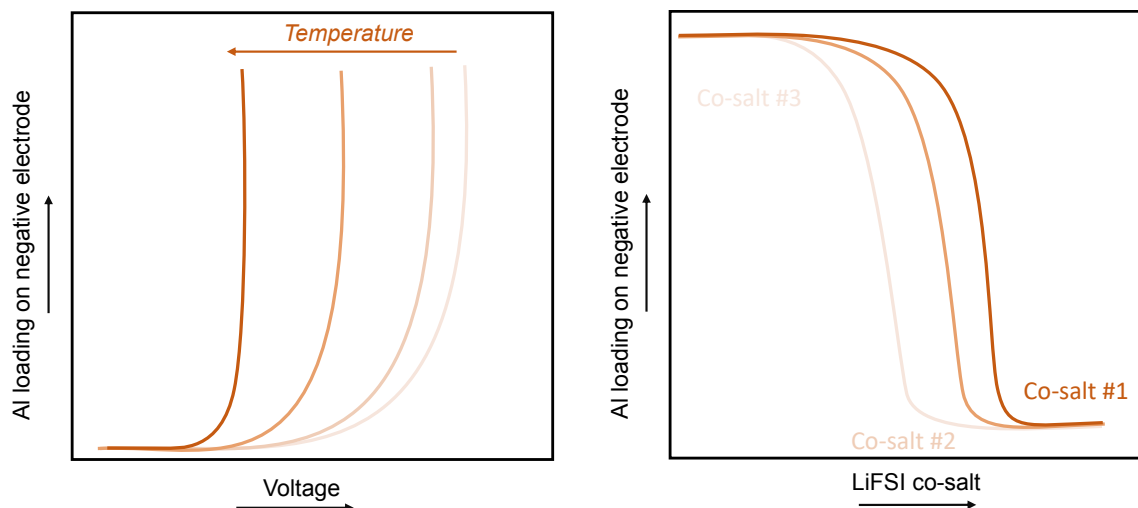
Figure 8.4. Schematic illustration of the onset on Al corrosion in LiFSI electrolytes at different temperatures as a function of cell voltage, and Al loading versus LiFSI co-salt concentration.

NMR can be used to identify how much co-salt is consumed during formation or cycling to prevent Al corrosion, which can guide electrolyte optimization. Since some co-salts like $LiBF_4$ and LiDFOB can be detrimental to FCE and gassing, using the smallest necessary concentration will only be achievable if we quantify how much is consumed during formation to passivate the Al current collector. Finally, once an ideal co-salt concentration has been identified, operating voltage window for that electrolyte must be identified.

References

(1) Frith, J. T.; Lacey, M. J.; Ulissi, U. A Non-Academic Perspective on the Future of Lithium-Based Batteries. *Nat Commun* **2023**, *14* (1), 420. https://doi.org/10.1038/s41467-023-35933-2.

(2) Rising Battery Prices Threaten to Derail the Arrival of Affordable EVs. *Bloomberg.com*. December 6, 2022. https://www.bloomberg.com/news/articles/2022-12-06/rising-battery-prices-threaten-to-derail-the-arrival-of-affordable-evs (accessed 2023-02-04).

(3) *Electric Cars Closing In on Gas Guzzlers as Battery Costs Plunge - Bloomberg*. https://www.bloomberg.com/news/articles/2020-12-16/electric-cars-closing-in-on-gas-guzzlers-as-battery-costs-plunge (accessed 2021-01-17).

(4) Hirsh, H. S.; Li, Y.; Tan, D. H. S.; Zhang, M.; Zhao, E.; Meng, Y. S. Sodium-Ion Batteries Paving the Way for Grid Energy Storage. *Advanced Energy Materials* **2020**, *10* (32), 2001274. https://doi.org/10.1002/aenm.202001274.

(5) Dunn, B.; Kamath, H.; Tarascon, J.-M. Electrical Energy Storage for the Grid: A Battery of Choices. *Science* **2011**, *334* (6058), 928–935. https://doi.org/10.1126/science.1212741.

(6) Li, J.; Fleetwood, J.; Hawley, W. B.; Kays, W. From Materials to Cell: State-of-the-Art and Prospective Technologies for Lithium-Ion Battery Electrode Processing. *Chem. Rev.* **2022**, *122* (1), 903–956. https://doi.org/10.1021/acs.chemrev.1c00565.

(7) Harper, G.; Sommerville, R.; Kendrick, E.; Driscoll, L.; Slater, P.; Stolkin, R.; Walton, A.; Christensen, P.; Heidrich, O.; Lambert, S.; Abbott, A.; Ryder, K.; Gaines, L.; Anderson, P. Recycling Lithium-Ion Batteries from Electric Vehicles. *Nature* **2019**, *575* (7781), 75–86. https://doi.org/10.1038/s41586-019-1682-5.

(8) Sharifi-Asl, S.; Lu, J.; Amine, K.; Shahbazian-Yassar, R. Oxygen Release Degradation in Li-Ion Battery Cathode Materials: Mechanisms and Mitigating Approaches. *Advanced Energy Materials* **2019**, *9* (22), 1900551. https://doi.org/10.1002/aenm.201900551.

(9) Duan, J.; Tang, X.; Dai, H.; Yang, Y.; Wu, W.; Wei, X.; Huang, Y. Building Safe Lithium-Ion Batteries for Electric Vehicles: A Review. *Electrochem. Energ. Rev.* **2020**, *3* (1), 1–42. https://doi.org/10.1007/s41918-019-00060-4.

(10) Zeng, X.; Li, M.; Abd El-Hady, D.; Alshitari, W.; Al-Bogami, A. S.; Lu, J.; Amine, K. Commercialization of Lithium Battery Technologies for Electric Vehicles. *Advanced Energy Materials* **2019**, *9* (27), 1900161. https://doi.org/10.1002/aenm.201900161.

(11) Huang, Y.; Dong, Y.; Li, S.; Lee, J.; Wang, C.; Zhu, Z.; Xue, W.; Li, Y.; Li, J. Lithium Manganese Spinel Cathodes for Lithium-Ion Batteries. *Advanced Energy Materials* **2021**, *11* (2), 2000997. https://doi.org/10.1002/AENM.202000997.

(12) Obrovac, M. N.; Chevrier, V. L. Alloy Negative Electrodes for Li-Ion Batteries. *Chem. Rev.* **2014**, *114* (23), 11444–11502. https://doi.org/10.1021/cr500207g.

(13) Ma, D.; Cao, Z.; Hu, A. Si-Based Anode Materials for Li-Ion Batteries: A Mini Review. *Nano-Micro Lett.* **2014**, *6* (4), 347–358. https://doi.org/10.1007/s40820-014-0008-2.

(14) Goriparti, S.; Miele, E.; De Angelis, F.; Di Fabrizio, E.; Proietti Zaccaria, R.; Capiglia, C. Review on Recent Progress of Nanostructured Anode Materials for Li-Ion Batteries. *Journal of Power Sources* **2014**, *257*, 421–443. https://doi.org/10.1016/j.jpowsour.2013.11.103.

(15) Lu, J.; Chen, Z.; Pan, F.; Cui, Y.; Amine, K. High-Performance Anode Materials for Rechargeable Lithium-Ion Batteries. *Electrochem. Energ. Rev.* **2018**, *1* (1), 35–53. https://doi.org/10.1007/s41918-018-0001-4.

(16) Peled, E.; Golodnitsky, D.; Ardel, G. Advanced Model for Solid Electrolyte Interphase Electrodes in Liquid and Polymer Electrolytes. *Journal of The Electrochemical Society* **1997**, *144* (8), L208. https://doi.org/10.1149/1.1837858.

(17) Harlow, J. E.; Ma, X.; Li, J.; Logan, E.; Liu, Y.; Zhang, N.; Ma, L.; Glazier, S. L.; Cormier, M. M. E.; Genovese, M.; Buteau, S.; Cameron, A.; Stark, J. E.; Dahn, J. R. A Wide Range of Testing Results on an Excellent Lithium-Ion Cell Chemistry to Be Used as Benchmarks for New Battery Technologies. *Journal of The Electrochemical Society* **2019**, *166* (13), A3031–A3044. https://doi.org/10.1149/2.0981913jes.

(18) An, S. J.; Li, J.; Daniel, C.; Mohanty, D.; Nagpure, S.; Wood, D. L. The State of Understanding of the Lithium-Ion-Battery Graphite Solid Electrolyte Interphase (SEI) and Its Relationship to Formation Cycling. *Carbon* **2016**, *105*, 52–76. https://doi.org/10.1016/J.CARBON.2016.04.008.

(19) Cherkashinin, G.; Nikolowski, K.; Ehrenberg, H.; Jacke, S.; Dimesso, L.; Jaegermann, W. The Stability of the SEI Layer, Surface Composition and the Oxidation State of Transition Metals at the Electrolyte-Cathode Interface Impacted by the Electrochemical Cycling: X-Ray Photoelectron Spectroscopy Investigation. *Physical Chemistry Chemical Physics* **2012**, *14* (35), 12321–12331. https://doi.org/10.1039/c2cp41134b.

(20) Parimalam, B. S.; MacIntosh, A. D.; Kadam, R.; Lucht, B. L. Decomposition Reactions of Anode Solid Electrolyte Interphase (SEI) Components with LiPF6. *Journal of Physical Chemistry C* **2017**, *121* (41), 22733–22738. https://doi.org/10.1021/acs.jpcc.7b08433.

(21) Song, W.; Harlow, J.; Logan, E.; Hebecker, H.; Coon, M.; Molino, L.; Johnson, M.; Dahn, J. R.; Metzger, M. A Systematic Study of Electrolyte Additives in Single Crystal and Bimodal $LiNi_{0.8}Mn_{0.1}Co_{0.1}O_2$/Graphite Pouch Cells. *Journal of The Electrochemical Society* **2021**. https://doi.org/10.1149/1945-7111/AC1E55.

(22) Zhang, S. S. A Review on Electrolyte Additives for Lithium-Ion Batteries. *Journal of Power Sources* **2006**, *162* (2), 1379–1394. https://doi.org/10.1016/j.jpowsour.2006.07.074.

(23) Plakhotnyk, A. V.; Ernst, L.; Schmutzler, R. Hydrolysis in the System $LiPF_6$-Propylene Carbonate-Dimethyl Carbonate-H_2O. *Journal of Fluorine Chemistry* **2005**, *126* (1), 27–31. https://doi.org/10.1016/j.jfluchem.2004.09.027.

(24) Ellis, L. D.; Hill, I. G.; Gering, K. L.; Dahn, J. R. Synergistic Effect of $LiPF_6$ and $LiBF_4$ as Electrolyte Salts in Lithium-Ion Cells. *J. Electrochem. Soc.* **2017**, *164* (12), A2426. https://doi.org/10.1149/2.0811712jes.

(25) Gallus, D. R.; Schmitz, R.; Wagner, R.; Hoffmann, B.; Nowak, S.; Cekic-Laskovic, I.; Schmitz, R. W.; Winter, M. The Influence of Different Conducting Salts on the Metal Dissolution and Capacity Fading of NCM Cathode Material. *Electrochimica Acta* **2014**, *134*, 393–398. https://doi.org/10.1016/j.electacta.2014.04.091.

(26) Shangguan, X.; Jia, G.; Li, F.; Wang, Q.; Bai, B. Mixed Salts of LiFSI and LiODFB for Stable $LiCoO_2$-Based Batteries. *J. Electrochem. Soc.* **2016**, *163* (13), A2797. https://doi.org/10.1149/2.1241613jes.

(27) Zeng, X.; Xu, G. L.; Li, Y.; Luo, X.; Maglia, F.; Bauer, C.; Lux, S. F.; Paschos, O.; Kim, S. J.; Lamp, P.; Lu, J.; Amine, K.; Chen, Z. Kinetic Study of Parasitic Reactions in Lithium-Ion Batteries: A Case Study on $LiNi_{0.6}Mn_{0.2}Co_{0.2}O_2$. *ACS Applied Materials and Interfaces* **2016**, *8* (5), 3446–3451. https://doi.org/10.1021.

(28) Krause, L. J.; Jensen, L. D.; Dahn, J. R. Measurement of Parasitic Reactions in Li Ion Cells by Electrochemical Calorimetry. *Journal of The Electrochemical Society* **2012**, *159* (7), A937–A943. https://doi.org/10.1149/2.021207jes.

(29) Birkl, C. R.; Roberts, M. R.; McTurk, E.; Bruce, P. G.; Howey, D. A. Degradation Diagnostics for Lithium Ion Cells. *Journal of Power Sources* **2017**, *341*, 373–386. https://doi.org/10.1016/j.jpowsour.2016.12.011.

(30) Henschel, J.; Horsthemke, F.; Stenzel, Y. P.; Evertz, M.; Girod, S.; Lürenbaum, C.; Kösters, K.; Wiemers-Meyer, S.; Winter, M.; Nowak, S. Lithium Ion Battery Electrolyte Degradation of Field-Tested Electric Vehicle Battery Cells – A Comprehensive Analytical Study. *Journal of Power Sources* **2020**, *447*. https://doi.org/10.1016/j.jpowsour.2019.227370.

(31) Smith, A. J.; Burns, J. C.; Xiong, D.; Dahn, J. R. Interpreting High Precision Coulometry Results on Li-Ion Cells. *J. Electrochem. Soc.* **2011**, *158* (10), A1136. https://doi.org/10.1149/1.3625232.

(32) Qian, Y.; Niehoff, P.; Börner, M.; Grützke, M.; Mönnighoff, X.; Behrends, P.; Nowak, S.; Winter, M.; Schappacher, F. M. Influence of Electrolyte Additives on the Cathode Electrolyte Interphase (CEI) Formation on $LiNi_{1/3}Mn_{1/3}Co_{1/3}O_2$ in Half Cells with Li Metal Counter Electrode. *Journal of Power Sources* **2016**, *329*, 31–40. https://doi.org/10.1016/j.jpowsour.2016.08.023.

(33) Dong, P.; Wang, D.; Yao, Y.; Li, X.; Zhang, Y.; Ru, J.; Ren, T. Stabilizing Interface Layer of $LiNi_{0.5}Co_{0.2}Mn_{0.3}O_2$ Cathode Materials under High Voltage Using p-Toluenesulfonyl Isocyanate as Film Forming Additive. *Journal of Power Sources* **2017**, *344*, 111–118. https://doi.org/10.1016/j.jpowsour.2017.01.116.

(34) Hu, M.; Pang, X.; Zhou, Z. Review Recent Progress in High-Voltage Lithium Ion Batteries. *Journal of Power Sources* **2013**, *237*, 229–242. https://doi.org/10.1016/j.jpowsour.2013.03.024.

(35) Michan, A. L.; Parimalam, B. S.; Leskes, M.; Kerber, R. N.; Yoon, T.; Grey, C. P.; Lucht, B. L. Fluoroethylene Carbonate and Vinylene Carbonate Reduction: Understanding Lithium-Ion Battery Electrolyte Additives and Solid Electrolyte Interphase Formation. **2016**. https://doi.org/10.1021/acs.chemmater.6b02282.

(36) Heiskanen, S. K.; Kim, J.; Lucht, B. L. Generation and Evolution of the Solid Electrolyte Interphase of Lithium-Ion Batteries. *Joule* **2019**, *3* (10), 2322–2333. https://doi.org/10.1016/j.joule.2019.08.018.

(37) Hall, D. S.; Allen, J. P.; Glazier, S. L.; Ellis, L. D.; Ma, L.; Peters, J. M.; Hill, I. G.; Dahn, J. R. The Solid-Electrolyte Interphase Formation Reactions of Ethylene Sulfate and Its Synergistic Chemistry with Prop-1-Ene-1,3-Sultone in Lithium-Ion Cells. *Journal of The Electrochemical Society* **2017**, *164* (14), A3445–A3453. https://doi.org/10.1149/2.0181714jes.

(38) Brown, Z. L.; Jurng, S.; Nguyen, C. C.; Lucht, B. L. Effect of Fluoroethylene Carbonate Electrolytes on the Nanostructure of the Solid Electrolyte Interphase and Performance of Lithium Metal Anodes. *ACS Appl. Energy Mater.* **2018**, *1*. https://doi.org/10.1021/acsaem.8b00705.

(39) Rinkel, B. L. D.; Hall, D. S.; Temprano, I.; Grey, C. P. Electrolyte Oxidation Pathways in Lithium-Ion Batteries. *Journal of the American Chemical Society* **2020**, *142* (35). https://doi.org/10.1021/jacs.0c06363.

(40) Parimalam, B. S.; Lucht, B. L. Reduction Reactions of Electrolyte Salts for Lithium Ion Batteries: $LiPF_6$, $LiBF_4$, LiDFOB, LiBOB, and LiTFSI. *J. Electrochem. Soc.* **2018**, *165* (2), A251. https://doi.org/10.1149/2.0901802jes.

(41) Jung, R.; Metzger, M.; Maglia, F.; Stinner, C.; Gasteiger, H. A. Oxygen Release and Its Effect on the Cycling Stability of $LiNi_xMn_yCo_zO_2$ (NMC) Cathode Materials for Li-Ion Batteries. *Journal of The Electrochemical Society* **2017**, *164* (7), A1361–A1377. https://doi.org/10.1149/2.0021707jes.

(42) Märker, K.; Reeves, P. J.; Xu, C.; Griffith, K. J.; Grey, C. P. Evolution of Structure and Lithium Dynamics in $LiNi_{0.8}Mn_{0.1}Co_{0.1}O_2$ (NMC811) Cathodes during Electrochemical Cycling. *Chemistry of Materials* **2019**, *31* (7), 2545–2554. https://doi.org/10.1021/acs.chemmater.9b00140.

(43) Gauthier, R.; Luscombe, A.; Bond, T.; Bauer, M.; Johnson, M.; Harlow, J.; Louli, A. J.; Dahn, J. R. How Do Depth of Discharge, C-Rate and Calendar Age Affect Capacity Retention, Impedance Growth, the Electrodes, and the Electrolyte in Li-Ion Cells? *Journal of The Electrochemical Society* **2022**, *169* (2), 020518. https://doi.org/10.1149/1945-7111/AC4B82.

(44) Nam, G. W.; Park, N.-Y.; Park, K.-J.; Yang, J.; Liu, J.; Yoon, C. S.; Sun, Y.-K. Capacity Fading of Ni-Rich NCA Cathodes: Effect of Microcracking Extent. *ACS Energy Letters* **2019**, *4* (12), 2995–3001. https://doi.org/10.1021/ACSENERGYLETT.9B02302.

(45) Yin, S.; Deng, W.; Chen, J.; Gao, X.; Zou, G.; Hou, H.; Ji, X. Fundamental and Solutions of Microcrack in Ni-Rich Layered Oxide Cathode Materials of Lithium-Ion Batteries. *Nano Energy* **2021**, *83*, 105854. https://doi.org/10.1016/J.NANOEN.2021.105854.

(46) Smith, A. J.; Dahn, J. R. Delta Differential Capacity Analysis. *Journal of The Electrochemical Society* **2012**, *159* (3), A290–A293. https://doi.org/10.1149/2.076203JES/XML.

(47) Li, J. Comparison of Single Crystal and Polycrystalline $LiNi_{0.5}Mn_{0.3}Co_{0.2}O_2$ Positive Electrode Materials for High Voltage Li-Ion Cells. *J. Electrochem. Soc.* **2017**, *164*. https://doi.org/10.1149/2.0991707jes.

(48) Weber, R.; Fell, C. R.; Dahn, J. R.; Hy, S. Operando X-Ray Diffraction Study of Polycrystalline and Single-Crystal $Li_xNi_{0.5}Mn_{0.3}Co_{0.2}O_2$. *Journal of The Electrochemical Society* **2017**, *164* (13), A2992–A2999. https://doi.org/10.1149/2.0441713jes.

(49) Bond, T.; Gauthier, R.; Eldesoky, A.; Harlow, J.; Dahn, J. R. In Situ Imaging of Electrode Thickness Growth and Electrolyte Depletion in Single-Crystal vs Polycrystalline $LiNi_xMn_yCo_zO_2$/Graphite Pouch Cells Using Multi-Scale Computed Tomography. *Journal of The Electrochemical Society* **2022**, *169* (2), 020501. https://doi.org/10.1149/1945-7111/AC4B83.

(50) Cho, W.; Kim, S. M.; Song, J. H.; Yim, T.; Woo, S. G.; Lee, K. W.; Kim, J. S.; Kim, Y. J. Improved Electrochemical and Thermal Properties of Nickel Rich $LiNi_{0.6}Co_{0.2}Mn_{0.2}O_2$ Cathode Materials by SiO_2 Coating. *Journal of Power Sources* **2015**, *282*, 45–50. https://doi.org/10.1016/j.jpowsour.2014.12.128.

(51) Zhao, W.; Zou, L.; Jia, H.; Zheng, J.; Wang, D.; Song, J.; Hong, C.; Liu, R.; Xu, W.; Yang, Y.; Xiao, J.; Wang, C.; Zhang, J.-G. Optimized Al Doping Improves Both Interphase Stability and Bulk Structural Integrity of Ni-Rich NMC Cathode Materials. *ACS Applied Energy Materials* **2020**, *3* (4), 3369–3377. https://doi.org/10.1021/ACSAEM.9B02372.

(52) Li, H.; Liu, A.; Zhang, N.; Wang, Y.; Yin, S.; Wu, H.; Dahn, J. R. An Unavoidable Challenge for Ni-Rich Positive Electrode Materials for Lithium-Ion Batteries. **2019**. https://doi.org/10.1021/acs.chemmater.9b02372.

(53) Gilbert, J. A.; Shkrob, I. A.; Abraham, D. P. Transition Metal Dissolution, Ion Migration, Electrocatalytic Reduction and Capacity Loss in Lithium-Ion Full Cells. *Journal of The Electrochemical Society* **2017**, *164* (2), A389–A399. https://doi.org/10.1149/2.1111702jes.

(54) Jung, R.; Linsenmann, F.; Thomas, R.; Wandt, J.; Solchenbach, S.; Maglia, F.; Stinner, C.; Tromp, M.; Gasteiger, H. A. Nickel, Manganese, and Cobalt Dissolution from Ni-Rich NMC and Their Effects on NMC622-Graphite Cells. *Journal of The Electrochemical Society* **2019**, *166* (2), A378–A389. https://doi.org/10.1149/2.1151902jes.

(55) Thompson, L. M.; Stone, W.; Eldesoky, A.; Smith, N. K.; McFarlane, C. R. M.; Kim, J. S.; Johnson, M. B.; Petibon, R.; Dahn, J. R. Quantifying Changes to the Electrolyte and Negative Electrode in Aged NMC532/Graphite Lithium-Ion Cells. *Journal of The Electrochemical Society* **2018**, *165* (11), A2732–A2740. https://doi.org/10.1149/2.0721811jes.

(56) Ma, L.; Young, S.; Ellis, L. D.; Huang, Q.; Ma, X.; Chatzidakis, M.; Li, H.; Thompson, L.; Eldesoky, A.; McFarlane, C. R. M.; Botton, G. A.; Hill, I. G.; Dahn, J. R. Impact of a Titanium-Based Surface Coating Applied to Li[$Ni_{0.5}Mn_{0.3}Co_{0.2}$]O_2 on Lithium-Ion Cell Performance. *ACS Applied Energy Materials* **2018**, *1* (12), 7052–7064. https://doi.org/10.1021/acsaem.8b01472.

(57) Smith, A. J.; Burns, J. C.; Trussler, S.; Dahn, J. R. Precision Measurements of the Coulombic Efficiency of Lithium-Ion Batteries and of Electrode Materials for Lithium-Ion Batteries. *Journal of The Electrochemical Society* **2009**, *157* (2), A196. https://doi.org/10.1149/1.3268129.

(58) Smith, A. J.; Burns, J. C.; Zhao, X.; Xiong, D.; Dahn, J. R. A High Precision Coulometry Study of the SEI Growth in Li/Graphite Cells. *Journal of The Electrochemical Society* **2011**, *158* (5), A447. https://doi.org/10.1149/1.3557892.

(59) Aiken, C. P.; Xia, J.; Wang, D. Y.; Stevens, D. A.; Trussler, S.; Dahn, J. R. An Apparatus for the Study of in Situ Gas Evolution in Li-Ion Pouch Cells. *Journal of the Electrochemical Society* **2014**, *161* (10). https://doi.org/10.1149/2.0151410jes.

(60) Landesfeind, J.; Hattendorff, J.; Ehrl, A.; Wall, W. A.; Gasteiger, H. A. Tortuosity Determination of Battery Electrodes and Separators by Impedance Spectroscopy. *Journal of The Electrochemical Society* **2016**, *163* (7), 1373–1387. https://doi.org/10.1149/2.1141607jes.

(61) Nelson, K. J.; d'Eon, G. L.; Wright, A. T. B.; Ma, L.; Xia, J.; Dahn, J. R. Studies of the Effect of High Voltage on the Impedance and Cycling Performance of Li[$Ni_{0.4}Mn_{0.4}Co_{0.2}$]O_2 /Graphite Lithium-Ion Pouch Cells. *Journal of The Electrochemical Society* **2015**, *162* (6), A1046–A1054. https://doi.org/10.1149/2.0831506jes.

(62) Waag, W.; Käbitz, S.; Sauer, D. U. Experimental Investigation of the Lithium-Ion Battery Impedance Characteristic at Various Conditions and Aging States and Its Influence on the Application. *Applied Energy* **2013**, *102*, 885–897. https://doi.org/10.1016/J.APENERGY.2012.09.030.

(63) Petibon, R.; Aiken, C. P.; Sinha, N. N.; Burns, J. C.; Ye, H.; VanElzen, C. M.; Jain, G.; Trussler, S.; Dahn, J. R. Study of Electrolyte Additives Using Electrochemical Impedance Spectroscopy on Symmetric Cells. *Journal of the Electrochemical Society* **2013**, *160* (1). https://doi.org/10.1149/2.005302jes.

(64) Buteau, S.; Dahn, J. R. Analysis of Thousands of Electrochemical Impedance Spectra of Lithium-Ion Cells through a Machine Learning Inverse Model. *J. Electrochem. Soc.* **2019**, *166* (8), A1611. https://doi.org/10.1149/2.1051908jes.

(65) Mo Seong, W.; Park, K.-Y.; Hwan Lee, M.; Moon, S.; Oh, K.; Park, H.; Lee, S.; Kang, K. Abnormal Self-Discharge in Lithium-Ion Batteries. *Energy & Environmental Science* **2018**, *11* (4), 970–978. https://doi.org/10.1039/C8EE00186C.

(66) Blyr, A.; Sigala, C.; Amatucci, G.; Guyomard, D.; Chabre, Y.; Tarascon, J.-M. Self-Discharge of $LiMn_2O_4$/C Li-Ion Cells in Their Discharged State: Understanding by Means of Three-Electrode Measurements. *J. Electrochem. Soc.* **1998**, *145* (1), 194. https://doi.org/10.1149/1.1838235.

(67) Barcellona, S.; Piegari, L. Effect of Current on Cycle Aging of Lithium Ion Batteries. *Journal of Energy Storage* **2020**, *29*. https://doi.org/10.1016/j.est.2020.101310.

(68) Amine, K.; Liu, J.; Belharouak, I. High-Temperature Storage and Cycling of C-$LiFePO_4$/Graphite Li-Ion Cells. *Electrochemistry Communications* **2005**, *7* (7), 669–673. https://doi.org/10.1016/j.elecom.2005.04.018.

(69) Sinha, N. N.; Smith, A. J.; Burns, J. C.; Jain, G.; Eberman, K. W.; Scott, E.; Gardner, J. P.; Dahn, J. R. The Use of Elevated Temperature Storage Experiments to Learn about Parasitic Reactions in Wound $LiCoO_2$/Graphite Cells. *J. Electrochem. Soc.* **2011**, *158* (11), A1194. https://doi.org/10.1149/2.007111jes.

(70) Louli, A. J.; Li, J.; Trussler, S.; Fell, C. R.; Dahn, J. R. Volume, Pressure and Thickness Evolution of Li-Ion Pouch Cells with Silicon-Composite Negative Electrodes. *Journal of The Electrochemical Society* **2017**, *164* (12), A2689–A2696. https://doi.org/10.1149/2.1691712jes.

(71) Shi, H.; Reimers, J. N.; Dahn, J. R. Structure-Refinement Program for Disordered Carbons. *Journal of Applied Crystallography* **1993**, *26* (6), 827–836. https://doi.org/10.1107/S0021889893003784.

(72) Haschke, M. *Laboratory Micro-X-Ray Fluorescence Spectroscopy: Instrumentation and Applications*; Springer Science & Business Media, 2014.

(73) Eldesoky, A.; Logan, E. R.; Johnson, M. B.; McFarlane, C. R. M.; Dahn, J. R. Scanning Micro X-Ray Fluorescence (µXRF) as an Effective Tool in Quantifying Fe Dissolution in $LiFePO_4$ Cells: Towards a Mechanistic Understanding of Fe Dissolution. *Journal of The Electrochemical Society* **2020**, *167* (13), 130539. https://doi.org/10.1149/1945-7111/abba62.

(74) Dahn, J. R.; Trussler, S.; Hatchard, T. D.; Bonakdarpour, A.; Mueller-Neuhaus, J. R.; Hewitt, K. C.; Fleischauer, M. Economical Sputtering System to Produce Large-Size Composition-Spread Libraries Having Linear and Orthogonal Stoichiometry Variations. *Chemistry of Materials* **2002**, *14* (8), 3519–3523. https://doi.org/10.1021/cm020236x.

(75) Delacourt, C.; Kwong, A.; Liu, X.; Qiao, R.; Yang, W. L.; Lu, P.; Harris, S. J.; Srinivasan, V. Effect of Manganese Contamination on the Solid-Electrolyte-Interphase Properties in Li-Ion Batteries. *Journal of The Electrochemical Society* **2013**, *160* (8), A1099–A1107. https://doi.org/10.1149/2.035308jes.

(76) Bottomley, P. A.; Griffiths, J. R. *Handbook of Magnetic Resonance Spectroscopy In Vivo: MRS Theory, Practice and Applications*; John Wiley & Sons, 2016.

(77) Rankin, N. J.; Preiss, D.; Welsh, P.; Burgess, K. E. V.; Nelson, S. M.; Lawlor, D. A.; Sattar, N. The Emergence of Proton Nuclear Magnetic Resonance Metabolomics in the Cardiovascular Arena as Viewed from a Clinical Perspective. *Atherosclerosis* **2014**, *237* (1), 287–300. https://doi.org/10.1016/j.atherosclerosis.2014.09.024.

(78) Xiong, D. J.; Ellis, L. D.; Petibon, R.; Hynes, T.; Liu, Q. Q.; Dahn, J. R. Studies of Gas Generation, Gas Consumption and Impedance Growth in Li-Ion Cells with Carbonate or Fluorinated Electrolytes Using the Pouch Bag Method. *Journal of The Electrochemical Society* **2017**, *164* (2), A340–A347. https://doi.org/10.1149/2.1091702jes.

(79) Zhang, B.; Metzger, M.; Solchenbach, S.; Payne, M.; Meini, S.; Gasteiger, H. A.; Garsuch, A.; Lucht, B. L. Role of 1,3-Propane Sultone and Vinylene Carbonate in Solid Electrolyte Interface Formation and Gas Generation. *Journal of Physical Chemistry C* **2015**, *119* (21), 11337–11348. https://doi.org/10.1021/ACS.JPCC.5B00072.

(80) Mao, Z.; Farkhondeh, M.; Pritzker, M.; Fowler, M.; Chen, Z. Calendar Aging and Gas Generation in Commercial Graphite/NMC-LMO Lithium-Ion Pouch Cell. *J. Electrochem. Soc.* **2017**, *164* (14), A3469. https://doi.org/10.1149/2.0241714jes.

(81) Glazier, S. L.; Odom, S. A.; Kaur, A. P.; Dahn, J. R. Determining Parasitic Reaction Enthalpies in Lithium-Ion Cells Using Isothermal Microcalorimetry. *Journal of The Electrochemical Society* **2018**, *165* (14), A3449. https://doi.org/10.1149/2.0761814JES.

(82) Logan, E. R.; Eldesoky, A.; Eastwood, E.; Hebecker, H.; Aiken, C. P.; Metzger, M.; Dahn, J. R. The Use of LiFSI and LiTFSI in LiFePO$_4$/Graphite Pouch Cells to Improve High-Temperature Lifetime. *J. Electrochem. Soc.* **2022**, *169* (4), 040560. https://doi.org/10.1149/1945-7111/ac67f9.

(83) Liang, L.; Zhang, W.; Zhao, F.; Denis, D. K.; Zaman, F. uz; Hou, L.; Yuan, C. Surface/Interface Structure Degradation of Ni-Rich Layered Oxide Cathodes toward Lithium-Ion Batteries: Fundamental Mechanisms and Remedying Strategies. *Advanced Materials Interfaces* **2020**, *7* (3). https://doi.org/10.1002/admi.201901749.

(84) Liu, G.; Xu, N.; Zou, Y.; Zhou, K.; Yang, X.; Jiao, T.; Yang, W.; Yang, Y.; Zheng, J. Stabilizing Ni-Rich LiNi$_{0.83}$Co$_{0.12}$Mn$_{0.05}$O$_2$ with Cyclopentyl Isocyanate as a Novel Electrolyte Additive. *ACS Applied Materials and Interfaces* **2021**, *13*, 12069–12078. https://doi.org/10.1021/ACSAMI.1C00443/ASSET/IMAGES/LARGE/AM1C00443_0010.JPEG.

(85) Sun, H. H.; Ryu, H.-H.; Kim, U.-H.; Weeks, J. A.; Heller, A.; Sun, Y.-K.; Mullins, C. B. Beyond Doping and Coating: Prospective Strategies for Stable High-Capacity Layered Ni-Rich Cathodes. *ACS Energy Letters* **2020**, *5* (4), 1136–1146. https://doi.org/10.1021/acsenergylett.0c00191.

(86) Liu, Y.; Harlow, J.; Dahn, J. Microstructural Observations of "Single Crystal" Positive Electrode Materials Before and After Long Term Cycling by Cross-Section Scanning Electron Microscopy. *Journal of The Electrochemical Society* **2020**, *167* (2), 020512. https://doi.org/10.1149/1945-7111/ab6288.

(87) Dechent, P.; Epp, A.; Jöst, D.; Preger, Y.; Attia, P. M.; Li, W.; Sauer, D. U. ENPOLITE: Comparing Lithium-Ion Cells across Energy, Power, Lifetime, and Temperature. *ACS Energy Letters* **2021**, *6* (6), 2351–2355. https://doi.org/10.1021/ACSENERGYLETT.1C00743/ASSET/IMAGES/LARGE/NZ1C00743_0004.JPEG.

(88) Ecker, M.; Nieto, N.; Käbitz, S.; Schmalstieg, J.; Blanke, H.; Warnecke, A.; Sauer, D. U. Calendar and Cycle Life Study of Li(NiMnCo)O_2-Based 18650 Lithium-Ion Batteries. *Journal of Power Sources* **2014**, *248*, 839–851. https://doi.org/10.1016/J.JPOWSOUR.2013.09.143.

(89) Käbitz, S.; Gerschler, J. B.; Ecker, M.; Yurdagel, Y.; Emmermacher, B.; André, D.; Mitsch, T.; Sauer, D. U. Cycle and Calendar Life Study of a Graphite|LiNi$_{1/3}$Mn$_{1/3}$Co$_{1/3}$O$_2$ Li-Ion High Energy System. Part A: Full Cell Characterization. *Journal of Power Sources* **2013**, *239*, 572–583. https://doi.org/10.1016/j.jpowsour.2013.03.045.

(90) Ecker, M.; Gerschler, J. B.; Vogel, J.; Käbitz, S.; Hust, F.; Dechent, P.; Sauer, D. U. Development of a Lifetime Prediction Model for Lithium-Ion Batteries Based on Extended Accelerated Aging Test Data. *Journal of Power Sources* **2012**, *215*, 248–257. https://doi.org/10.1016/j.jpowsour.2012.05.012.

(91) Ouyang, M.; Chu, Z.; Lu, L.; Li, J.; Han, X.; Feng, X.; Liu, G. Low Temperature Aging Mechanism Identification and Lithium Deposition in a Large Format Lithium Iron Phosphate Battery for Different Charge Profiles. *Journal of Power Sources* **2015**, *286*, 309–320. https://doi.org/10.1016/J.JPOWSOUR.2015.03.178.

(92) Leng, F.; Tan, C. M.; Pecht, M. Effect of Temperature on the Aging Rate of Li Ion Battery Operating above Room Temperature. *Scientific Reports 2015 5:1* **2015**, *5* (1), 1–12. https://doi.org/10.1038/srep12967.

(93) Gao, Y.; Jiang, J.; Zhang, C.; Zhang, W.; Jiang, Y. Aging Mechanisms under Different State-of-Charge Ranges and the Multi-Indicators System of State-of-Health for Lithium-Ion Battery with Li(NiMnCo)O_2 Cathode. *Journal of Power Sources* **2018**, *400*, 641–651. https://doi.org/10.1016/J.JPOWSOUR.2018.07.018.

(94) De Sutter, L.; Berckmans, G.; Marinaro, M.; Smekens, J.; Firouz, Y.; Wohlfahrt-Mehrens, M.; Van Mierlo, J.; Omar, N. Comprehensive Aging Analysis of Volumetric Constrained Lithium-Ion Pouch Cells with High Concentration Silicon-Alloy Anodes. *Energies 2018, Vol. 11, Page 2948* **2018**, *11* (11), 2948. https://doi.org/10.3390/EN11112948.

(95) Watanabe, S.; Kinoshita, M.; Hosokawa, T.; Morigaki, K.; Nakura, K. Capacity Fade of $LiAl_yNi_{1-x-Y}Co_xO_2$ Cathode for Lithium-Ion Batteries during Accelerated Calendar and Cycle Life Tests (Surface Analysis of $LiAl_yNi_{1-x-Y}Co_xO_2$ Cathode after Cycle Tests in Restricted Depth of Discharge Ranges). *Journal of Power Sources* **2014**, *258*, 210–217. https://doi.org/10.1016/j.jpowsour.2014.02.018.

(96) Preger, Y.; Barkholtz, H. M.; Fresquez, A.; Campbell, D. L.; Juba, B. W.; Romàn-Kustas, J.; Ferreira, S. R.; Chalamala, B. Degradation of Commercial Lithium-Ion Cells as a Function of Chemistry and Cycling Conditions. *Journal of The Electrochemical Society* **2020**, *167* (12), 120532. https://doi.org/10.1149/1945-7111/ABAE37.

(97) Taskovic, T.; Eldesoky, A.; Song, W.; Bauer, M.; Dahn, J. R. High Temperature Testing of NMC/Graphite Cells for Rapid Cell Performance Screening and Studies of Electrolyte Degradation. *Journal of The Electrochemical Society* **2022**, *169* (4), 040538. https://doi.org/10.1149/1945-7111/AC6453.

(98) Li, J.; Downie, L. E.; Ma, L.; Qiu, W.; Dahn, J. R. Study of the Failure Mechanisms of $LiNi_{0.8}Mn_{0.1}Co_{0.1}O_2$ Cathode Material for Lithium Ion Batteries. *J. Electrochem. Soc.* **2015**, *162* (7), A1401. https://doi.org/10.1149/2.1011507jes.

(99) Liu, Y.; Song, W.; Eldesoky, A.; Harlow, J.; Logan, E. R.; Li, H.; Dahn, J. R. The Impact of Upper Cut-Off Voltage on the Cycling Performance of Li-Ion Cells with Positive Electrodes Having Various Nickel Contents. *J. Electrochem. Soc.* **2022**, *169* (4), 040531. https://doi.org/10.1149/1945-7111/ac6456.

(100) Park, N.-Y.; Ryu, H.-H.; Park, G.-T.; Noh, T.-C.; Sun, Y.-K. Optimized Ni-Rich NCMA Cathode for Electric Vehicle Batteries. *Advanced Energy Materials* **2021**, *11* (9), 2003767. https://doi.org/10.1002/AENM.202003767.

(101) Kim, J.; Lee, H.; Cha, H.; Yoon, M.; Park, M.; Cho, J. Prospect and Reality of Ni-Rich Cathode for Commercialization. *Advanced Energy Materials* **2018**, *8* (6), 1702028. https://doi.org/10.1002/aenm.201702028.

(102) Downie, L. E.; Dahn, J. R. Determination of the Voltage Dependence of Parasitic Heat Flow in Lithium Ion Cells Using Isothermal Microcalorimetry. *Journal of The Electrochemical Society* **2014**, *161* (12), A1782–A1787. https://doi.org/10.1149/2.0301412JES/XML.

(103) Schweidler, S.; De Biasi, L.; Schiele, A.; Hartmann, P.; Brezesinski, T.; Janek, J. Volume Changes of Graphite Anodes Revisited: A Combined Operando X-Ray Diffraction and in Situ Pressure Analysis Study. *Journal of Physical Chemistry C* **2018**, *122* (16), 8829–8835. https://doi.org/10.1021/acs.jpcc.8b01873.

(104) Sahore, R.; Dogan, F.; Bloom, I. D. Identification of Electrolyte-Soluble Organic Cross-Talk Species in a Lithium-Ion Battery via a Two-Compartment Cell. *Chemistry of Materials* **2019**, *31* (8), 2884–2891. https://doi.org/10.1021/ACS.CHEMMATER.9B00063.

(105) Michalak, B.; Berkes, B. B.; Sommer, H.; Brezesinski, T.; Janek, J. Electrochemical Cross-Talk Leading to Gas Evolution and Capacity Fade in $LiNi_{0.5}Mn_{1.5}O_4$/Graphite Full-Cells. *Journal of Physical Chemistry C* **2017**, *121* (1), 211–216. https://doi.org/10.1021/acs.jpcc.6b11184.

(106) Jayawardana, C.; Rodrigo, N.; Parimalam, B.; Lucht, B. L. Role of Electrolyte Oxidation and Difluorophosphoric Acid Generation in Crossover and Capacity Fade in Lithium Ion Batteries. *ACS Energy Letters* **2021**, *6* (11), 3788–3792. https://doi.org/10.1021/ACSENERGYLETT.1C01657

(107) Dahn, H. M.; Smith, A. J.; Burns, J. C.; Stevens, D. A.; Dahn, J. R. User-Friendly Differential Voltage Analysis Freeware for the Analysis of Degradation Mechanisms in Li-Ion Batteries. *Journal of The Electrochemical Society* **2012**, *159* (9), A1405–A1409. https://doi.org/10.1149/2.013209JES/XML.

(108) Dubarry, M.; Svoboda, V.; Hwu, R.; Liaw, B. Y. Incremental Capacity Analysis and Close-to-Equilibrium OCV Measurements to Quantify Capacity Fade in Commercial Rechargeable Lithium Batteries. *Electrochem. Solid-State Lett.* **2006**, *9* (10), A454. https://doi.org/10.1149/1.2221767.

(109) Taskovic, T.; Thompson, L.; Eldesoky, A.; Lumsden, M.; Dahn, J. R. Optimizing Electrolyte Additive Loadings in NMC532/Graphite Cells: Vinylene Carbonate and Ethylene Sulfate. *Journal of the Electrochemical Society* **2021**, *168* (1), 010514. https://doi.org/10.1149/1945-7111/abd833.

(110) Thompson, L. M.; Harlow, J. E.; Eldesoky, A.; Bauer, M. K. G.; Cheng, J. H.; Stone, W. S.; Taskovic, T.; McFarlane, C. R. M.; Dahn, J. R. Study of Electrolyte and Electrode Composition Changes vs Time in Aged Li-Ion Cells. *Journal of The Electrochemical Society* **2021**, *168* (2), 020532. https://doi.org/10.1149/1945-7111.

(111) Glazier, S. L.; Li, J.; Louli, A. J.; Allen, J. P.; Dahn, J. R. An Analysis of Artificial and Natural Graphite in Lithium Ion Pouch Cells Using Ultra-High Precision Coulometry, Isothermal Microcalorimetry, Gas Evolution, Long Term Cycling and Pressure Measurements. *Journal of The Electrochemical Society* **2017**, *164* (14), A3545–A3555. https://doi.org/10.1149/2.0421714jes.

(112) Huang, Q.; Glazier, S. L.; Louli, A. J.; McArthur, M.; Liu, C.; Schrooten, J.; Dahn, J. R. Effects of Graphite Heat-Treatment Temperature on Single-Crystal Li[$Ni_5Mn_3Co_2$]O_2 /Graphite Pouch Cells. *Journal of The Electrochemical Society* **2020**, *167* (8), 080543. https://doi.org/10.1149/1945-7111/ab9381.

(113) Zheng, T.; Dahn, J. R. The Effect of Turbostratic Disorder on the Staging Transitions in Lithium Intercalated Graphite. *Synthetic Metals* **1995**, *73* (1), 1–7. https://doi.org/10.1016/0379-6779(95)03289-4.

(114) Zheng, T.; Dahn, J. R. *Effect of Turbostratic Disorder in Graphitic Carbon Hosts on the Intercalation of Lithium*; 1995; Vol. 51.

(115) Liu, Y.; Hamam, I.; Dahn, J. R. A Study of Vinylene Carbonate and Prop-1-Ene-1,3 Sultone Electrolyte Additives Using Polycrystalline Li[$Ni_{0.6}Mn_{0.2}Co_{0.2}$]O_2 in Positive/Positive Symmetric Cells. *Journal of The Electrochemical Society* **2020**, *167* (11), 110527. https://doi.org/10.1149/1945-7111/aba36a.

(116) Mundszinger, M.; Farsi, S.; Rapp, M.; Golla-Schindler, U.; Kaiser, U.; Wachtler, M. Morphology and Texture of Spheroidized Natural and Synthetic Graphites. *Carbon* **2017**, *111*, 764–773. https://doi.org/10.1016/j.carbon.2016.10.060.

(117) Natarajan, C.; Fujimoto, H.; Mabuchi, A.; Tokumitsu, K.; Kasuh, T. Effect of Mechanical Milling of Graphite Powder on Lithium Intercalation Properties. *Journal of Power Sources* **2001**, *92* (1), 187–192. https://doi.org/10.1016/S0378-7753(00)00528-0.

(118) Shi, H.; Barker, J.; Saïdi, M. Y.; Koksbang, R. Structure and Lithium Intercalation Properties of Synthetic and Natural Graphite. *J. Electrochem. Soc.* **1996**, *143* (11), 3466. https://doi.org/10.1149/1.1837238.

(119) Tao Zheng; J. S. Xue, and; Dahn*, J. R. Lithium Insertion in Hydrogen-Containing Carbonaceous Materials. *Chemistry of Materials* **1996**, *8* (2), 389–393. https://doi.org/10.1021/CM950304Y.

(120) Ding, Y. S.; Li, W. N.; Iaconetti, S.; Shen, X. F.; DiCarlo, J.; Galasso, F. S.; Suib, S. L. Characteristics of Graphite Anode Modified by CVD Carbon Coating. *Surface and Coatings Technology* **2006**, *200* (9), 3041–3048. https://doi.org/10.1016/J.SURFCOAT.2005.05.040.

(121) Yoshio, M.; Wang, H.; Fukuda, K. Spherical Carbon-Coated Natural Graphite as a Lithium-Ion Battery-Anode Material. *Angewandte Chemie International Edition* **2003**, *42* (35), 4203–4206. https://doi.org/10.1002/ANIE.200351203.

(122) Ohta, N.; Nagaoka, K.; Hoshi, K.; Bitoh, S.; Inagaki, M. Carbon-Coated Graphite for Anode of Lithium Ion Rechargeable Batteries: Graphite Substrates for Carbon Coating. *Journal of Power Sources* **2009**, *194* (2), 985–990. https://doi.org/10.1016/J.JPOWSOUR.2009.06.013.

(123) Ma, L.; Ellis, L.; Glazier, S. L.; Ma, X.; Liu, Q.; Li, J.; Dahn, J. R. $LiPO_2F_2$ as an Electrolyte Additive in $Li[Ni_{0.5}Mn_{0.3}Co_{0.2}]O_2$/Graphite Pouch Cells. *Journal of The Electrochemical Society* **2018**, *165* (5), A891. https://doi.org/10.1149/2.0381805JES.

(124) Ma, L.; Glazier, S. L.; Petibon, R.; Xia, J.; Peters, J. M.; Liu, Q.; Allen, J.; Doig, R. N. C.; Dahn, J. R. A Guide to Ethylene Carbonate-Free Electrolyte Making for Li-Ion Cells. *Journal of The Electrochemical Society* **2016**, *164* (1), A5008. https://doi.org/10.1149/2.0191701JES.

(125) Logan, E. R.; Hebecker, H.; Ma, X.; Quinn, J.; HyeJeong, Y.; Kumakura, S.; Paulsen, J.; Dahn, J. R. A Comparison of the Performance of Different Morphologies of $LiNi_{0.8}Mn_{0.1}Co_{0.1}O_2$ Using Isothermal Microcalorimetry, Ultra-High Precision Coulometry, and Long-Term Cycling. *Journal of The Electrochemical Society* **2020**, *167* (6), 060530. https://doi.org/10.1149/1945-7111/AB8620.

(126) Liu, Q. Q.; Petibon, R.; Du, C. Y.; Dahn, J. R. Effects of Electrolyte Additives and Solvents on Unwanted Lithium Plating in Lithium-Ion Cells. *Journal of The Electrochemical Society* **2017**, *164* (6), A1173. https://doi.org/10.1149/2.1081706JES.

(127) Broussely, M.; Biensan, P.; Bonhomme, F.; Blanchard, P.; Herreyre, S.; Nechev, K.; Staniewicz, R. J. Main Aging Mechanisms in Li Ion Batteries. *Journal of Power Sources* **2005**, *146* (1–2), 90–96. https://doi.org/10.1016/J.JPOWSOUR.2005.03.172.

(128) Broussely, M.; Herreyre, S.; Biensan, P.; Kasztejna, P.; Nechev, K.; Staniewicz, R. J. Aging Mechanism in Li Ion Cells and Calendar Life Predictions. *Journal of Power Sources* **2001**, *97–98*, 13–21. https://doi.org/10.1016/S0378-7753(01)00722-4.

(129) Sarre, G.; Blanchard, P.; Broussely, M. Aging of Lithium-Ion Batteries. *Journal of Power Sources* **2004**, *127* (1–2), 65–71. https://doi.org/10.1016/J.JPOWSOUR.2003.09.008.

(130) Wu, S. huang; Lee, P. H. Storage Fading of a Commercial 18650 Cell Comprised with NMC/LMO Cathode and Graphite Anode. *Journal of Power Sources* **2017**, *349*, 27–36. https://doi.org/10.1016/j.jpowsour.2017.03.002.

(131) Sulzer, V.; Mohtat, P.; Aitio, A.; Lee, S.; Yeh, Y. T.; Steinbacher, F.; Khan, M. U.; Lee, J. W.; Siegel, J. B.; Stefanopoulou, A. G.; Howey, D. A. The Challenge and Opportunity of Battery Lifetime Prediction from Field Data. *Joule* **2021**, *5* (8), 1934–1955. https://doi.org/10.1016/j.joule.2021.06.005.

(132) Aurbach, D.; Markovsky, B.; Rodkin, A.; Levi, E.; Cohen, Y. S.; Kim, H. J.; Schmidt, M. On the Capacity Fading of $LiCoO_2$ Intercalation Electrodes: The Effect of Cycling, Storage, Temperature, and Surface Film Forming Additives. *Electrochimica Acta* **2002**, *47* (27), 4291–4306. https://doi.org/10.1016/S0013-4686(02)00417-6.

(133) Logan, E. R.; Tonita, E. M.; Gering, K. L.; Li, J.; Ma, X.; Beaulieu, L. Y.; Dahn, J. R. A Study of the Physical Properties of Li-Ion Battery Electrolytes Containing Esters. *Journal of The Electrochemical Society* **2018**, *165* (2), A21–A30. https://doi.org/10.1149/2.0271802jes.

(134) Campion, C. L.; Li, W.; Lucht, B. L. Thermal Decomposition of $LiPF_6$-Based Electrolytes for Lithium-Ion Batteries. *Journal of The Electrochemical Society* **2005**, *152* (12), A2327. https://doi.org/10.1149/1.2083267.

(135) Gyenes, B.; Stevens, D. A.; Chevrier, V. L.; Dahn, J. R. Understanding Anomalous Behavior in Coulombic Efficiency Measurements on Li-Ion Batteries. *J. Electrochem. Soc.* **2014**, *162* (3), A278. https://doi.org/10.1149/2.0191503jes.

(136) Lewerenz, M.; Fuchs, G.; Becker, L.; Sauer, D. U. Irreversible Calendar Aging and Quantification of the Reversible Capacity Loss Caused by Anode Overhang. *Journal of Energy Storage* **2018**, *18*, 149–159. https://doi.org/10.1016/j.est.2018.04.029.

(137) Lewerenz, M.; Münnix, J.; Schmalstieg, J.; Käbitz, S.; Knips, M.; Sauer, D. U. Systematic Aging of Commercial $LiFePO_4$|Graphite Cylindrical Cells Including a Theory Explaining Rise of Capacity during Aging. *Journal of Power Sources* **2017**, *345*, 254–263. https://doi.org/10.1016/j.jpowsour.2017.01.133.

(138) Ma, X.; Harlow, J. E.; Li, J.; Ma, L.; Hall, D. S.; Buteau, S.; Genovese, M.; Cormier, M.; Dahn, J. R. Editors' Choice—Hindering Rollover Failure of Li[$Ni_{0.5}Mn_{0.3}Co_{0.2}$]O_2/Graphite Pouch Cells during Long-Term Cycling. *J. Electrochem. Soc.* **2019**, *166* (4), A711. https://doi.org/10.1149/2.0801904jes.

(139) Davidsson Kurland, S. Energy Use for GWh-Scale Lithium-Ion Battery Production. *Environmental Research Communications* **2020**, *2* (1), 012001. https://doi.org/10.1088/2515-7620/ab5e1e.

(140) Ding, Y.; Cano, Z. P.; Yu, A.; Lu, J.; Chen, · Zhongwei. Automotive Li-Ion Batteries: Current Status and Future Perspectives. **1918**, *2*, 1–28. https://doi.org/10.1007/s41918-018-0022-z.

(141) Amine, K.; Liu, J.; Kang, S.; Belharouak, I.; Hyung, Y.; Vissers, D.; Henriksen, G. Improved Lithium Manganese Oxide Spinel/Graphite Li-Ion Cells for High-Power Applications. *Journal of Power Sources*; Elsevier, 2004; Vol. 129, pp 14–19. https://doi.org/10.1016/j.jpowsour.2003.11.007.

(142) Thackeray, M. M.; Amine, K. $LiMn_2O_4$ Spinel and Substituted Cathodes. *Nat Energy* **2021**, *6* (5), 566–566. https://doi.org/10.1038/s41560-021-00815-8.

(143) Zhan, C.; Wu, T.; Lu, J.; Amine, K. Dissolution, Migration, and Deposition of Transition Metal Ions in Li-Ion Batteries Exemplified by Mn-Based Cathodes-A Critical Review. *Energy and Environmental Science* **2018**, *11* (2), 243–257. https://doi.org/10.1039/c7ee03122j.

(144) Pieczonka, N. P. W. W.; Liu, Z.; Lu, P.; Olson, K. L.; Moote, J.; Powell, B. R.; Kim, J.-H. H. Understanding Transition-Metal Dissolution Behavior in $LiNi_{0.5}Mn_{1.5}O_4$ High-Voltage Spinel for Lithium Ion Batteries. *The Journal of Physical Chemistry C* **2013**, *117* (31), 15947–15957. https://doi.org/10.1021/jp405158m.

(145) Yang, L.; Takahashi, M.; Wang, B. A Study on Capacity Fading of Lithium-Ion Battery with Manganese Spinel Positive Electrode during Cycling. *Electrochimica Acta* **2006**, *51* (16), 3228–3234. https://doi.org/10.1016/j.electacta.2005.09.014.

(146) Gowda, S. R.; Gallagher, K. G.; Croy, J. R.; Bettge, M.; Thackeray, M. M.; Balasubramanian, M. Oxidation State of Cross-over Manganese Species on the Graphite Electrode of Lithium-Ion Cells. *Physical Chemistry Chemical Physics* **2014**, *16* (15), 6898–6902. https://doi.org/10.1039/c4cp00764f.

(147) Wandt, J.; Freiberg, A.; Thomas, R.; Gorlin, Y.; Siebel, A.; Jung, R.; Gasteiger, H. A.; Tromp, M. Transition Metal Dissolution and Deposition in Li-Ion Batteries Investigated by Operando X-Ray Absorption Spectroscopy. *Journal of Materials Chemistry A* **2016**, *4* (47), 18300–18305. https://doi.org/10.1039/C6TA08865A.

(148) Chen, Z.; Qin, Y.; Amine, K.; Sun, Y.-K. Role of Surface Coating on Cathode Materials for Lithium-Ion Batteries. *J. Mater. Chem.* **2010**, *20* (36), 7606–7612. https://doi.org/10.1039/C0JM00154F.

(149) Joshi, T.; Eom, K.; Yushin, G.; Fuller, T. F. Effects of Dissolved Transition Metals on the Electrochemical Performance and SEI Growth in Lithium-Ion Batteries. *Journal of The Electrochemical Society* **2014**, *161* (12), A1915–A1921. https://doi.org/10.1149/2.0861412jes.

(150) Wang, C.; Xing, L.; Vatamanu, J.; Chen, Z.; Lan, G.; Li, W.; Xu, K. Overlooked Electrolyte Destabilization by Manganese (II) in Lithium-Ion Batteries. *Nature Communications 2019 10:1* **2019**, *10* (1), 1–9. https://doi.org/10.1038/s41467-019-11439-8.

(151) Han, H.-B.; Zhou, S.-S.; Zhang, D.-J.; Feng, S.-W.; Li, L.-F.; Liu, K.; Feng, W.-F.; Nie, J.; Li, H.; Huang, X.-J.; Armand, M.; Zhou, Z.-B. Lithium Bis(Fluorosulfonyl)Imide (LiFSI) as Conducting Salt for Nonaqueous Liquid Electrolytes for Lithium-Ion Batteries: Physicochemical and Electrochemical Properties. *Journal of Power Sources* **2011**, *196* (7), 3623–3632. https://doi.org/10.1016/j.jpowsour.2010.12.040.

(152) Abouimrane, A.; Ding, J.; Davidson, I. J. Liquid Electrolyte Based on Lithium Bis-Fluorosulfonyl Imide Salt: Aluminum Corrosion Studies and Lithium Ion Battery Investigations. *Journal of Power Sources* **2009**, *189* (1), 693–696. https://doi.org/10.1016/j.jpowsour.2008.08.077.

(153) Smith, A. J.; Smith, S. R.; Byrne, T.; Burns, J. C.; Dahn, J. R. Synergies in Blended $LiMn_2O_4$ and $Li[Ni_{1/3}Mn_{1/3}Co_{1/3}]O_2$ Positive Electrodes. *Journal of The Electrochemical Society* **2012**, *159* (10), A1696–A1701. https://doi.org/10.1149/2.056210JES/PDF.

(154) Jobst, N. M.; Hoffmann, A.; Klein, A.; Zink, S.; Wohlfahrt-Mehrens, M. Ternary Cathode Blend Electrodes for Environmentally Friendly Lithium-Ion Batteries. *ChemSusChem* **2020**, *13* (15), 3928–3936. https://doi.org/10.1002/cssc.202000251.

(155) Gao, Y.; Dahn, J. R. Correlation between the Growth of the 3.3 V Discharge Plateau and Capacity Fading in $Li_{1+x}Mn_{2-x}O_4$ Materials. *Solid State Ionics* **1996**, *84* (1), 33–40. https://doi.org/10.1016/S0167-2738(96)83003-7.

(156) Gao, Y.; Dahn, J. R. Synthesis and Characterization of $Li_{1+x}Mn_{2-x}O_4$ for Li-Ion Battery Applications. *J. Electrochem. Soc.* **1996**, *143* (1), 100. https://doi.org/10.1149/1.1836393.

(157) Schlueter, S.; Genieser, R.; Richards, D.; Hoster, H. E.; Mercer, M. P. Quantifying Structure Dependent Responses in Li-Ion Cells with Excess Li Spinel Cathodes: Matching Voltage and Entropy Profiles through Mean Field Models. *Phys. Chem. Chem. Phys.* **2018**, *20* (33), 21417–21429. https://doi.org/10.1039/C8CP02989J.

(158) Zhou, F.; Bao, C. Analysis of the Lithium-Ion Battery Capacity Degradation Behavior with a Comprehensive Mathematical Model. *Journal of Power Sources* **2021**, *515*, 230630. https://doi.org/10.1016/J.JPOWSOUR.2021.230630.

(159) Ochida, M.; Domi, Y.; Doi, T.; Tsubouchi, S.; Nakagawa, H.; Yamanaka, T.; Abe, T.; Ogumi, Z. Influence of Manganese Dissolution on the Degradation of Surface Films on Edge Plane Graphite Negative-Electrodes in Lithium-Ion Batteries. *J. Electrochem. Soc.* **2012**, *159* (7), A961–A966. https://doi.org/10.1149/2.031207jes.

(160) Li, C.; Zeng, S.; Wang, P.; Li, Z.; Yang, L.; Zhao, D.; Wang, J.; Liu, H.; Li, S. Mechanism of Aluminum Corrosion in LiFSI-Based Electrolyte at Elevated Temperatures. *Transactions of Nonferrous Metals Society of China* **2021**, *31* (5), 1439–1451. https://doi.org/10.1016/S1003-6326(21)65588-7.

(161) Sahore, R.; O' Hanlon, D. C.; Tornheim, A.; Lee, C.-W.; Garcia, J. C.; Iddir, H.; Balasubramaniam, M.; Bloom, I. Revisiting the Mechanism Behind Transition-Metal Dissolution from Delithiated $LiNi_xMn_yCo_zO_2$ (NMC) Cathodes. *Journal of the Electrochemical Society* **2020**, *167*. https://doi.org/10.1149/1945-7111/ab6826.

(162) Logan, E. R.; Tonita, E. M.; Gering, K. L.; Ma, L.; Bauer, M. K. G.; Li, J.; Beaulieu, L. Y.; Dahn, J. R. A Study of the Transport Properties of Ethylene Carbonate-Free Li Electrolytes. *J. Electrochem. Soc.* **2018**, *165* (3), A705. https://doi.org/10.1149/2.0981803jes.

(163) Ellis, L. D.; Xia, J.; Louli, A. J.; Dahn, J. R. Effect of Substituting $LiBF_4$ for $LiPF_6$ in High Voltage Lithium-Ion Cells Containing Electrolyte Additives. *J. Electrochem. Soc.* **2016**, *163* (8), A1686. https://doi.org/10.1149/2.0851608jes.

(164) Hamam, I.; Omessi, R.; Rathore, D.; Geng, C.; Cooke, R.; Plucknett, K.; Bishop, D. P.; Zaker, N.; Botton, G. A.; Yang, C.; Dahn, J. R. Correlating the Mechanical Strength of Positive Electrode Material Particles to Their Capacity Retention. *Cell Reports Physical Science* **2022**, *3* (1), 100714. https://doi.org/10.1016/j.xcrp.2021.100714.

(165) Boulanger, T.; Eldesoky, A.; Buechele, S.; Taskovic, T.; Azam, S.; Aiken, C.; Logan, E.; Metzger, M. Investigation of Redox Shuttle Generation in LFP/Graphite and NMC811/Graphite Cells. *J. Electrochem. Soc.* **2022**, *169* (4), 040518. https://doi.org/10.1149/1945-7111/ac62c6.

(166) Logan, E. R.; Hebecker, H.; Eldesoky, A.; Luscombe, A.; Johnson, M. B.; Dahn, J. R. Performance and Degradation of $LiFePO_4$/Graphite Cells: The Impact of Water Contamination and an Evaluation of Common Electrolyte Additives. *Journal of The Electrochemical Society* **2020**, *167* (13), 130543. https://doi.org/10.1149/1945-7111.

(167) Burns, J. C.; Sinha, N. N.; Coyle, D. J.; Jain, G.; VanElzen, C. M.; Lamanna, W. M.; Xiao, A.; Scott, E.; Gardner, J. P.; Dahn, J. R. The Impact of Varying the Concentration of Vinylene Carbonate Electrolyte Additive in Wound Li-Ion Cells. *J. Electrochem. Soc.* **2011**, *159* (2), A85. https://doi.org/10.1149/2.028202jes.

(168) Jarry, A.; Gottis, S.; Yu, Y. S.; Roque-Rosell, J.; Kim, C.; Cabana, J.; Kerr, J.; Kostecki, R. The Formation Mechanism of Fluorescent Metal Complexes at the $Li_xNi_{0.5}Mn_{1.5}O_{4-\delta}$/Carbonate Ester Electrolyte Interface. *Journal of the American Chemical Society* **2015**, *137* (10), 3533–3539. https://doi.org/10.1021/ja5116698.

(169) Brown, Z. L.; Lucht, B. L. Synergistic Performance of Lithium Difluoro(Oxalato)Borate and Fluoroethylene Carbonate in Carbonate Electrolytes for Lithium Metal Anodes. *J. Electrochem. Soc.* **2019**, *166*. https://doi.org/10.1149/2.0181903jes.

(170) Zhu, Y.; Li, Y.; Bettge, M.; Abraham, D. P. Positive Electrode Passivation by LiDFOB Electrolyte Additive in High-Capacity Lithium-Ion Cells. *J. Electrochem. Soc.* **2012**, *159*. https://doi.org/10.1149/2.083212jes.

(171) Takeuchi, E. S.; Gan, H.; Palazzo, M.; Leising, R. A.; Davis, S. M. Anode Passivation and Electrolyte Solvent Disproportionation: Mechanism of Ester Exchange Reaction in Lithium-Ion Batteries. *J. Electrochem. Soc.* **1997**, *144* (6), 1944. https://doi.org/10.1149/1.1837726.

(172) Zhang, S. S.; Xu, K.; Jow, T. R. Study of $LiBF_4$ as an Electrolyte Salt for a Li-Ion Battery. *J. Electrochem. Soc.* **2002**, *149* (5), A586. https://doi.org/10.1149/1.1466857.

(173) Lux, S. F.; Lucas, I. T.; Pollak, E.; Passerini, S.; Winter, M.; Kostecki, R. The Mechanism of HF Formation in $LiPF_6$ Based Organic Carbonate Electrolytes. *Electrochemistry Communications* **2012**, *14* (1), 47–50. https://doi.org/10.1016/j.elecom.2011.10.026.

(174) *Lithium iron phosphate comes to America*. Chemical & Engineering News. https://cen.acs.org/energy/energy-storage-/Lithium-iron-phosphate-comes-to-America/101/i4 (accessed 2023-03-15).

(175) Logan, E. R.; Hebecker, H.; Eldesoky, A.; Luscombe, A.; Johnson, M. B.; Dahn, J. R. Performance and Degradation of $LiFePO_4$/Graphite Cells: The Impact of Water Contamination and an Evaluation of Common Electrolyte Additives. *Journal of The Electrochemical Society* **2020**, *167* (13), 130543. https://doi.org/10.1149/1945-7111.

(176) Hellqvist Kjell, M.; Malmgren, S.; Ciosek, K.; Behm, M.; Edström, K.; Lindbergh, G. Comparing Aging of Graphite/$LiFePO_4$ Cells at 22 °C and 55 °C – Electrochemical and Photoelectron Spectroscopy Studies. *Journal of Power Sources* **2013**, *243*, 290–298. https://doi.org/10.1016/j.jpowsour.2013.06.011.

(177) Dubarry, M.; Truchot, C.; Liaw, B. Y. Cell Degradation in Commercial $LiFePO_4$ Cells with High-Power and High-Energy Designs. *Journal of Power Sources* **2014**, *258*, 408–419. https://doi.org/10.1016/j.jpowsour.2014.02.052.

(178) Kim, J.-H.; Woo, S. C.; Park, M.-S.; Kim, K. J.; Yim, T.; Kim, J.-S.; Kim, Y.-J. Capacity Fading Mechanism of $LiFePO_4$-Based Lithium Secondary Batteries for Stationary Energy Storage. *Journal of Power Sources* **2013**, *229*, 190–197. https://doi.org/10.1016/j.jpowsour.2012.12.024.

(179) Li, D.; Danilov, D. L.; Xie, J.; Raijmakers, L.; Gao, L.; Yang, Y.; Notten, P. H. L. Degradation Mechanisms of C_6/$LiFePO_4$ Batteries: Experimental Analyses of Calendar Aging. *Electrochimica Acta* **2016**, *190*, 1124–1133. https://doi.org/10.1016/j.electacta.2015.12.161.

(180) Wang, J.; Yang, J.; Tang, Y.; Li, R.; Liang, G.; Sham, T.-K.; Sun, X. Surface Aging at Olivine $LiFePO_4$: A Direct Visual Observation of Iron Dissolution and the Protection Role of Nano-Carbon Coating. *J. Mater. Chem. A* **2013**, *1* (5), 1579–1586. https://doi.org/10.1039/C2TA00521B.

(181) Wang, J.; Tang, Y.; Yang, J.; Li, R.; Liang, G.; Sun, X. Nature of $LiFePO_4$ Aging Process: Roles of Impurity Phases. *Journal of Power Sources* **2013**, *238*, 454–463. https://doi.org/10.1016/j.jpowsour.2013.04.061.

(182) Li, D.; Danilov, D.; Gao, L.; Yang, Y.; Notten, P. H. L. Degradation Mechanisms of C_6/$LiFePO_4$ Batteries: Experimental Analyses of Cycling-Induced Aging. *Electrochimica Acta* **2016**, *210*, 445–455. https://doi.org/10.1016/j.electacta.2016.05.091.

(183) Stich, M.; Göttlinger, M.; Kurniawan, M.; Schmidt, U.; Bund, A. Hydrolysis of $LiPF_6$ in Carbonate-Based Electrolytes for Lithium-Ion Batteries and in Aqueous Media. *Journal of Physical Chemistry C* **2018**, *122* (16), 8836–8842. https://doi.org/10.1021/acs.jpcc.8b02080.

(184) Koltypin, M.; Aurbach, D.; Nazar, L.; Ellis, B. On the Stability of $LiFePO_4$ Olivine Cathodes under Various Conditions (Electrolyte Solutions, Temperatures). *Electrochemical and Solid-State Letters* **2007**, *10* (2). https://doi.org/10.1149/1.2403974.

(185) Xia, J.; Sinha, N. N.; Chen, L. P.; Dahn, J. R. A Comparative Study of a Family of Sulfate Electrolyte Additives. *J. Electrochem. Soc.* **2013**, *161* (3), A264. https://doi.org/10.1149/2.015403jes.

(186) Hong, E.-S.; Okada, S.; Sonoda, T.; Gopukumar, S.; Yamaki, J. Thermal Stability of Electrolytes with Mixtures of $LiPF_6$ and $LiBF_4$ Used in Lithium-Ion Cells. *J. Electrochem. Soc.* **2004**, *151* (11), A1836. https://doi.org/10.1149/1.1802136.

(187) Taskovic, T.; Eldesoky, A.; Aiken, C. P.; Dahn, J. R. Low-Voltage Operation and Lithium Bis(Fluorosulfonyl)Imide Electrolyte Salt Enable Long Li-Ion Cell Lifetimes at 85 °C. *J. Electrochem. Soc.* **2022**, *169* (10), 100547. https://doi.org/10.1149/1945-7111/ac9a81.

(188) Ehteshami, N.; Ibing, L.; Stolz, L.; Winter, M.; Paillard, E. Ethylene Carbonate-Free Electrolytes for Li-Ion Battery: Study of the Solid Electrolyte Interphases Formed on Graphite Anodes. *Journal of Power Sources* **2020**, *451*, 227804. https://doi.org/10.1016/j.jpowsour.2020.227804.

(189) Eshetu, G. G.; Grugeon, S.; Gachot, G.; Mathiron, D.; Armand, M.; Laruelle, S. LiFSI vs. LiPF$_6$ Electrolytes in Contact with Lithiated Graphite: Comparing Thermal Stabilities and Identification of Specific SEI-Reinforcing Additives. *Electrochimica Acta* **2013**, *102*, 133–141. https://doi.org/10.1016/j.electacta.2013.03.171.

(190) Kang, S.-J.; Park, K.; Park, S.-H.; Lee, H. Unraveling the Role of LiFSI Electrolyte in the Superior Performance of Graphite Anodes for Li-Ion Batteries. *Electrochimica Acta* **2018**, *259*, 949–954. https://doi.org/10.1016/j.electacta.2017.11.018.

(191) Xu, M.; Zhou, L.; Hao, L.; Xing, L.; Li, W.; Lucht, B. L. Investigation and Application of Lithium Difluoro(Oxalate)Borate (LiDFOB) as Additive to Improve the Thermal Stability of Electrolyte for Lithium-Ion Batteries. *Journal of Power Sources* **2011**, *196* (16), 6794–6801. https://doi.org/10.1016/j.jpowsour.2010.10.050.

(192) Buechele, S.; Adamson, A.; Eldesoky, A.; Boetticher, T.; Hartmann, L.; Boulanger, T.; Azam, S.; Johnson, M. B.; Taskovic, T.; Logan, E.; Metzger, M. Identification of Redox Shuttle Generated in LFP/Graphite and NMC811/Graphite Cells. *J. Electrochem. Soc.* **2023**, *170* (1), 010511. https://doi.org/10.1149/1945-7111/acaf44.

(193) Buechele, S.; Logan, E.; Boulanger, T.; Azam, S.; Eldesoky, A.; Song, W.; Johnson, M. B.; Metzger, M. Reversible Self-Discharge of LFP/Graphite and NMC811/Graphite Cells Originating from Redox Shuttle Generation. *J. Electrochem. Soc.* **2023**, *170* (1), 010518. https://doi.org/10.1149/1945-7111/acb10c.

(194) Eldesoky, A.; Logan, E. R.; Johnson, M. B.; McFarlane, C. R. M.; Dahn, J. R. Scanning Micro X-Ray Fluorescence (μXRF) as an Effective Tool in Quantifying Fe Dissolution in LiFePO$_4$ Cells: Towards a Mechanistic Understanding of Fe Dissolution. *Journal of The Electrochemical Society* **2020**, *167* (13), 130539. https://doi.org/10.1149/1945-7111/ABBA62.

(195) Wang, D. Y.; Xia, J.; Ma, L.; Nelson, K. J.; Harlow, J. E.; Xiong, D.; Downie, L. E.; Petibon, R.; Burns, J. C.; Xiao, A.; Lamanna, W. M.; Dahn, J. R. A Systematic Study of Electrolyte Additives in Li[$Ni_{1/3}Mn_{1/3}Co_{1/3}$]O_2 (NMC)/Graphite Pouch Cells. *J. Electrochem. Soc.* **2014**, *161* (12), A1818. https://doi.org/10.1149/2.0511412jes.

(196) Louli, A. J.; Eldesoky, A.; Weber, R.; Genovese, M.; Coon, M.; deGooyer, J.; Deng, Z.; White, R. T.; Lee, J.; Rodgers, T.; Petibon, R.; Hy, S.; Cheng, S. J. H.; Dahn, J. R. Diagnosing and Correcting Anode-Free Cell Failure via Electrolyte and Morphological Analysis. *Nature Energy* **2020**, *5* (9), 693–702. https://doi.org/10.1038/s41560-020-0668-8.

(197) Nie, M.; Abraham, D. P.; Chen, Y.; Bose, A.; Lucht, B. L. Silicon Solid Electrolyte Interphase (SEI) of Lithium Ion Battery Characterized by Microscopy and Spectroscopy. *J. Phys. Chem. C* **2013**, *117* (26), 13403–13412. https://doi.org/10.1021/jp404155y.

(198) Ma, L.; Xia, J.; Dahn, J. R. Improving the High Voltage Cycling of Li[$Ni_{0.42}Mn_{0.42}Co_{0.16}$]$O_2$ (NMC442)/Graphite Pouch Cells Using Electrolyte Additives. *J. Electrochem. Soc.* **2014**, *161* (14), A2250. https://doi.org/10.1149/2.1041414jes.

(199) Xia, J.; Liu, Q.; Hebert, A.; Hynes, T.; Petibon, R.; Dahn, J. R. Succinic Anhydride as an Enabler in Ethylene Carbonate-Free Linear Alkyl Carbonate Electrolytes for High Voltage Li-Ion Cells. *J. Electrochem. Soc.* **2017**, *164* (6), A1268. https://doi.org/10.1149/2.1341706jes.

(200) Tarnopolskiy, V.; Kalhoff, J.; Nádherná, M.; Bresser, D.; Picard, L.; Fabre, F.; Rey, M.; Passerini, S. Beneficial Influence of Succinic Anhydride as Electrolyte Additive on the Self-Discharge of 5 V $LiNi_{0.4}Mn_{1.6}O_4$ Cathodes. *Journal of Power Sources* **2013**, *236*, 39–46. https://doi.org/10.1016/j.jpowsour.2013.02.030.

Appendix A. Supporting Data

Chapter 3
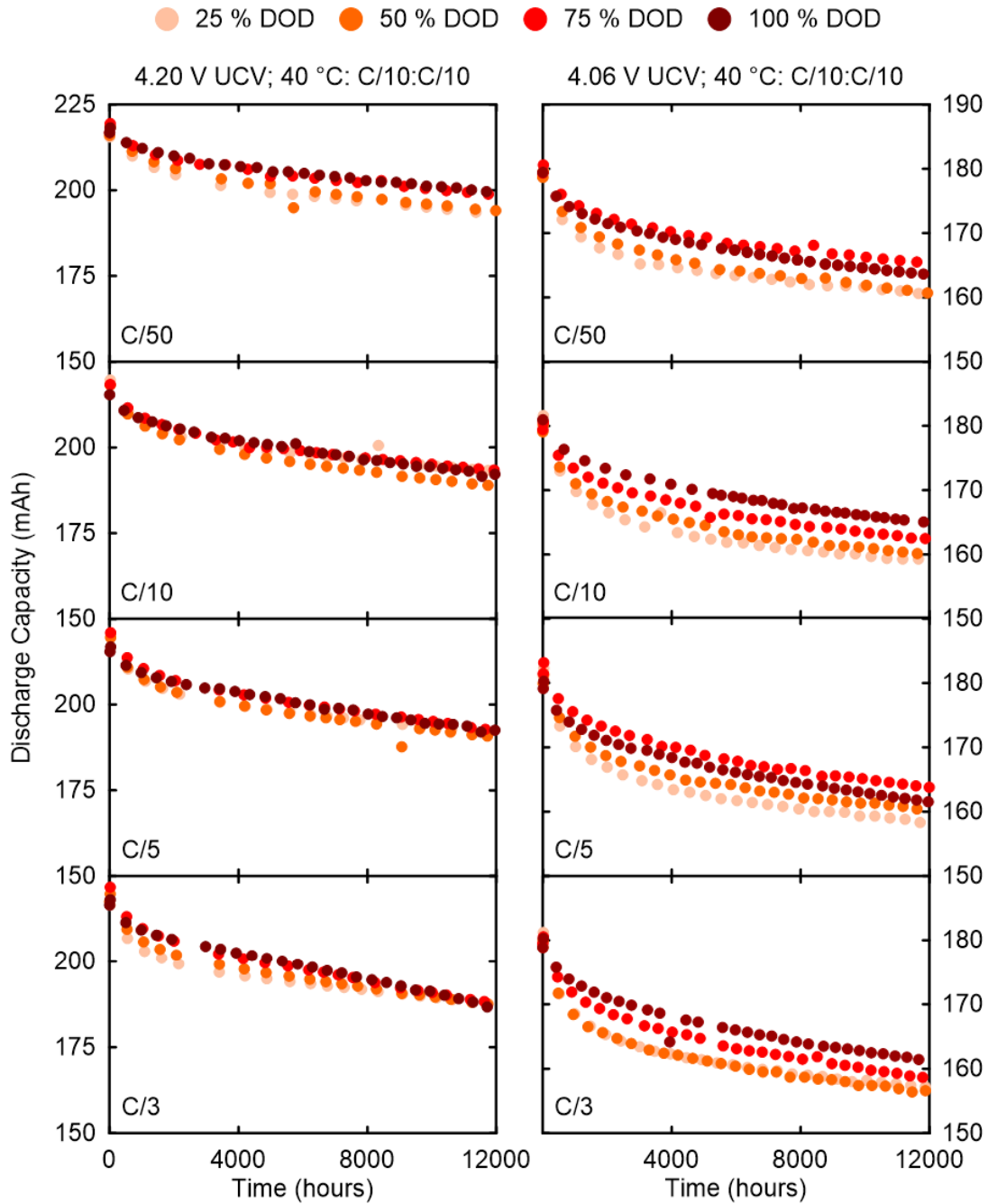
Figure A.1. Checkup cycle discharge capacity (mAh) versus time (hours) for NMC811/AG cells cycling to 4.06 and 4.20 V UCV at 40 ºC. All data shown here is for the C/10:C/10, 100 % DOD, cycles performed periodically to check the low-rate capacity of the cells.
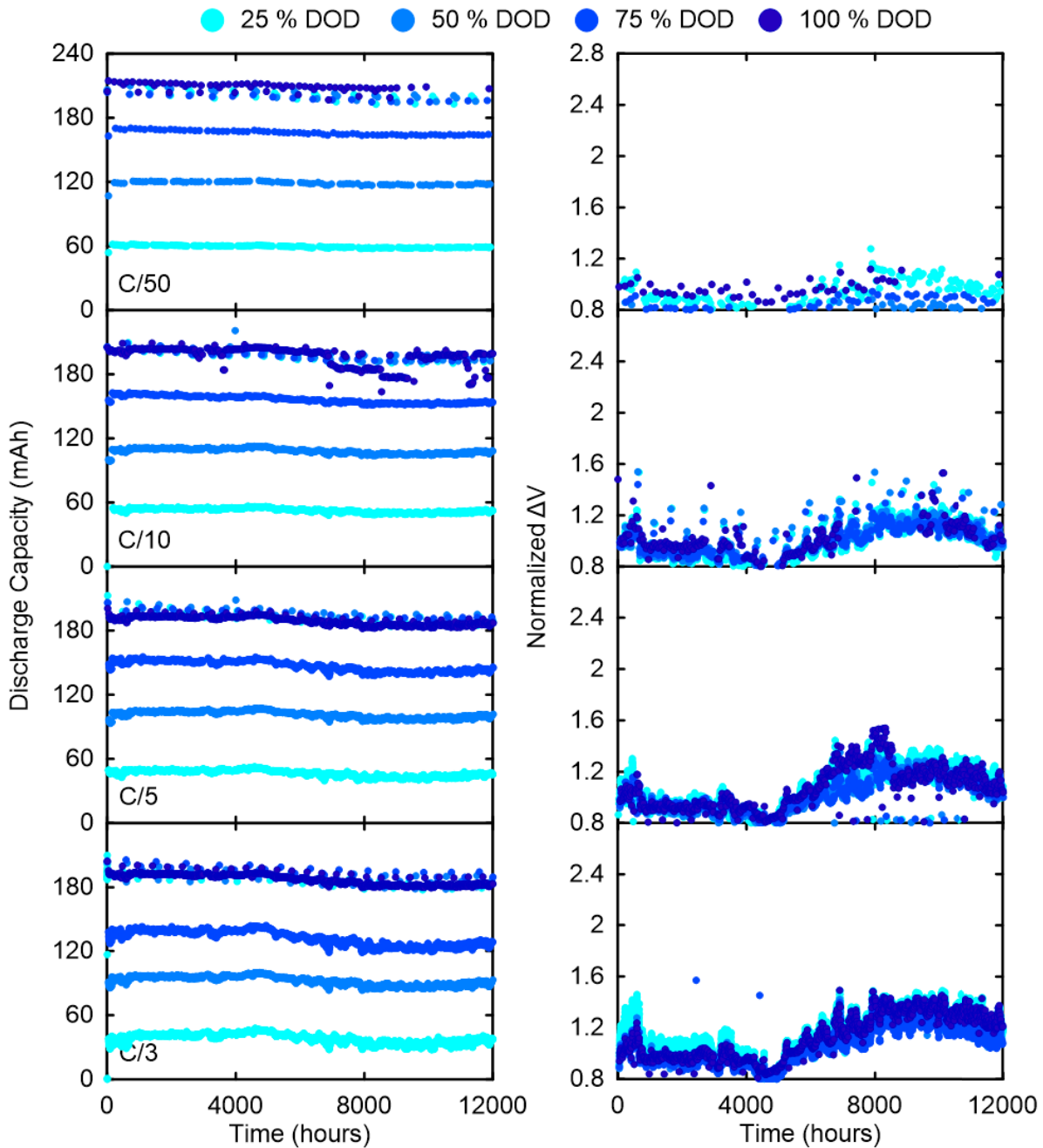
Figure A.2. Discharge capacity (mAh) and normalized ΔV versus time (hours) for NMC811/AG cells cycling to 4.20 V UCV at RT at 25, 50, 75, and 100 % DOD. The C-rate is indicated in each panel.
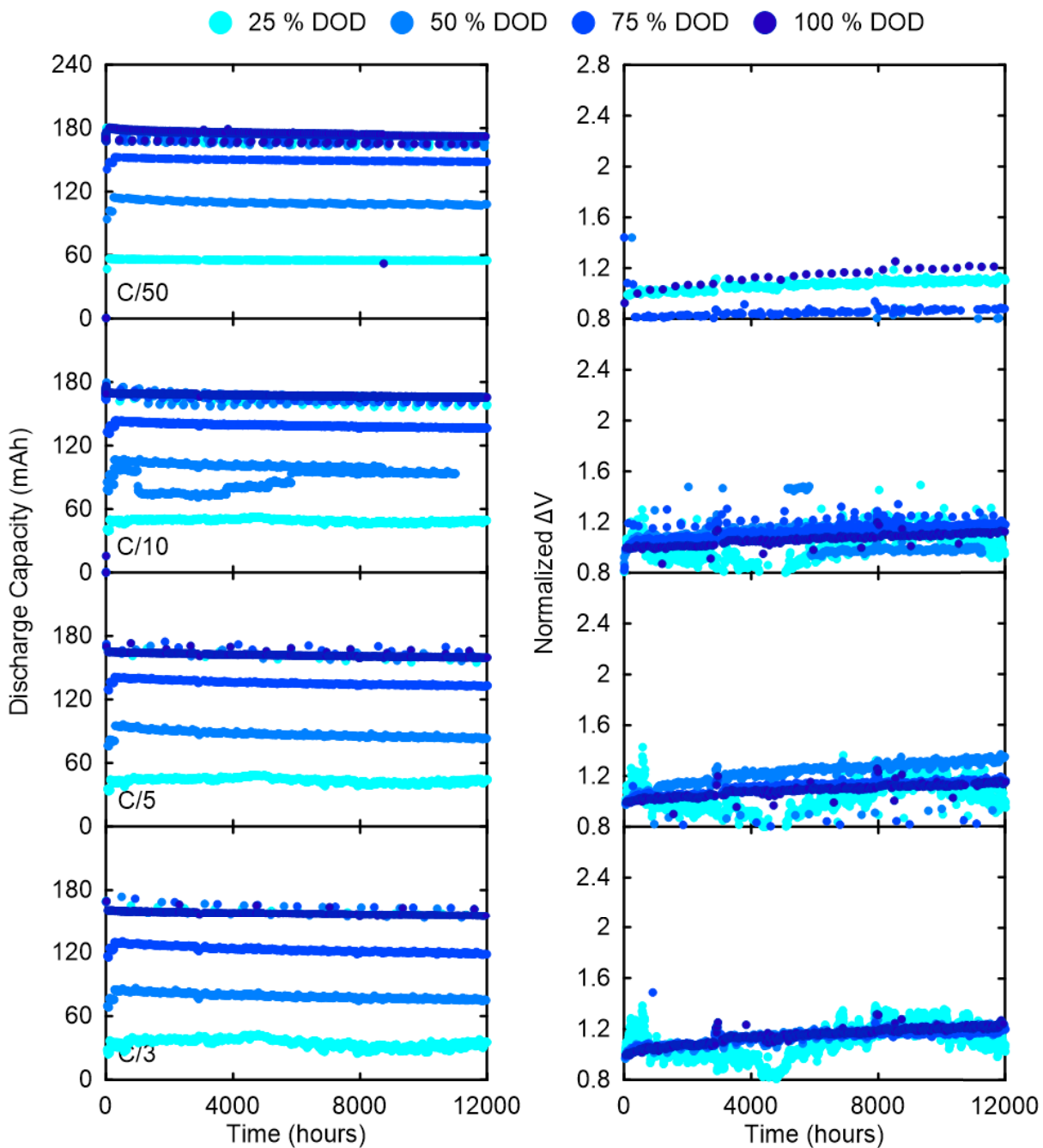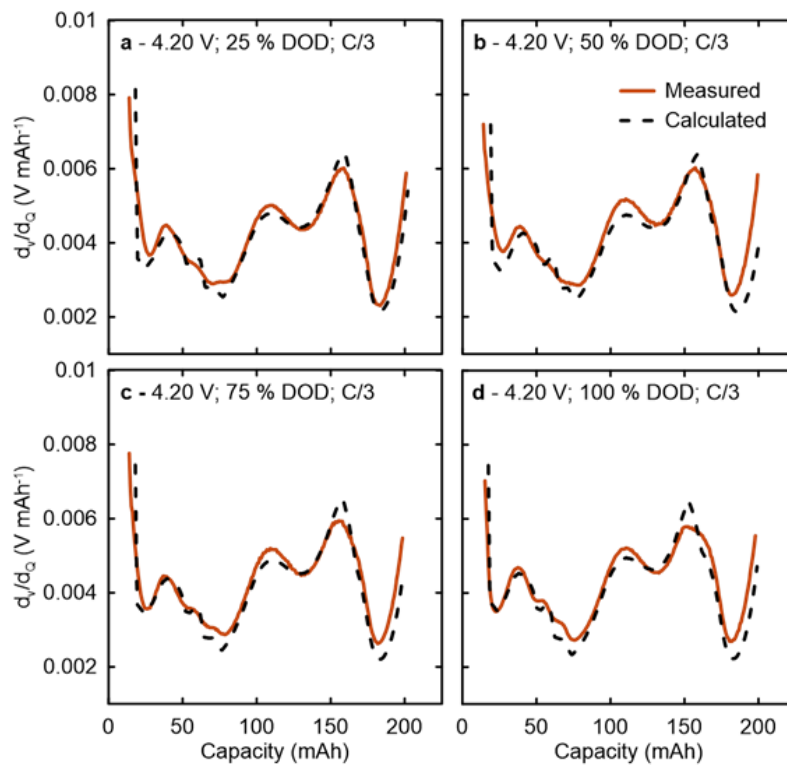
Figure A.3. Discharge capacity (mAh) and normalized ΔV versus time (hours) for NMC811/AG cells cycling to 4.06 V UCV at RT at 25, 50, 75, and 100 % DOD. The C-rate is indicated in each panel.

Figure A.4. Measured and calculated dV/dQ vs. Q curves for the cells in Figure 3.7.
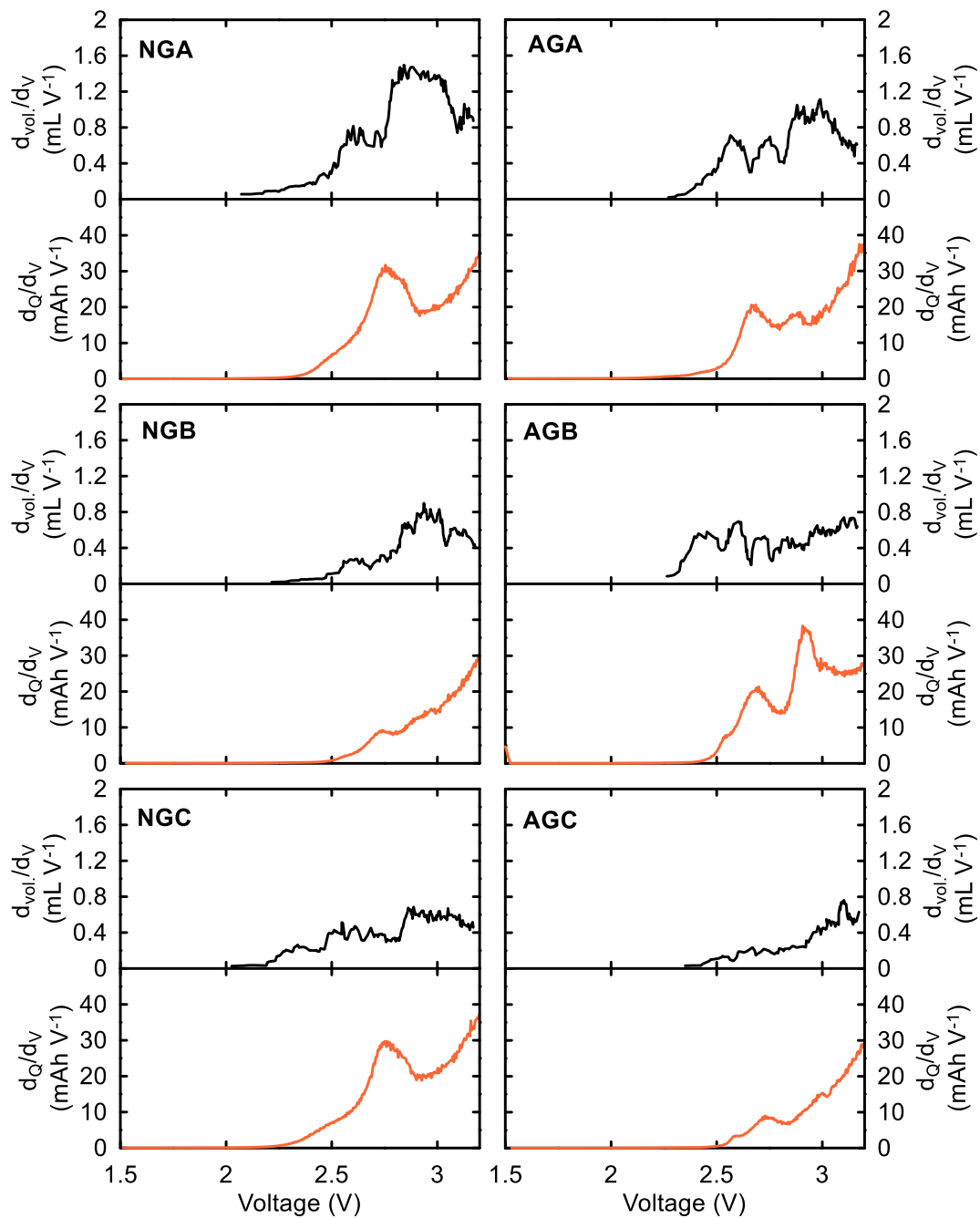
Figure A.5. Change in volume with respect to voltage (dVol/dV, mL V^{-1}) and d$_Q$/d$_V$ versus voltage for NMC811/Graphite pouch cells. Cells were filled with 2FEC1LFO electrolyte and charged to 4.2 V at C/100 and 40 °C. A 7-point running average of dVol/dV is plotted to reduce the noise in the data.
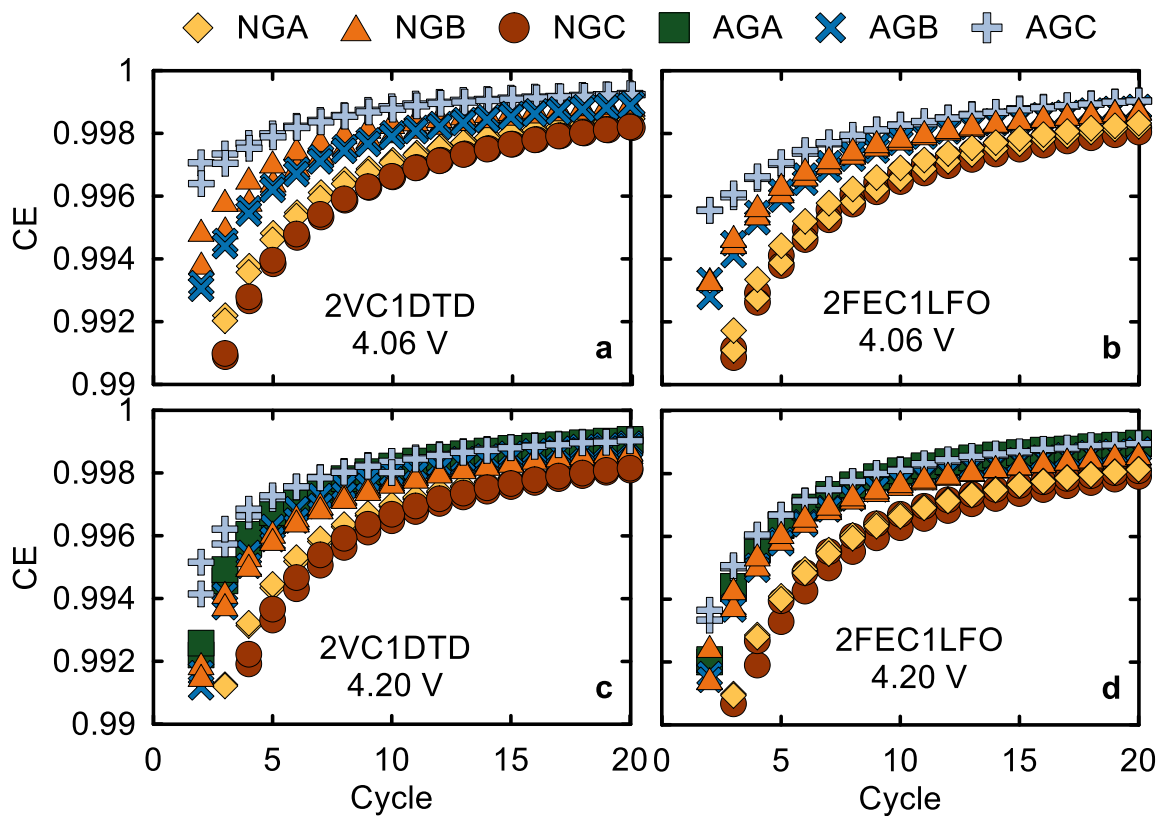
Figure A.6. CE versus cycle number for NMC811/Graphite cells cycled with 2VC1DTD or 2FEC1LFO electrolytes. UCVs were either 4.06 V or 4.20 V. All cycling was done at 40 °C with C/20:C/20 rates.
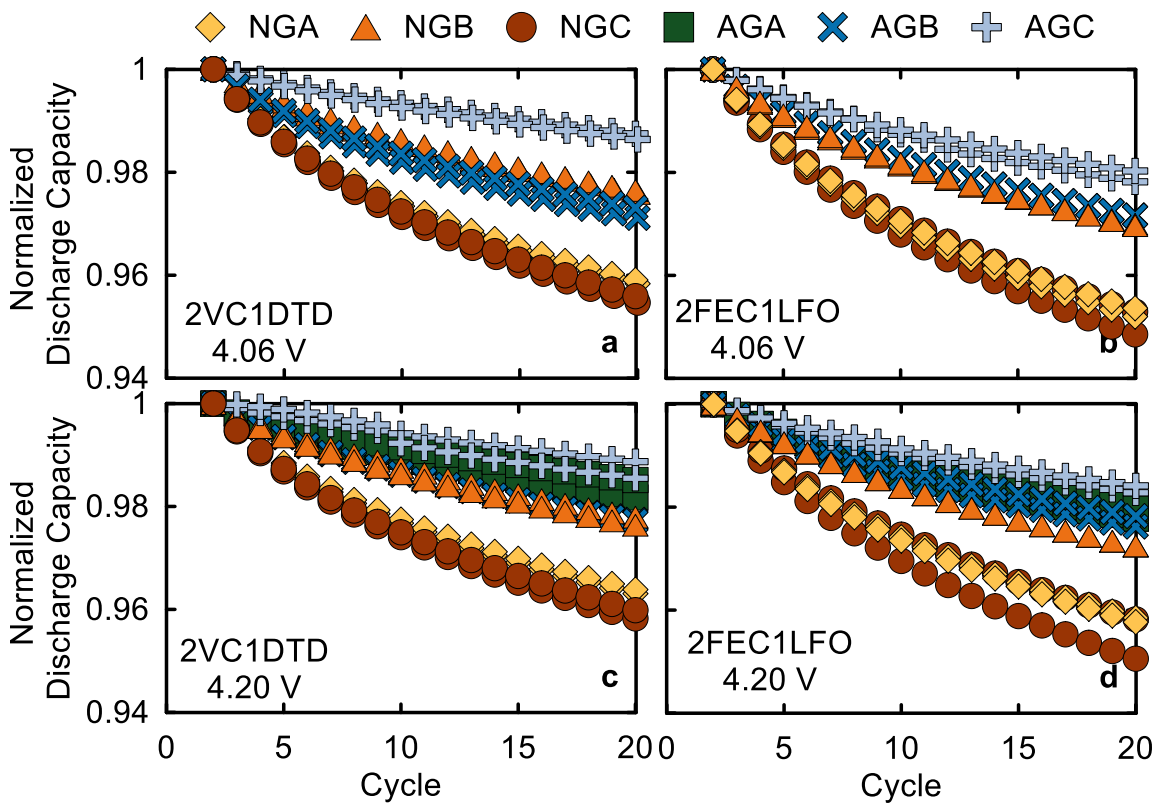
Figure A.7. Normalized discharge capacity versus cycle number for NMC811/Graphite cells cycled with 2VC1DTD or 2FEC1LFO electrolytes. UCVs were either 4.06 V or 4.20 V. All cycling was done at 40 °C with C/20:C/20 rates.
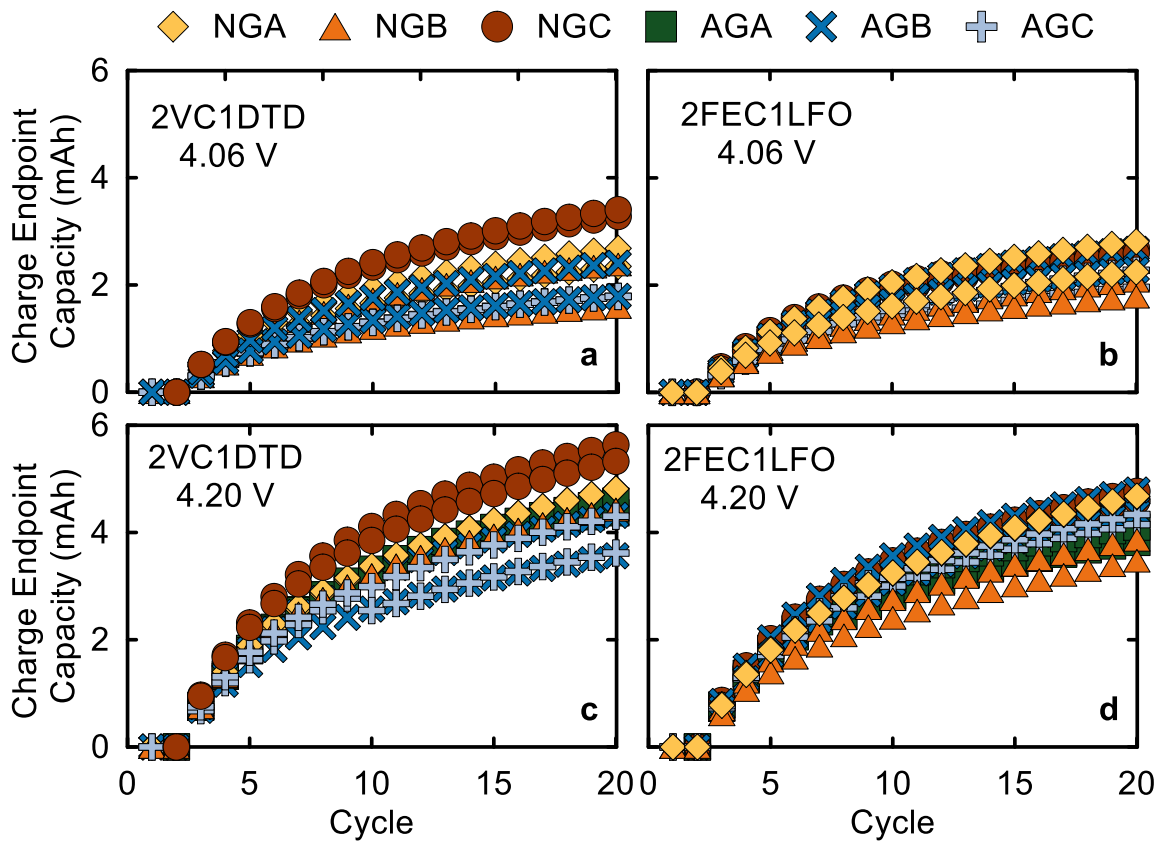
Figure A.8. Charge endpoint capacity slippage (mAh) versus cycle number for NMC811/Graphite cells cycled with 2VC1DTD or 2FEC1LFO electrolytes. UCVs were either 4.06 V or 4.20 V. All cycling was done at 40 °C with C/20:C/20 rates.
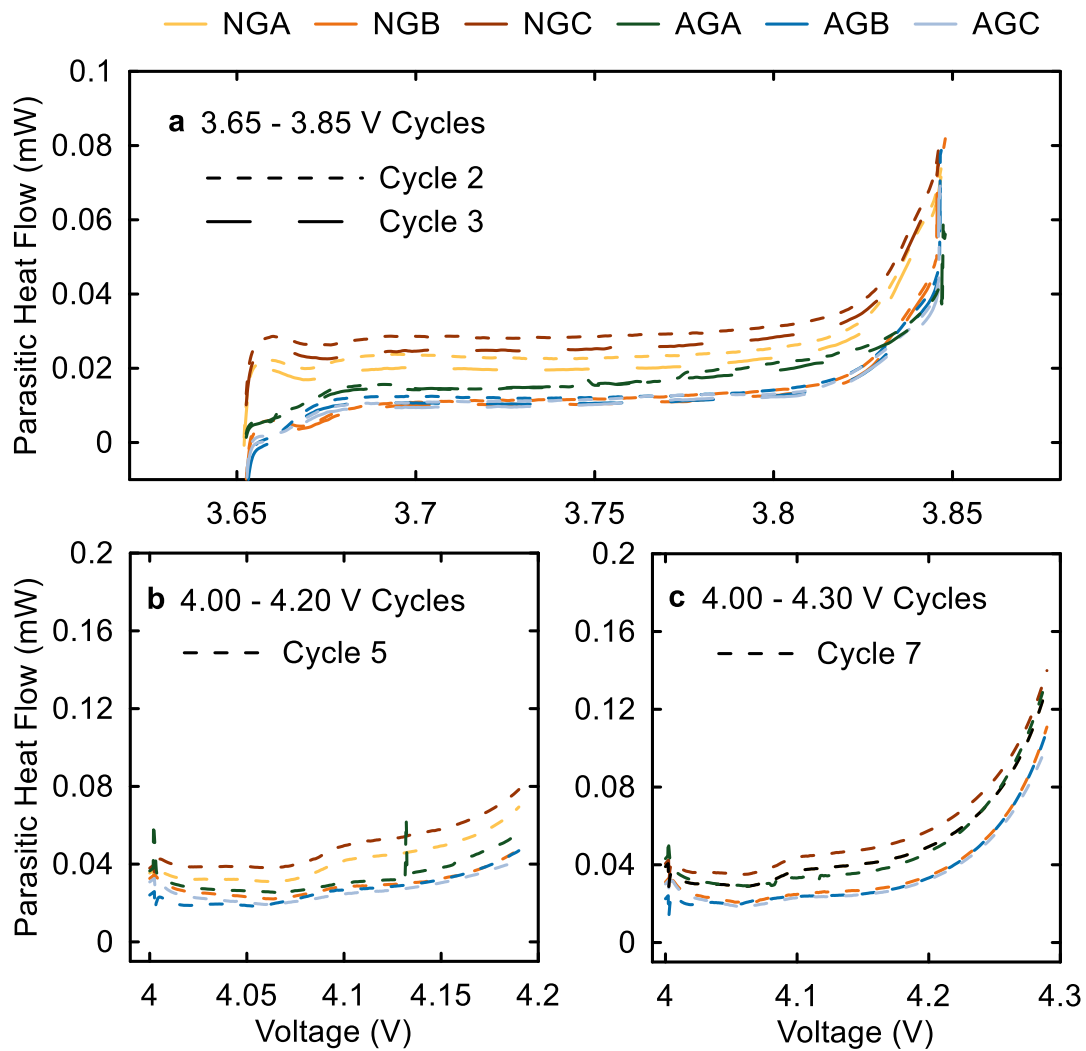
Figure A.9. Parasitic heat flow (mW) versus voltage (V) for cells cycled between (a) 3.65-3.85 V, (b) 4.0-4.20 V, and (C) 4.0-4.30 V. All cycles were at C/150 and 40 °C
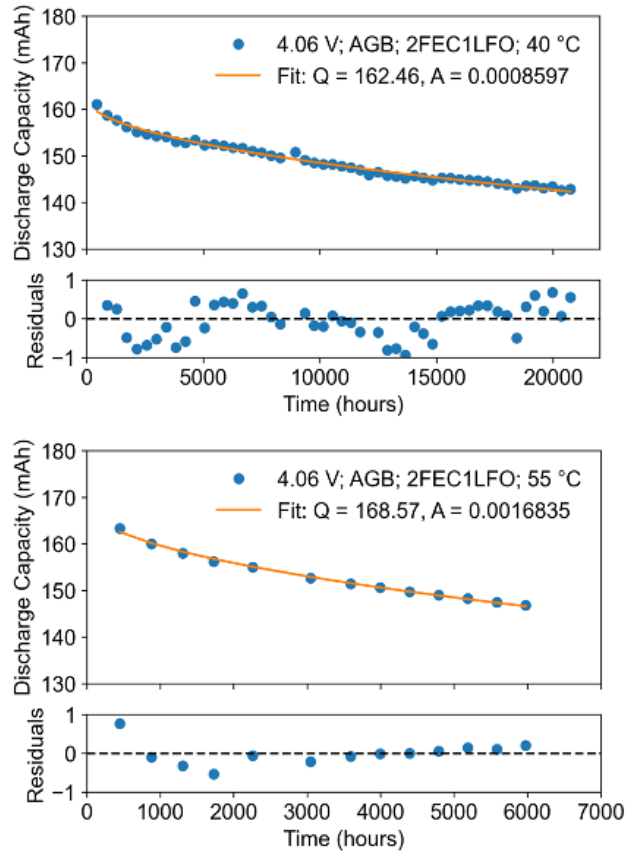
Figure A.10. Measured and calculated capacity loss for NMC811/AGB cells with 2FEC1LFO cycled at 40 °C or 55 °C.

Table A.1. Summary of the square root time fitting parameters A and Q_o for NMC811/Graphite cells.

Graphite	Additive	Temp (°C)	Q_o (mAh)	A ($h^{-0.5}$)	Avg. A	Range in A
NGA	2VC1DTD	~20	153.76	0.00134	0.00141	0.000131
NGA	2VC1DTD	~20	153.30	0.00147		
NGA	2VC1DTD	40	155.52	0.00201	0.00207	0.000113
NGA	2VC1DTD	40	153.37	0.00212		
NGA	2VC1DTD	55	157.51	0.00353	0.00354	0.000000
NGB	2VC1DTD	~20	160.87	0.00130	0.00124	0.000125
NGB	2VC1DTD	~20	160.06	0.00118		
NGB	2VC1DTD	40	168.36	0.00103	0.00111	0.000016
NGB	2VC1DTD	40	167.29	0.00119		
NGB	2VC1DTD	55	168.48	0.00202	0.00203	0.000000
AGC	2VC1DTD	~20	158.78	0.00062	0.00051	0.00021
AGC	2VC1DTD	~20	157.18	0.00041		
AGC	2VC1DTD	40	170.89	0.00090	0.00089	0.000027
AGC	2VC1DTD	40	168.75	0.00088		
AGC	2VC1DTD	55	172.45	0.00131	0.00131	0.000000
AGB	2VC1DTD	~20	158.02	0.00079	0.00081	0.000028
AGB	2VC1DTD	~20	159.39	0.00082		

AGB	2VC1DTD	40	162.65	0.00083	0.00084	0.000000
AGB	2VC1DTD	55	167.58	0.00131	0.00131	0.000000
NGC	2VC1DTD	~20	155.01	0.00127	0.00153	0.000511
NGC	2VC1DTD	~20	154.78	0.00178		
NGC	2VC1DTD	40	154.511	0.00241	0.00242	0.000029
NGC	2VC1DTD	40	156.74	0.00243		
NGC	2VC1DTD	55	158.94	0.0037	0.00375	0.000000
NGA	2FEC1LFO	~20	153.28	0.00137	0.00128	0.000184
NGA	2FEC1LFO	~20	154.56	0.00118		
NGA	2FEC1LFO	40	156.23	0.00248	0.00242	0.000115
NGA	2FEC1LFO	40	155.24	0.00236		
NGA	2FEC1LFO	55	159.07	0.00351	0.00352	0.000000
NGB	2FEC1LFO	~20	160.50	0.00102	0.00113	0.000206
NGB	2FEC1LFO	~20	159.84	0.00122		
NGB	2FEC1LFO	40	167.75	0.00141	0.00136	0.000106
NGB	2FEC1LFO	40	168.54	0.00130		
NGB	2FEC1LFO	55	168.19	0.00222	0.00222	0.000000
AGC	2FEC1LFO	~20	162.23	0.00063	0.00062	0.000040
AGC	2FEC1LFO	~20	161.51	0.00059		

AGC	2FEC1LFO	55	171.15	0.00167	0.00167	0.000000
AGC	2FEC1LFO	40	169.16	0.00074	0.00094	0.000390
AGC	2FEC1LFO	40	168.23	0.00113		
AGB	2FEC1LFO	~20	160.19	0.00074	0.00076	0.000041
AGB	2FEC1LFO	~20	162.44	0.00078		
AGB	2FEC1LFO	40	162.86	0.00094	0.00094	0.000091
AGB	2FEC1LFO	40	162.46	0.00085		
AGB	2FEC1LFO	55	168.57	0.00168	0.00168	0.000000
NGC	2FEC1LFO	~20	154.30	0.00179	0.00155	0.000491
NGC	2FEC1LFO	~20	154.41	0.00130		
NGC	2FEC1LFO	40	153.71	0.00286	0.00292	0.000100
NGC	2FEC1LFO	40	154.31	0.00296		
NGC	2FEC1LFO	55	158.15	0.00441	0.00441	0.000000
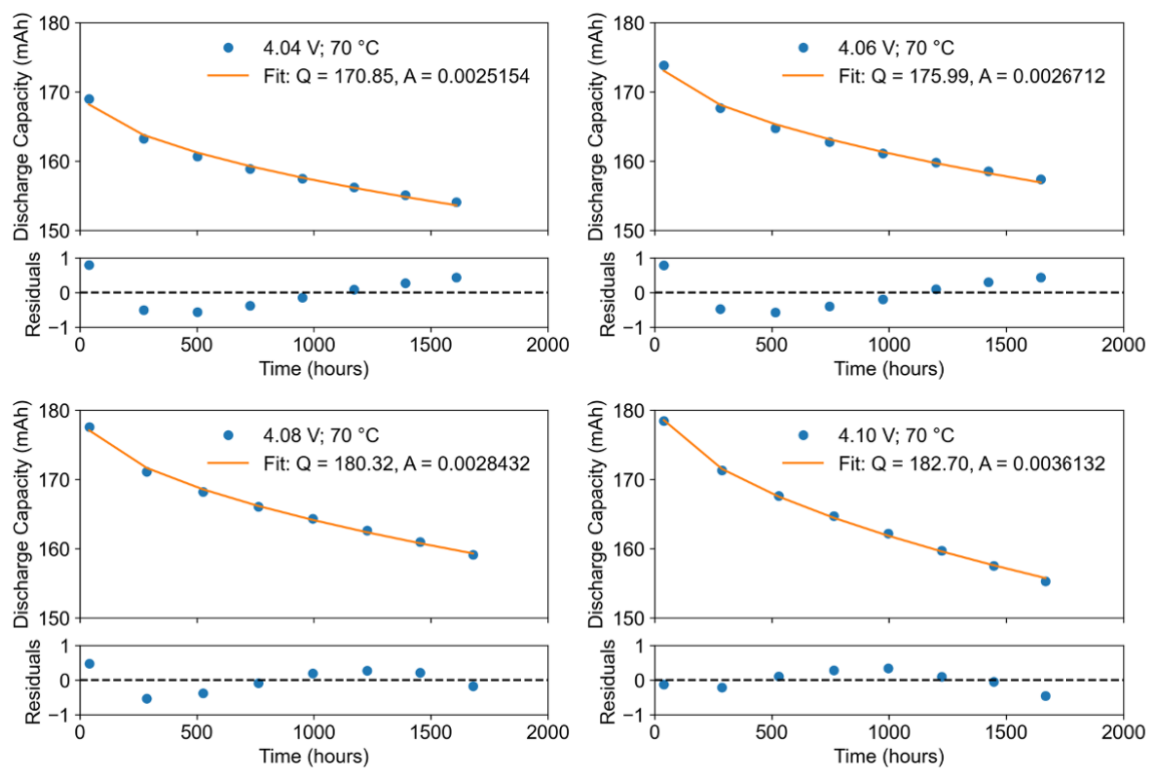
Figure A.11. Measured and calculated capacity loss for NMC811/AGC cells cycled to 4.04 V, 4.06 V, 4.08 V, or 4.10 V UCV at 70 °C with 2VC1DTD electrolyte.
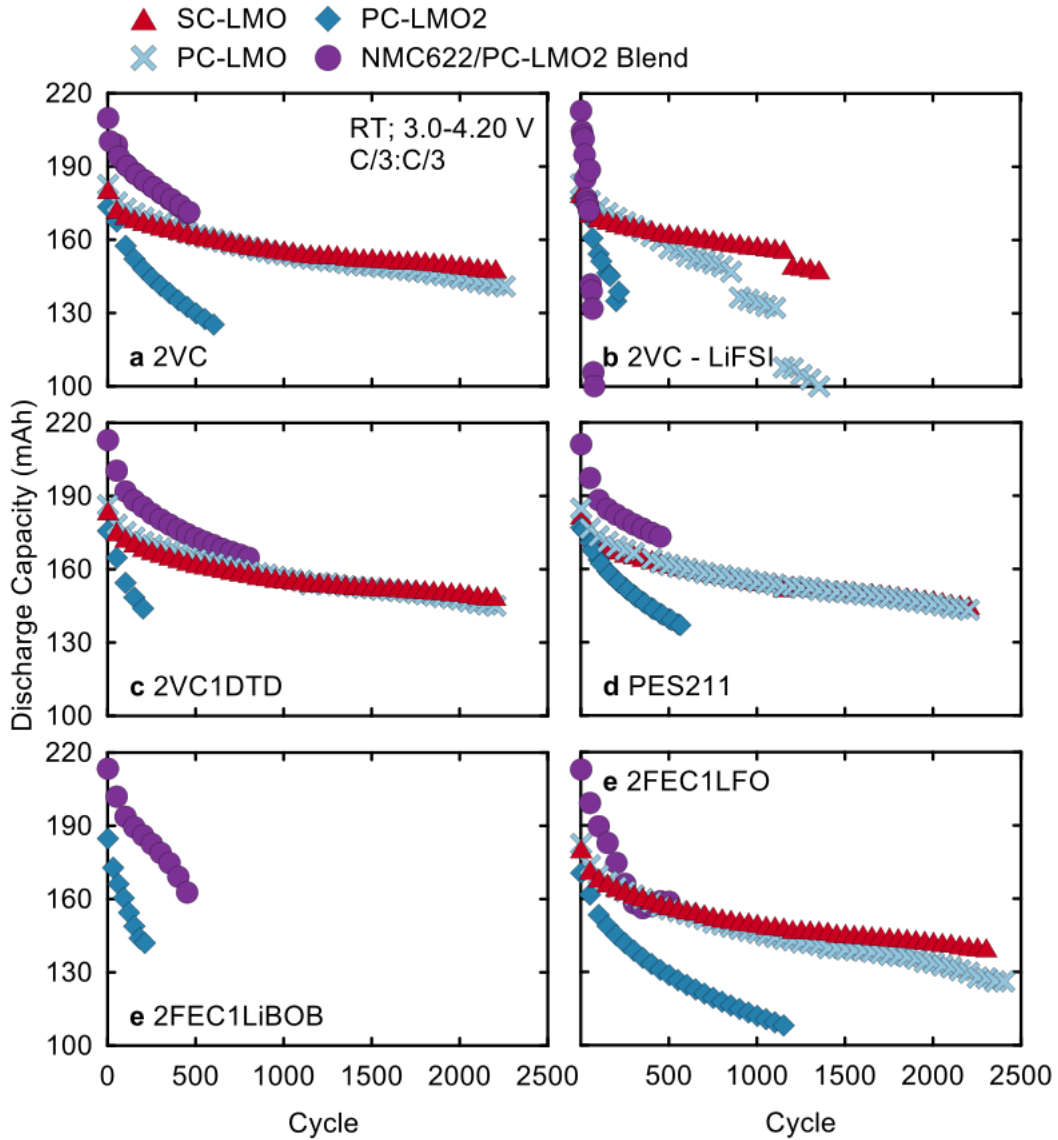
Figure A.12. Discharge capacity (mAh) versus cycle number for the LMO/AG pouch cells with (a) 2VC; (b) 2VC-LiFSI; (c) 2VC1DTD; (d) PES211; (e) 2FEC1LiBOB; and (f) 2FEC1LFO electrolytes. Cycling was done at RT at C/3:C/3 and 3.0-4.20 V.
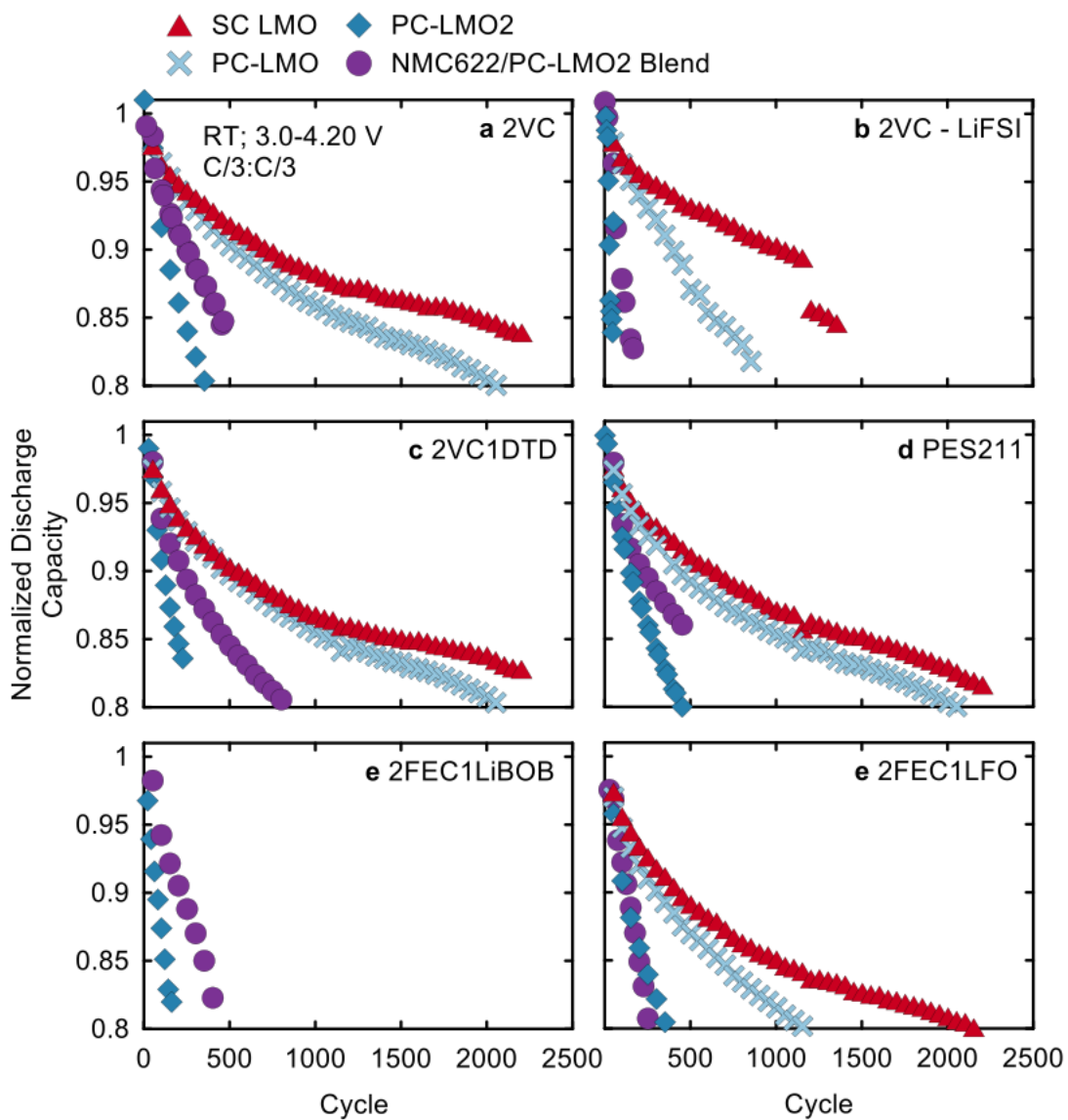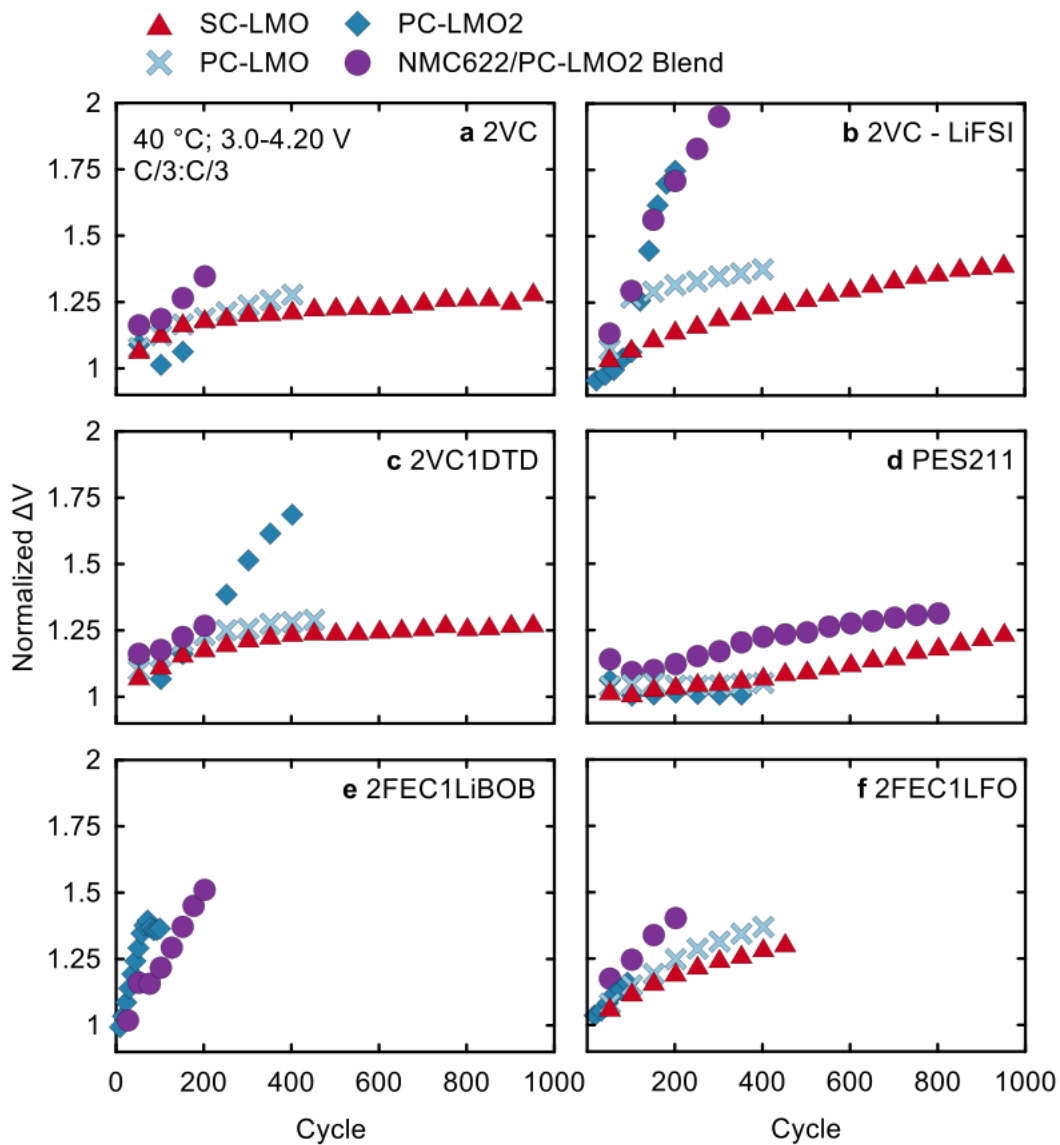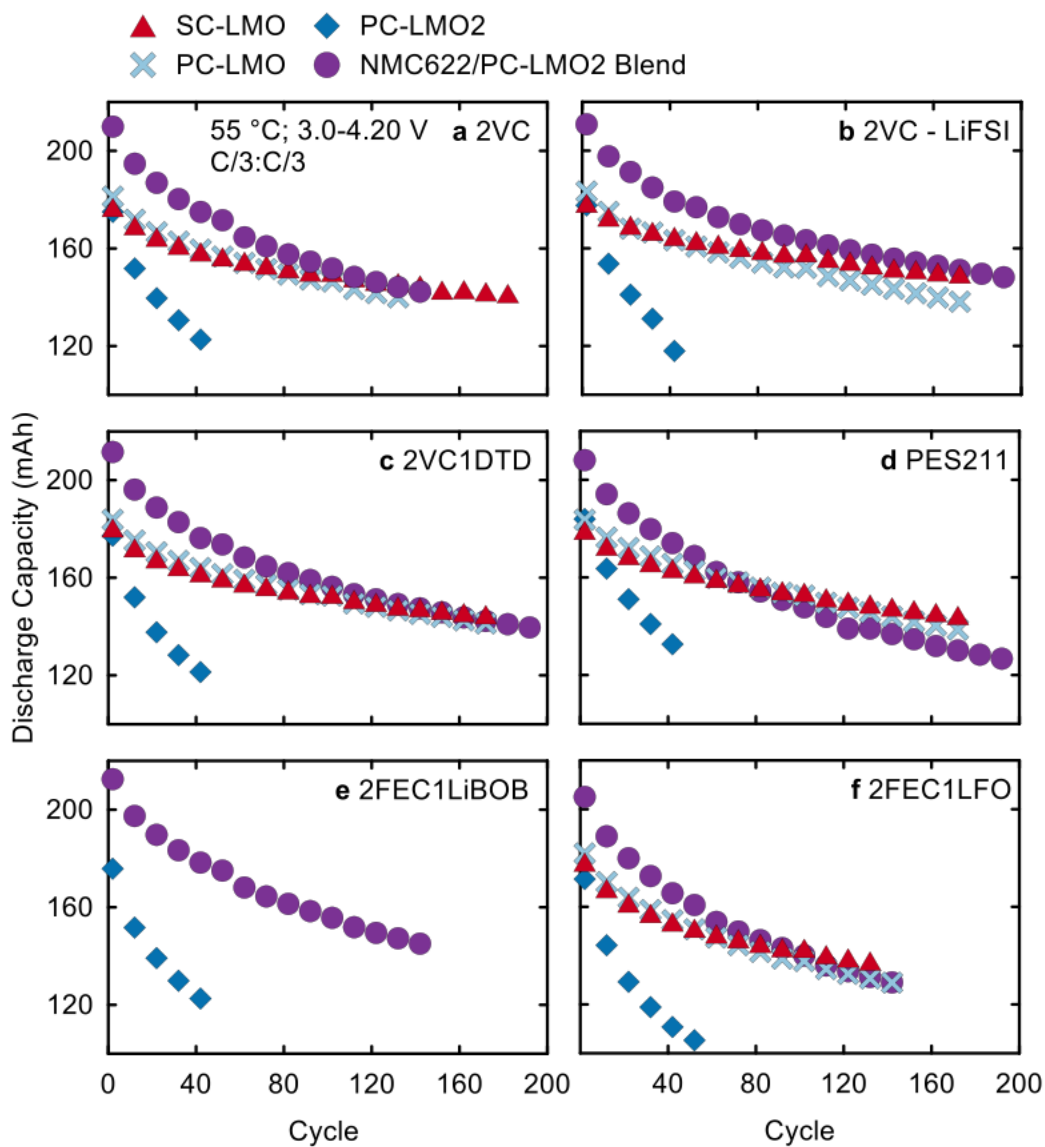
Figure A.13. Normalized discharge capacity versus cycle number for the LMO/AG pouch cells with (a) 2VC; (b) 2VC-LiFSI; (c) 2VC1DTD; (d) PES211; (e) 2FEC1LiBOB; and (f) 2FEC1LFO electrolytes. Cycling was done at RT at C/3:C/3 and 3.0-4.20 V.
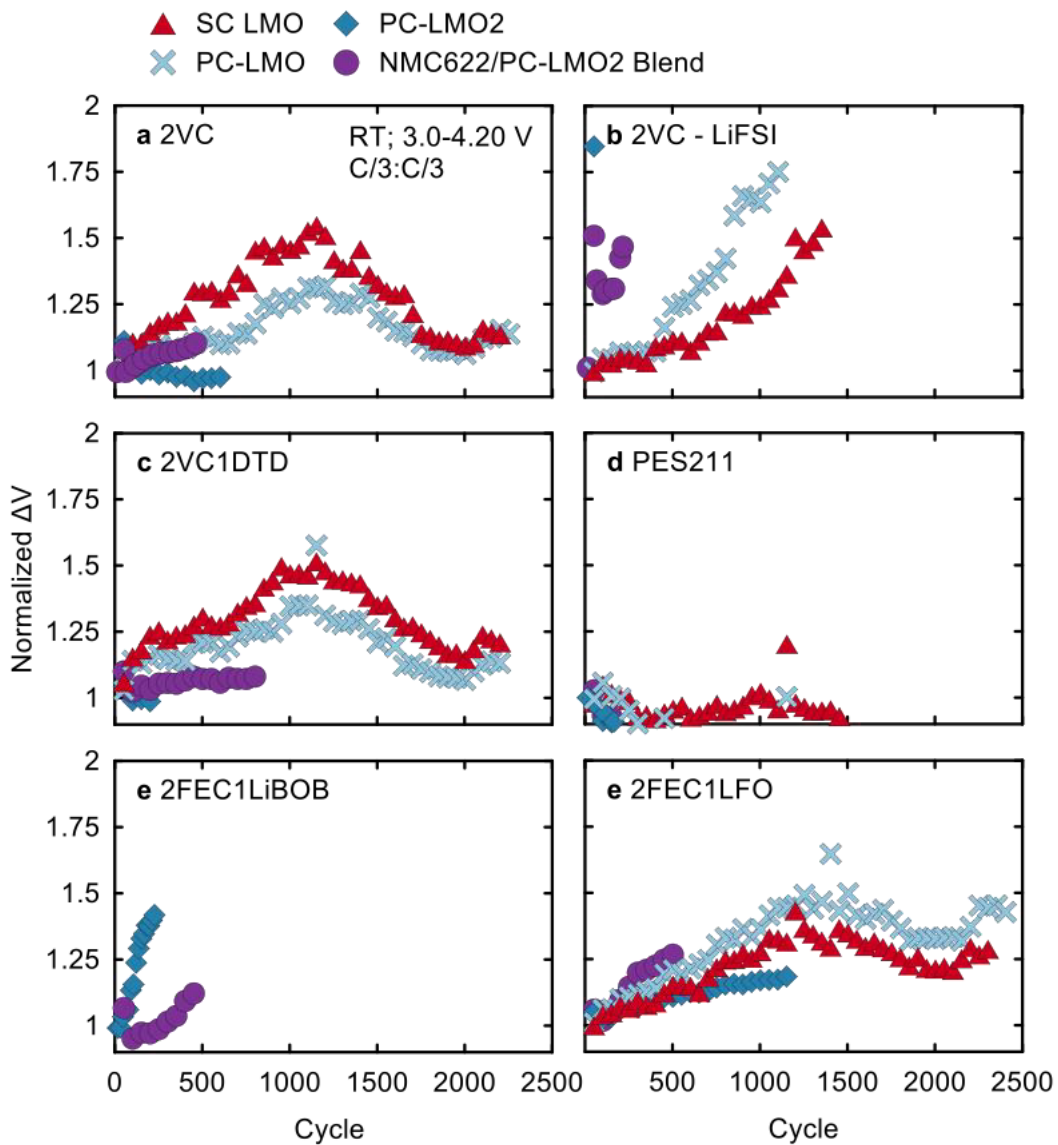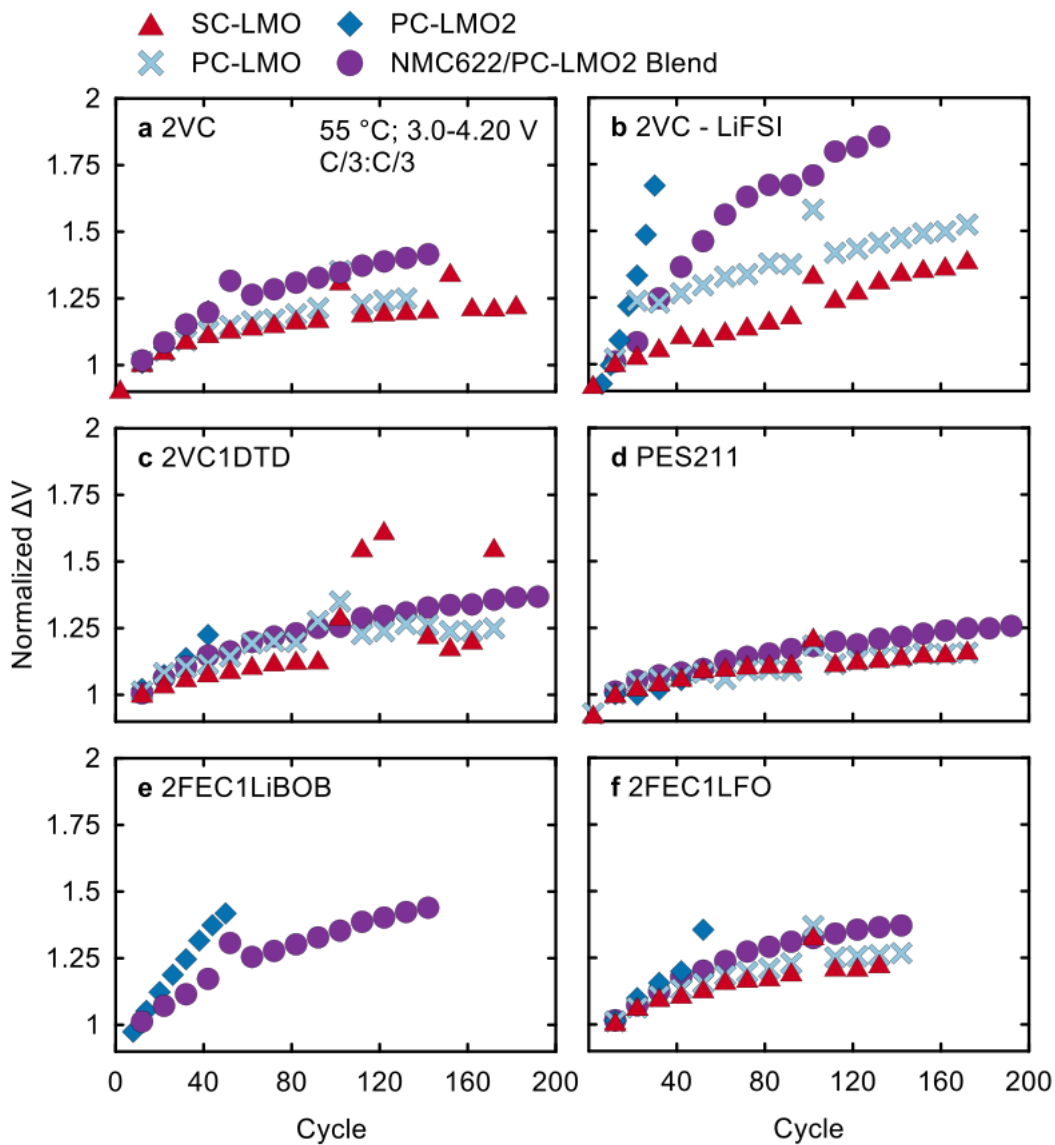
Figure A.14. Normalized ΔV versus cycle number for the LMO/AG pouch cells with (a) 2VC; (b) 2VC-LiFSI; (c) 2VC1DTD; (d) PES211; (e) 2FEC1LiBOB; and (f) 2FEC1LFO electrolytes. Cycling was done at RT at C/3:C/3 and 3.0-4.20 V.
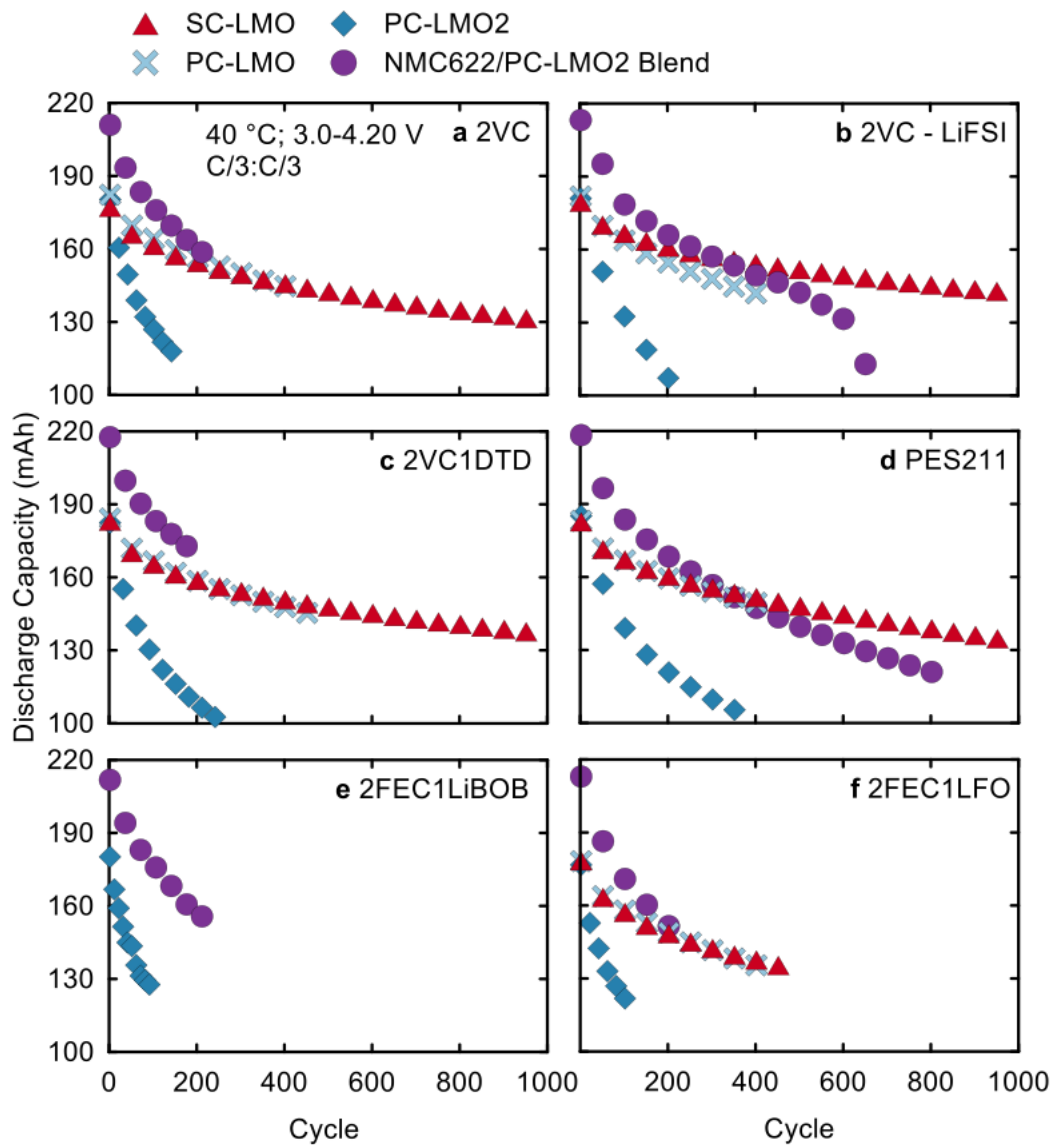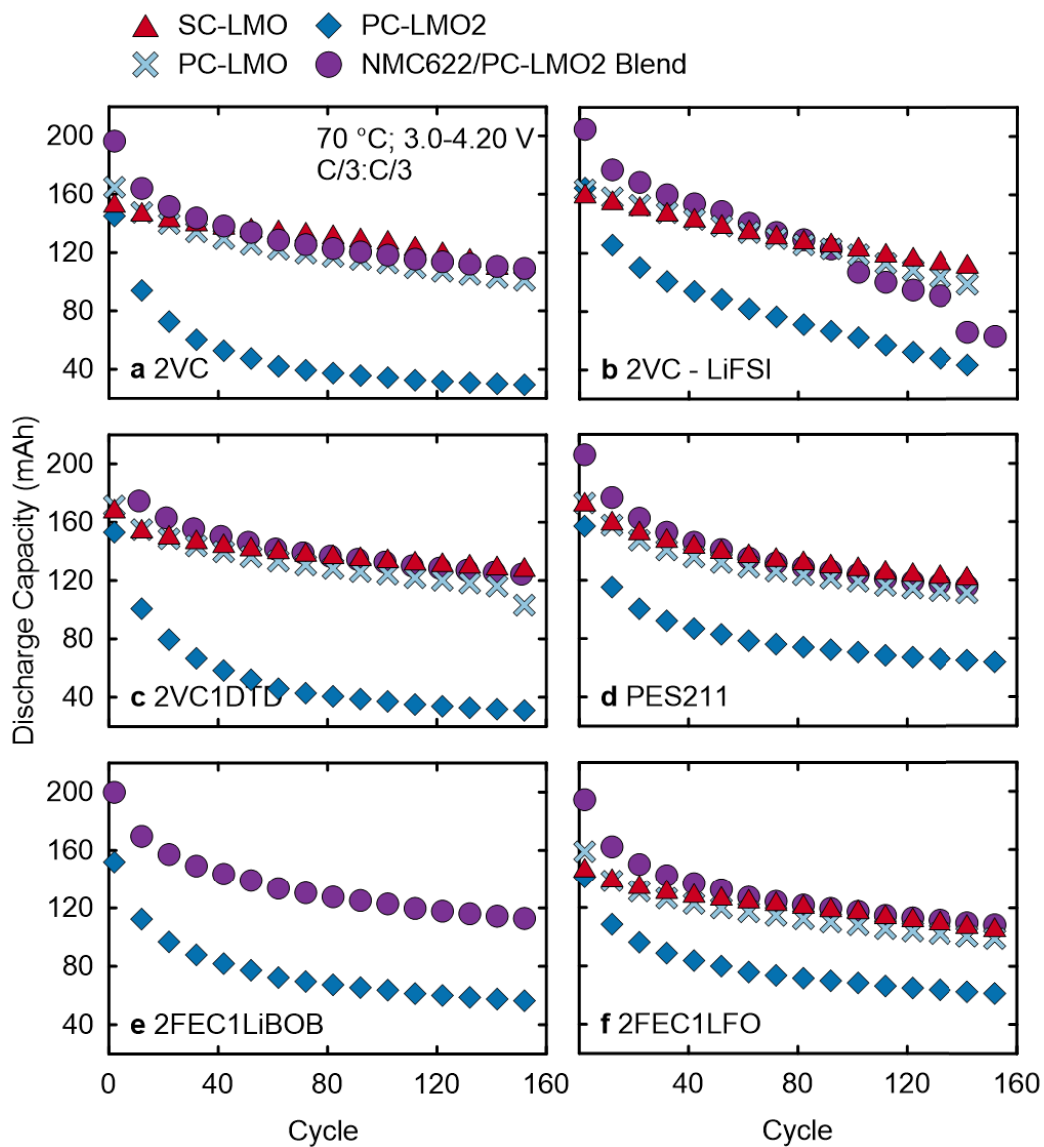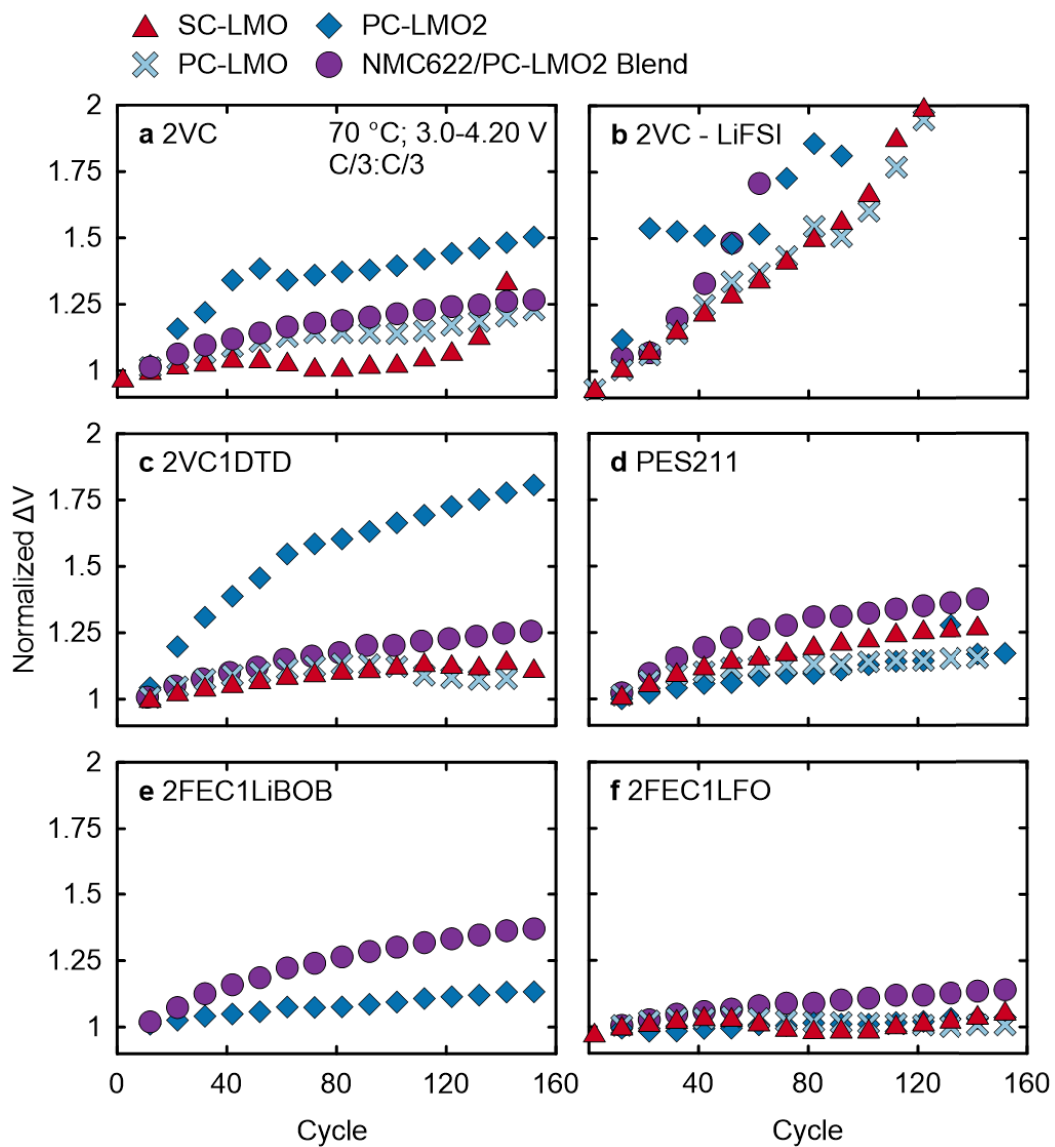
Figure A.15. Discharge capacity (mAh) versus cycle number for the LMO/AG pouch cells with (a) 2VC; (b) 2VC-LiFSI; (c) 2VC1DTD; (d) PES211; (e) 2FEC1LiBOB; and (f) 2FEC1LFO electrolytes. Cycling was done at 40 °C at C/3:C/3 and 3.0-4.20 V.
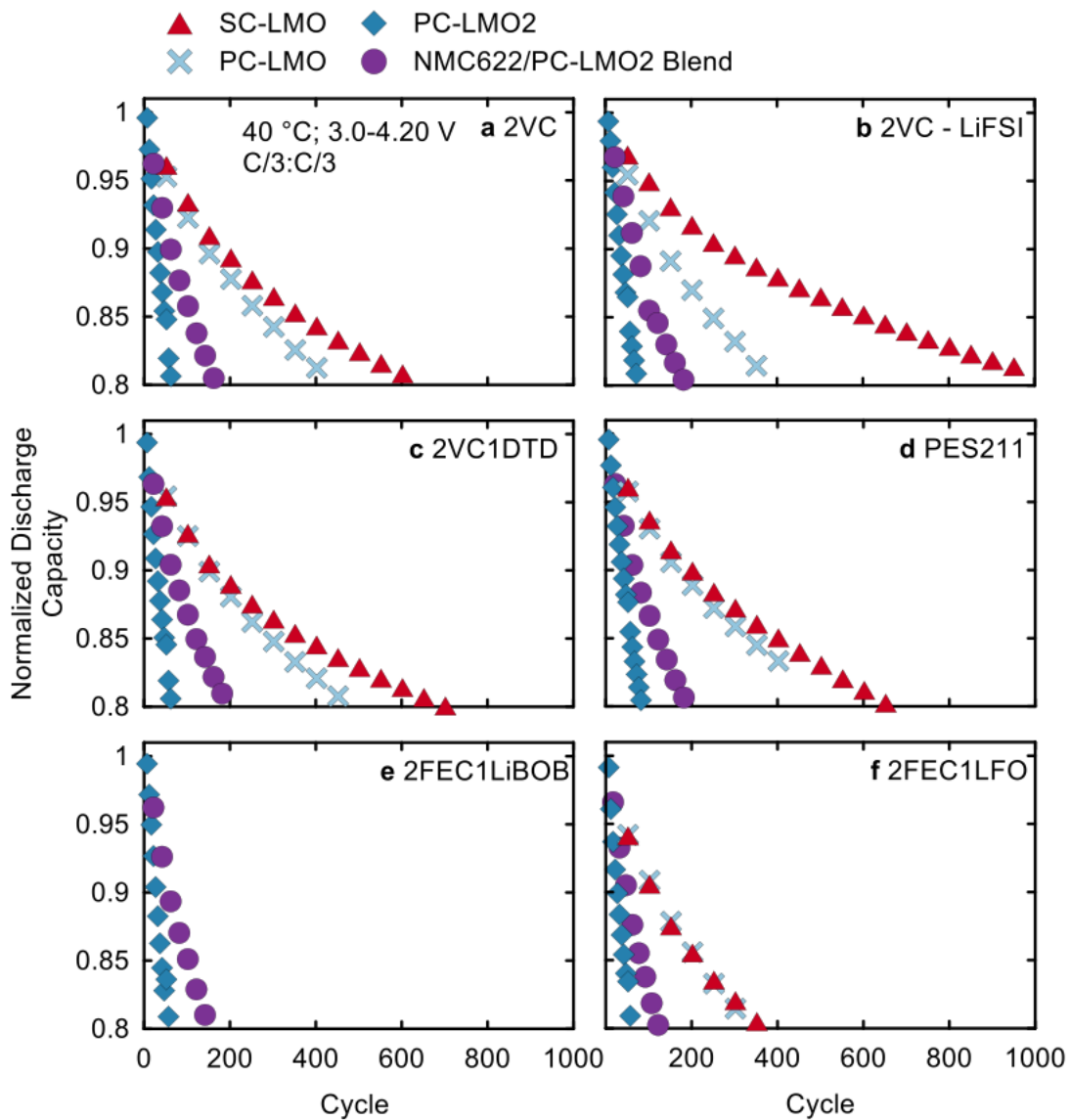
Figure A.16. Normalized discharge capacity versus cycle number for the LMO/AG pouch cells with (a) 2VC; (b) 2VC-LiFSI; (c) 2VC1DTD; (d) PES211; (e) 2FEC1LiBOB; and (f) 2FEC1LFO electrolytes. Cycling was done at 40 °C at C/3:C/3 and 3.0-4.20 V.

Figure A.17. Normalized ΔV versus cycle number for the LMO/AG pouch cells with (a) 2VC; (b) 2VC-LiFSI; (c) 2VC1DTD; (d) PES211; (e) 2FEC1LiBOB; and (f) 2FEC1LFO electrolytes. Cycling was done at 40 °C at C/3:C/3 and 3.0-4.20 V.
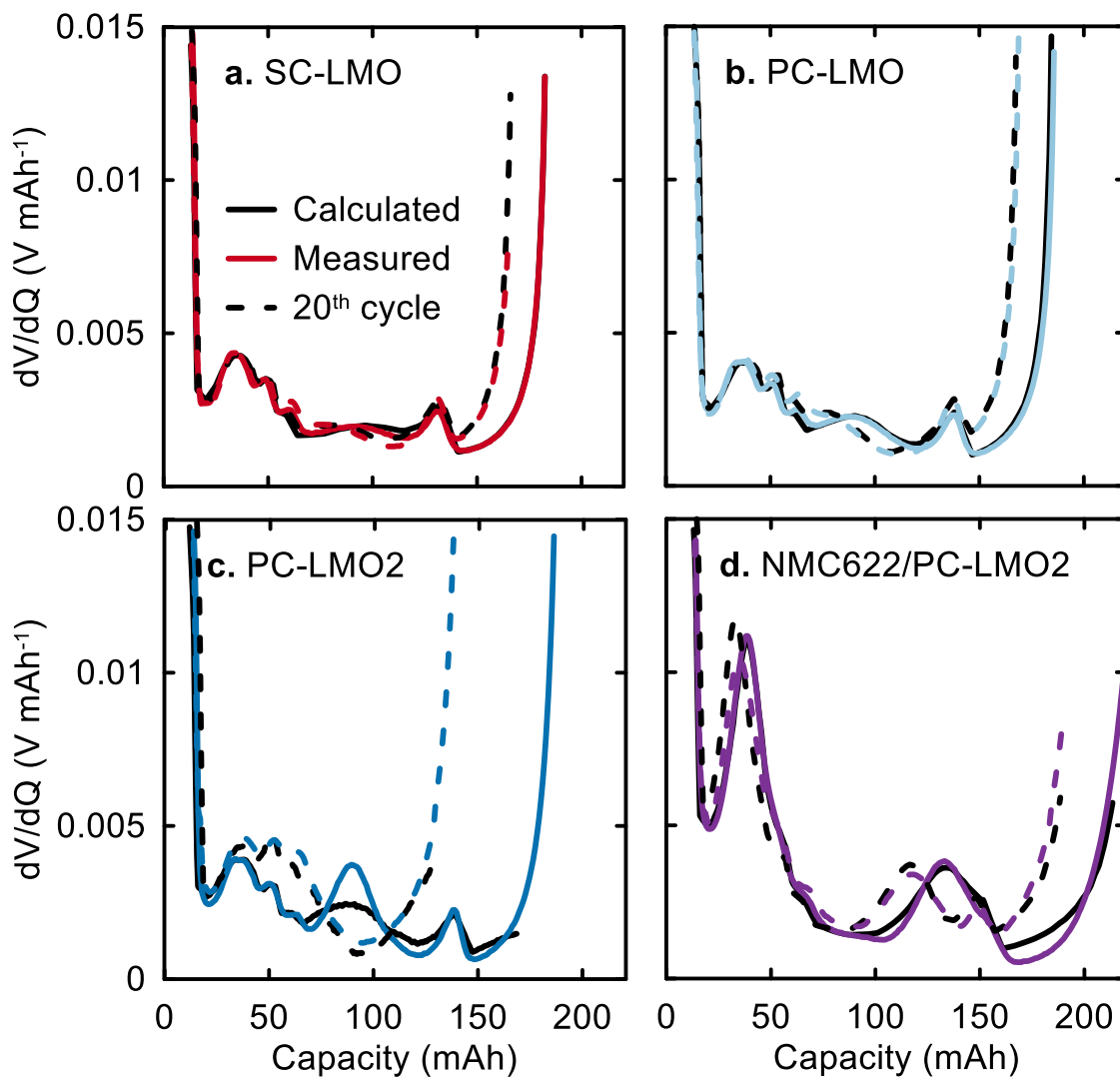
Figure A.18. Discharge capacity (mAh) versus cycle number for the LMO/AG pouch cells with (a) 2VC; (b) 2VC-LiFSI; (c) 2VC1DTD; (d) PES211; (e) 2FEC1LiBOB; and (f) 2FEC1LFO electrolytes. Cycling was done at 55 °C at C/3:C/3 and 3.0-4.20 V.

Figure A.19. Normalized ΔV versus cycle number for the LMO/AG pouch cells with (a) 2VC; (b) 2VC-LiFSI; (c) 2VC1DTD; (d) PES211; (e) 2FEC1LiBOB; and (f) 2FEC1LFO electrolytes. Cycling was done at 55 °C at C/3:C/3 and 3.0-4.20 V.

Figure A.20. Discharge capacity (mAh) versus cycle number for the LMO/AG pouch cells with (a) 2VC; (b) 2VC-LiFSI; (c) 2VC1DTD; (d) PES211; (e) 2FEC1LiBOB; and (f) 2FEC1LFO electrolytes. Cycling was done at 70 °C at C/3:C/3 and 3.0-4.20 V.

Figure A.21. Normalized ΔV versus cycle number for the LMO/AG pouch cells with (a) 2VC; (b) 2VC-LiFSI; (c) 2VC1DTD; (d) PES211; (e) 2FEC1LiBOB; and (f) 2FEC1LFO electrolytes. Cycling was done at 70 °C at C/3:C/3 and 3.0-4.20 V.

Figure A.22. Measured and calculated dV/dQ versus Q curves for the different LMO/AG cells with 2VC1DTD electrolyte. Solid lines shows the 1st cycle and dashed lines show the 20th cycle.
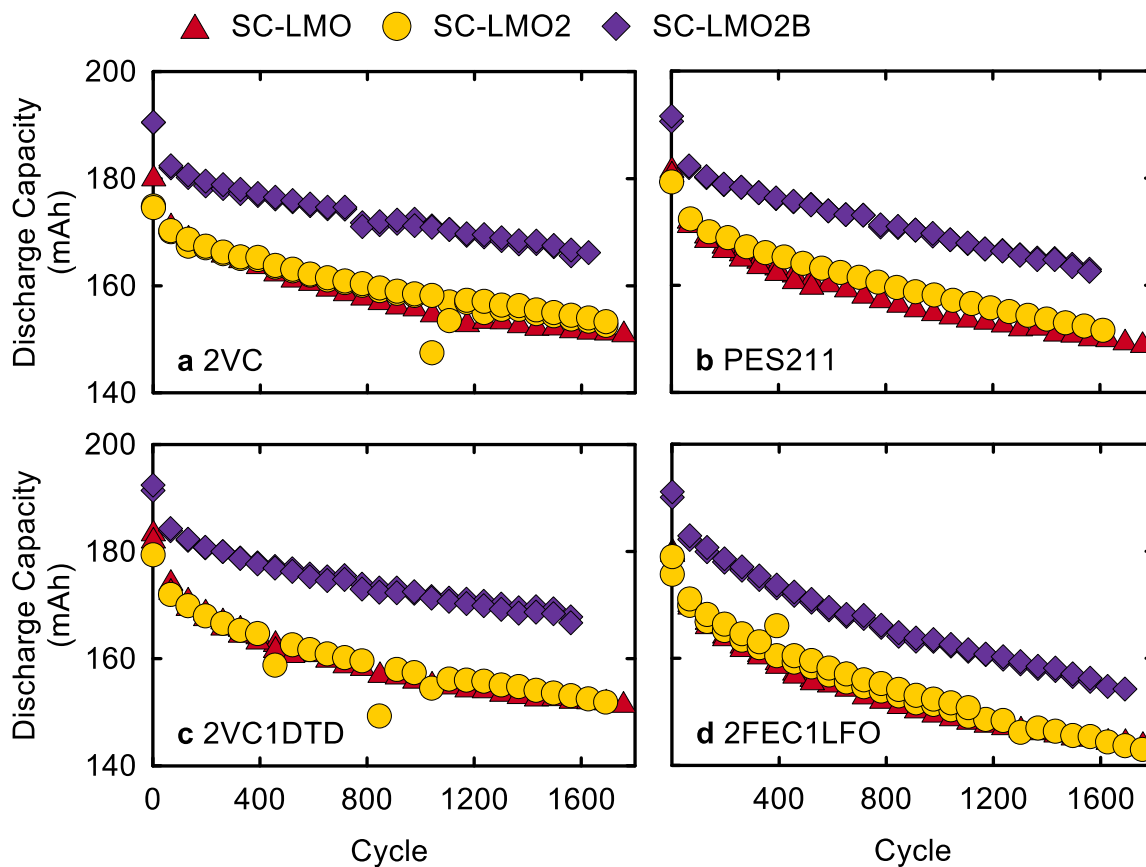
Figure A.23. Discharge capacity versus cycle number for SC-LMO, SC-LMO2, and SC-LMO2B pouch cells cycled at RT with (a) 2VC; (b) PES211; (c) 2VC1DTD; or (d) 2FEC1LFO electrolytes. All cycling was done at C/3:C/3 and 3.0-4.20 V.
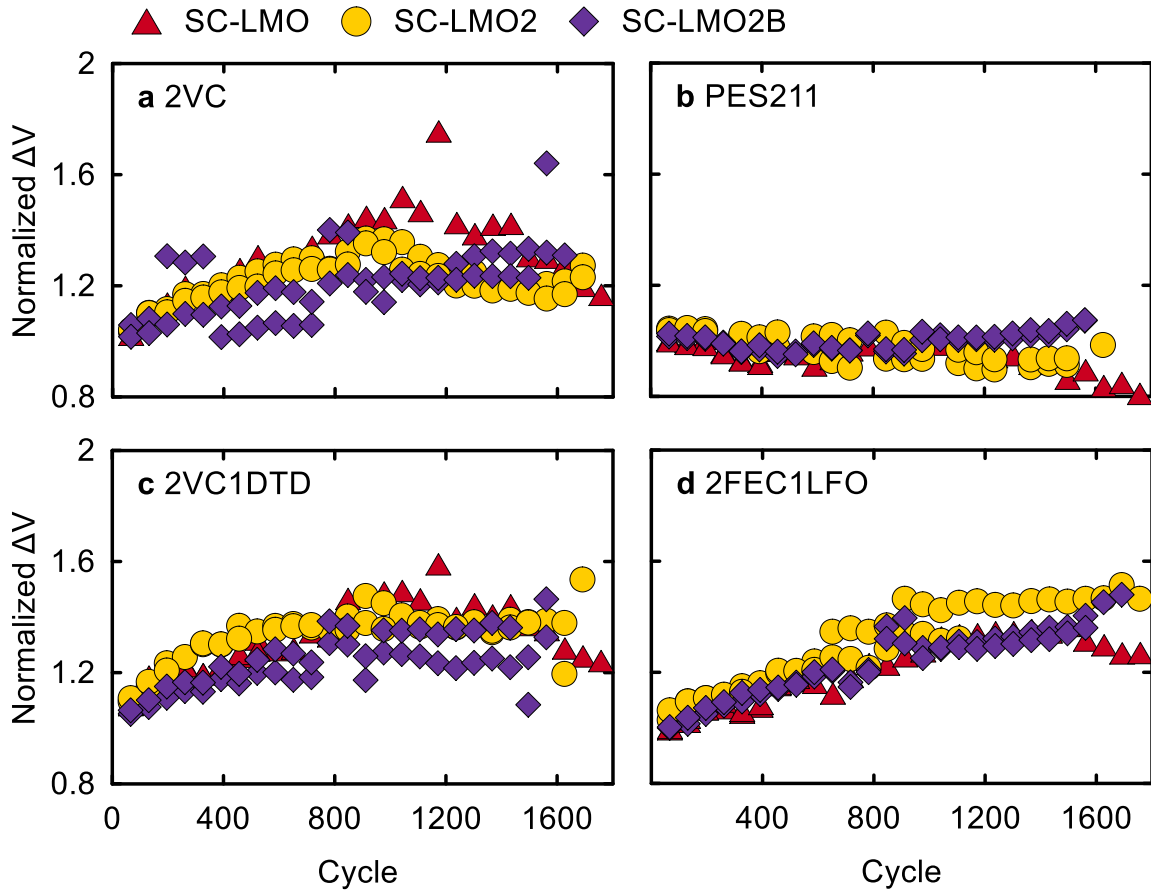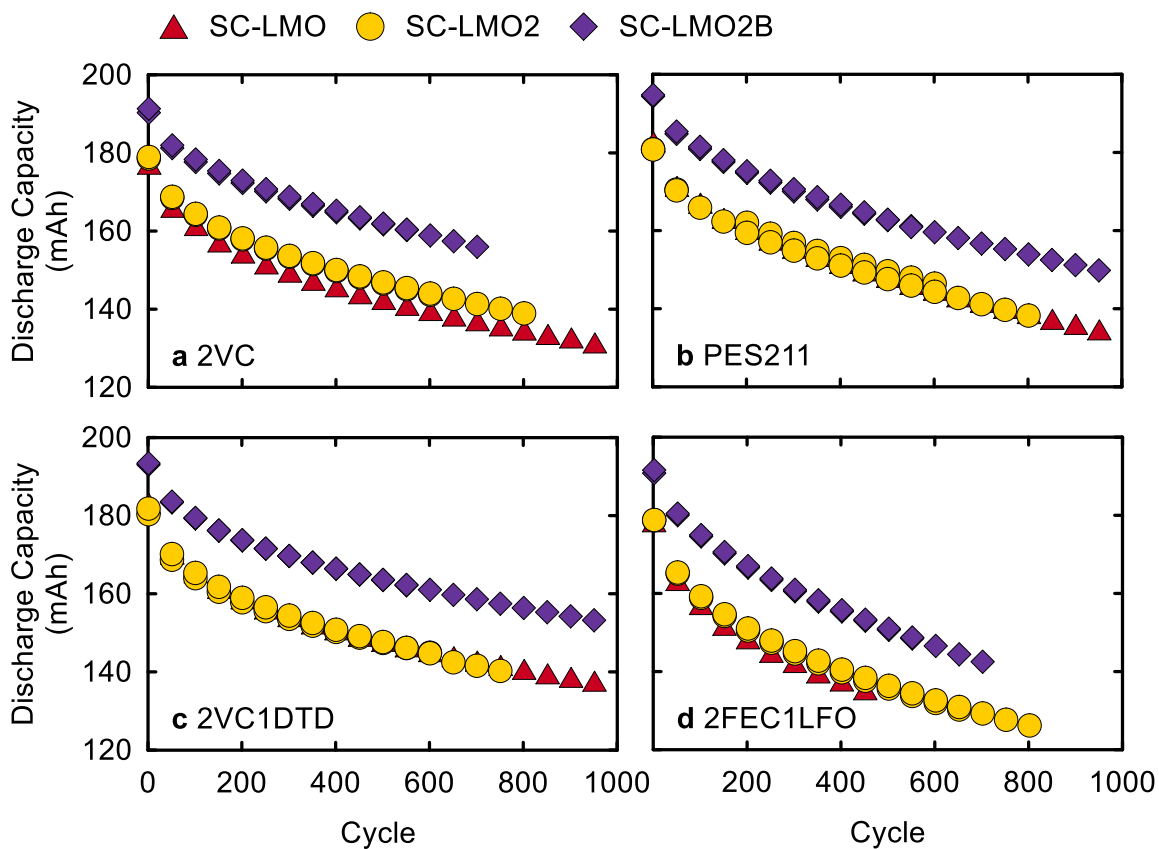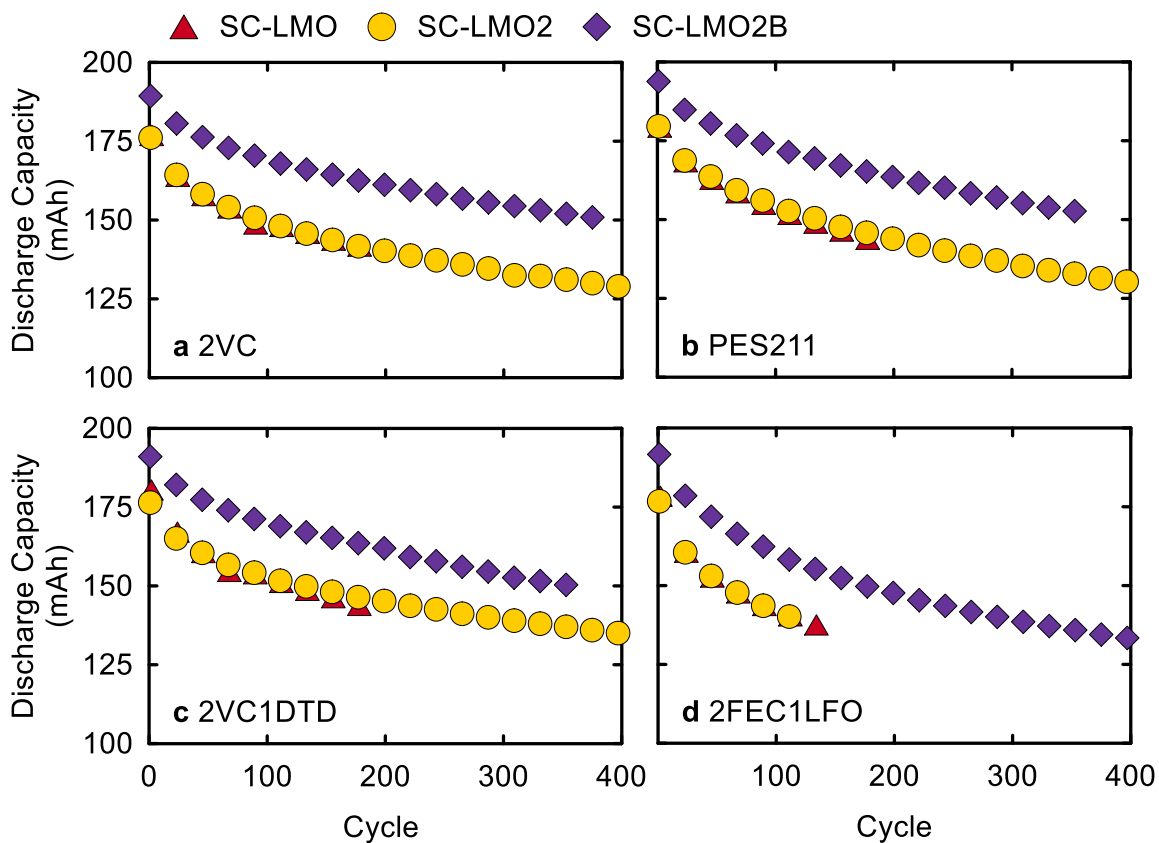
Figure A.24. Normalized ΔV versus cycle number for SC-LMO, SC-LMO2, and SC-LMO2B pouch cells cycled at RT with (a) 2VC; (b) PES211; (c) 2VC1DTD; or (d) 2FEC1LFO electrolytes. All cycling was done at C/3:C/3 and 3.0-4.20 V.
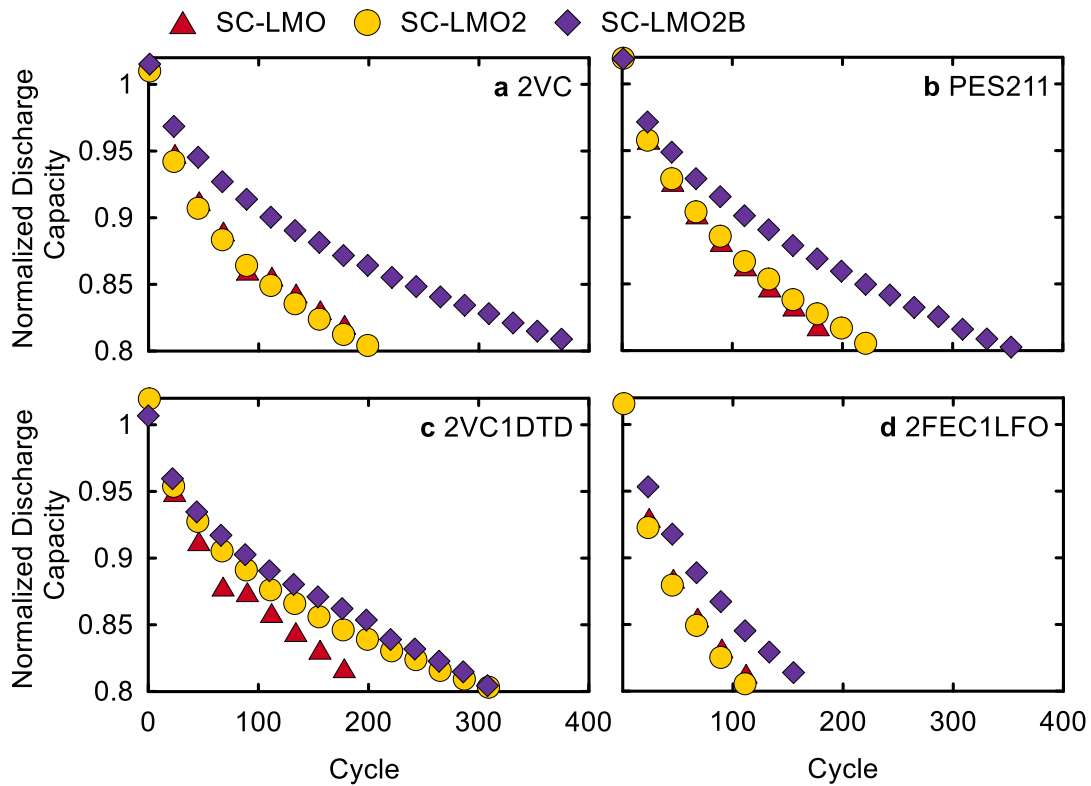
Figure A.25. Discharge capacity (mAh) versus cycle number for SC-LMO, SC-LMO2, and SC-LMO2B pouch cells cycled at 40 °C with (a) 2VC; (b) PES211; (c) 2VC1DTD; or (d) 2FEC1LFO electrolytes. All cycling was done at C/3:C/3 and 3.0-4.20 V.

Figure A.26. Discharge capacity (mAh) versus cycle number for SC-LMO, SC-LMO2, and SC-LMO2B pouch cells cycled at 55 °C with (a) 2VC; (b) PES211; (c) 2VC1DTD; or (d) 2FEC1LFO electrolytes. All cycling was done at C/3:C/3 and 3.0-4.20 V.
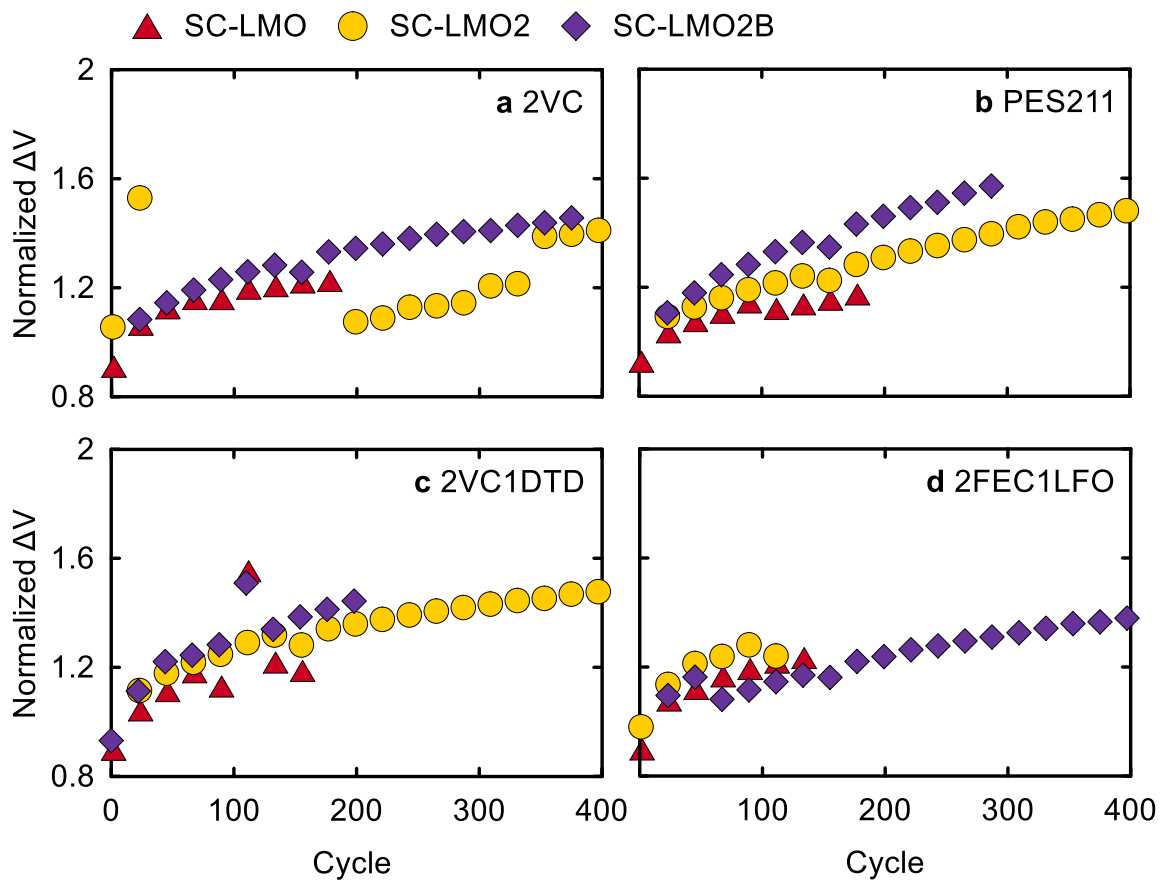
Figure A.27. Normalized discharge capacity versus cycle number for SC-LMO, SC-LMO2, and SC-LMO2B pouch cells cycled at 55 °C with (a) 2VC; (b) PES211; (c) 2VC1DTD; or (d) 2FEC1LFO electrolytes. All cycling was done at C/3:C/3 and 3.0-4.20 V.

Figure A.28. Normalized ΔV versus cycle number for SC-LMO, SC-LMO2, and SC-LMO2B pouch cells cycled at 55 °C with (a) 2VC; (b) PES211; (c) 2VC1DTD; or (d) 2FEC1LFO electrolytes. All cycling was done at C/3:C/3 and 3.0-4.20 V.
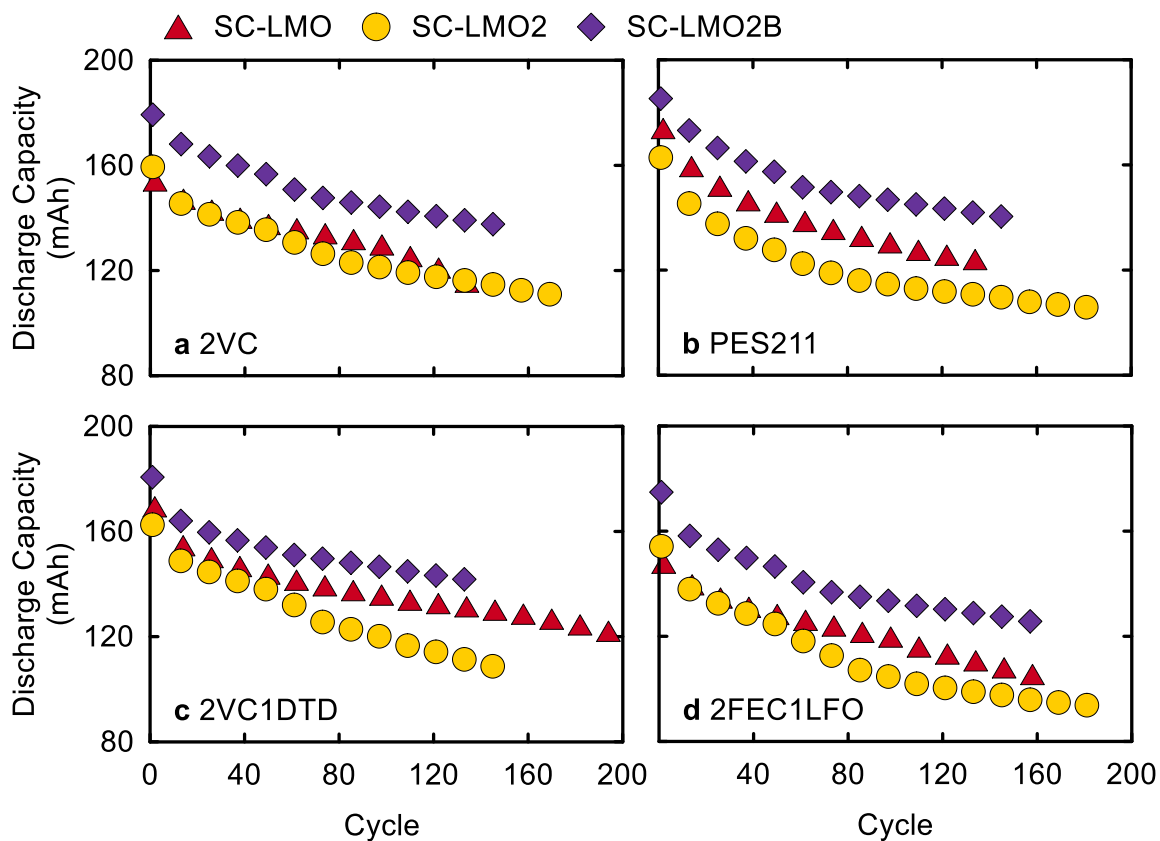
Figure A.29. Discharge capacity (mAh) versus cycle number for SC-LMO, SC-LMO2, and SC-LMO2B pouch cells cycled at 70 °C with (a) 2VC; (b) PES211; (c) 2VC1DTD; or (d) 2FEC1LFO electrolytes. All cycling was done at C/3:C/3 and 3.0-4.20 V.
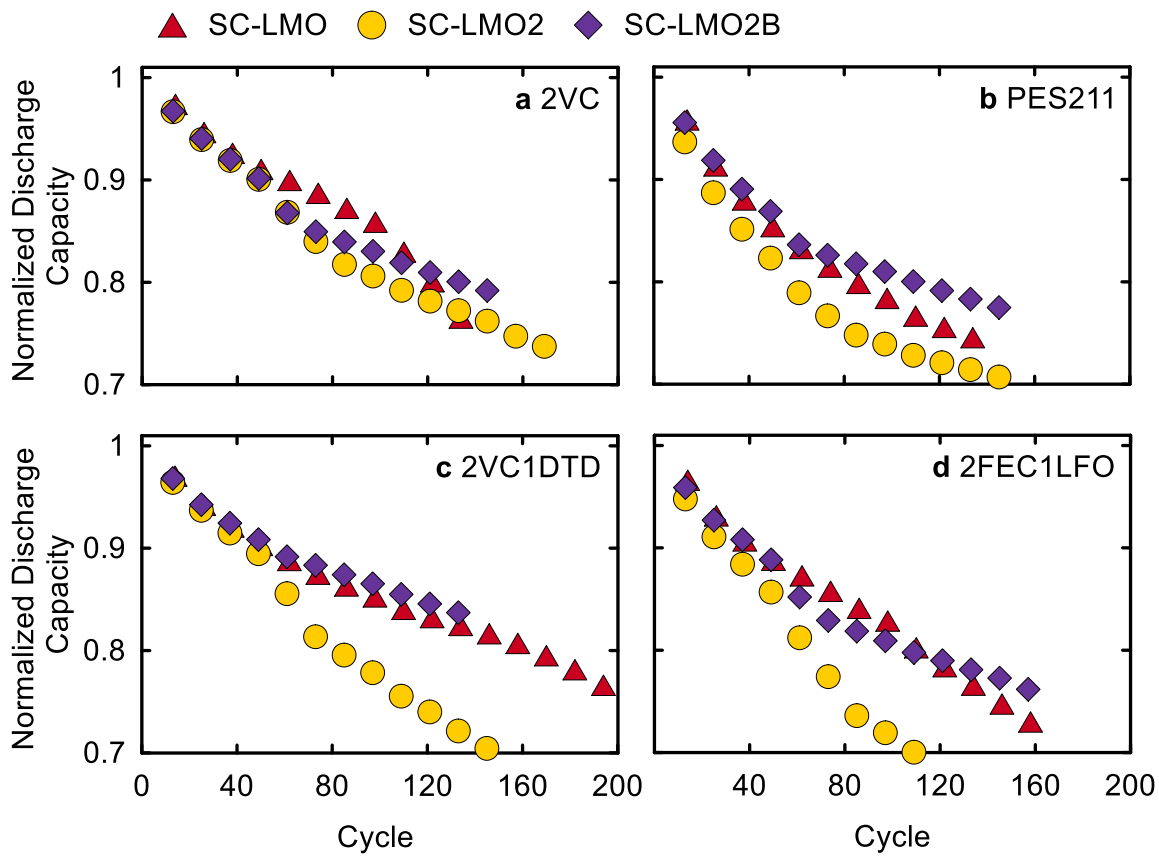
Figure A.30. Normalized discharge capacity versus cycle number for SC-LMO, SC-LMO2, and SC-LMO2B pouch cells cycled at 70 °C with (a) 2VC; (b) PES211; (c) 2VC1DTD; or (d) 2FEC1LFO electrolytes. All cycling was done at C/3:C/3 and 3.0-4.20 V.
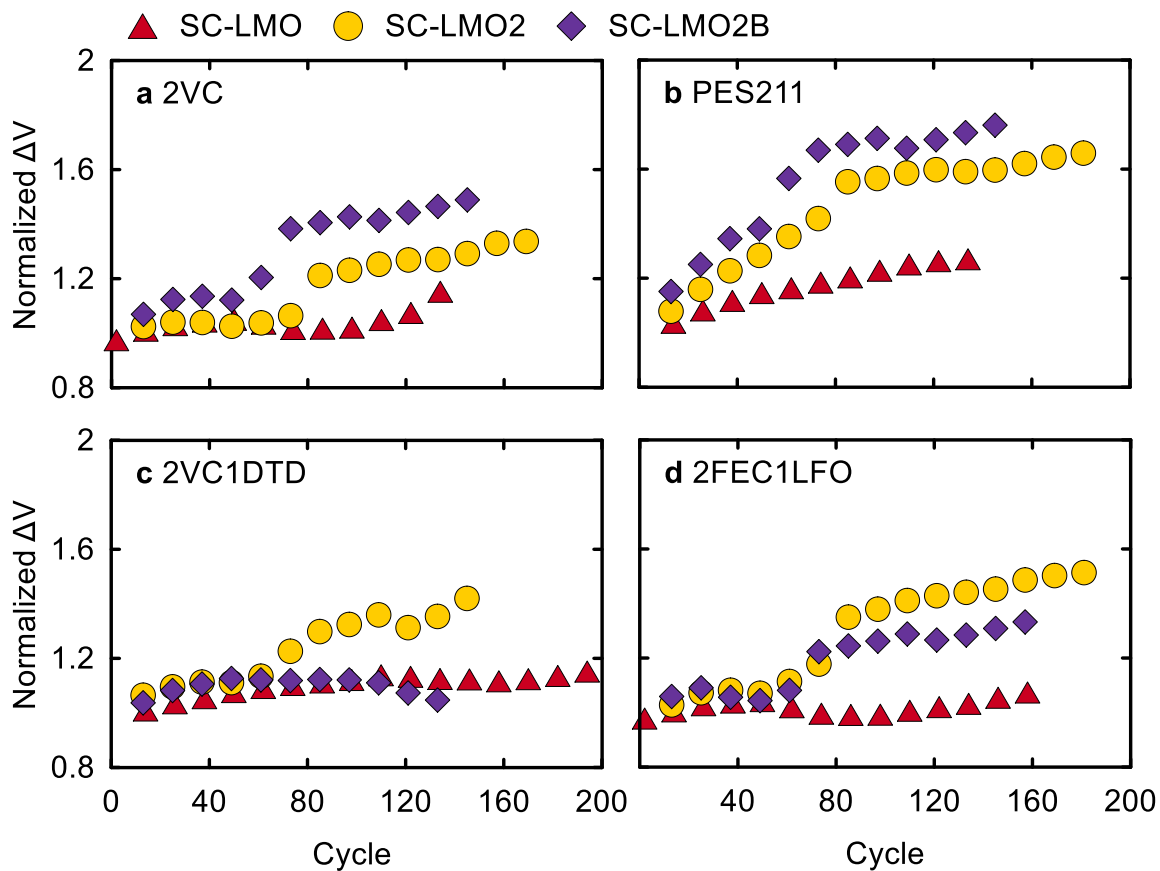
Figure A.31. Normalized ΔV versus cycle number for SC-LMO, SC-LMO2, and SC-LMO2B pouch cells cycled at 70 °C with (a) 2VC; (b) PES211; (c) 2VC1DTD; or (d) 2FEC1LFO electrolytes. All cycling was done at C/3:C/3 and 3.0-4.20 V.